

PL-TR-97-2123

# **INFRASOUND AND THE INFRASONIC MONITORING OF ATMOSPHERIC NUCLEAR EXPLOSIONS:**

## **A Literature Review**

**J. Michael McKisic**

**Tracor Applied Sciences, Inc.  
1601 Research Boulevard  
Rockville, MD 20850-3173**

**28 February 1997**

**Final Report**

**September 7, 1995 to February 28, 1997**

**Approved for public release; distribution unlimited.**



**DEPARTMENT OF ENERGY  
Office of Non-Proliferation  
and National Security  
WASHINGTON, DC 20585**


**[DTIC QUALITY INSPECTED 3]**



**PHILLIPS LABORATORY  
Directorate of Geophysics  
AIR FORCE MATERIEL COMMAND  
HANSCOM AFB, MA 01731-3010**

**19980311 119**

"This technical report has been reviewed and is approved for publication"



CLAIRE A MARCOTTE  
PL/GP R&D Contracts Liaison



CHARLES P. PIKE, Director  
Business Management Division

This report has been reviewed by the ESC Public Affairs Office (PA) and is releasable to the National Technical Information Service (NTIS).

Qualified requesters may obtain additional copies from the Defense Technical Information Center (DTIC). All others should apply to the National Technical Information Service (NTIS).

If your address has changed, if you wish to be removed from the mailing list, or if the addressee is no longer employed by your organization, please notify PL/IM, 29 Randolph Road, Hanscom AFB, MA 01731-3010. This will assist us in maintaining a current mailing list.

Do not return copies of this report unless contractual obligations or notices on a specific document require that it be returned.

**REPORT DOCUMENTATION PAGE**Form Approved  
OMB No. 0704-0188

Public reporting burden for this collection of information is estimated to average 1 hour per response, including the time for reviewing instructions, searching existing data sources, gathering and maintaining the data needed, and completing and reviewing the collection of information. Send comments regarding this burden estimate or any other aspect of this collection of information, including suggestions for reducing this burden, to Washington Headquarters Services, Directorate for Information Operations and Reports, 1215 Jefferson Davis Highway, Suite 1204, Arlington, VA 22202-4302, and to the Office of Management and Budget, Paperwork Reduction Project (0704-0188), Washington, DC 20503.

<b>1. AGENCY USE ONLY (Leave blank)</b>		<b>2. REPORT DATE</b> 28 February 1997	<b>3. REPORT TYPE AND DATES COVERED</b> Final 7 September 1995 to February 28, 1997	
<b>4. TITLE AND SUBTITLE</b> Infrasound and the Infrasonic Monitoring of Atmospheric Nuclear Explosions: A Literature Review			<b>5. FUNDING NUMBERS</b> PE: 69120H PR DENN TA GM WU AZ Contract: F19628-95-C-0191	
<b>6. AUTHOR(S)</b> J. Michael McKisic				
<b>7. PERFORMING ORGANIZATION NAME(S) AND ADDRESS(ES)</b> Tracor Applied Sciences, Inc. 1601 Research Boulevard Rockville, MD 20850-3173			<b>8. PERFORMING ORGANIZATION REPORT NUMBER</b>	
<b>9. SPONSORING / MONITORING AGENCY NAME(S) AND ADDRESS(ES)</b> Phillips Laboratory 29 Randolph Road Hanscom AFB, MA 01731-3010  R&D Contracts Liaison: Claire Marcotte			<b>10. SPONSORING / MONITORING AGENCY REPORT NUMBER</b>  PL-TR-97-2123	
<b>11. SUPPLEMENTARY NOTES</b>  This research was sponsored by the Department of Energy, Office of Non-Proliferation and National Security, Washington, DC 20585				
<b>12a. DISTRIBUTION / AVAILABILITY STATEMENT</b>  Approved for public release; distribution unlimited			<b>12b. DISTRIBUTION CODE</b>	
<b>13. ABSTRACT (Maximum 200 words)</b> <p>This report reviews unclassified past work in infrasound and atmospheric acoustics deemed relevant to current interests in monitoring compliance with a CTBT (Comprehensive Test Ban Treaty). The report is one of four resulting from a DOE sponsored seventeen month investigation and review of past work in infrasound.</p> <p>The purpose of the report is to update previous reviews and to provide members of the research and development and governmental policy making communities, with an interest in or responsibility for monitoring compliance to CTBT, with a thorough and relatively self-contained document summarizing the primary essentials of current and past work in infrasonic research.</p> <p>Following a background section, the report reviews: (1) the measurement of infrasound; (2) early work in infrasound and atmospheric acoustics; (3) propagation and explosive source modeling; (4) various natural and man made sources of infrasound and (5) data and waveforms from a number of nuclear and chemical explosions. The report contains one Appendix which provides waveforms of atmospheric nuclear explosions recorded on Columbia University's Lamont-Doherty Laboratory's microbarograph arrays as originally published by <i>Donn and Ewing</i> (1967).</p>				
<b>14. SUBJECT TERMS</b> Infrasound; Infrasonic Monitoring; CTBT Compliance; Atmospheric Nuclear Explosions; Long Range Acoustic Propagation in the Atmosphere; Explosion Source Modeling; Background Sources of Infrasonic Noise; and Nuclear Explosion Waveforms			<b>15. NUMBER OF PAGES</b> 320	
			<b>16. PRICE CODE</b>	
<b>17. SECURITY CLASSIFICATION OF REPORT</b> Unclassified	<b>18. SECURITY CLASSIFICATION OF THIS PAGE</b> Unclassified	<b>19. SECURITY CLASSIFICATION OF ABSTRACT</b> Unclassified	<b>20. LIMITATION OF ABSTRACT</b> SAR	

## TABLE OF CONTENTS

	<u>Page</u>
1.0 INTRODUCTION	1
2.0 BACKGROUND	6
2.1 General Discussion	6
2.2 Acoustic-Gravity Waves	36
3.0 THE MEASUREMENT OF INFRASOUND	50
4.0 EARLY WORK IN INFRASOUND AND ATMOSPHERIC ACOUSTICS: 1874 - 1949	68
5.0 PROPAGATION AND SOURCE MODELING	89
6.0 NATURAL AND MAN MADE SOURCES OF INFRASOUND	140
6.1 Aurora	140
6.2 Avalanches	149
6.3 Bolides or Meteorites	151
6.4 Bridges	163
6.5 Earthquakes	163
6.6 Industrial Sources	168
6.7 Jet Stream	169
6.8 Microbaroms	173
6.9 Microbursts	179
6.10 Missile Launches	182
6.11 Mountain Associated Waves	189
6.12 Satellite Re-Entry	195
6.13 Severe Storms	197
6.14 Solar Eclipse	215



6.15 Solitary Waves	217
6.16 Sonic Boom	220
6.17 Thunder and Lightning	226
6.18 Volcanoes	234
7.0 WAVEFORM DATA PRODUCED BY NUCLEAR AND CHEMICAL ATMOSPHERIC EXPLOSIONS	243
8.0 REFERENCES	268
APPENDIX A: THE LAMONT-DOHERTY WAVEFORM LIBRARY	290

## ABSTRACT

This report reviews unclassified past work in infrasound and atmospheric acoustics deemed relevant to current interests in monitoring compliance to a CTBT (Comprehensive Test Ban Treaty). The report is one of four resulting from a DOE (Department of Energy) sponsored seventeen month investigation and review of past work in infrasound. Other project related reports include: an annotated bibliography of selected papers in infrasound [McKisic (1996a)]; a review of past work in the infrasonic monitoring of atmospheric nuclear explosions [McKisic (1996b)]; and a collection of relevant environmental data involving northern and southern hemispheric temperature, wind speed and cloud cover data [McKisic, (1996c)].

The purpose of the report is to update previous reviews and to provide members of the research and development and governmental policy making communities with an interest in or responsibility for monitoring compliance to a CTBT with a relatively self-contained document summarizing the primary essentials of current and past work in infrasonic research.

For purposes of exposition, the report is divided into eight main sections and one Appendix which provides waveforms of atmospheric nuclear explosions recorded on Columbia University's Lamont-Doherty Laboratory's microbarograph network [Donn and Shaw (1967)].

Section 2.0 (Background) provides an overall description of the temperature, wind and sound speed structure of the northern and southern hemispheric atmospheres to illustrate how these variables effect long range sound propagation. A brief listing of past work in the area of acoustic-gravity wave propagation and generation *per se* is provided along with a short introduction to the subject specialized to an isothermal atmosphere. Recent theoretical work on incorporating point mass and energy injection sources into atmospheric propagation models [Kanamori, Mori and Harkrider (1994)] is also discussed as the subject is of considerable interest to the infrasonic modeling community.

Section 3.0 (The Measurement of Infrasound) reviews past and current technology and instrumentation involved the measurement of infrasound and discusses some of the signal processing techniques which have been used to estimate source-location and reduce background clutter: e.g., the cross-correlation and impulse response methods and the f-k spectral estimation method.

Section 4.0 (Early Work in Infrasound and Atmospheric Acoustics: 1874-1949) provides a high level review of some of the earliest work in atmospheric acoustics which revolved around studies of pressure waves caused by the eruption of the Krakatoa volcano, the impact of the great Siberian meteorite and the oscillations of the earth's atmosphere, and studies on the formation of zones of audibility and silence.

Section 5.0 (Propagation and Source Modeling) reviews past work relevant to the modeling of long range pulse propagation in the atmosphere beginning with the pioneering work of Scorer (1950) and ending with the recent work of Pierce (1990) who derived a new and approximate wave equation applicable to an unsteady and inhomogeneous fluid which may find use in both atmospheric and underwater acoustics.

Section 6.0 (Natural and Man Made Sources of Infrasound) reviews work performed to understand the background infrasonic noise field which was conducted, in large part, as a result of the requirements of past atmospheric nuclear explosion monitoring

efforts. The section reviews eighteen separate sources of infrasound or acoustic-gravity waves.

Section 7.0 (Data and Waveforms from Nuclear and Chemical Explosions) provides selected examples of waveforms produced by nuclear and chemical explosions encountered during the conduct of the review. They are provided, as are those presented in Appendix A, for their general interest and as examples which theorists can use to test and validate computer propagation models.

The main body of the report concludes with Section 8.0 which provides a listing of all references cited in the report.

### **ACKNOWLEDGMENTS**

The author would like to express his sincere appreciation to Dr. Robert Blandford of AFTAC for suggesting this work and to Ms. Leslie Casey of the DOE for her support and encouragement during its conduct. Special appreciation is due Drs. Dean Clauter and Eugene Smart at AFTAC and Drs. Douglas Revelle and Rodney Whitaker of the Los Alamos National Laboratory for their assistance in locating some of the references. Dr. Delaine Reiter of the Phillips Laboratory served as Contract Monitor.

## 1.0 INTRODUCTION

This report reviews unclassified past work in infrasound and atmospheric acoustics deemed relevant to current interests in monitoring compliance to a CTBT (Comprehensive Test Ban Treaty). The report is one of four resulting from a DOE (DOE) sponsored seventeen month investigation and review of past work in infrasound. Other project related reports include: an annotated bibliography of selected papers in infrasound [McKisic (1996a)]; a review of past work in the infrasonic monitoring of atmospheric nuclear explosions [McKisic (1996b)]; and a collection of relevant environmental data involving northern and southern hemispheric temperature, wind speed and cloud cover data [McKisic, (1996c)].

Prior reviews or collections of papers on various aspects of infrasound include:

- *Haurwitz* (1941) who developed various analytical and geometrical optics based expressions for atmospheric propagation including the effects of temperature and wind;
- *Ingard* (1953) who reviewed such meteorological effects as viscosity, humidity, temperature, wind, ground attenuation and turbulence on atmospheric sound propagation;
- *Cox* (1958) who reviewed atmospheric sound propagation from a ray theory point of view deriving a number of simple analytical forms for intensity and travel time, as well as discussing the so-called anomalous or abnormal sound propagation in the atmosphere;
- the Special 1971 issue of the *Geophysical Journal of the Royal Astronomical Society* (1971);
- *Georges and Young* (1972) who reviewed infrasonic sensing techniques, fundamental concepts and various sources of infrasound [e.g., microbaroms, earthquakes, auroral waves, volcanoes, meteorites, weather fronts, severe storms, etc.];
- *Gossard and Hooke* (1975) whose excellent text presents a very complete summary of the generation, propagation and detection of infrasound and acoustic-gravity waves in addition to several other topics;

- *Kulichkov* (1992) who reviewed several geophysical sources of infrasound [auroras, microbaroms, sonic booms, thunderstorms, volcanic eruptions, explosions]; and
- *Wilson, Olson and Spell* (1995) who also reviewed various geophysical sources of infrasound [auroral infrasonic waves (AIWs), microbaroms, volcanic infrasound, earthquake infrasound and mountain associated waves (MAWs)].

The purpose of the report is to update previous reviews and to provide members of the research and development and governmental policy making communities with an interest in or responsibility for monitoring compliance to a CTBT with a relatively self-contained document summarizing the primary essentials of current and past work in infrasonic research. The report is aimed, primarily, to those readers not having a background in the physics of infrasound and reviews only aeroacoustics work of relevance to long range sound propagation in the atmosphere.

For purposes of exposition, the report is divided into eight main sections and one Appendix which provides waveforms of atmospheric nuclear explosions recorded on Columbia University's Lamont-Doherty Laboratory's microbarograph network [*Donn and Shaw* (1967)].

Section 2.0 (Background) is divided into two subsections. The first is intended to provide an overall description of the temperature, wind and sound speed structure of the atmosphere and to illustrate how these variables effect long range sound propagation. Because of current concerns with infrasonic monitoring in the southern hemisphere, the subsection is written in such a way as to contrast the properties and behavior of the southern atmosphere with those of the much better known northern hemisphere.

The second subsection provides a brief listing of past work in the area of acoustic-gravity wave propagation and generation *per se* and provides a brief introduction to the subject specialized to an isothermal atmosphere. Recent theoretical work on incorporating point mass and energy injection sources into atmospheric propagation models [*Kanamori,*

*Mori, and Harkrider* (1994)] is also discussed as the subject is of considerable interest to the infrasonic modeling community.

Section 3.0 (The Measurement of Infrasound) reviews past and current technology and instrumentation involved the measurement of infrasound and discusses some of the signal processing techniques which have been used to estimate source-location and reduce background clutter: e.g., the cross-correlation and impulse response methods and the f-k spectral estimation method.

Section 4.0 (Early Work in Infrasound and Atmospheric Acoustics: 1874-1949) provides a high level review of some of the earliest work in atmospheric acoustics which revolved around studies of pressure waves caused by the eruption of the Krakatoa volcano, the impact of the great Siberian meteorite and the oscillations of the earth's atmosphere, and studies on the formation of zones of audibility and silence.

Section 5.0 (Propagation and Source Modeling) reviews past work relevant to the modeling of long range pulse propagation in the atmosphere beginning with the pioneering work of *Scorer* (1950) and ending with the recent work of *Pierce* (1990) who derived a new and approximate wave equation applicable to an unsteady and inhomogeneous fluid which may find use in both atmospheric and underwater acoustics. The review of the work is presented in chronological order and is intended to illustrate that improvements in modeling were made possible by an improved understanding of the earth's atmosphere and properties.

Section 6.0 (Natural and Man Made Sources of Infrasound) reviews work performed to understand the background infrasonic noise field which was conducted, in large part, as a result of the requirements of past atmospheric nuclear explosion monitoring efforts. The section reviews eighteen separate sources of infrasound or acoustic-gravity waves and can be regarded as updating past reviews on the subject. Where possible, example waveforms produced by each source have been provided. Table 1, reproduced

# Passive Sensing of Acoustic-Gravity Waves

## Observed Characteristics of Natural Acoustic-Gravity Waves

OBSERVED CHARACTERISTICS	WAVE TYPE		NATURE OF SOURCE	VOLCANO and METEOR IMPACT	"AURORAL"	"MICROBAROMS"	"FRONTAL PASSAGE"	"SEVERE WEATHER"	"JET STREAM"	"MOUNTAIN ASSOCIATED"	"BOUNDARY LAYER GRAVITY WAVES"
	WAVE PERIOD (Seconds)	WAVE AMPLITUDE (μbar 0 peak)									
WAVE PERIOD (Seconds)	12-25 (0.5-80)*	12-25 (1-30)	IMPULSIVE via Seismic	EXPLOSIVE	SERIES OF IMPULSES (Bow Shock?)	CONTINUOUS (Air-Sea-Wave interaction?)	PRESSURE JUMP & BUOYANCY OSCILLATIONS?	UNKNOWN (1. Penetrative Convection? 2. Lightning? 3. Turbulence?)	UNKNOWN (Shear Instabilities?)	OROGRAPHIC?	AERODYNAMIC SHEAR INSTABILITIES?
WAVE AMPLITUDE (μbar 0 peak)	1-10 (0.1-20)	1-2 (0.1-20)	Direct Air Wave	up to 5000	10-400	5-7 (2-8)	180-1500 (180-1800)	12-60 (6-300)	20-70 (10-120)	20-70 (10-120)	300-900 (250-1500)
DURATION	up to 1 hr. Depends mainly on distance and dispersive properties of media.	up to 1 hr. Depends mainly on distance and dispersive properties of media.			Seconds to hours	0.1-1 (0.1-5)	(50-2000)	0.5-3 (0.1-20)	50-200 (10-1000)	0.5-3 (0.1-10)	25-200 (10-1000)
HORIZONTAL TRACE SPEED (m/sec)	3k-15k	340 (320-360)	Vertical	from Source	400-1200	340	2-20	330-360 (330-450)	15-75	340 (330-360)	5-20 (2-20?)
DIRECTION OF TRAVEL		from Epicenter ±60°		from Source	from intersection of Midnight Meridian with Auroral Zone	from certain Oceanic "Centers of Activity," e.g., North Atlantic Gulf of Alaska	Direction of Frontal Travel	from Centers of Strong Convective Activity; Mainly Midwest	Flow Direction	Coastal/Mountain locations; e.g., West Coast of Canada, Argentina/Chile	Mean Wind
TRANSVERSE COHERENCE DISTANCE (to zero correlation)	not measured	not measured		~ 141	Large at Low Latitudes; 10° Azimuth & Elevation Fluctuations	~ 21	not measured	~ 141	not measured	~ 141	1-151
DISTINGUISHING PROPERTIES	Seismic Dispersion	Long Periods precede Short Periods		Long Periods precede Short Periods	High Speeds; Short Impulse precedes Long Periods. Observed at Magnetic Latitudes >30°	Nearly Monochromatic; Beaded Wave Envelope; Low Coherence	Large Amplitude; Often Wavelet	Azimuth Change with Time; Spring/Summer Peak	Low Phase Velocities	Fixed Azimuth for up to Days; Local Winter Occurrence	Probably Exist down to Smaller Scales than Presently Studied; Usually Advected by Mean Wind

\* Figures indicate nominal values; those in parentheses indicate extremes.

[After Georges and Young (1972)]

Table 1. A listing of observed characteristics of infrasonic waves produced by natural sources. [Table adopted from *Georges and Young (1972)*.]

from the excellent review of *Georges and Young* (1972), provides a concise summary of known important infrasound sources and their properties as of 1972.

Section 7.0 (Waveform Data Produced by Nuclear and Chemical Atmospheric Explosions) provides selected examples of waveforms produced by nuclear and chemical explosions encountered during the conduct of the review. They are provided, as are those presented in Appendix A, for their general interest and as examples which theorists can use to test and validate computer propagation models.

The main body of the report concludes with Section 8.0 which provides a listing of all references cited in the report.



## 2.0 BACKGROUND

In this section, a general background discussion on the atmosphere and its influence on sound propagation is provided and the basic physics of the generation and propagation of acoustic-gravity waves is provided.

### 2.1 General Discussion

The long range propagation of sound in the atmosphere is controlled by the latter's distributions of temperature and wind velocity as a function of height above the earth's surface and as a function of horizontal range. In the absence of wind, temperature is the controlling factor as it determines sound speed in a gas such as the earth's atmosphere through *Laplace's* relation

$$c = (\gamma p / \rho)^{1/2} \quad (2.1)$$

where  $\gamma$  is the ratio of the specific heat of air at constant pressure to the specific heat at constant volume (i.e.,  $\gamma = C_p/C_v$ ),  $p$  is the pressure and  $\rho$  is the density. For an ideal gas, the equation of state can be written

$$p = \frac{\rho R T}{M} \quad (2.2)$$

where  $R$  is the universal gas constant [ $=8.314$  joule/(mole)(K<sup>0</sup>)],  $T$  is the absolute temperature and  $M$  is the molecular weight of the gas. Substitution of (2.2) into (2.1) leads to the expression

$$c = \left( \frac{\gamma R T}{M} \right)^{1/2} \quad (2.3)$$

For dry air,  $\gamma = 1.403$ , and  $M = 2.897 \times 10^{-2}$  kg/mole so that, numerically, Eq. (2.1) becomes

$$c \approx 20.07 \sqrt{T} \quad (2.4)$$

Figure 1 provides the details of the temperature structure of the earth's atmosphere as a function of height from the surface of the earth to an altitude of 400 km based on data for the U.S. Standard Atmosphere 1976 [NOAA/NASA/USAF (1976)]. The

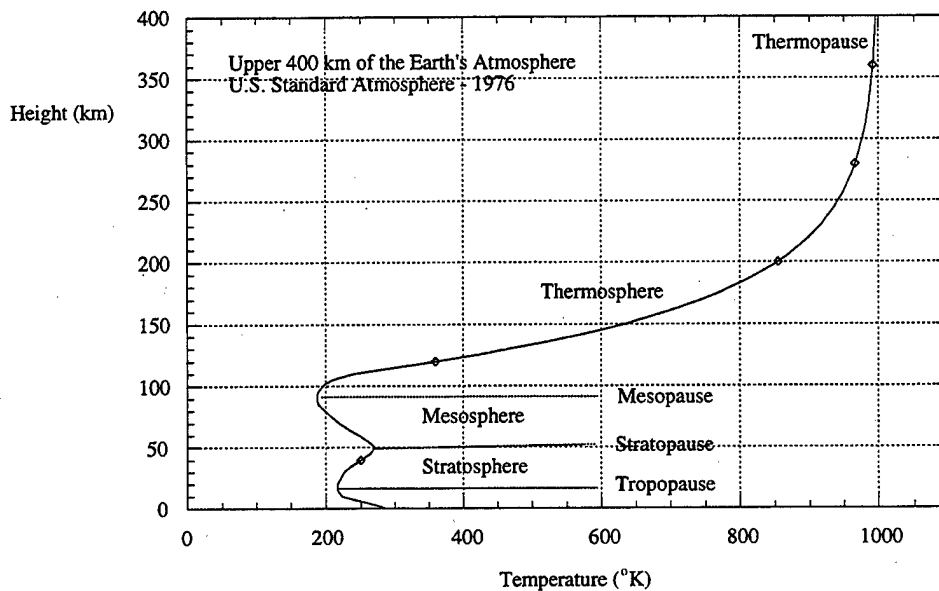


Figure 1. The temperature structure of the earth's atmosphere from the surface of the earth to an altitude of 400 km based on the conventions of the U.S. Standard Atmosphere 1976 [NOAA, NASA, USAF (1976)].

figure is useful for indicating the approximate heights of the atmosphere's major divisions: troposphere, stratosphere, mesosphere and thermosphere. Figure 2 provides more detail on the temperature structure of the earth's atmosphere from the surface of the earth to an altitude of 120 km which is the most important region for acoustic propagation and, accordingly, for issues involving the infrasonic monitoring of atmospheric nuclear explosions.

As indicated in the figures, temperature decreases with increasing height in the troposphere (literally, "the turning or changing sphere") or lowest part of the atmosphere until a region is reached at approximately 15 km in altitude in which the temperature remains constant with increasing height: the tropopause. As discussed, for example, by Wallace and Hobbs (1976), Kato (1981) and by Gill (1982), the troposphere or "convective layer" is characterized by strong vertical mixing and contains more than 80% of the atmosphere's mass. The region accounts for virtually all of the earth's water vapor and

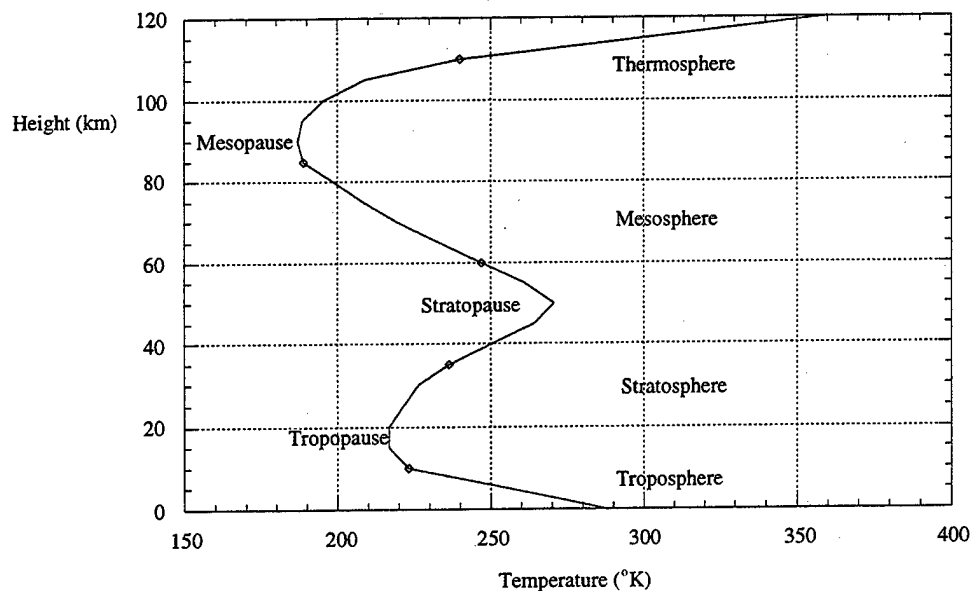


Figure 2. The temperature of the earth's atmosphere from the earth's surface to an altitude of 120 km based on the conventions of the U.S. Standard Atmosphere 1976 [NOAA/NASA/USAF (1976)].

clouds as well as all precipitation and thunderstorm activity. The decrease in temperature with increasing height in the troposphere is primarily caused by the thermodynamics of adiabatic expansion.

Above the tropopause, in the region referred to as the stratosphere (literally, "the layered sphere") temperature increases with increasing height until another region is reached, at approximately 50 km in altitude, where the temperature remains constant with increasing height: the stratopause. The stratosphere, together with the troposphere contain approximately 99% of the atmospheric mass. The stratosphere is physically characterized by very small vertical mixing as is evident from the very abrupt decrease in water vapor concentration and increase in ozone concentration occurring at the tropopause-stratosphere boundary, and by the observed long residence times of volcanic and nuclear explosion debris. The reason that the temperature increases with increasing height in the stratosphere is "due to radiative heating by ozone O<sub>3</sub>. The heat balance is established between ultraviolet

absorption of  $O_3$  and infrared radiation from water vapor ( $H_2O$ ), carbon dioxide ( $CO_2$ ) and  $O_2$ ". [Kato (1981)].

Above the stratopause, in the region referred to as the mesosphere, the temperature again decreases with increasing height until another region is reached, at an altitude of approximately 90 km, in which the temperature remains constant with increasing altitude: the mesosphere. The observed mesospheric decrease in temperature with increasing height is due to "radiative heating by dissociation of molecular oxygen in the lower thermosphere, and by ionization of O, etc," [Kato (1981)].

The mesosphere (literally "middle sphere"), like the troposphere, is characterized by vertical mixing and "during summer there is sometimes enough lifting to produce thin cloud layers in the upper mesosphere over parts of the polar regions. Under ordinary conditions the concentrations in these clouds are far too small to render them visible from the ground. However, at twilight mesospheric clouds are sometimes still in sunlight while the lower atmosphere is in the earth's shadow. Under such conditions such clouds are visible from the ground as *noctilucent clouds*" [Wallace and Hobbs (1977)].

Finally, above the mesopause, there is the thermosphere which extends to a height of 1000 km and in which the temperature increases with increasing height until an asymptote is reached, at an altitude of approximately 500 km, which is essentially isothermal: the thermopause. The temperature distribution of the thermosphere above 120 km is controlled by solar activity and the asymptotic temperature ranges between 500°K (a "quiet sun") and 2000°K (an "active sun"). The solar activity for the U.S. Standard Atmosphere 1976 is taken to be moderate as the asymptotic temperature is seen to be 1000°K. Figure 3 provides the sound speed profile of the earth's atmosphere from the earth's surface to an altitude of 120 km based on data from the U.S. Standard Atmosphere 1976 model and as computed from Eq. (2.4). The profile is seen to be inhomogeneous and characterized by two channels the axes of which are located at the approximate altitudes

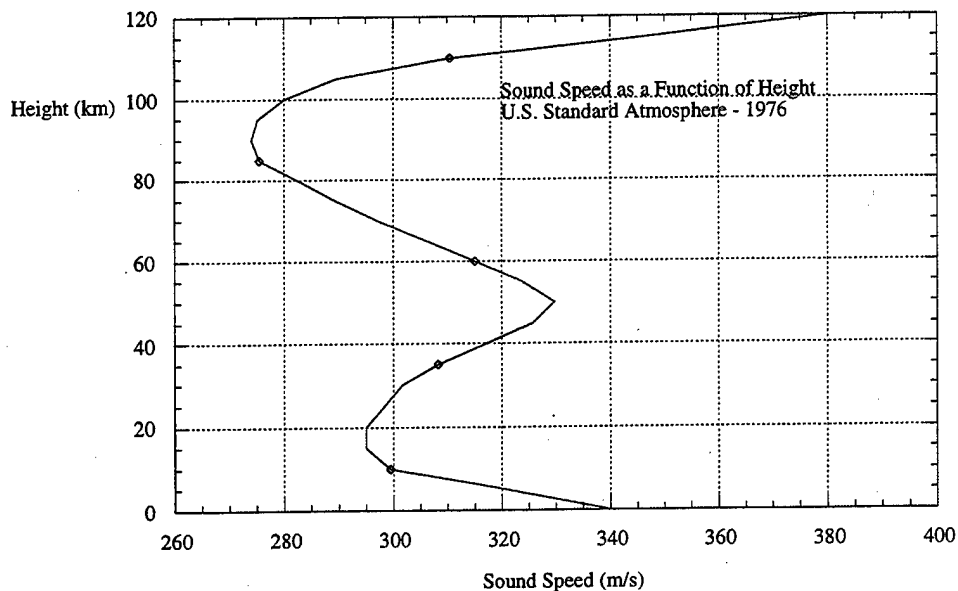


Figure 3. Sound speed (m/s) as a function of height for the U.S. Standard Atmosphere 1976 [NOAA/NASA/USAF (1976)]. As indicated, there are two distinct sound channels: a lower channel with an axis at approximately 18 km and an upper sound channel with an axis at approximately 90 km height.

of 18 km and 90 km. The fact that the profile is inhomogeneous implies that acoustic propagation will be controlled by refraction (i.e., the acoustic ray paths will not correspond to straight lines) and the existence of sound channels implies that, under the appropriate conditions, acoustic energy can be trapped in the channels and propagated to significant ranges. The channels are the atmospheric analog to the well known SOFAR (Sound Fixing and Ranging) channel in the ocean which is responsible for the very efficient and long range propagation of low frequency acoustic energy in that medium. Figure 4 provides a ray trace for acoustic energy propagating from a source located on the earth's surface to a horizontal range of 1000 km. As indicated, there are reflections from both the stratosphere and the ionosphere.

In addition to temperature, the other variable which controls acoustic propagation in the atmosphere is the wind which determines the effective sound speed,  $c_{eff}$ , through the

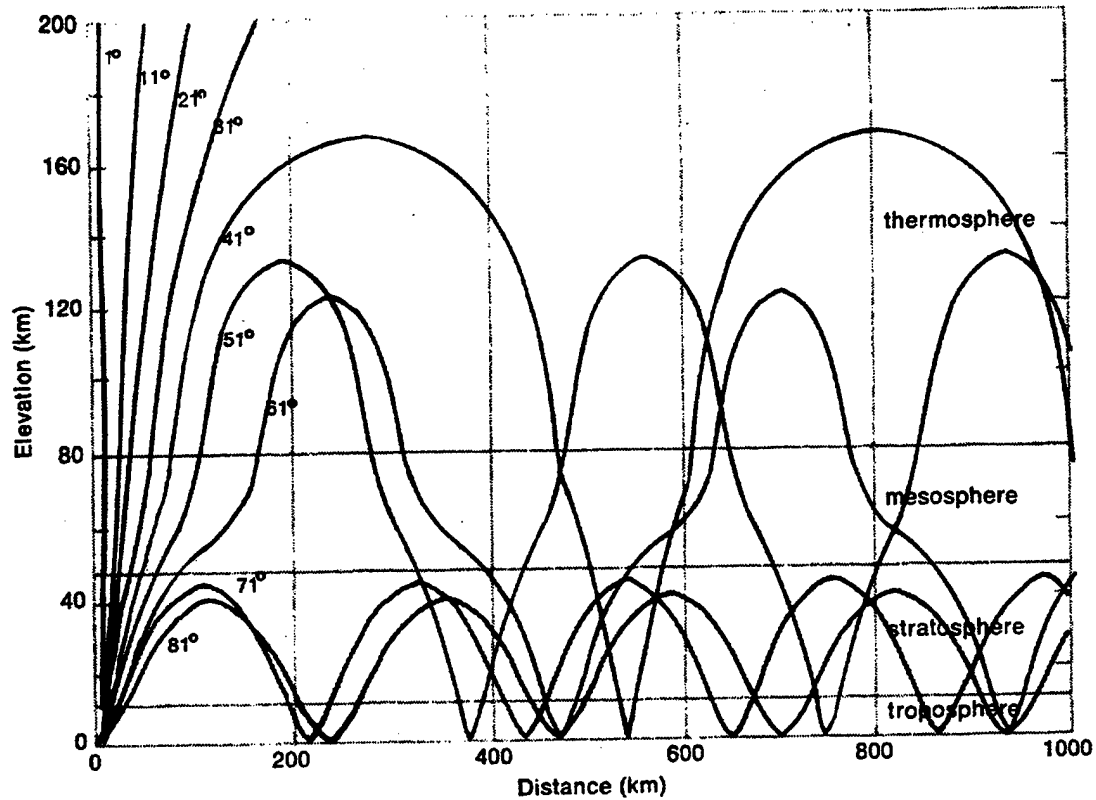


Figure 4. Ray paths for a sound source on the ground to a range of 1000 km including both stratospheric and ionospheric reflections. [Figure adopted from *Donn* (1978).]

relation

$$c_{\text{eff}} = c_T + \mathbf{n} \cdot \mathbf{v} \quad (2.5)$$

where in the above,  $c_T$ , is the contribution due to temperature and the last term is the contribution of the wind. The latter contribution enters as the "dot product" of a unit vector in the direction of propagation,  $\mathbf{n}$ , and the vector wind velocity,  $\mathbf{v}$ . The wind velocity is, in general, a strong function of height in the atmosphere, season, time of day and location. Eq. (2.5) implies that it is the component of the wind velocity in the direction of propagation which contributes to the effective sound speed. The transverse component of the wind is also important for atmospheric propagation as it produces horizontal refraction which contributes to significant uncertainty in bearing estimates from arrays of acoustic or infrasonic sensors (microbarographs) [e.g., *Georges and Beasley* (1977)].

For purposes of infrasonic monitoring, it is important to know and to characterize the variability of sound speed, as controlled by temperature and wind speed, as functions of season and hemispheric location. Such a characterization is made possible in an average sense through the existence of a data set referred to as the COSPAR (Committee on Space Research) International Reference Atmosphere: 1986 (0 km to 120 km). The data set is available from NASA's National Space Science Data Center and includes only the lower part (0 km to 120 km) of CIRA (COSPAR International Reference Atmosphere)-86. The latter consists of tables of the monthly mean values of temperature and zonal wind for the latitude range  $80^{\circ}\text{S}$  to  $80^{\circ}\text{N}$ . Two files exist, one in pressure coordinates, including also the geopotential heights, and one in height coordinates, including pressure values.

Figures 5 through 12 provide the zonally averaged CIRA-86 temperature profiles as a function of season (January, April, July and October), of atmospheric height in 5 km intervals, and as a function of latitude in the range extending from  $80^{\circ}\text{S}$  to  $80^{\circ}\text{N}$  for both the northern and southern hemispheres.

Inspection of the figures shows, first of all, that the profiles are essentially form invariant and that, for a given season and hemisphere, the primary variation in the temperature profiles is caused by changes in latitude which affect the locations of the tropopause, stratopause and mesopause. In addition, the location of the stratopause is almost always at an altitude of 50 km.

In January, the depth of the mesopause is seen to be approximately 10 km lower in the southern hemisphere than in the northern hemisphere (Figures 5 and 6). In the southern hemisphere the temperature of the mesopause increases by some  $50^{\circ}\text{K}$  as the equator is approached from  $80^{\circ}\text{S}$  whereas in the northern hemisphere the temperature of the mesopause increases by some  $20^{\circ}$  as  $80^{\circ}\text{N}$  is approached from the equator. The variability in the temperature of the stratopause does not appear to be as linear with change in latitude as is the case for the mesopause. In the southern hemisphere, the zonally

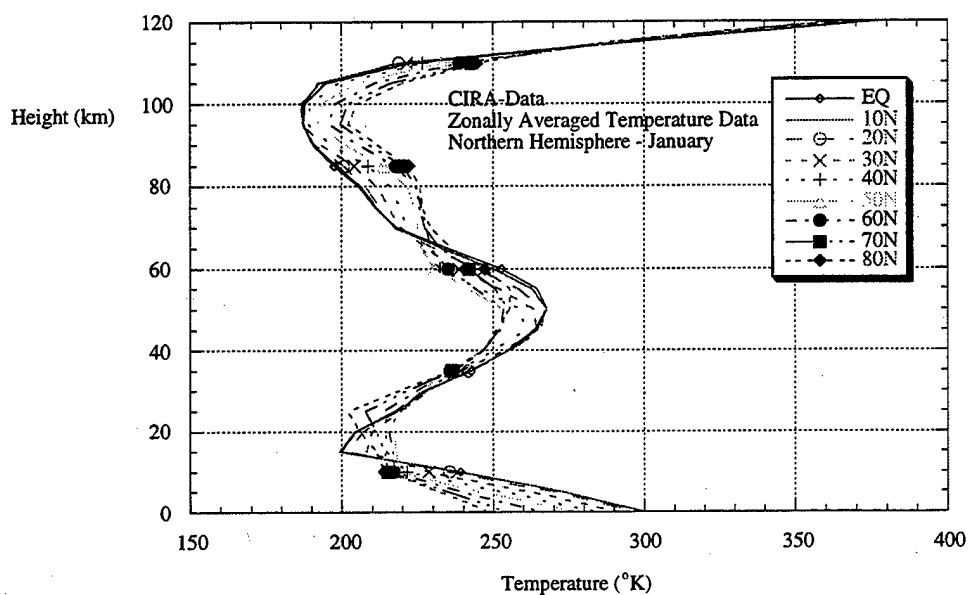


Figure 5. Zonally averaged temperature data as a function of height during the month of January for the northern hemisphere. [Figure constructed based on the CIRA-86 data set.]

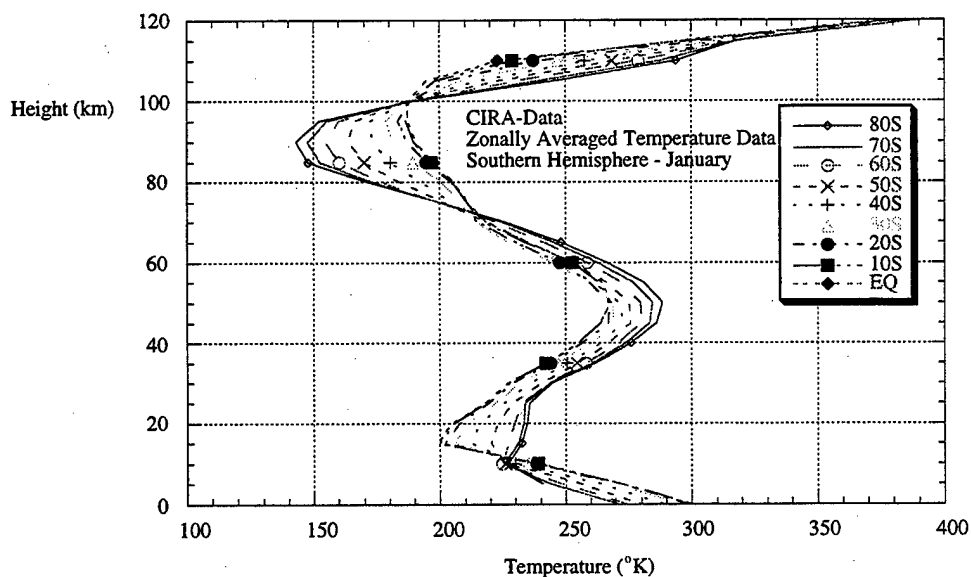


Figure 6. Zonally averaged temperature data as a function of height during the month of January for the southern hemisphere. [Figure constructed based on the CIRA-86 data set.]



averaged temperature of the tropopause decreases some  $32^{\circ}\text{K}$  from  $232.5^{\circ}\text{K}$  to  $199.8^{\circ}\text{K}$  as the equator is approached from  $80^{\circ}\text{N}$ . In the northern hemisphere, the temperature of the tropopause increases from the equator with increasing latitude until  $60^{\circ}\text{N}$ , beyond which the temperature of the tropopause decreases with increasing latitude.

Figures 7 and 8 compare northern and southern hemispheric temperature profiles for the month of April. The structures of the profiles are quite similar and there is far less latitudinal variability as was in evidence for the January profiles. In the northern hemisphere, there is more latitudinal variability in mesospheric temperature than in the southern hemisphere, whereas there is more latitudinal variability in the temperature of the stratopause in the southern hemisphere than in the northern hemisphere.

Figures 9 and 10 compare northern and southern hemisphere temperature profiles for the month of July. The northern hemisphere exhibits more variability in mesopause and stratopause temperatures than does the southern hemisphere. However, the opposite is true for tropopause temperatures in the southern hemisphere. The mesopause temperature decreases as the equator is approached from  $80^{\circ}\text{S}$  in the southern hemisphere and decreases with increasing latitude in the northern hemisphere. In the northern hemisphere, the temperature of the stratopause increases non-monotonically from  $265^{\circ}\text{K}$  at the equator to  $284.5^{\circ}\text{K}$  at  $80^{\circ}\text{N}$ . In the southern hemisphere the temperature of the tropopause increases from  $80^{\circ}\text{S}$  to  $40^{\circ}\text{S}$  and then decreases with decreasing longitude until the equator is reached. In the northern hemisphere, the temperature of the tropopause increases monotonically from  $202^{\circ}\text{K}$  to  $231^{\circ}\text{K}$  as the latitude increases from the equator to  $80^{\circ}\text{N}$ .

Finally, Figures 11 and 12 compare northern and southern hemisphere profiles for the month of October. The southern hemisphere exhibits more latitudinal variability in the temperature of the mesopause than does the northern hemisphere, whereas the reverse is true for the temperature of the stratopause if one neglects the southern hemisphere data at

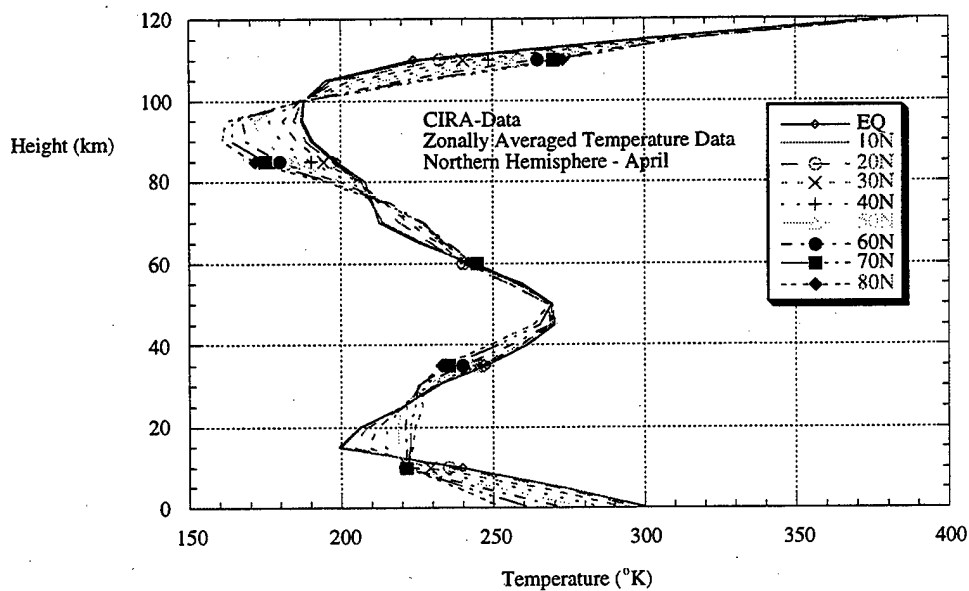


Figure 7. Zonally averaged temperature data as a function of height during the month of April for the northern hemisphere. [Figure constructed based on the CIRA-86 data set.]

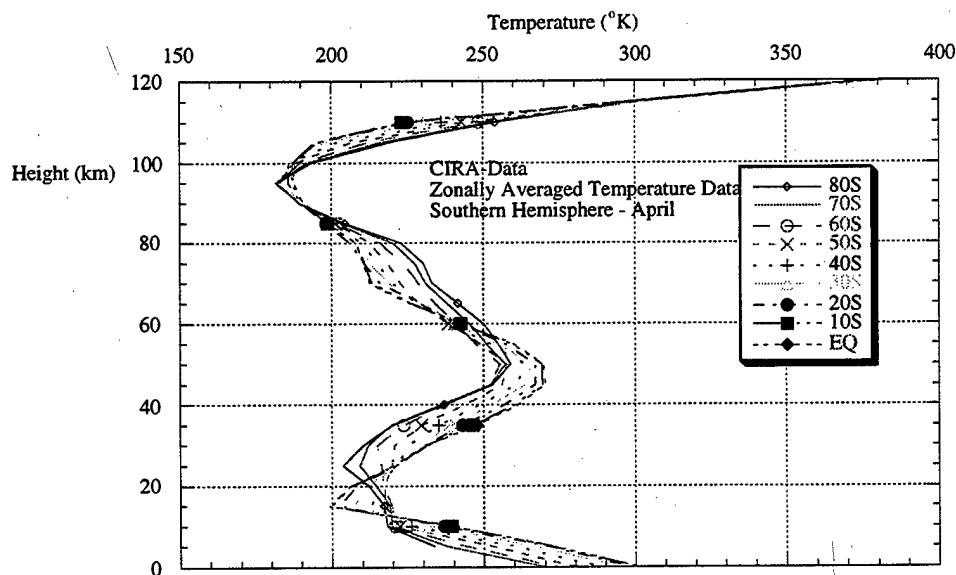


Figure 8. Zonally averaged temperature data as a function of height during the month of April for the southern hemisphere. [Figure constructed based on the CIRA-86 data set.]

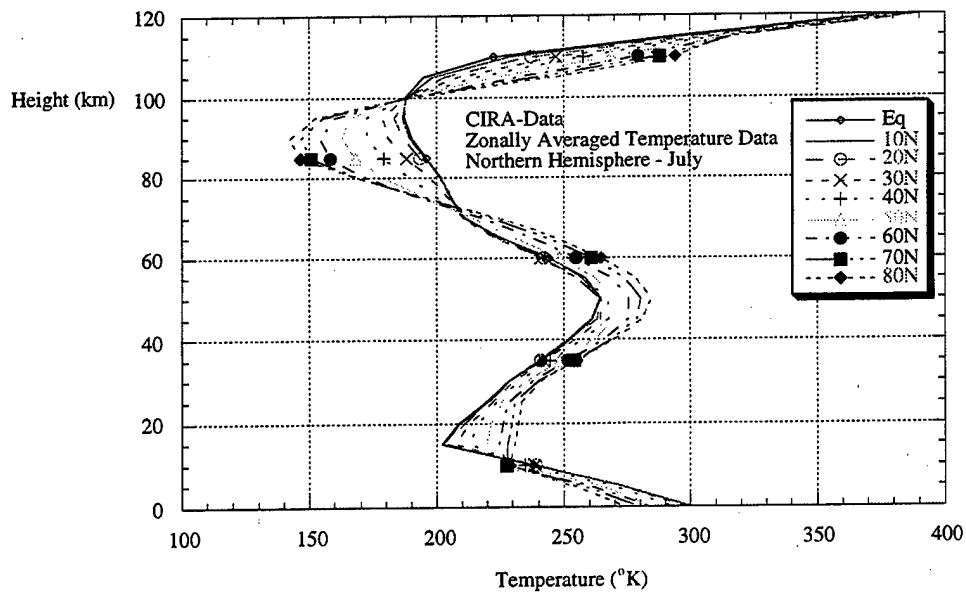


Figure 9. Zonally averaged temperature data as a function of height during the month of July for the northern hemisphere. [Figure constructed based on the CIRA-86 data set.]

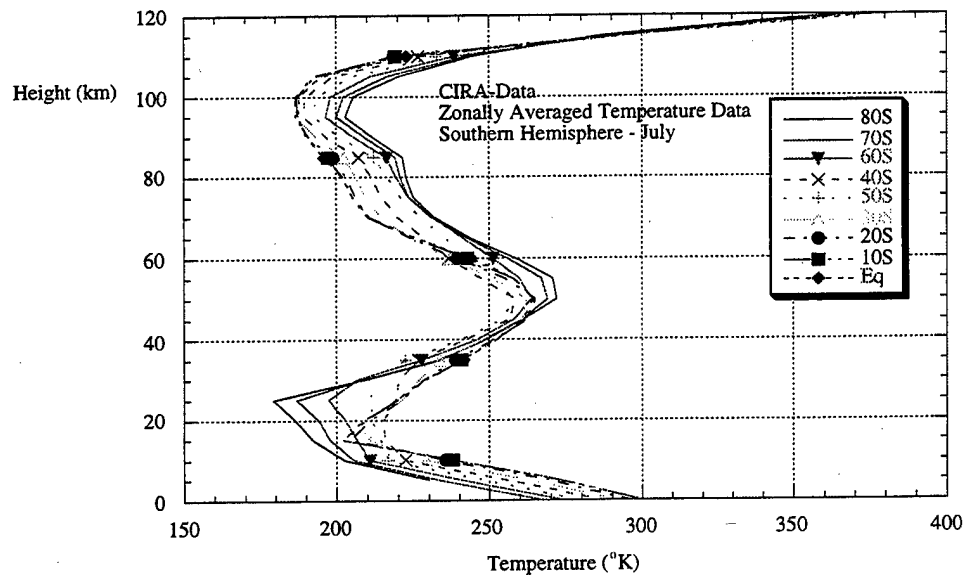


Figure 10. Zonally averaged temperature data as a function of height during the month of July for the southern hemisphere. [Figure constructed based on the CIRA-86 data set.]

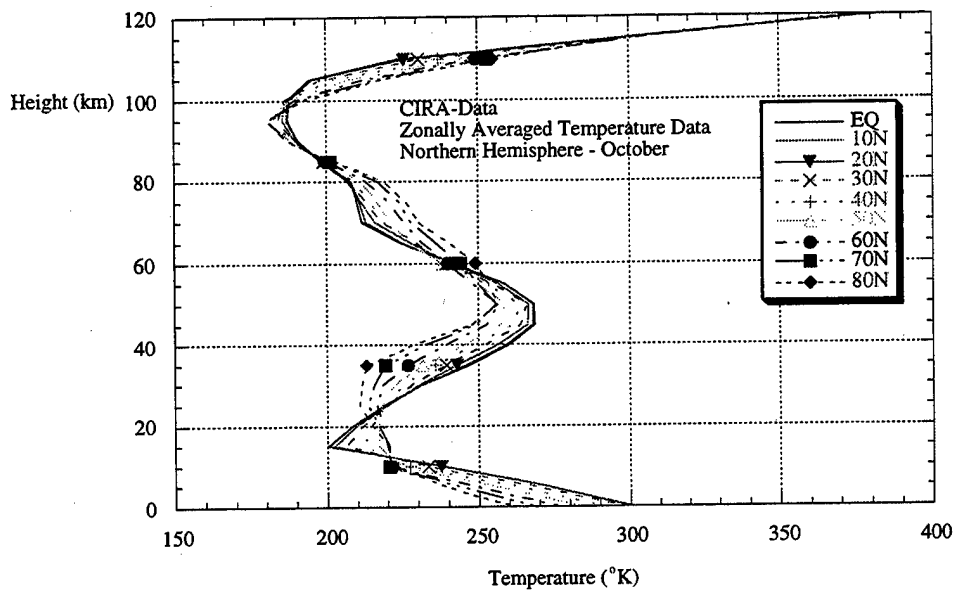


Figure 11. Zonally averaged temperature data as a function of height during the month of October for the northern hemisphere. [Figure constructed based on the CIRA-86 data set.]

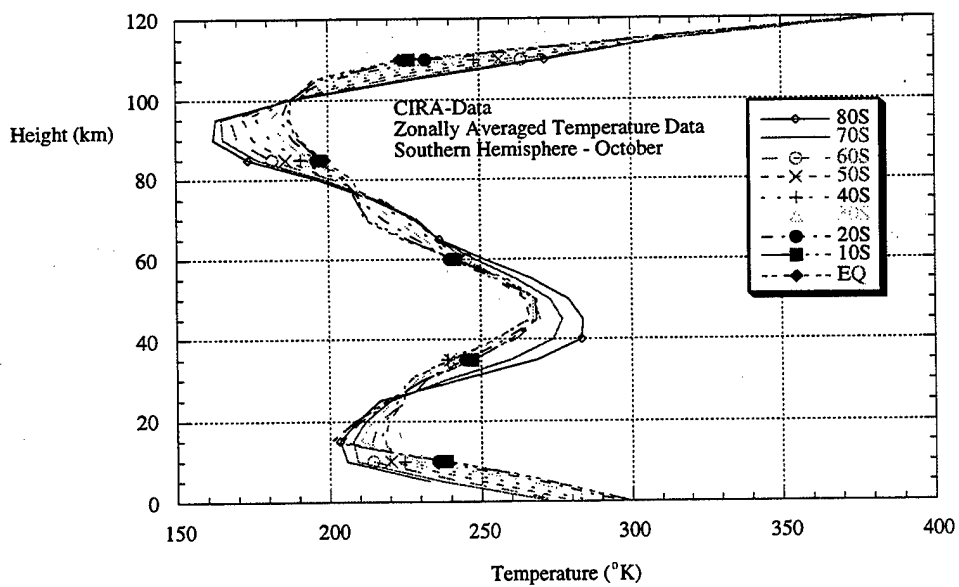


Figure 12. Zonally averaged temperature data as a function of height during the month of October for the southern hemisphere. [Figure constructed based on the CIRA-86 data set.]

70°S and at 80°S. In the southern hemisphere, the mesopause temperature increases monotonically from 162.4°K at 80°S to 190.1°K at the equator. In the northern hemisphere, there is no general trend of stratopause temperature with latitude.

Given the somewhat detailed presentation of atmospheric temperature data, it may be helpful to the general reader to present the temperature data in a summarized form as has been done in Figure 13 which displays a meridional cross section of zonally averaged temperatures (in °C) for the northern and southern hemispheres.

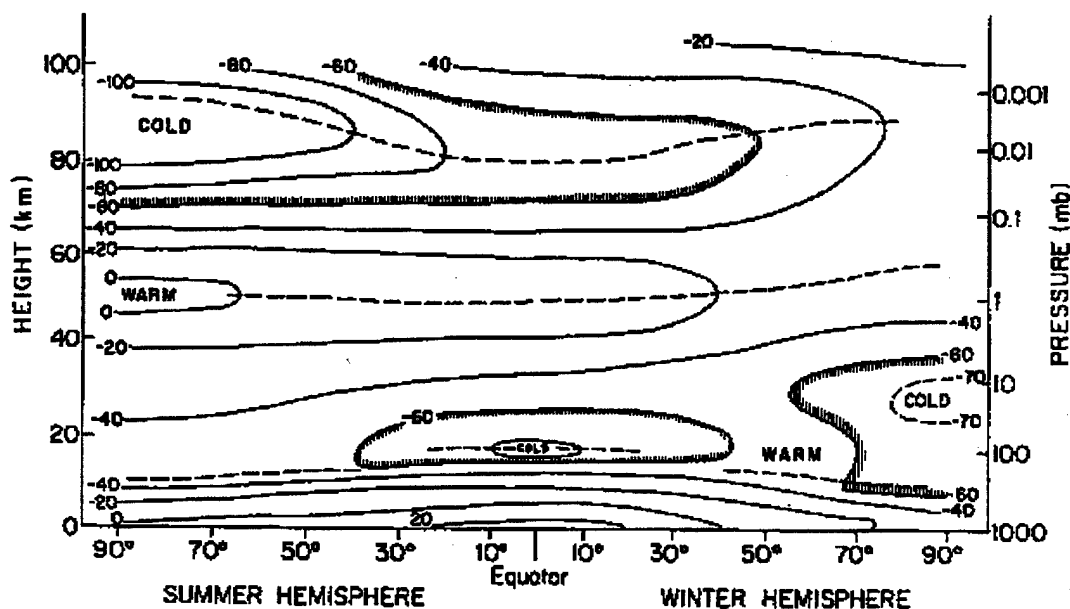


Figure 13. Meridional cross section of longitudinally averaged temperature in degrees Celcius at the time of the solstices. Dashed lines indicate tropopause, stratopause, and mesopause. [Figure adopted from *Wallace and Hobbs* (1977).]

The wind speed data from the CIRA-86 database is presented in Figures 14 through 21 which provide information on the seasonal variability of wind speed in the northern and southern hemispheres. Positive values of wind speed correspond to winds blowing from the west to the east ("westerly winds"), and negative values of wind speed correspond to winds blowing from the east to the west ("easterly winds"). Inspection of the figures clearly illustrates that wind speed exhibits significantly higher variability than does

temperature, that the profiles are characterized by significant wind shear and that quite often the magnitude of the wind speed can be an appreciable fraction of the sound speed.

Figures 14 and 15 compare the January latitudinal variation of wind speed for the northern and southern hemispheres. In both hemispheres the tropospheric winds tend to be westerly. The stratospheric winds in the northern hemisphere are quite variable in both magnitude and direction as the latitude changes from the equator to more northern latitudes. In the southern hemisphere, the stratospheric winds are seen to be easterly, less variable with latitude than those in the northern hemisphere but of a magnitude which is a significant fraction of the sound speed. For example, at 80°S and at a stratospheric altitude of 50 km, the magnitude of the wind speed is 69.5 m/s and that of the sound speed is 329 m/s so that  $|v| = 0.21 c$ . The winds above 80 km are seen to be generally of opposite directions and of the same magnitudes in the two hemispheres except in the northern hemispheric region extending from the equator to 20°N. Figures 16 and 17 compare April zonally averaged wind speed data for the northern and southern hemispheres where the significantly greater variability and magnitude of the winds in the southern hemisphere is evident. In both hemispheres, the tropospheric winds tend to be westerly and of about the same magnitude and both regions exhibit significant shear for stratospheric winds. For example, in the southern hemisphere the wind at an altitude of 30 km is easterly and of magnitude 20 m/s. At an altitude of 50 km, the wind is westerly and of about the same magnitude. The winds above 80 km tend to be westerly in both hemispheres.

Figures 18 and 19 compare July zonally averaged wind speed data for the northern and southern hemispheres and show that the southern hemisphere winds are of significantly greater variability than those of the north. In the northern hemisphere, the stratospheric winds in the altitude range extending from 20 km to 40 km are consistently easterly whereas in the southern hemisphere the winds are predominantly westerly except at the equator and 10°S. The winds above 80 km exhibit significant wind shear in both hemispheres.

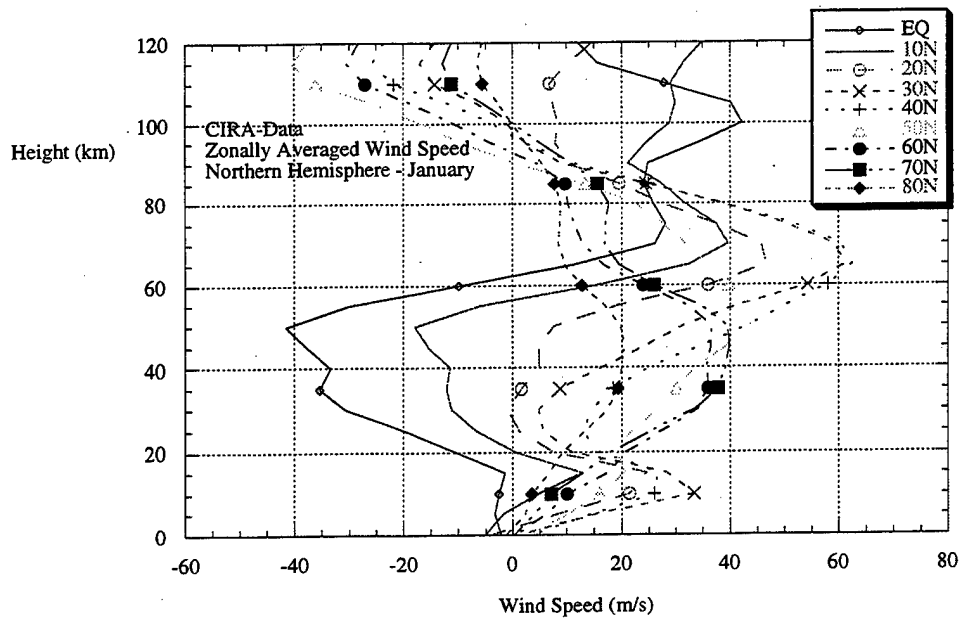


Figure 14. Zonally averaged wind speed as a function of height during the month of January for the northern hemisphere. [Figure constructed based on the CIRA-86 data set.]

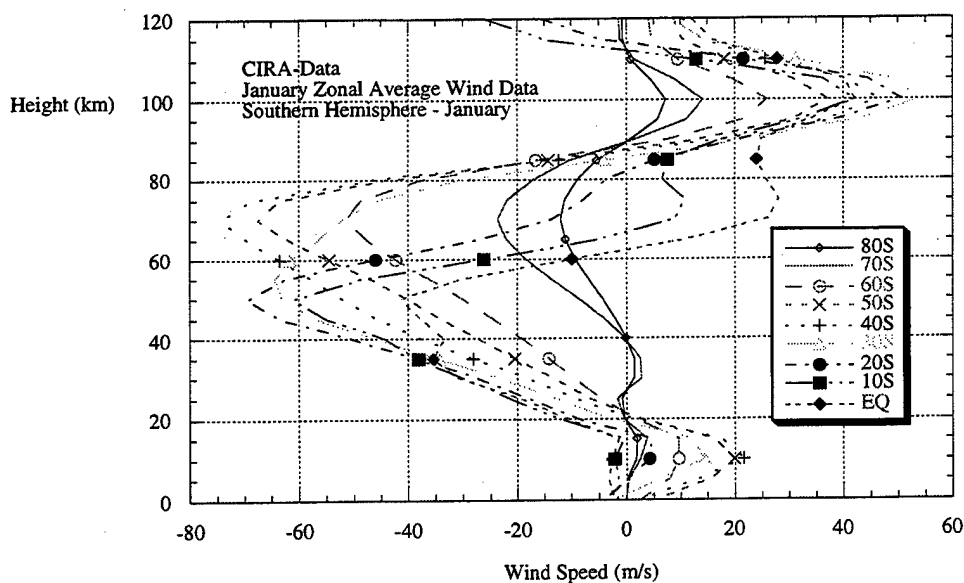


Figure 15. Zonally averaged wind speed as a function of height during the month of January for the southern hemisphere. [Figure constructed based on the CIRA-86 data set.]

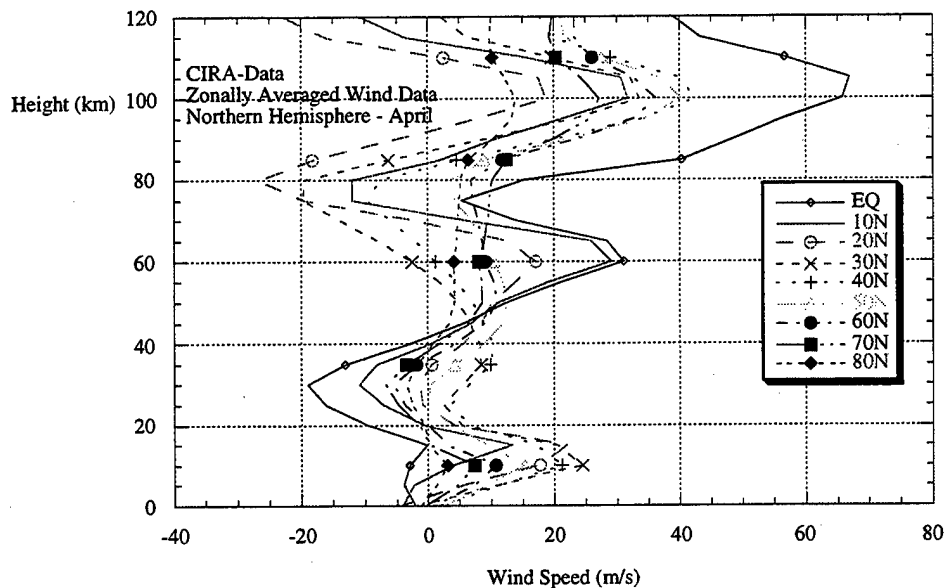


Figure 16. Zonally averaged wind speed as a function of height during the month of April for the northern hemisphere. [Figure constructed based on the CIRA-86 data set.]

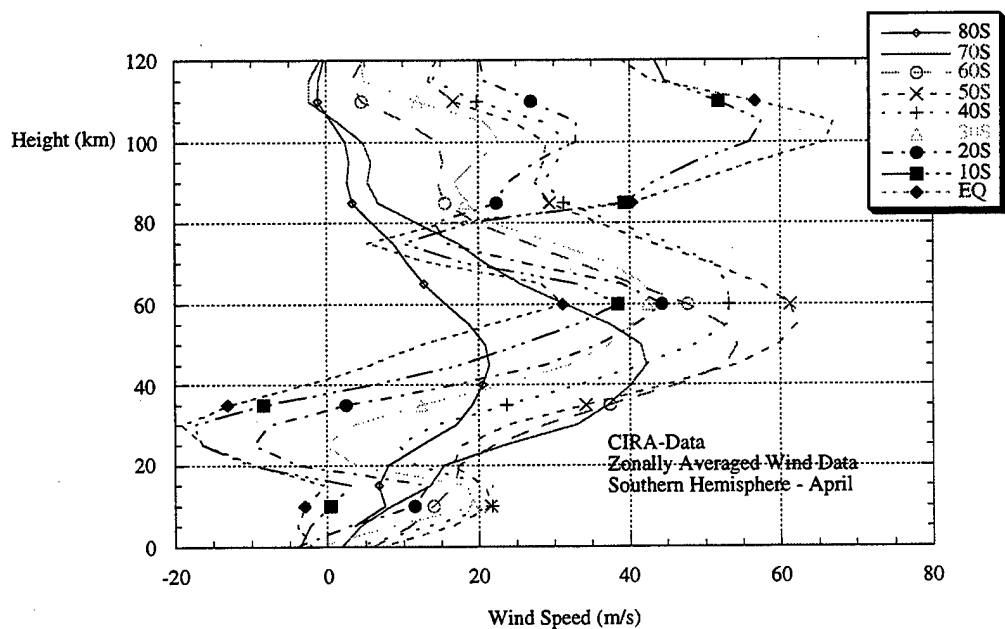


Figure 17. Zonally averaged wind speed as a function of height during the month of April for the southern hemisphere. [Figure constructed based on the CIRA-86 data set.]



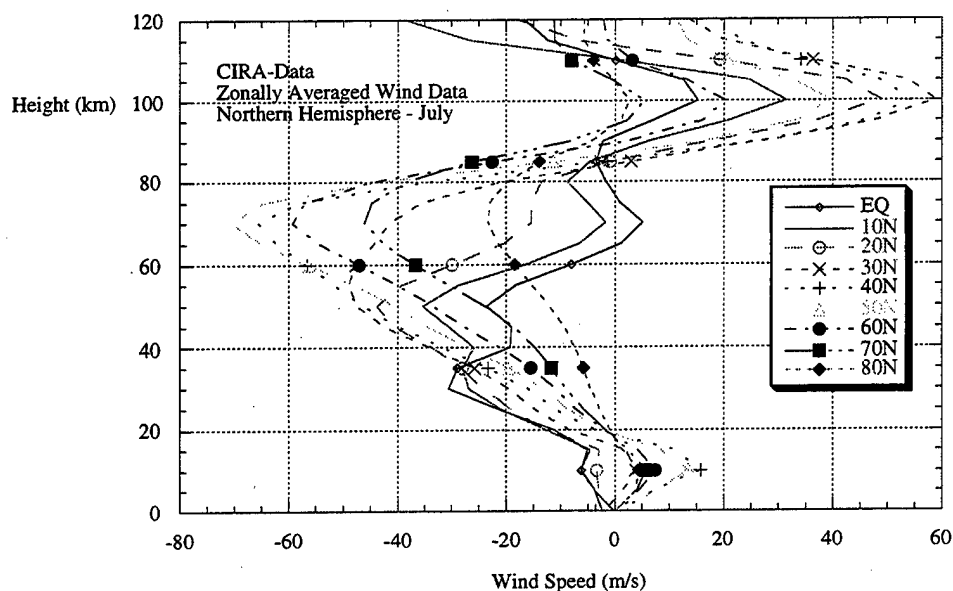


Figure 18. Zonally averaged wind speed as a function of height during the month of July for the northern hemisphere. [Figure constructed based on the CIRA-86 data set.]

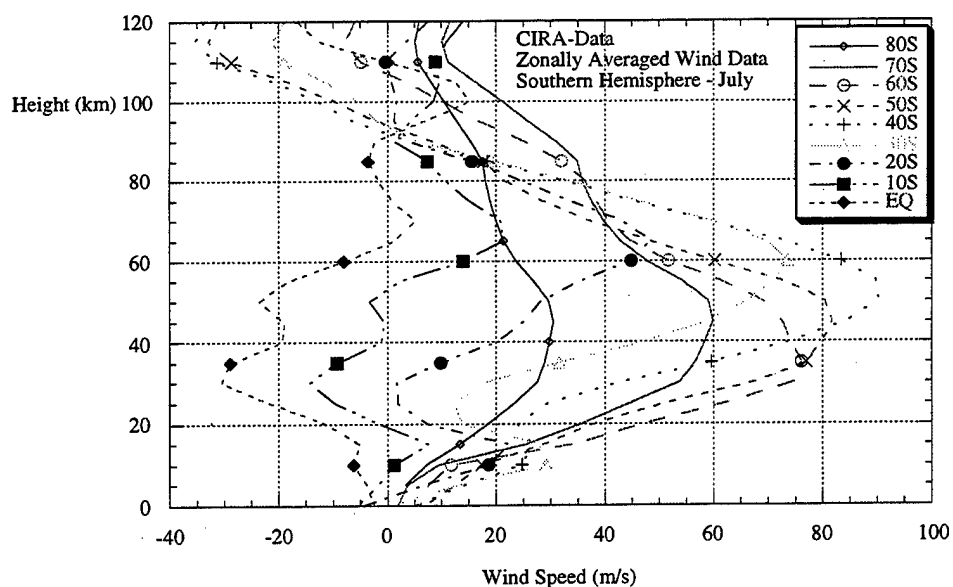


Figure 19. Zonally averaged wind speed as a function of height during the month of July for the southern hemisphere. [Figure constructed based on the CIRA-86 data set.]

Finally, Figures 20 and 21 compare October zonally averaged wind speed data for the two hemispheres and show that the winds in both hemispheres are quite variable. The winds above 80 km and in the troposphere are generally westerly and there is significant shear in the stratospheric and mesospheric winds in both hemispheres.

As a way of summarizing the differences and similarities in the northern and southern hemispheric wind speed fields, Figure 22 provides a latitude-height cross section of longitudinally averaged zonal wind at the time of the solstices. As is evident from the figure, the strongest winds are the mesospheric jets which propagate to the west (easterly winds) in the summer hemisphere and to the east (westerly winds) in the winter hemisphere. It is evident that there are also concentrated wind jets in the troposphere both of which are westerly and that these winds are about four times higher than those in the summer hemisphere.

Wind influences propagation in the atmosphere primarily by its effect on the sound speed profile and the effects are strongly dependent on whether the propagation is "upwind" or "downwind". In the stratosphere and mesosphere, the magnitude of the wind velocity can be a significant fraction of the sound speed magnitude.

To illustrate the importance of wind in determining the effective sound speed, as defined by Eq. (2.5), and to contrast the differences between the northern and southern hemispheres, Figures 23 through 24 present a comparison of zonally averaged sound speed, wind speed and effective sound speed profiles. Profiles are presented for two latitudes: 40°N and 40°S; and for four seasons: January, April, July and October.

Figure 23 compares the sound speed profiles, as determined by temperature alone for the month of January. The profiles are quite similar, particularly in the troposphere. The temperature in the southern hemisphere is evidently higher in the stratosphere and lower in the mesosphere than in the northern hemisphere, as mirrored in

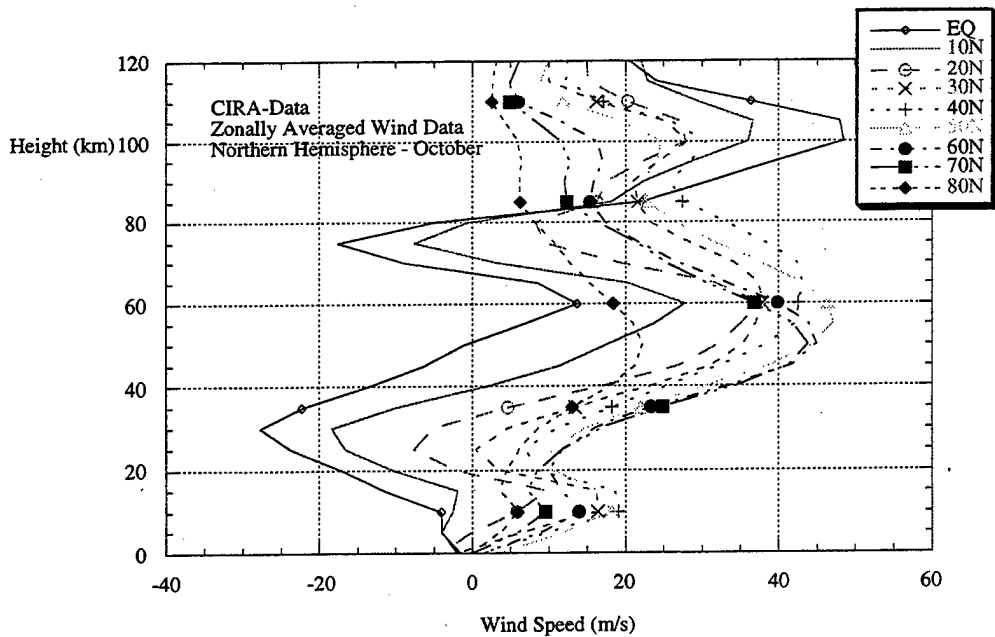


Figure 20. Zonally averaged wind speed as a function of height during the month of October for the northern hemisphere. [Figure constructed based on the CIRA-86 data set.]

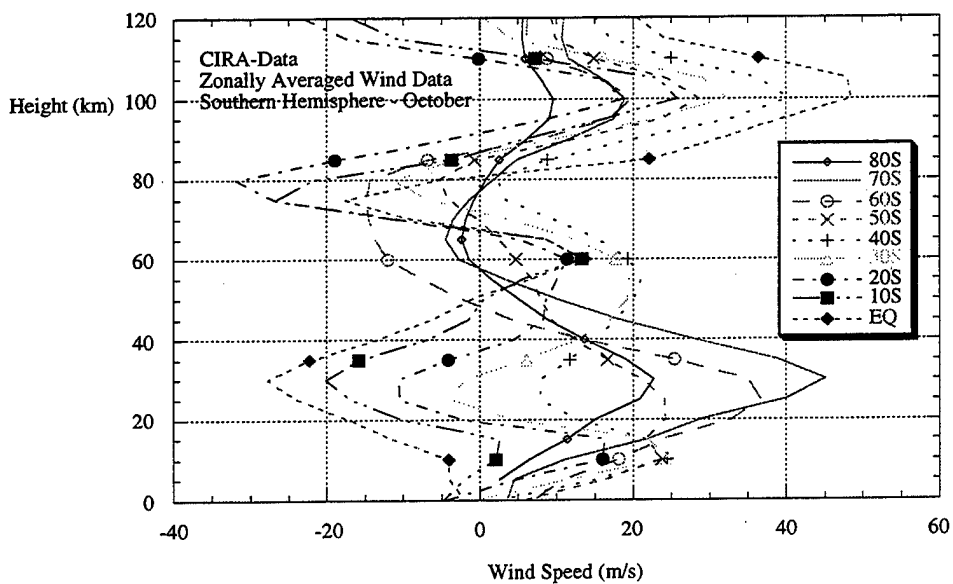


Figure 21. Zonally averaged wind speed as a function of height during the month of October for the southern hemisphere. [Figure constructed based on the CIRA-86 data set.]

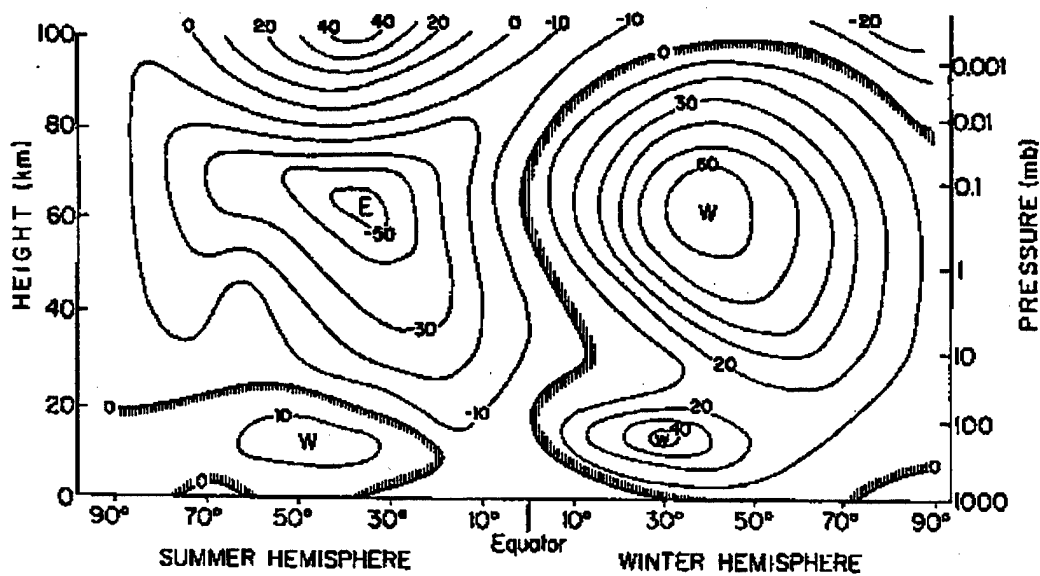


Figure 22. A meridional cross section of longitudinally averaged zonal wind in meters per second at the time of the solstices. [Figure adopted from *Wallace and Hobbs (1977)*.]

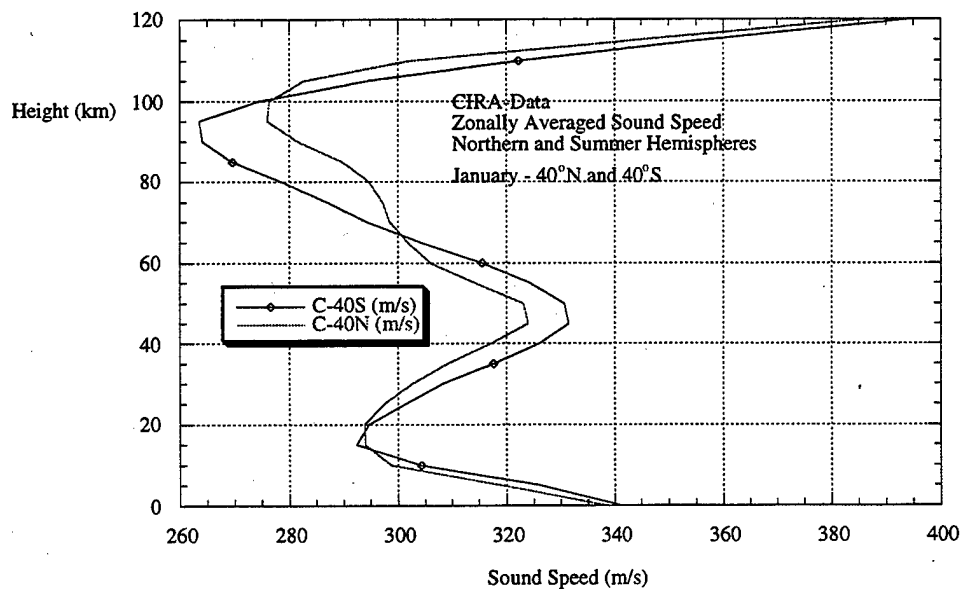


Figure 23. Zonally averaged sound speed as a function of height at 40°N and 40°S for the month of January.

the sound speed profiles. The profiles also exhibit the usual stratospheric and mesospheric upper atmosphere ducts.

Figures 24 and 25 present similar data for wind speed and effective sound speed as a function of altitude. The strong mesospheric jets illustrated previously in Figure 21 are clearly in evidence with westerly mesospheric winds in the northern hemisphere and easterly winds in the southern hemisphere. Tropospheric winds are quite similar at the two latitudes below the level of the tropopause.

Figure 25 presents the effective sound speed as computed by Eq. (2.5) using the sound speed as computed by Eq. (2.4) and the data in Figures 23 and 24. Inspection of Figure 25 and comparison with Figure 23 forcefully demonstrates the influence of the wind when directed west-to-east (upwind or UPW) and when directed east-to-west (downwind or DWN) in determining the effective sound speed profiles. Indeed, the downwind profile (CZEFF-DNW-40°S) has been extensively modified and no

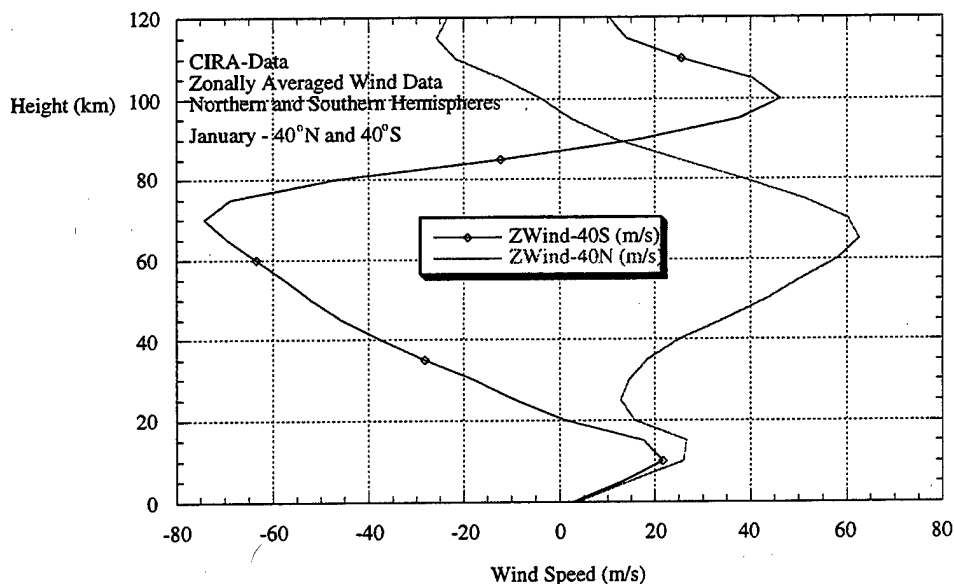


Figure 24. Zonally averaged wind speed as a function of altitude for latitudes 40°N and 40°S for the month of January.

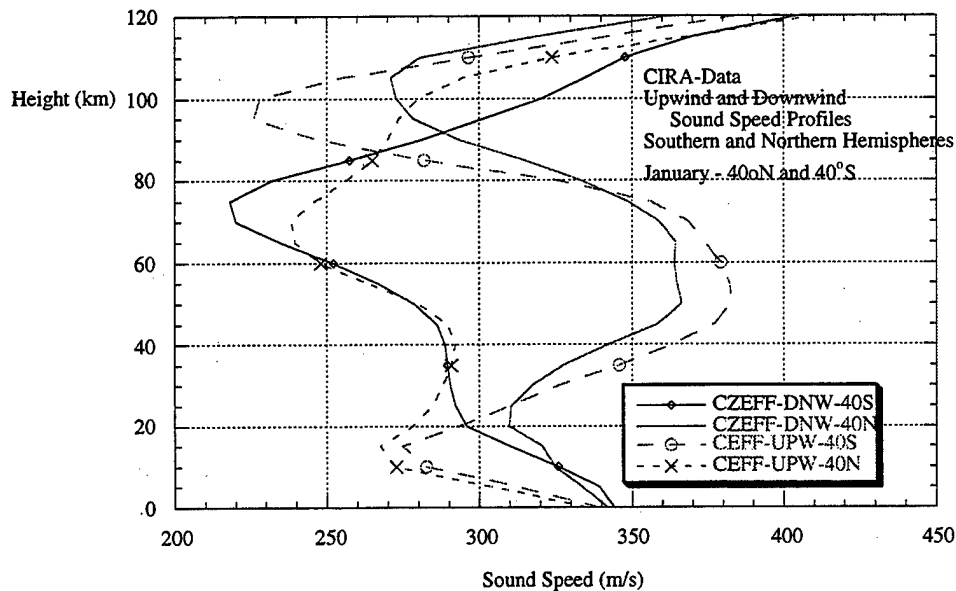


Figure 25. Zonally averaged effective sound speed as a function of altitude for latitudes 40°N and 40°S for the month of January.

longer displays the "canonical" double duct structure.

Figure 26 compares the sound speed profiles, as determined by temperature alone, for the month of April and for latitudes 40°N and 40°S, and the profiles are observed to be almost identical. The wind speed profiles, as exhibited in Figure 27, are seen, however, to be quite different at all levels above 30 km and virtually identical below the tropopause. The very strong mesospheric jets are again in evidence with the direction to the east at the southern latitude and to the west in the northern latitude.

The resultant effective sound speed profiles are compared in Figure 28 and are found to be extensively modified: particularly so for the UPW-40S and UPW-40N profiles although the profiles are virtually the same in the troposphere and thermosphere. The DNW-40S and UPW-40N retain the typical double duct structure, are virtually identical in the troposphere but differ significantly from each other up to altitudes of 100 km.

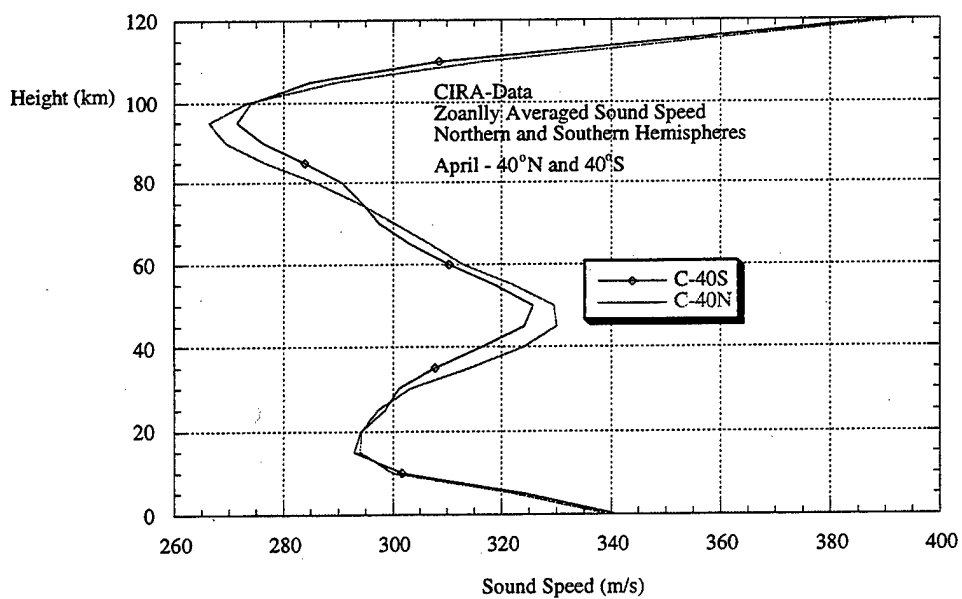


Figure 26. Zonally averaged sound speed as a function of altitude for latitudes 40°N and 40°S for the month of April.

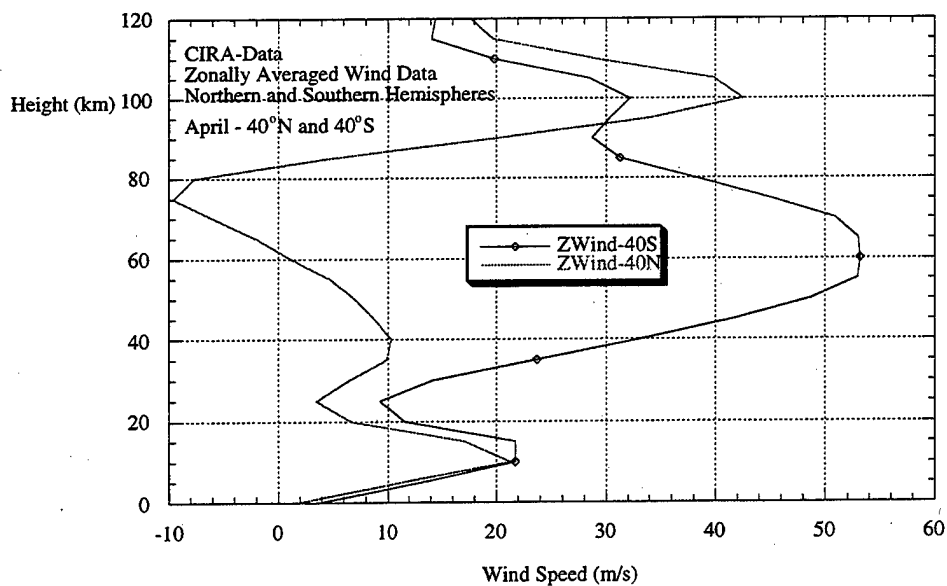


Figure 27. Zonally averaged wind speed as a function of altitude for latitudes 40°N and 40°S for the month of April.

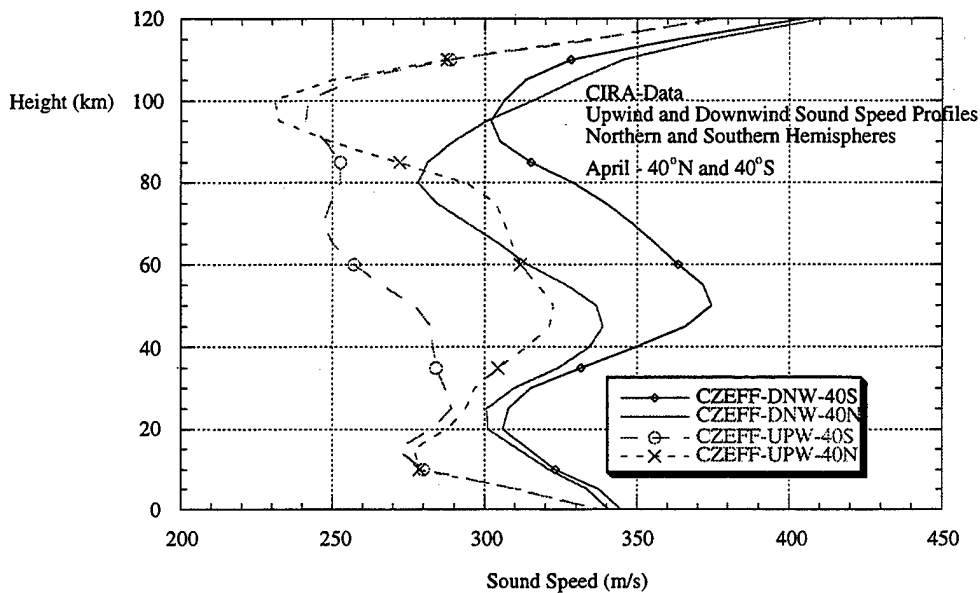


Figure 28. Zonally averaged effective sound speed as a function of altitude for latitudes  $40^{\circ}\text{N}$  and  $40^{\circ}\text{S}$  for the month of April.

Figure 29 compares the temperature dependent sound speed profiles for the month of July and it is evident that the tropospheric components are almost identical. The stratosphere is warmer at the northern latitude than at the southern altitude and the reverse is true for the mesosphere. Figure 30 compares the July zonally averaged wind speed profiles for the two latitudes and the very pronounced mesospheric jets are in evidence with westwardly propagation in the southern hemisphere and easterly propagation in the northern hemisphere. There are slight differences between the profiles in the troposphere but significant differences in the thermosphere.

Figure 31 compares the upwind and downwind July effective sound speed profiles and the differences between these and those in Figure 2.29 are clearly significant. Indeed, the DWN-40N and UPW-40S profiles exhibit only a single mesospheric sound speed duct rather than the more typical stratospheric and mesospheric ducts. The DWN-40S and UPW-40N profiles are the same in the troposphere but differ significantly at all other altitudes.



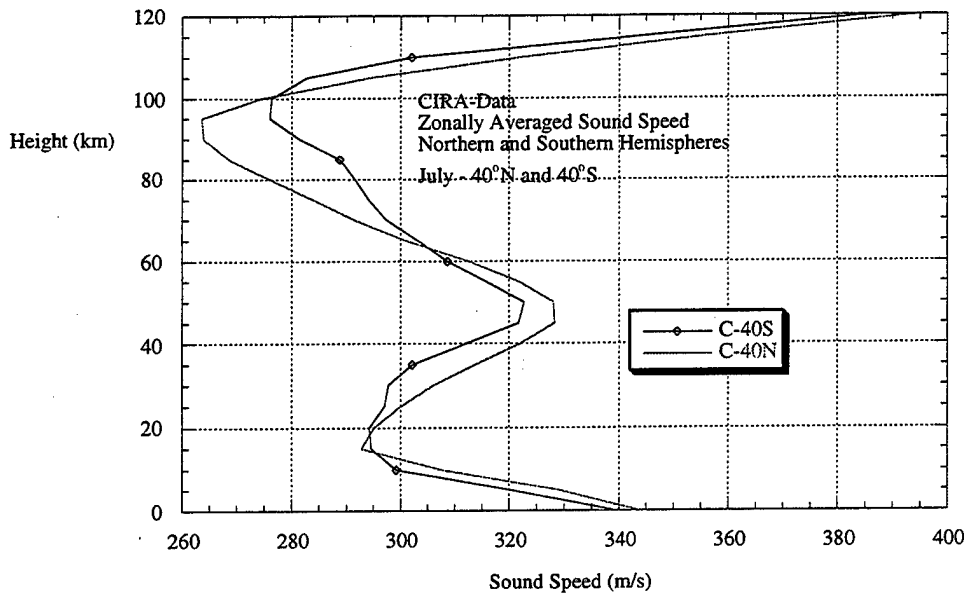


Figure 29. Zonally averaged effective sound speed as a function of altitude for latitudes 40°N and 40°S for the month of July.

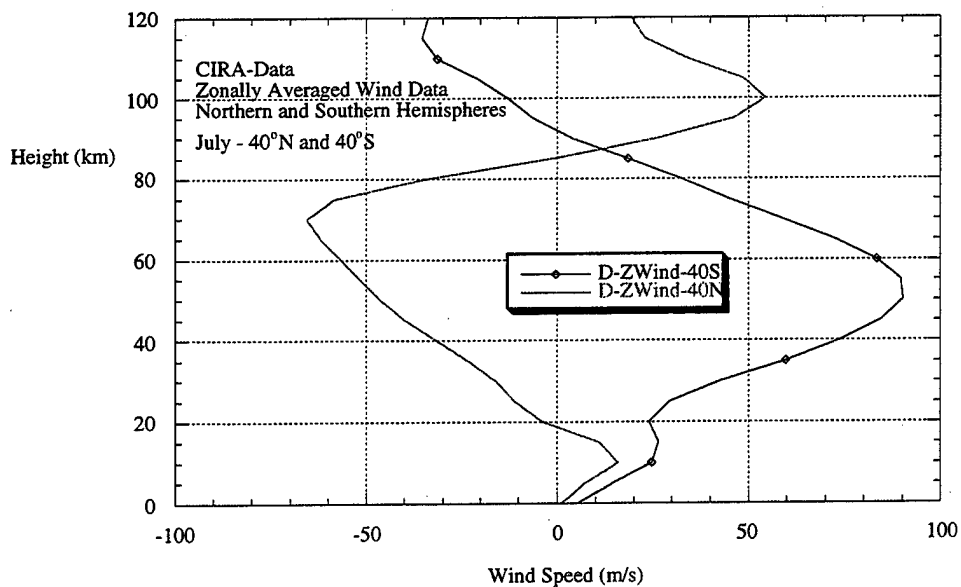


Figure 30. Zonally averaged wind speed as a function of altitude for latitudes 40°N and 40°S for the month of July.

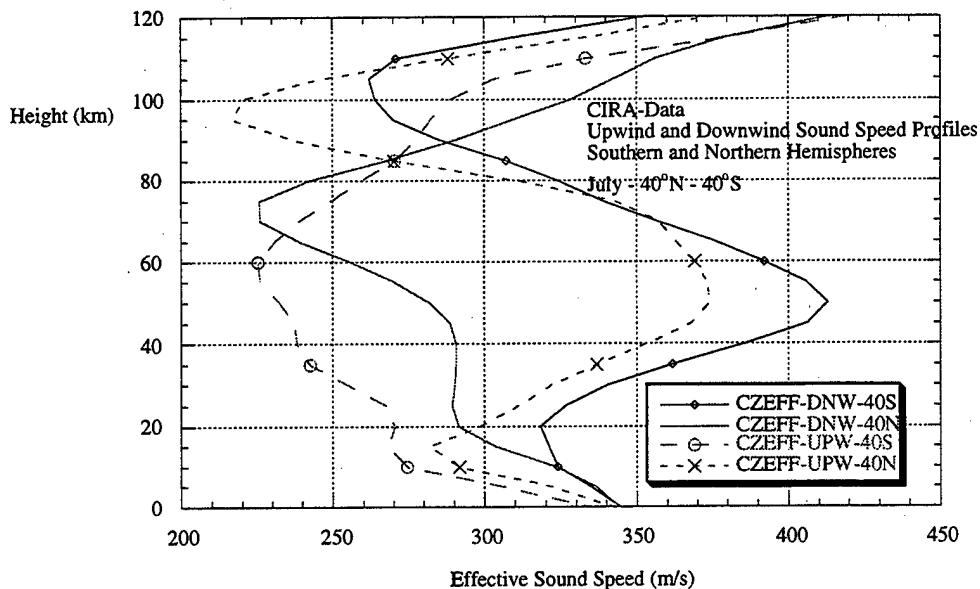


Figure 31. Zonally averaged effective sound speed as a function of altitude for latitudes 40°N and 40°S for the month of July.

Finally, Figure 32 compares the temperature dependent sound speed profiles as a function of altitude for the month of October and the profiles are seen to be virtually identical. The wind speed profiles, shown in Figure 33 are also similar in structure at the lowest and highest altitudes but differ significantly in the region between 30 km and 90 km. The wind direction is, however, westerly at both latitudes and at all altitudes, although the mesospheric jet is much stronger in the northern hemisphere.

The zonally averaged upwind and downwind effective sound speed profiles for the month of October are provided in Figure 34. Inspection of the figure shows that the downwind profiles at both latitudes, CZEFF-DNW-40S and CZEFF-DNW-40N, are quite similar: particularly so up to a height of 40 km. The upwind profiles are essentially the same in the troposphere and thermosphere but differ in the intermediate altitude region extending from 25 km to 85 km.

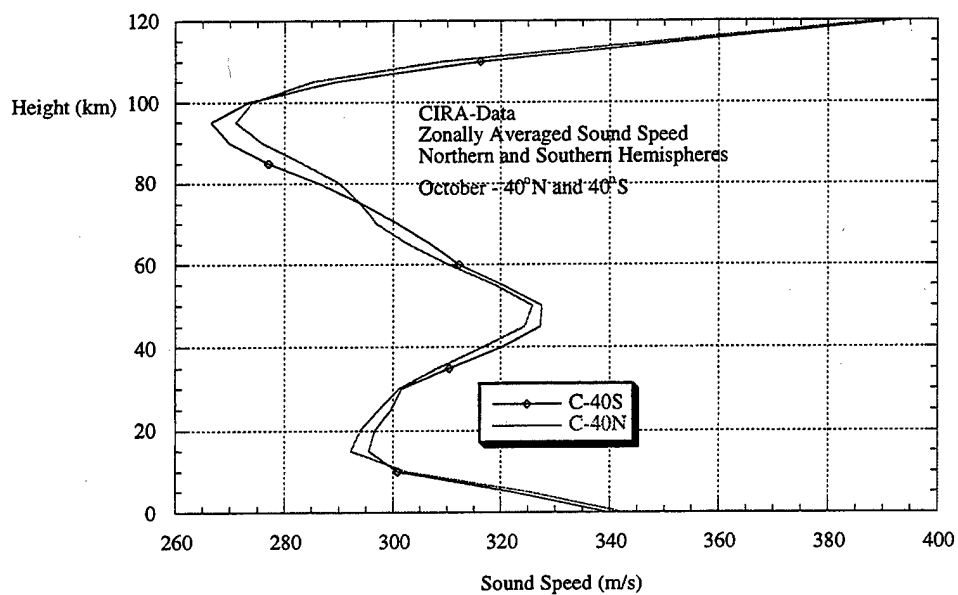


Figure 32. Zonally averaged sound speed as a function of altitude for latitudes 40°N and 40°S for the month of October.

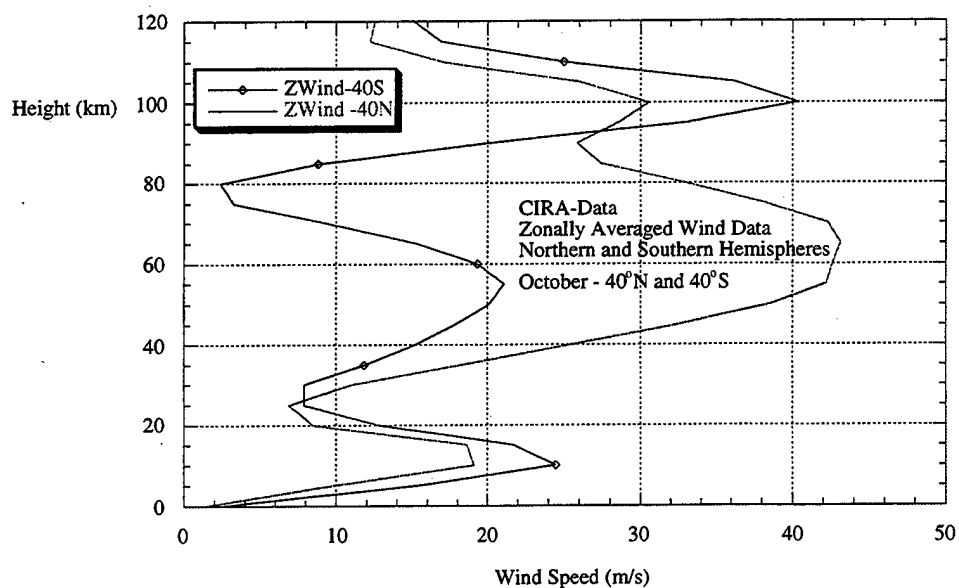


Figure 33. Zonally averaged wind speed as a function of altitude for latitudes 40°N and 40°S for the month of October.

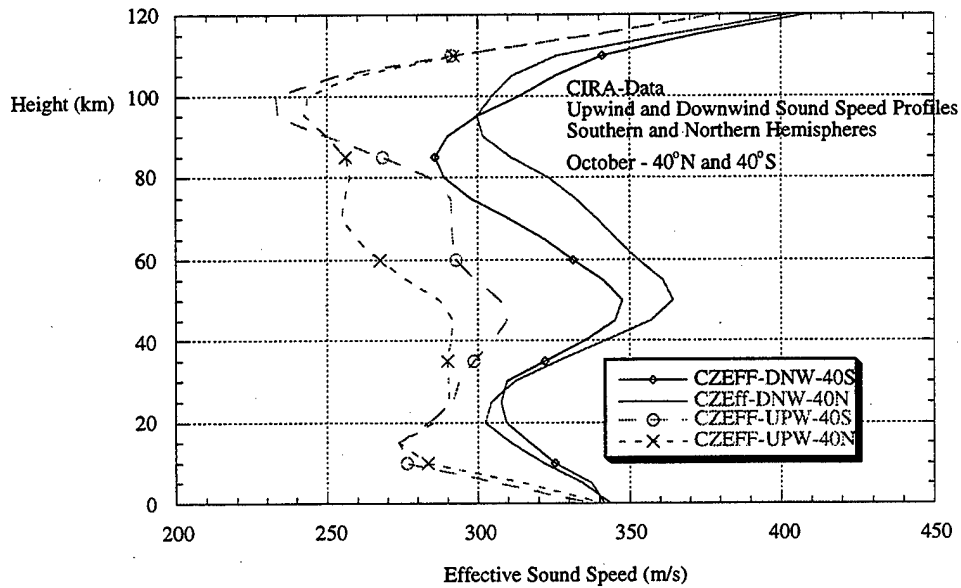


Figure 34. Zonally averaged effective sound speed as a function of altitude for latitudes  $40^{\circ}\text{N}$  and  $40^{\circ}\text{S}$  for the month of October.

As an example of the significant effects that winds and propagation direction can have on acoustic propagation in the atmosphere, Figure 35 provides a computer-generated plot of the very complicated behavior of acoustic ray paths for propagation in the U.S. Standard Atmosphere 1962 for a source at a height of 5 km above the earth's surface [Georges and Young (1972)]. In conducting the modeling, the acoustic frequency was taken to be 300 Hz and the propagation conditions are seen to be distinctly different for propagation in the downwind and upwind directions. For more realistic wind speed profiles it is reasonable to expect an even more complicated ray path pattern and, based on the data presented above, the pattern will be a strong function of hemispheric location and season.

In addition to effecting ray paths and rendering propagation in the atmosphere anisotropic, upper atmospheric winds and propagation direction significantly influence the form of the received pulse from a nuclear or chemical explosion in the atmosphere: a

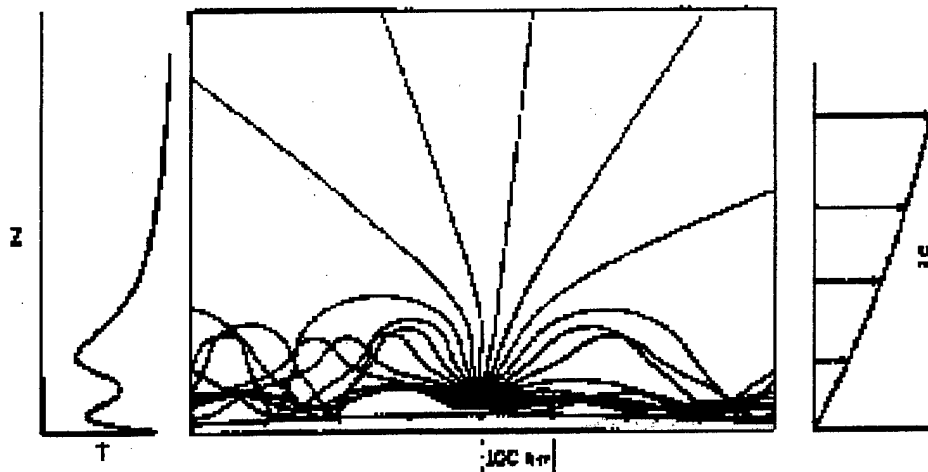


Figure 35. Acoustic ray paths for a source at 5 km altitude in the U.S. Standard Atmosphere 1962. The temperature profile is shown to the left of the central panel in the figure and the assumed logarithmic wind speed profile is indicated to the right of the central panel. [Figure adopted from *Georges and Young (1972)*.]

circumstance which is illustrated in Figure 36. The figure illustrates the synthesis of a received pulse by two gravity wave modes and six acoustic modes. In addition, the effects

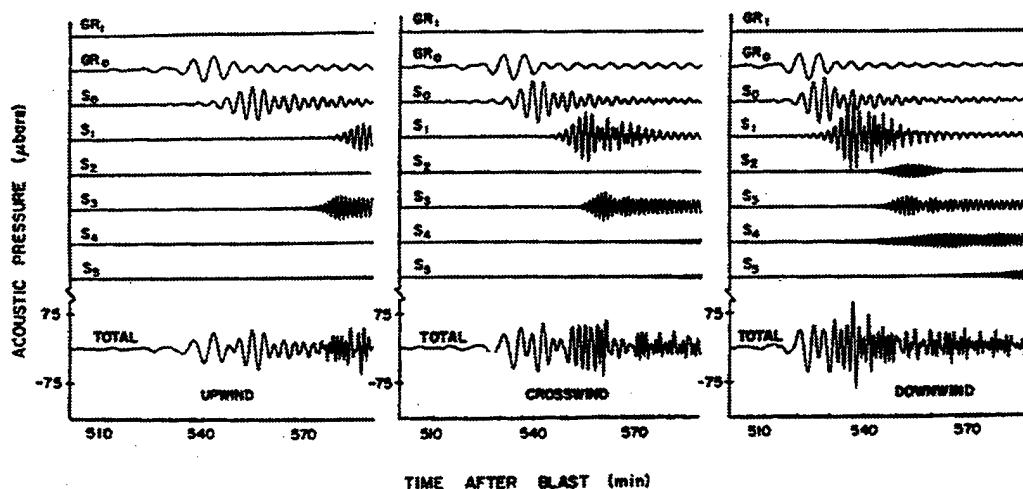


Figure 36. An illustration of pulse construction and the theoretical effect of winds on pulse dispersion as computed by a full wave propagation model for an explosive source in the atmosphere [e.g., the model of *Pierce and Kinney (1976)*]. As indicated, the first two gravity wave modes ( $GR_0$  and  $GR_1$ ) and the first six acoustic modes ( $S_0$ -to- $S_6$ ) are used in computing the waveforms. The atmospheric model used is the COSPAR 1962 standard atmosphere for a subtropical summer region. The observer is on the ground and at 10,000 km range from the explosion. Propagation upwind is seen to significantly increase the time between the low and high frequency regions of the composite waveform. [Figure adopted from *Pierce, Posey and Iliff (1971)*.]

of upwind, crosswind and downwind propagation are shown for the individual modes making up the total waveform and propagation upwind is seen to significantly increase the time between the low and high frequency regions of the composite waveform.

The interest in infrasound as a monitoring tool derives not simply because of the extraordinary acoustic energy release from a nuclear explosion and its subsequent propagation in the atmosphere, but because infrasound propagates virtually unattenuated as is illustrated in Figure 37 which plots the estimated attenuation for air-to-ground paths [Beranek (1960)].

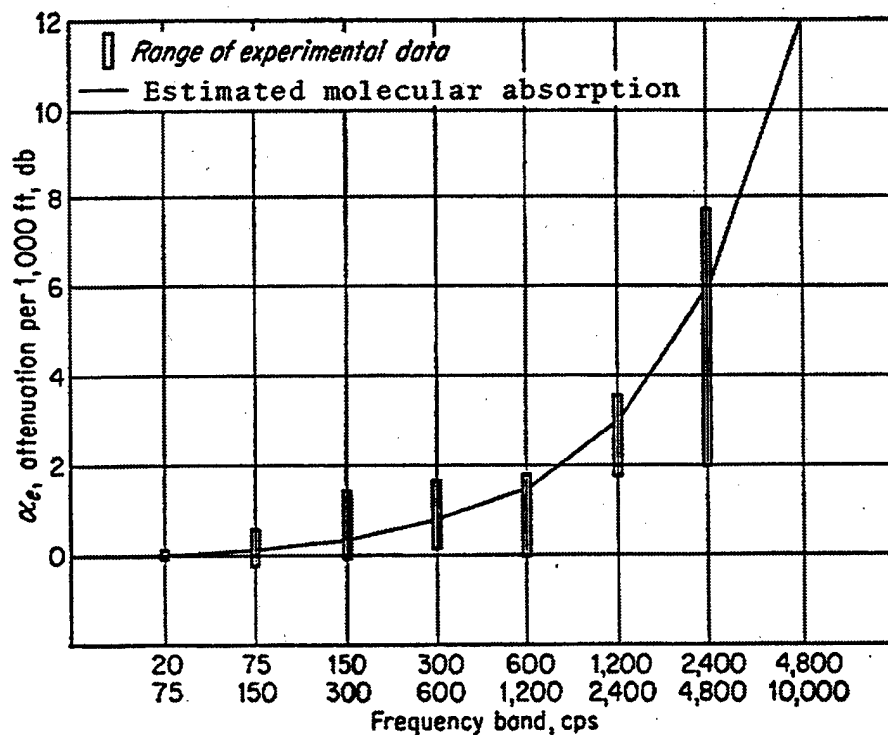


Figure 37. The estimated attenuation coefficient for air-to-ground acoustic propagation. The range of available experimental data are indicated by the vertical bars. [Figure adopted from Beranek (1960).]

The formal expression for attenuation which is valid to an altitude of approximately 60 km is known as the Stokes-Kirchhoff attenuation expression and is given by [Landau and Lifshitz (1959), Lighthill (1956) and Morse and Ingard (1968)]

$$\alpha = \frac{\omega^2}{2\rho c^3} \left[ \left( \frac{4}{3}\mu + \zeta \right) + \kappa \left( \frac{1}{C_v} - \frac{1}{C_p} \right) \right] \quad (2.6)$$

where  $\omega$  is the circular frequency ( $=2\pi f$ ),  $\mu$  is the ordinary viscosity coefficient,  $\zeta$  is the "second" or bulk viscosity coefficient,  $\kappa$  is the thermal conductivity, and  $C_v$  and  $C_p$  are the specific heats at constant volume and pressure respectively. Figure 38 plots the attenuation coefficient as a function of altitude for a frequency of 1 Hz where it is seen that attenuation increases significantly with atmospheric height.

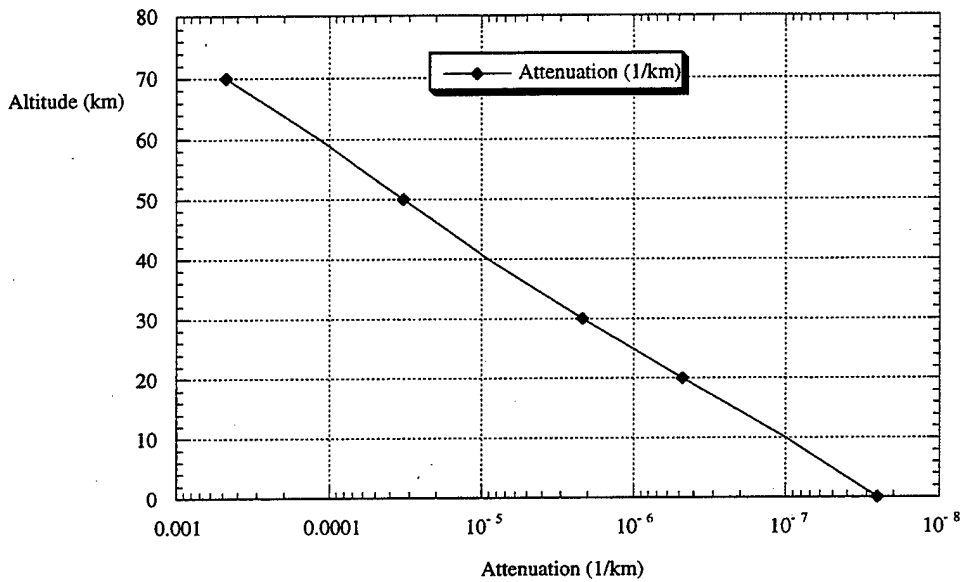


Figure 38. The attenuation coefficient (1/km) as a function of altitude up to 70 km for an assumed frequency of 1 Hz. [Figure based on data computed by *Cotten, Donn and Oppenheim* (1971).]

## 2.2 Acoustic-Gravity Waves

The generation of acoustic-gravity and infrasonic waves and their propagation in the atmosphere has received significant attention in the literature and at least four excellent texts are extant which summarize a significant amount of the work: *Gossard and Hooke* (1975), *Kato* (1981), *Gill* (1982), *Houghton* (1986) and *Salby* (1996).

Most of the work was motivated by the atmospheric testing of nuclear weapons and the literature can be conveniently divided into two parts: one part deals with acoustic-gravity waves in general, and with applicability to the lower atmosphere, and another part deals with acoustic-gravity waves in general, but with a focus on upper atmospheric or ionospheric phenomena.

Selected references which are of interest to those interested in infrasonic monitoring of compliance to a CTBT treaty include the five texts referred to above and the following archival literature articles: *Weston* (1962) who discusses the spectrum of acoustic-gravity waves for two general types of atmospheres; *Tolstoy* (1963) who provides a comprehensive development and review including the effects of earth rotation; *Clark* (1963) who investigates the effects of winds on acoustic-gravity wave propagation; *Francis* (1973) who provides a comprehensive discussion of acoustic-gravity waves; *Wiin-Nielson* (1965) who considers wave propagation in atmospheres having vertically stratified wind and temperature structures; *Midgeley and Liemohn* (1966) who consider propagation in a generally stratified atmosphere; *Tolstoy* (1967) who studies the propagation of long-period gravity waves (or surface waves) in the atmosphere as well as reviewing the earlier literature; *Einaudi and Hines* (1970) who apply the WKB approximation to acoustic-gravity wave propagation; *Liu and Yeh* (1971) who study propagation in an isothermal atmosphere considering wave excitation by mass, momentum and heat production; and *Tolstoy* (1973) who studies gravity wave generation in the troposphere by random forces.

Examples of the work which is primarily focused on wave propagation in the upper atmosphere (ionosphere and thermosphere) and with TIDS (traveling ionospheric disturbances) include the work of: *Hines* (1960); *Hines* (1963); *Obayashi* (1963); *Pitteway and Hines* (1963); *Wickersham* (1966); *Hines and Reddy* (1967); *Daniels* (1967); *Breitling, Kupperman and Gassmann* (1967); *Hines* (1967); *Tolstoy* (1969); *Tolstoy and Pan* (1970); *Tolstoy and Lau* (1971); *Yeh and Liu* (1974) and *Francis* (1975).



In the following, for completeness, a very brief description of acoustic-gravity waves is presented following the basic developments in *Kanamori, Mori and Harkrider* (1994), *Gill* (1982) and *Salby* (1996).

The equation of state is given by

$$p_o = \rho_o R T_o \quad (2.7)$$

and the equation of hydrostatic equilibrium is given by

$$\frac{\partial p_o}{\partial z} = -g \rho_o \quad (2.8)$$

where the subscripts "o" indicate background values,  $g$  is the acceleration due to gravity,  $R$  is the universal gas constant,  $T_o$  is the temperature, assumed to be isothermal for the present, and  $z$  is the altitude taken as positive upward.

Eqs. (2.7) and (2.8) imply that the background pressure and density decrease exponentially with atmospheric height. For example, solving Eq. (2.7) for the density and substituting into Eq. (2.8) gives

$$\frac{\partial p_o}{\partial z} = \frac{-g p_o}{R T_o}$$

or, alternatively,

$$\frac{dp_o}{p_o} = - \frac{g dz}{R T_o}$$

which is directly integrable from the earth's surface  $z=0$  to an arbitrary atmospheric height,  $z$ , to yield

$$p_o(z) = p_o(0) e^{-\frac{gz}{R T_o}} \quad (2.9)$$

which illustrates the exponential decrease in the background pressure with height. Proceeding in a similar fashion by eliminating the pressure from Eqs. (2.7) and (2.8), yields the analog of Eq. (2.9) for the background density decrease with increasing altitude:

$$\rho_o(z) = \rho_o(0) e^{-\frac{gz}{R T_o}} \quad (2.10)$$

For the isothermal atmosphere under consideration, the sound speed,  $c$ , and atmospheric scale height,  $H$ , are constant and given, respectively, by

$$c^2 = \gamma \frac{p_o}{\rho_o} \quad (2.11)$$

and by

$$H = \frac{RT_o}{g} \quad (2.12)$$

so that, from inspection of Eqs. (2.9) and (2.10), one physical interpretation of the scale height is that altitude in the atmosphere for which the background pressure and density fall off to 1/e of their values at the earth's surface.

With the neglect of the earth's rotation, winds, and the atmosphere's viscosity and, in the absence of a source, the linearized equations for the conservation of momentum in a Cartesian system of coordinates take the form

$$\rho_o \frac{\partial u}{\partial t} = - \frac{\partial p}{\partial x}, \quad (2.13a)$$

$$\rho_o \frac{\partial v}{\partial t} = - \frac{\partial p}{\partial y}, \quad (2.13b)$$

$$\rho_o \frac{\partial w}{\partial t} = - \frac{\partial p}{\partial z} - \rho g, \quad (2.13c)$$

where in the above,  $\rho_o$  is the background density,  $u, v$  and  $w$  are the  $x, y, z$  components of the velocity,  $p$  is the pressure and  $g$  is the acceleration due to gravity. All of the non-subscripted quantities refer to perturbations above background values.

The linearized equation for the conservation of mass is given by

$$\frac{\partial \rho}{\partial t} + w \frac{\partial \rho_o}{\partial z} + \rho_o \left( \frac{\partial u}{\partial x} + \frac{\partial v}{\partial y} + \frac{\partial w}{\partial z} \right) = 0 \quad (2.14)$$

and the linearized equation for the conservation of energy is given by

$$\frac{\partial p}{\partial t} - g \rho_o w = c^2 \left( \frac{\partial \rho}{\partial t} + w \frac{\partial \rho_o}{\partial z} \right). \quad (2.15)$$

From the foregoing equations, two subsidiary equations for the pressure and the vertical particle velocity can be developed. The first relation is developed by differentiating Eqs. (2.14) and (2.15) with respect to time and eliminating the  $\partial^2 \rho / \partial t^2$  term to obtain the relation

$$\frac{1}{c^2} \frac{\partial^2 p}{\partial t^2} - \frac{g \rho_o}{c^2} \frac{\partial w}{\partial t} = -\rho_o \left[ \frac{\partial^2 u}{\partial t \partial x} + \frac{\partial^2 v}{\partial t \partial y} + \frac{\partial^2 w}{\partial t \partial z} \right]. \quad (2.16)$$

The first two momentum equations, are then used to eliminate the terms involving  $u$  and  $v$  to obtain

$$\left[ \frac{\partial^2}{\partial x^2} + \frac{\partial^2}{\partial y^2} - \frac{1}{c^2} \frac{\partial^2}{\partial t^2} \right] p = \rho_o \frac{\partial}{\partial t} \left[ \frac{\partial w}{\partial z} - \frac{g w}{c^2} \right]. \quad (2.17)$$

The second equation involving  $p$  and  $w$  is obtained by differentiating the third momentum equation with respect to time and using both Eqs. (2.14) and (2.15) to obtain

$$\frac{\partial^2 w}{\partial t^2} - g \left[ \frac{1}{\rho_o} \frac{\partial \rho_o}{\partial z} + \frac{g}{c^2} \right] w = - \frac{1}{\rho_o} \frac{\partial}{\partial z} \left( \frac{\partial p}{\partial z} + \frac{g p}{c^2} \right). \quad (2.18)$$

Next, the dispersion relation for acoustic-gravity waves is derived by seeking plane wave-solutions to Eqs. (2.17) and (2.18) in the  $x$ - $z$  plane. Specifically, solutions of the form

$$p(x, z, t) = p_o e^{az} e^{i(kx + mz + \omega t)} \quad (2.19)$$

and

$$w(x, z, t) = e^{az} e^{i(kx + mz + \omega t)} \quad (2.20)$$

are assumed where  $\omega$  is the propagation angular frequency,  $k$  and  $m$  are the horizontal and vertical wavenumbers, respectively and the first exponential factor is introduced to accommodate parameter changes with respect to altitude. Substitution of Eqs. (2.19) and (2.20) into Eqs. (2.17) and (2.18) then leads to two equations having constant coefficients which lead to the acoustic-gravity wave dispersion relation given by

$$m^2 = k^2 \left( \frac{N^2 - \omega^2}{\omega^2} \right) + \left( \frac{\omega^2 - \omega_a^2}{c^2} \right) \quad (2.21)$$

where, in the above,  $N$  is the Brunt-Vaisala or buoyancy frequency given by

$$N^2 = \frac{(\gamma - 1)g}{\gamma H}, \quad (2.22)$$

and  $\omega_a$  is the acoustic cut-off frequency (defined below) given by

$$\omega_a^2 = \frac{\gamma g}{4H} = \frac{c^2}{4H^2}. \quad (2.23)$$

The parameter,  $a$ , is fixed as

$$a = \frac{1}{2H}. \quad (2.24)$$

For an atmospheric scale height of 8 km and a sound speed of 331 m/s, the acoustic and Brunt-Vaisala frequencies are 0.0207 rad/s and 0.0187 rad/s, corresponding, respectively, to periods of 303.54 s and 336.0 s. In general, for an isothermal atmosphere,

$$\omega_a / N = \frac{\gamma}{2\sqrt{\gamma-1}} = 1.11 \text{ for } \gamma = 1.4. \quad (2.25)$$

The dispersion relation of Eq. (2.21) is fundamental and describes acoustic-gravity waves which involve both the restoring forces of compression and buoyancy. The asymptotic forms of "pure acoustic waves" or "pure gravity waves" are reached in two limits. The acoustic wave, or high frequency limit, is reached when the frequency of propagating waves is much larger than the Brunt-Vaisala frequency ( $\omega^2 \gg N^2$ ) or, equivalently, in the limit when buoyancy is neglected ( $N=0$ ). In this case, the dispersion relation becomes

$$m^2 + k^2 + \frac{1}{4H^2} \approx \frac{\omega^2}{c^2} \quad (2.26)$$

which is the dispersion relation which would maintain for acoustic waves corrected for stratification (i.e., with the  $1/(4H^2)$  factor added).

The gravity wave, or low frequency (long period), limit is reached when the frequency the propagating waves is much smaller than the acoustic cut-off frequency ( $\omega^2 \ll \omega_a^2$ ) or when the compressibility of the medium vanishes ( $c = \infty$ ), in which case the dispersion relation becomes

$$m^2 + k^2 + \frac{1}{4H^2} \approx \frac{k^2 N^2}{\omega^2}. \quad (2.27)$$

For propagation frequencies such that  $m^2 > 0$ , inspection of Eqs. (2.19) and (2.20) shows that waves can propagate in the vertical. For propagation frequencies such that  $m^2 < 0$ , the vertical wavenumber is pure-imaginary and vertical wave propagation is not possible.

Figure 39, which contours the dispersion relation of Eq. (2.21) as a function of normalized frequency and horizontal wavenumber, provides a graphical means

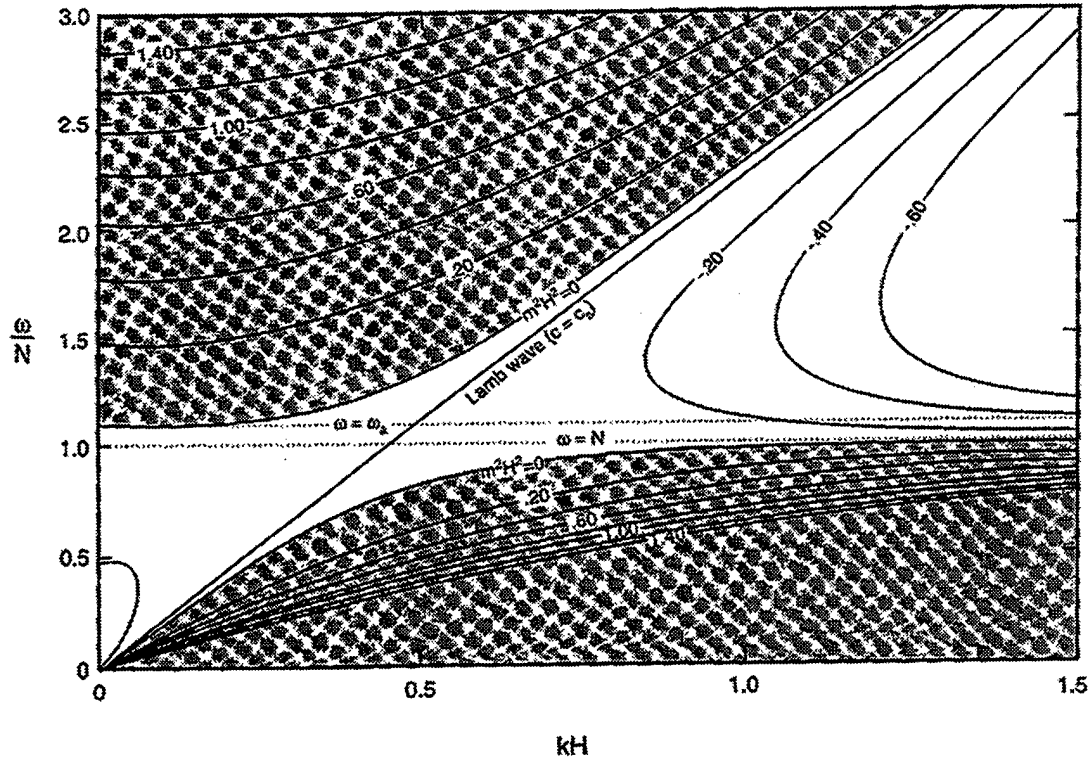


Figure 39. The vertical wavenumber squared contoured as a function of normalized frequency ( $\omega/N$ ) and horizontal wavenumber ( $kH$ ). [Figure adopted from *Salby* (1996).]

of summarizing the characteristics of acoustic-gravity wave propagation. The shaded region in the upper part of the figure is the acoustic wave domain in which  $m \geq 0$  and the frequency of the propagating waves is greater than the acoustic cut-off frequency ( $\omega_a$ ). The shaded region in the lower part of the figure corresponds to the gravity wave domain in which  $m \geq 0$  and the frequency of the propagating waves is less than the Brunt-Vaisala frequency,  $N$ . In the unshaded region, only vertically evanescent wave propagation is possible and wave propagation is in the horizontal direction. As noted by *Gill* (1982), "the horizontal component of the group velocity is given by the slope of the curves of constant  $m$ ".

The solid line separating the acoustic and gravity wave domains denotes the so-called Lamb wave or mode, discovered by *Lamb* (1909), which propagates with the speed of sound [denoted by  $c_s$  by *Salby* (1996).]

Figure 40 contrasts the vertical structure of propagating and evanescent waves. For purely vertically propagating waves,  $m^2 > 0$  and  $k=0$ , and the expression for the vertical particle velocity is

$$w(z,t) = e^{\left[\frac{1}{2H} + im\right]z} e^{i\alpha t} \quad (2.28)$$

whereas for evanescent waves,  $m^2 < 0$  and  $k=0$ , imply

$$w(z,t) = e^{\left[\frac{1}{2H} - m\right]z} e^{i\alpha t} \quad (2.29)$$

The energy density,  $E$ , from Eqs. (2.28) and (2.29) satisfies the proportionality conditions

$$E \propto \rho |w|^2 = \rho w w^* = \rho_0 (0) \quad (2.30)$$

so that the energy density is constant with altitude for vertically propagating waves and, for evanescent waves,

$$E \propto \rho |w|^2 = \rho w w^* = \rho_0 (0) e^{\left[2m - \frac{1}{H}\right]z}, \quad (2.31)$$

is exponentially damped.

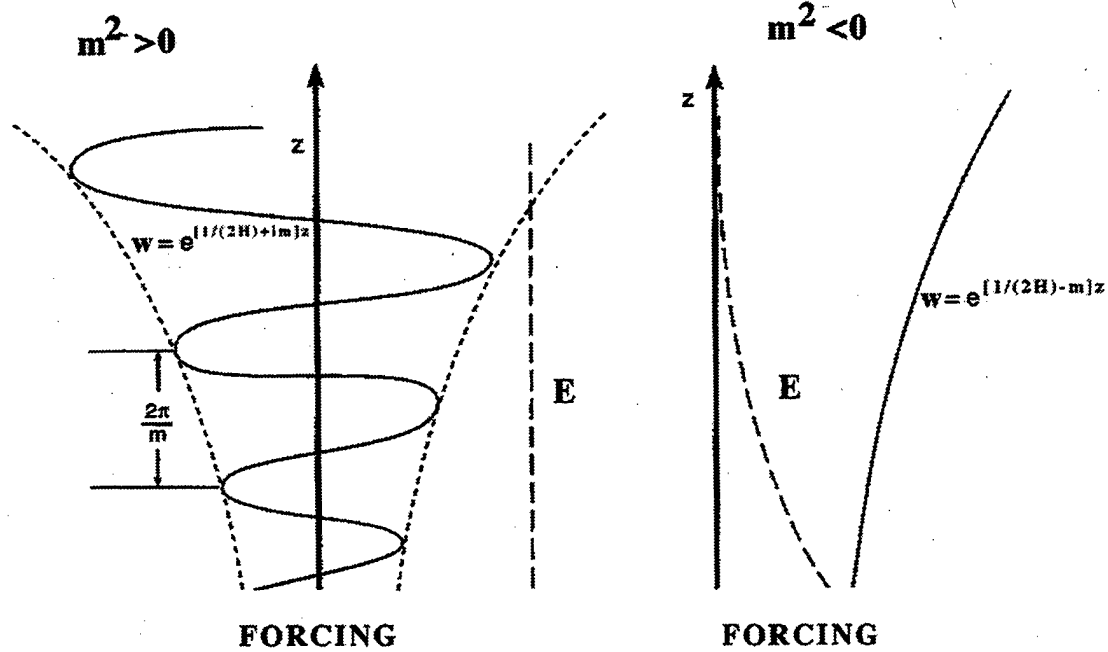


Figure 40. The vertical structure of the vertical particle velocity,  $w$ , and the associated energy density  $E$ . For propagating waves (left-hand panel), the energy density is constant with altitude whereas the vertical particle velocity amplifies with altitude. For non-propagating waves (right-hand panel), the energy density decreases with height and the particle velocity either decreases or increases with altitude depending on the sign of  $m$ . [Figure adopted from Salby (1996).]

Figure 41 contours the "intrinsic frequency" ( $\omega/N$ ) of acoustic-gravity waves in the acoustic wave domain ( $\omega > \omega_a$ ) as a function of vertical and horizontal wavenumber. The contours of  $\omega/N$  are elliptical rather than circular because of stratification. The intrinsic group velocity,  $c_g$ , the gradient of frequency in wavenumber space, is directed perpendicular to the contours of constant frequency and is seen to be almost parallel to the phase velocity: a circumstance implying weak dispersion.

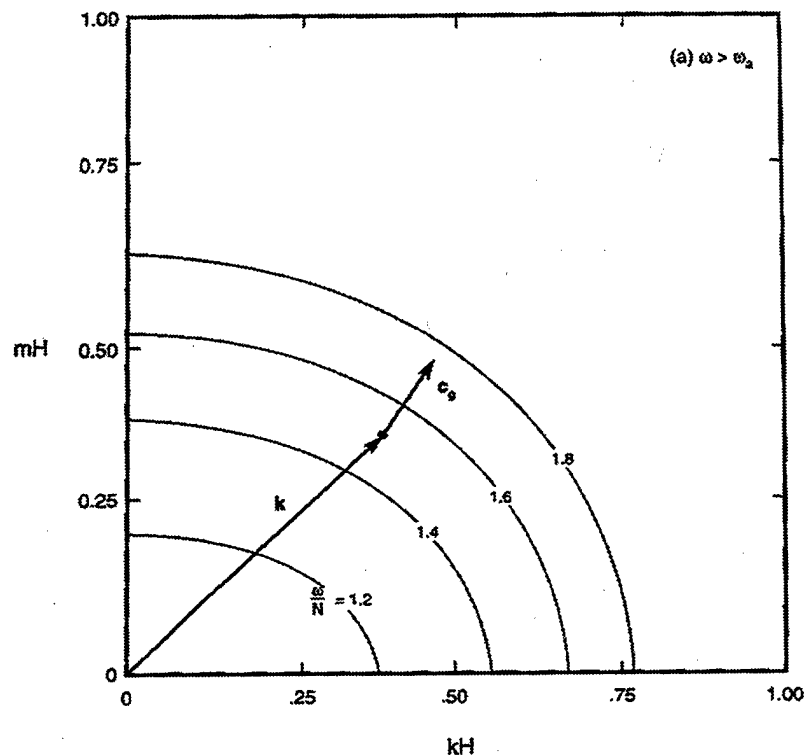


Figure 41. Contours of intrinsic frequency ( $\omega/N$ ) as a function of horizontal and vertical wavenumber in the acoustic wave domain ( $\omega > \omega_a$ ).  $c_g$  denotes the group velocity. [Figure adopted and modified from *Salby* (1996).]

Figure 42 presents similar contours of intrinsic or normalized frequency in the gravity-wave domain ( $\omega < N$ ) and it is seen that intrinsic group velocity is directed perpendicular to the direction of the phase velocity. In the gravity-wave sector, the contours of intrinsic frequency are hyperbolic. Figure 43 illustrates the relationship between the phase and group velocities in a different way for "packets" of acoustic and gravity waves propagating away from a source.

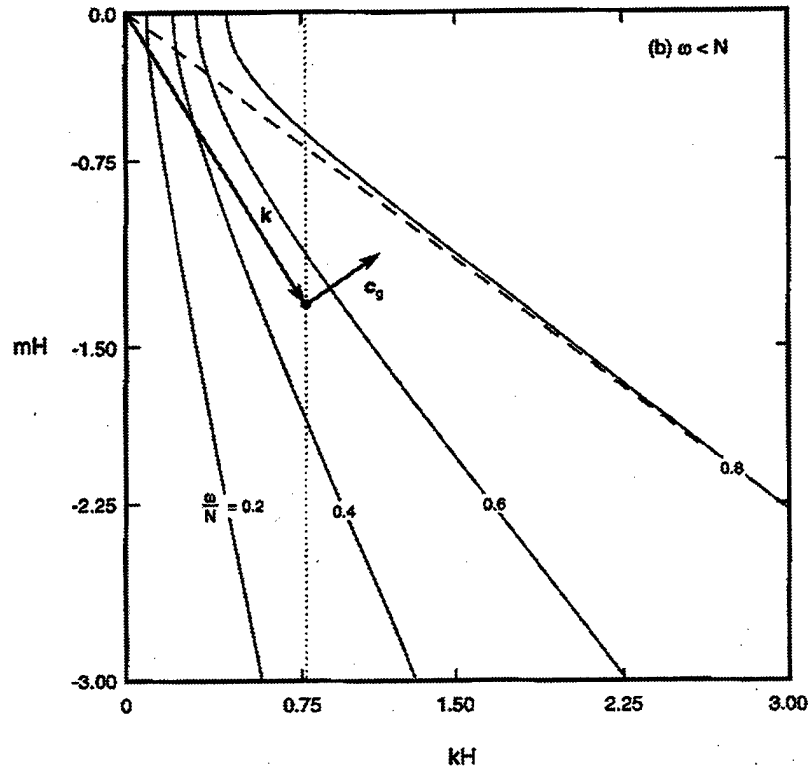


Figure 42. Contours of intrinsic frequency ( $\omega/N$ ) as a function of horizontal and vertical wavenumber in the gravity wave domain ( $\omega < N$ ).  $c_g$  denotes the group velocity. [Figure adopted and modified from *Salby* (1996).]

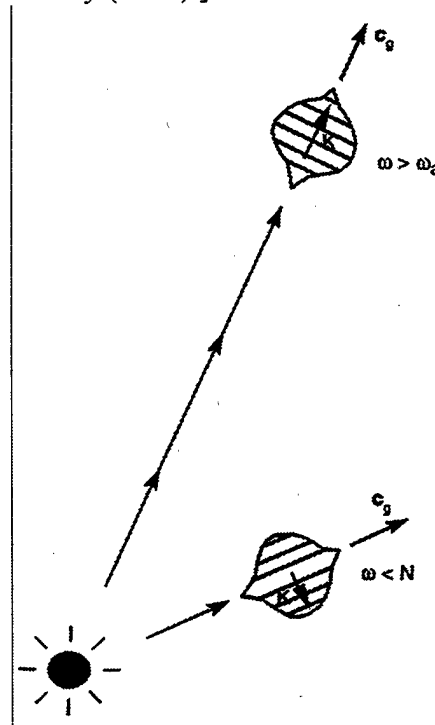


Figure 43. Wave packets of acoustic and gravity waves propagating away from a source and illustrating the relationships between the phase and group velocities. [Figure adopted from *Salby* (1996).]



The dispersion relation for the Lamb mode, which is physically the normal mode in an unbounded, stratified and compressible atmosphere, is obtained from Eq. (2.32) in the long wavelength limit ( $k \sim 0$ ) as

$$m^2 + \frac{1}{4H^2} = \frac{N^2 k^2}{\omega^2}. \quad (2.32)$$

The requirements that the vertical particle velocity vanish at the earth's surface (rigid boundary condition) and that the energy in a vertical atmospheric column be finite, leads to the requirement that  $m^2 < 0$  (no vertical propagation) and to a pressure perturbation amplitude of the form

$$P_L(z) = e^{-\Gamma z}, \quad (2.33)$$

where [Gill (1982)]

$$\Gamma = \frac{1}{2} \left( \frac{g}{c^2} - \frac{N^2}{g} \right), \quad (2.34)$$

and the propagation speed is a constant, given by

$$c^2 = \gamma g H. \quad (2.35)$$

Accordingly, Lamb waves have an exponentially decreasing pressure amplitude as a function of increasing altitude and propagate horizontally with a constant phase speed.

For a non-isothermal atmosphere, wave propagation becomes significantly more complex as propagation characteristics become strong functions of position. Space, as well as excellent extant literature sources, does not permit any detailed discussion herein but, in brief, it is simply noted if the Brunt-Vaisala frequency and mean flow vary with height, the dispersion relation of Eq. (2.21) is replaced by the relationship [Salby (1996)]

$$m^2(z) = \frac{N^2(z)}{(c_x - \langle u \rangle)^2} - k^2 + \frac{\langle u(z) \rangle_{zz}}{(c_x - \langle u(z) \rangle)} \quad (2.36)$$

which is referred to as the Taylor-Goldstein relation where  $\langle u(z) \rangle$  denotes the mean velocity, and the subscripts  $x$  and  $zz$  denote first and second derivatives with respect to  $x$  (or range) and  $z$  (or altitude), respectively. For the situation under consideration, if  $m^2 > 0$ , the waves do not amplify with increasing altitude but are eventually reflected at an altitude referred to as the "turning level" so that vertical and downward propagation are coupled.

For  $m^2 < 0$ , the waves are still evanescent. In the circumstance that the denominator terms in Eq. (2.26) vanish, i.e., when  $(c_x - \langle u(z) \rangle) = 0$ , the vertical wavenumber becomes infinite or, equivalently, the vertical wavelength vanishes. The altitude at which this happens is referred to as the "critical layer" and the waves die out because of absorption.

This section is concluded by illustrating the incorporation of point energy and mass injection sources following the development of *Kanamori, More and Harkrider* (1994). This is done to highlight new results and to support the discussion in Section 6.0 of the excitation of Rayleigh waves by atmospheric coupling from a volcanic eruption.

As noted by *Kanamori, et al* (1994), the problem has been considered others: *Row* (1967), *Pierce* (1963), *Ben-Menachem and Singh* (1981) and *Harkrider* (unpublished note 1975). As mass injection source is introduced by adding a source term to the right-hand side of the conservation of mass equation [Eq. (2.14)] so that it is replaced by

$$\frac{\partial \rho}{\partial t} + w \frac{\partial \rho_0}{\partial z} + \rho_0 \left( \frac{\partial u}{\partial x} + \frac{\partial v}{\partial y} + \frac{\partial w}{\partial z} \right) = -4\pi F_M e^{i\omega t} \delta^3(R - R_s) \quad (2.37)$$

where  $F_M$  is the mass injected per unit time,  $R = (x, y, z)$  and  $R_s$  is the source point  $(0, 0, z_s)$ . An energy injection source is incorporated by adding a source term to the right-hand side of Eq. (2.15) so that it is replaced by

$$\frac{\partial p}{\partial t} - g \rho_0 w = c^2 \left( \frac{\partial \rho}{\partial t} + w \frac{\partial \rho_0}{\partial z} \right) - 4\pi F_E e^{i\omega t} \delta^3(R - R_s) \quad (2.38)$$

where  $F_E$  is the energy injected per unit time.

Following the same procedures used to derive Eqs. (2.17) and (2.18) the leads to Eqs. (2.35) and (2.36), respectively:

$$\left[ \frac{\partial^2}{\partial x^2} + \frac{\partial^2}{\partial y^2} - \frac{1}{c^2} \frac{\partial^2}{\partial t^2} \right] p = \rho_0 \frac{\partial}{\partial t} \left[ \frac{\partial w}{\partial z} - \frac{g w}{c^2} \right] - 4\pi i \omega \left( F_M + \frac{F_E}{c^2} \right) e^{i\omega t} \delta^3(R - R_s) \quad (2.39)$$

and

$$\frac{\partial^2 w}{\partial t^2} - g \left[ \frac{1}{\rho_o} \frac{\partial \rho_o}{\partial z} + \frac{g}{c^2} \right] w = -\frac{1}{\rho_o} \frac{\partial}{\partial z} \left( \frac{\partial p}{\partial z} + \frac{g p}{c^2} \right) + \frac{4\pi g F_E}{c^2 \rho_o} e^{i\omega t} \delta^3(R - R_s). \quad (2.40)$$

Assuming solutions to Eqs. (2.39) and (2.40) of the form

$$w(x, y, z, t) = w^*(x, y, z, t) e^{i\omega t} \quad (2.41)$$

and

$$p(x, y, z, t) = p^*(x, y, z, t) e^{i\omega t}, \quad (2.42)$$

the  $w^*$  variable can be eliminated and a single equation obtained for  $p^*$  of the form

$$\frac{1}{(R^*)^2} \frac{\partial}{\partial R^*} \left[ R^{*2} \frac{\partial}{\partial R^*} \left( \frac{p^*}{\rho_o^{1/2}} \right) \right] + \kappa^2 \left( \frac{p^*}{\rho_o^{1/2}} \right) = \frac{-4\pi i \omega}{\rho_o^{1/2}} \left[ F_M + \frac{F_E}{hc^2} \left( 1 + \frac{g}{\omega^2} \frac{\partial}{\partial z} \right) \right] \delta^3(R - R_s) \quad (2.43)$$

where in the above,

$$(R^*)^2 = r^2 + h(z - z_s)^2 \text{ and } r^2 = x^2 + y^2, \quad (2.44)$$

and

$$\kappa^2 = \frac{\omega^2}{c^2} \left( \frac{\omega^2 - \omega_a^2}{\omega^2 - N^2} \right), \quad (2.45)$$

where, as before  $\omega_a$  and  $N$  are respectively, the acoustic cut-off and buoyancy frequencies. Eq. (2.43) provides a convenient formalism for the incorporation of either a mass or energy injection point source and, as far as is presently known, is a new result.

For a point mass source,  $F_E=0$ , and a closed form expression can be obtained for the pressure field as given in Eq. (20) of *Kanamori, Mori and Harkrider* (1994). For a point energy source, a closed form particular solution can be obtained as given in Eq. (26) of the same paper. For a point mass source which varies as a step function, a closed form expression can also be derived for the pressure field at zero range with the result given by

$$p_H(0, z, t) = \frac{F_M e^{\left( \frac{z - z_s}{2H} \right)}}{|z - z_s|} \left\{ \delta(t - t_o) - \frac{\omega_a t_o J_1[\omega_a(t^2 - t_o^2)^{1/2}]}{(t^2 - t_o^2)^{1/2}} H(t - t_o) \right\}, \quad (2.46)$$

where the subscript H is used to denote the Heaviside step function,  $t_0$  is the time of the mass injection and  $J_1$  is a spherical Bessel function of order one.

As noted by *Kanamori, Mori and Harkrider* (1994), Eq. (2.46) was derived previously by *Row* (1967). The first term represents the direct arrival and the second is a term which oscillates at a frequency corresponding to the acoustic cut-off frequency.

For a finite range, the pressure field must be computed by numerically evaluating the integral

$$p_H(r, z, t) = \frac{F_M e^{\left(\frac{z-z_s}{2H}\right)}}{|z-z_s|} \int_{-\infty}^{+\infty} d\omega \frac{1}{R} \frac{(\omega^2 - N^2)^{1/2}}{(\omega^2 - \omega_c^2)^{1/2}} e^{i\omega\left(t \pm \frac{R}{C}\right)} \quad (2.47)$$

where in the above  $R^2 = r^2 + (z-z_s)^2$  and

$$C = \frac{c\omega}{(\omega^2 - \omega_a^2)^{1/2}}, \quad (2.48)$$

and

$$\omega_c = \frac{|z-z_s|N}{R}. \quad (2.49)$$

The results from some of the numerical evaluations of Eq. (2.43) are presented in Section 6.0

### 3.0 THE MEASUREMENT OF INFRASOUND

*Cook and Bedard* (1971) discuss general principles in the measurement of infrasound (frequencies below 20 Hz) and cite earlier work in the same area published by *Cook and Young* (1962) and *Cook* (1969). It is emphasized that naturally occurring infrasound typically produces pressure fluctuations in the range of 0.1  $\mu$ bar to 100  $\mu$ bar and several noise sources are listed: volcanic explosions, earthquakes, waves on the seas (microbaroms), large meteorites, severe storms and aurora in the polar regions.

The most common sensor type used in the detection of infrasound is a membrane-type microphone with a backing, or reference, volume of air as illustrated in Figure 44.

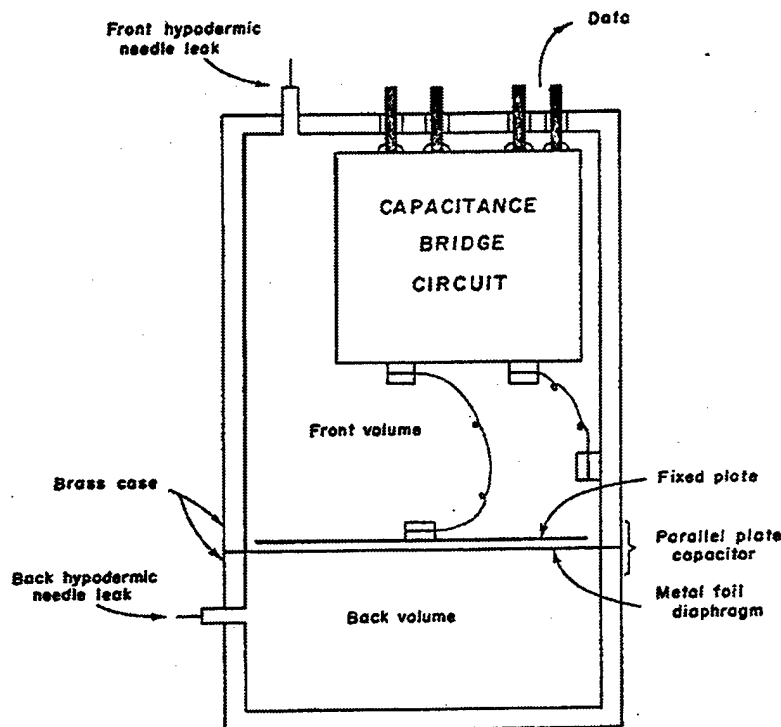


Figure 44. A capacitance type microphone with a backing volume of air. This type of sensor has been the most commonly used in the measurement of infrasound. [Figure adopted from *Smart* (1966).]

The pressure of the backing volume is the reference pressure to which the ambient, outside pressure is measured. The basic sensing element is a capacitor, one plate of which is fixed whereas the other is a flexible metal diaphragm which serves to divide the container into

two chambers. Each chamber is equipped with a capillary leak to the atmosphere. As pressure changes occur in the open atmosphere, one chamber responds more rapidly than the other and a pressure difference is created across the diaphragm, which flexes and changes the capacitance: the variable measured. The chamber referred to as the backing or reference volume is equipped with a slower leak than that of the front volume and by adjusting the size of the capillary leaks (or, equivalently, their time constants), the instrument can be made to act as a sensitive low-pass filter. In a common configuration, the capillary leak from the reference volume communicates to the front volume but this circumstance is not shown in the figure.

The most common background noise source encountered by capacitance type microphones (and others) is referred to as "wind noise" and is due to the advection of patches of atmospheric turbulence past the microphone by the wind. The important effects of wind noise or "the turbulent passage of the wind" on pressure levels is illustrated using Bernoulli's principle

$$p + \frac{1}{2}\rho v^2 = \text{constant} \quad (3.1)$$

which provides a relationship between pressure fluctuations,  $\Delta p$ , produced by a wind-speed fluctuation in the amount of  $\Delta v$  given by

$$\Delta p \approx \rho v(\Delta v). \quad (3.2)$$

Numerically, for a wind whose speed varies irregularly from 25 km/h to 40 km/h, the above relation predicts a random pressure fluctuation of 500  $\mu\text{bar}$ .

More quantitatively, Figure 45 compares the relative power of the background noise as a function of period from 1 s to 100 s and as a function of wind speed for wind speeds of 2.8 m/s and 4.3 m/s. The data indicate that the noise power is a strong function of both wind speed which is independent of the period: an approximate doubling of the wind speed produces a ten-fold increase in the noise power at all periods. The curves peak near a frequency of 50 Hz and fall off quite rapidly as the period is decreased, or as the frequency is increased.

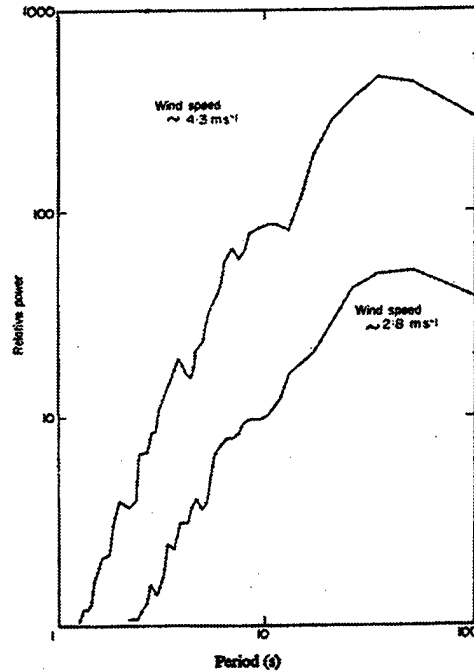


Figure 45. The relative power of the background or wind noise as a function of period for wind speeds of 2.8 m/s and 4.3 m/s. [Figure adopted from *McDonald, Douze and Herrin (1971)*.]

Noise contamination by wind noise has been most commonly reduced by connecting the capillary leak of the front volume of the capacitance microphone to what is commonly referred to as a Daniel's front end noise filter [*Daniels (1959)* and *Burridge (1971)*] which, "for sound waves greater than about 3 km (frequencies below 0.11 Hz) is essentially non-directional and does not attenuate the sound pressure appreciably. However, noise due to random pressure fluctuations in the period range of 1.0 - 30 s (1 Hz to .033 Hz), such as that caused by wind turbulence, is reduced considerably" [*Cook and Bedard (1971)*].

The pipe array was typically several hundreds of feet in length (sometimes 2,000') and perforated with small inlet ports equally spaced along its length and oriented with its length parallel to the expected direction of the infrasonic source to be monitored. A schematic diagram of a Daniels pipe array is provided in Figure 46 where the attachment to the microphone is located at the center of the array.

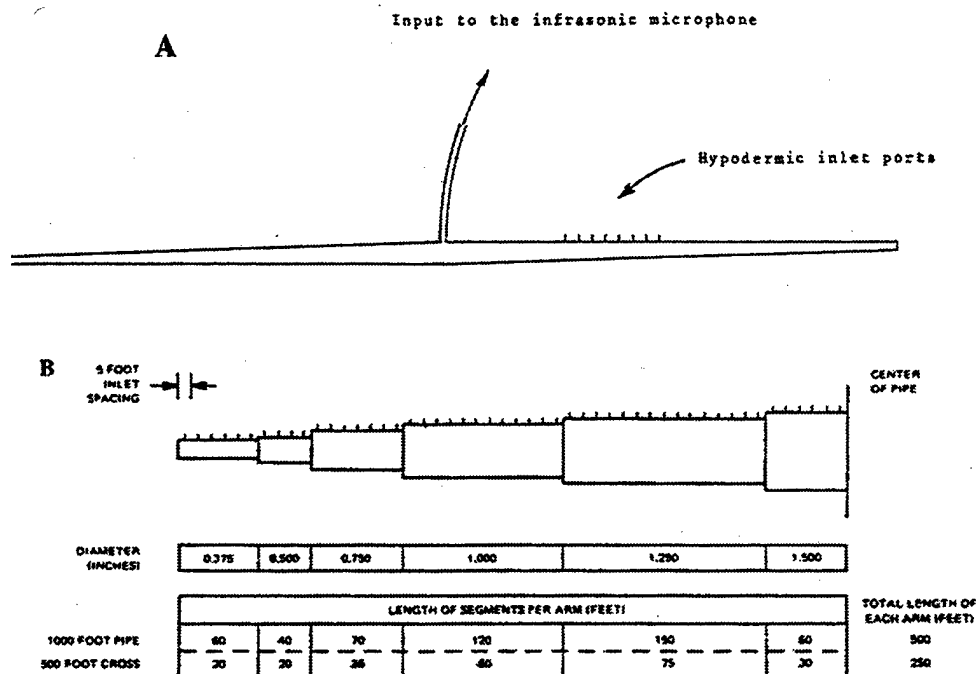


Figure 46. A schematic diagram of one type of Daniels pipe array designed to suppress wind noise at the input to an infrasonic microphone. Panel A shows the overall configuration illustrating the fixed-interval hypodermic needles which provide access to the outside. Excepting the input to the sensor at the center, the pipe is otherwise sealed. In practice, the taper was achieved by stepped reductions in the pipe diameter at regular intervals as shown in Panel B. [Figure adopted from *Smart* (1966).]

The physical idea behind the configuration was to exploit the fact that turbulent pressure fluctuations or "wind noise" were advected by the wind at much lower speeds than were the infrasonic signals and were of a much shorter correlation length than low frequency propagating waves from sources of interest. The signal arriving at each of the inlet ports would be added coherently along the length of the pipe and propagated at high speed down the length of pipe to the microbarograph. The signal from the wind noise would be totally or at least partially incoherent at each of the inlet ports and tend to add out of phase.

As pointed out by *Daniels* (1959), if there are  $N$  inlets along the pipe, each delivering a random signal of amplitude  $A$ , the total noise power will be given by  $NA^2$ . However, the total noise power for the signal of the same amplitude will be  $(NA)^2 = N^2A^2$  so that the improvement in signal-to-noise-ratio in power is :  $N$  or,  $10\text{Log}_{10}(N)$  in dB.



The pipe array proposed by *Daniels* (1959) consisted of a length of pipe of total length  $L$  made up from sections of pipe of smaller lengths and radii, with the smaller radii sections oriented to the end as shown in Figure 46. The general response of pipe array was shown to be of the form

$$P_0 = P_{GK} (\Delta S_K / S_N) \exp(-\sum_i \gamma_i l_i) \quad (3.3)$$

where  $P_0$  is the output pressure at the end of the array,  $S_N$  is the cross-sectional area of the large end of the line,  $\Delta S_K$  is the change in area at the  $k$ -th junction,  $\gamma_i$  is the propagation constant in the  $i$ -th segment of pipe,  $l_i$  is the length of the  $i$ -th segment and the summation is over all the segments from the  $k$ th to the end of the pipe. If the radii of all pipe segments times the square root of the frequency of interest is sufficiently large, the exponential term will be the same as that for free space. If the small end of the pipe array is pointed in the direction of the sound source, so that the phasing of the inputs is correct, the line microphone will be non-attenuating.

An example of the reduction in wind noise which was achieved with a microphone equipped with a 1980 ft (603.5m) noise reducing pipe array is provided in Figure 47 [*Daniels* (1959)]. In this example the wind speed ranged from 25 mph to 30 mph. The upper trace shows the output of the acoustic-electric transducer alone and the lower trace shows the response when attached to the pipe array. The reduction in the background noise level is 20 dB.

*McDonald, Douze and Herrin* (1971) conducted experiments demonstrating that the coherence of the wind noise as a function of distance between two sensors, depends on the orientation of the sensors with respect to the primary wind direction. The sensors used in their work were those designed and developed by the National Bureau of Standards (NBS) [*Priestley* (1966) and *Herrin and McDonald* (1971)] with inlets connected to a 50 ft length of thick-walled garden hose open at one end. Sensor coherence measurements were conducted at number of sensor separations and periods "with the wind blowing along the

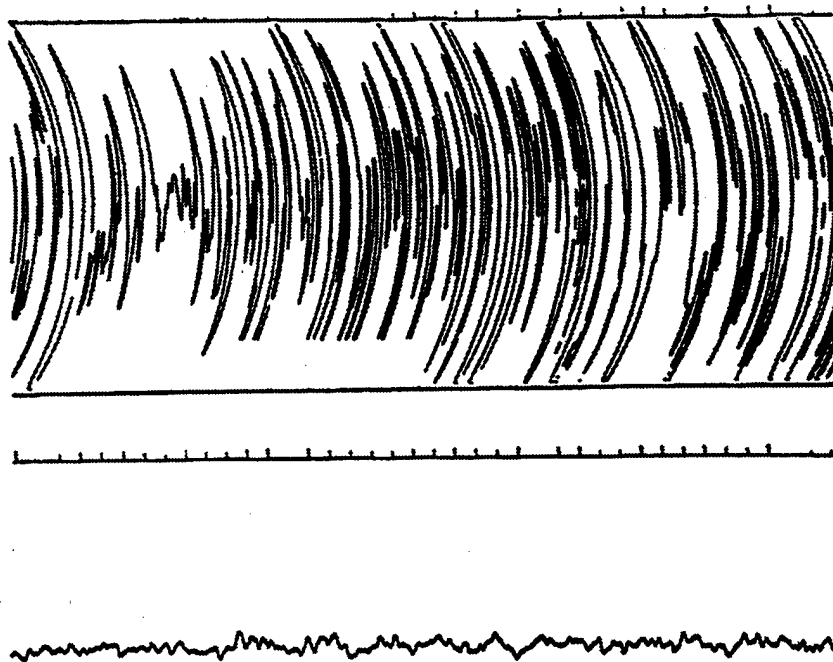


Figure 47. An example of the reduction in wind noise achieved with a microphone equipped with a 1980 ft (603.5 m) noise reducing pipe array. [Figure adopted from *Daniels* (1959).]

the direction of the line of the inlets and with the wind blowing perpendicular to the line of the inlets".

The coherence of the wind noise pressures was found to fall off rapidly as a function of decreasing period at all sensor separations and the rate of decrease was found to be much faster for an orientation perpendicular to the wind than for a parallel orientation: a circumstance illustrated in Panels A and B of Figure 48.

The capacitance microphone was not the only infrasound transducer which was investigated and, indeed, *Fehr* (1967) lists several others: the reluctance type (Pace Engineering Company), the electrochemical type or Solion [*Collins, Richie and English* (1964)], the thermistor type [*Fehr, Ben-Ary and Ryan* (1967)], and the manometer type [*Donn, Shaw and Hubbard* (1963)].

By way of illustration, the development of an electrochemical transducer was described by *Collins, Richie and English* (1964). The device was referred to as the Solion,

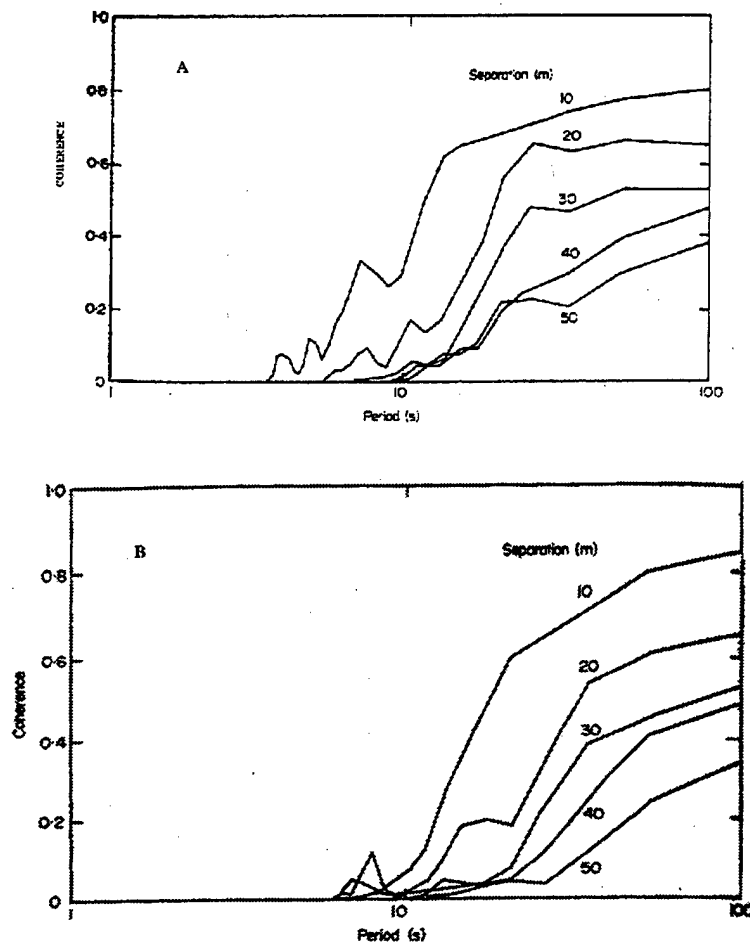


Figure 48. Noise coherence as a function of period and sensor separation for line microbarographs aligned parallel (Panel A) and perpendicular (Panel B) to the direction of wind propagation. [Figure adopted from *McDonald, Douze and Herrin (1971)*.]

named after "ions in solution", and was designed specifically for the detection of low frequency pressure waves in the atmosphere. The overall frequency response extended from 0.003 Hz (period of 10 s) to 50 Hz and the instrument had a dynamic range extending from 0.1  $\mu$ bar to 1,000  $\mu$ bar, achieved high stability and was remotely deployable.

A schematic of the Solion device is provided in Figure 49 and shows the device to consist of a central cathode surrounded by three anode plates which are mounted in a molded plastic which, in turn, is enclosed by a plastic compliant diaphragm. The device is one of a class of redox systems in which, "the electrochemical reactions are completely reversible, and the electrode system does not enter into the reaction, except to remove or

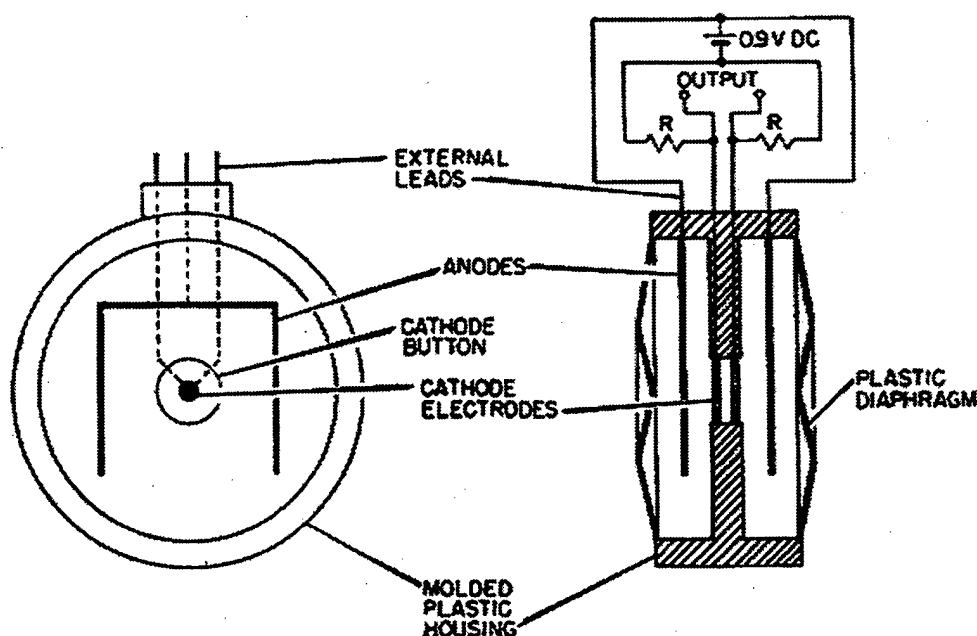


Figure 49. A schematic diagram of the solion linear-flow infrasonic microphone. [Figure adopted from *Collins, Richie and English* (1964).]

inject electrons. The redox system consists of an electrode set immersed in a solution containing soluble forms of the same chemical in two different oxidation states. For the solion transducer, this solution is generally an iodine/iodide water system. ... Electric current is transferred via ion flow between the electrodes."

In operation, a small potential difference is applied to the device and, in the absence of a fluctuating pressure field, there is no differential pressure between the diaphragms, and a minimal or "limiting" current is established. In the presence of a dynamic pressure field, there is a differential pressure between the diaphragms which produces a net electrolytic flow and an increased output current which turns out to be proportional to the differential pressure.

Just as several different infrasonic transducers were considered, simple line configuration was not the only one investigated for its utility in reducing wind noise. and, indeed, *Grover* (1971) reported on the investigation of several types of wind noise filters in tests conducted at the Blacknest Infrasonic Array (BNIA) in the U.K. In particular, the performance of a number of wind shield designs was determined and compared with the

performance of line and circular or ring pipe arrays utilizing different spacings for the inlet port holes. In all cases, the performance of the wind screen and pipe arrays were compared with a standard microbarograph with no noise filter.

The conclusions of the work were that the pipe arrays performed much better than the wind screens and that the ring configuration should "produce less attenuation of a signal, due to misphasing, than the same pipe operating as a linear center-fed array aligned in the direction of propagation and having dimensions of the same order as the signal wavelength". In addition to the configurations explicitly tested, *Grover* (1971) also made mention of other pipe designs such as spiral, star or cross-shaped configurations with the microbarograph located at the center.

In more recent times, *Noel and Whitaker* (1991) report the results of an experiment investigating and comparing the performance of various noise reducing arrays in an experiment set up and arranged within a distance of 7 m of each other. The configurations investigated consisted of:

- a "spider" having a centrally located Globe microphone and 12 sections of 50 ft (15.24 m) length porous hoses (soaker hose) extending radially from the microphone
- a single-arm perforated pipe of length 450 ft (137.16 m) connected to a Globe microphone at one end
- a four-armed cross of pipe arrays with each element having a length of 125 ft (38.1 m) and connected to a central Globe microphone
- a single-element microbarograph without a front end noise filter
- a single Globe microphone without a front end noise filter

the latter sensor, serving as the control sensor, much in the same spirit as *Grover* (1971). Figure 50 provides a schematic representation of the experimental setup. The experimental procedure used the single Globe microphone as a standard and utilized an underground explosion at the NTS, at a range of 256 km and referred to as INGOT, as a calibration signal. The spider and cross configurations were found to be most effective in reducing the

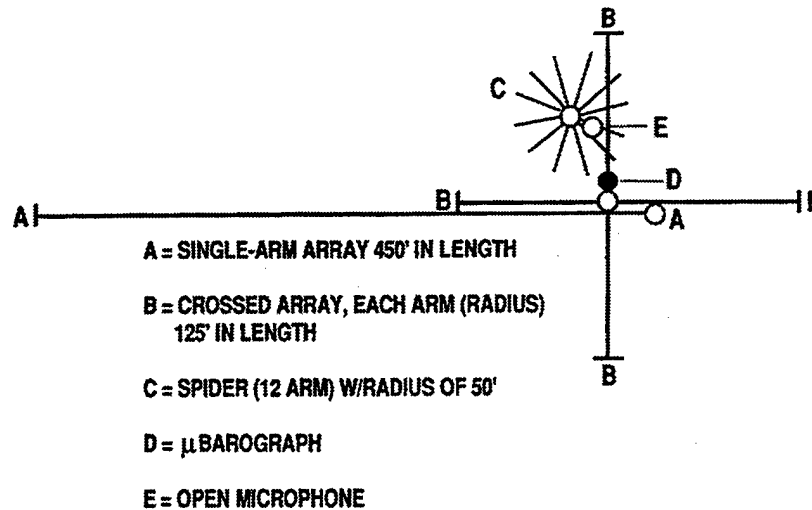


Figure 50. A schematic diagram of the experimental design used by investigators at the Los Alamos National Laboratory in their noise reduction studies. [Figure adopted from *Noel and Whitaker* (1991).]

wind noise and in faithfully preserving the signal characteristics of the underground nuclear explosion. For illustrative purposes, Figure 51 provides raw channel data for the various sensors during a period of average noise levels. Figure 52 shows the spider array actually deployed in the field.

Because both infrasonic and seismic waves propagate in an elastic media, similar signal processing algorithms have been utilized to analyze both wave types. However, because all atmospheric nuclear testing ended some 20 years ago, interests in earthquake studies and the need to monitor underground nuclear explosions, far more effort has been directed to the processing of seismic than infrasonic data. In the following, only a very high level review of the processing of infrasonic data is presented, deferring to the excellent and very complete discussion of the subject presented in *Gossard and Hooke* (1975).

With the exception of signals created by very large nuclear explosions or very large natural events such as volcanic eruptions, etc., infrasonic signals of interest typically have small signal-to-noise ratios. Indeed, usually the most important task in infrasonic monitoring is to first detect a coherent signal which can be hidden in a noise background

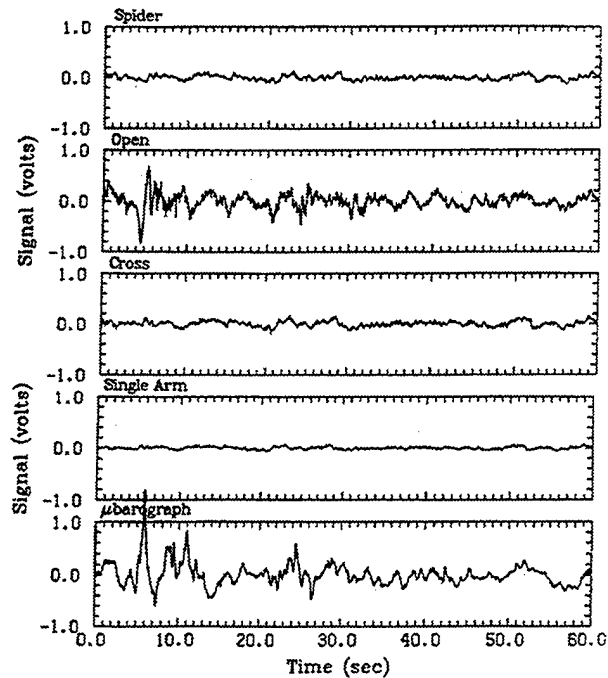


Figure 51. The raw channel data for each of the indicated sensors (Spider, Open, Cross, Single Arm and  $\mu$ bar) showing the background noise at 1401:20 UT corresponding to the average noise level during the experimental period. [Figure adopted from Noel and Whitaker (1991).]

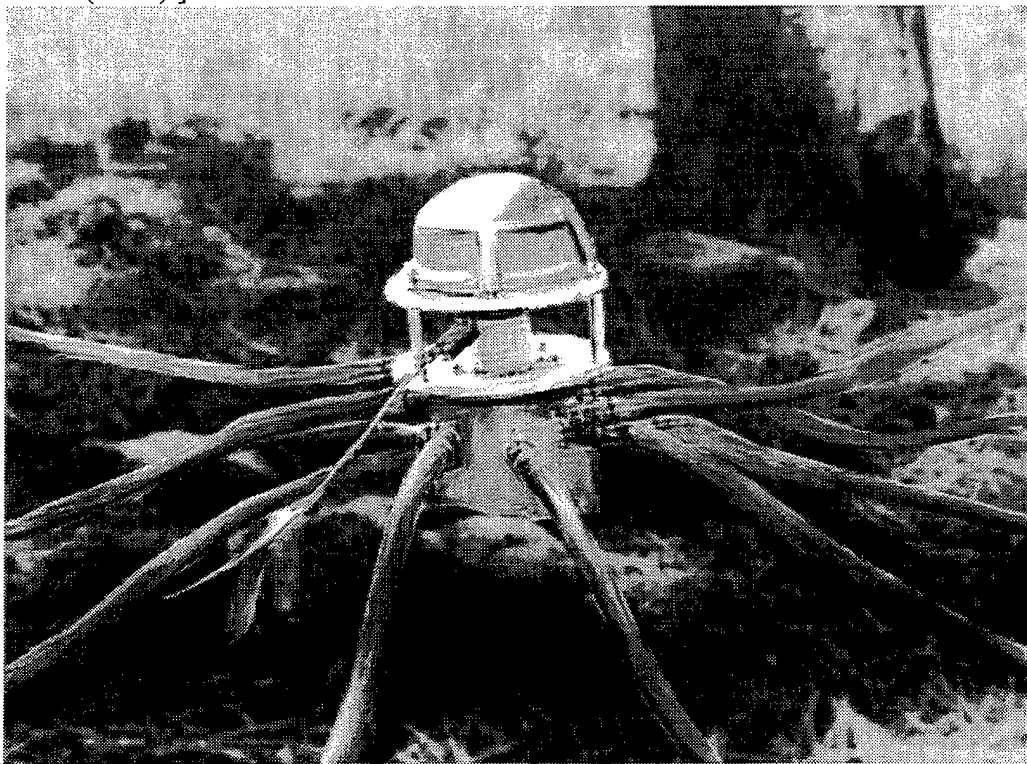


Figure 52. The Los Alamos Laboratory "spider" infrasonic sensor deployed in the field. [Figure adopted from Davidson and Whitaker (1992).]

which can itself be either coherent or incoherent. Given the detection of a signal, its properties must be enhanced so that key properties of the signal can be extracted: source type, path of propagation and source azimuth.

The infrasonic monitoring which will be involved in ensuring compliance to a CTBT will of necessity be concerned with the frequency band extending from 0.01 Hz to 10 Hz [*Conference on Disarmament*, (1995a)] which is a significantly higher band than was used in previous monitoring efforts concerned with the signals produced by explosions in the megaton range. Accordingly, it may perhaps prove necessary to develop new signal processing strategies to work in a higher frequency region.

An important signal processing issue associated with work at higher frequencies is the need to eliminate or significantly reduce the lower frequency background noise. By way of illustration, Figure 53 reproduces the power spectrum of the "normal" level of "background" fluctuations or turbulence which were recorded at San Diego, California during the time period extending from April 1, 1956 to November 1, 1956 and cover the period range extending from approximately one week to 0.2 s (5 Hz). According to *Gossard* (1960), the low frequency data (periods longer than 2 hr) were recorded on a "standard microbarograph located at the U.S. Navy Electronics Laboratory". The remainder of the spectra were measured using a sensitive low frequency microphone described by *Johnson and Chiles* (1957).

The composite spectrum receives contributions from many sources and inspection of the figure shows that the range of turbulent pressure fluctuations varies over ten orders of magnitude for the indicated period range. The overall slope of the spectrum is approximately  $f^{-2}$  and the two prominent spikes are due to the diurnal and semi-diurnal tides. As noted by *Gossard and Hooke* (1975) "at the higher frequencies, buoyancy waves, convective activity and wind advected turbulence are the primary contributors".



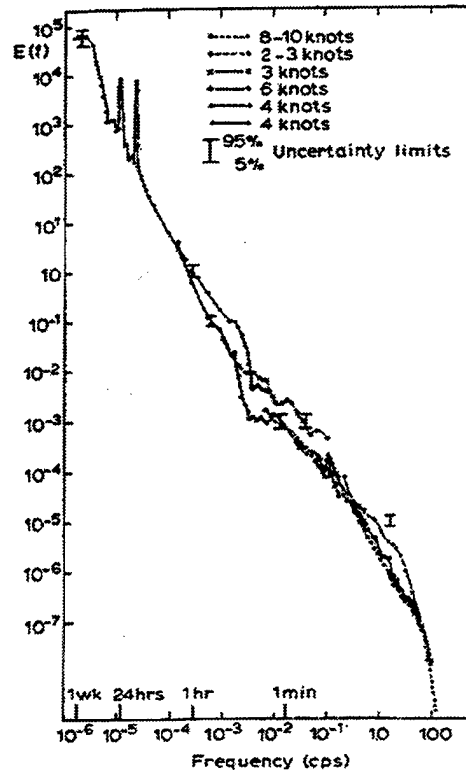


Figure 53. The power spectrum of "natural atmospheric pressure fluctuations recorded on pressure sensors located at the U.S. Navy Electronics Laboratory in San Diego, CA. The dimensions of  $E(f)$  are  $(\text{mb})^2/\text{rad sec}^{-1}$ . The rapid fall off in spectral power is attributed to degraded instrument response. [Figure adopted from *Gossard* (1960).]

Measurements of infrasound are typically made with two-dimensional arrays of sensors located on the ground and several geometries have been used (e.g., quadrilaterals, squares, triangles, etc.) over the years as well as a wide range of sensor separations: from a few kms to hundreds of kms. Figure 54 shows the current geometrical arrangement of sensors planned for use in a worldwide network of infrasonic monitoring stations [*Conference on Disarmament*, (1995b)].

As indicated in the figure, the arrangement consists of three sensors located at the corners of an equilateral triangle with a single sensor located at the center. This configuration has been shown to be the optimum arrangement for an array made up of four sensors [*Haubrich*, (1968)].

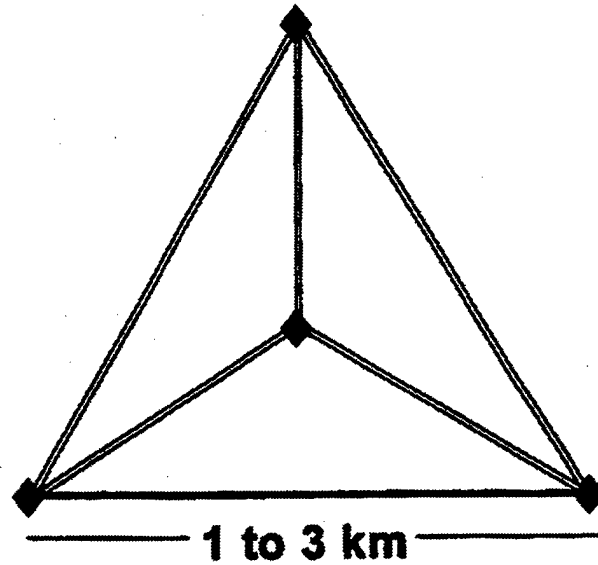


Figure 54. The four element array geometry to be used in the typical infrasound station deployed as part of the international network. The sensor locations are indicated by the diamonds and it is envisioned that each sensor element will consist of a low frequency microphone equipped with wind noise filters arranged in the "spider" configuration shown in Figure 52. [Figure adopted from *Conference on Disarmament*, (1995b).]

Regardless of the deployment geometry, the use of a spatial array accomplishes velocity, direction and wavelength filtering with the relative times of arrival at the individual sensors determining the signal propagation speed and direction. Because signal-to-noise signals for infrasonic signals are typically small, the most common approach used to estimate relative signal arrival times has been to compute the cross-correlation function,

$R_{xy}(\tau)$ , for the signals,  $x(t)$  and  $y(t)$ , recorded by two array elements

$$R_{xy}(\tau) = \lim (T \rightarrow \infty) \frac{1}{2T} \int_{-T}^T dt x(t) y(t + \tau) \quad (3.4)$$

where  $T$  is half the sample length and  $\tau$  is a lag time. Given an evaluation of this function, the determination of the difference in signal travel time between two sensors is taken to be that value of  $\tau$  for which the correlation function is a maximum. However, in the presence of contaminating noise, the interpretation is often difficult. The cross correlation is frequently normalized by dividing  $R_{xy}(\tau)$  by the square root of the product of the autocorrelation functions of  $x$  and  $y$  at zero delay (each computed as above, but as a correlation of the signal with itself, delayed).

The implementation of such a procedure helps somewhat but the interpretation is often still difficult. Some frequency domain functions have been found useful for resolving their problem and one such function is the cross-power spectrum,  $\Phi_{xy}(\omega)$ , which is defined as the Fourier transform of the cross-correlation function or as

$$\Phi_{xy}(\omega) = \frac{1}{\pi} \int_{-\infty}^{+\infty} d\tau e^{i\omega\tau} R_{xy}(\tau). \quad (3.5)$$

Given  $\Phi_{xy}(\omega)$ , the signal travel time between two sensors can be estimated in several ways. In one way, a transfer function between the two signals can be computed as

$$H(\omega) = \frac{\langle \Phi_{xy}(\omega) \rangle}{\langle \Phi_{xx}(\omega) \rangle} \quad (3.6)$$

where the  $\langle \dots \rangle$  notation indicates the possibility of using ensemble averaged values. The impulse response can be found by inverse Fourier transforming  $H(\omega)$  to obtain

$$h(\tau) = F^{-1} \left\{ \frac{\langle \Phi_{xy}(\omega) \rangle}{\langle \Phi_{xx}(\omega) \rangle} \right\}. \quad (3.7)$$

The value of  $\tau$  corresponding to the peak in the impulse response represents the most probable time delay between the two signals. The transfer function provides a very useful tool in determining the time delay between two signals and effectively removes the confusion present in the cross correlation by eliminating irrelevant information due to the power spectra (or the autocorrelation) of the two signals.

A measure of the validity of each time domain estimate can be obtained by computing the coherence function or "degree of causality" between the two signals. The coherence function is defined as

$$\gamma^2(\omega) = \frac{\langle |G_{xy}(\omega)|^2 \rangle}{\langle G_{xx}(\omega) \rangle \langle G_{yy}(\omega) \rangle}. \quad (3.8)$$

The coherence function varies from 0 to 1 and can be used directly to estimate the validity of the transfer function measurement or it can be used to estimate the signal-to-noise ratio as a function of frequency, using the relation

$$\frac{S(\omega)}{N(\omega)} = \frac{\gamma^2(\omega)}{1 - \gamma^2(\omega)}. \quad (3.9)$$

The determination of the time delay between two elements in an array specifies the location of the source as being on a three-dimensional hyperbolic surface. If the source is in the plane of the array, the surface becomes a hyperbolic curve in two-dimensions. If a third sensor is used to provide additional time delay measurements, two additional hyperbolic surfaces are determined. With high signal-to-noise and perfect time delay measurements, the source location will be on the intersection of these surfaces. If the source is far away relative to the dimensions of the array, the hyperbolas may only specify a bearing to the source. With lower time delay measurement accuracies, the three hyperbolae may not intersect at a single point, but will define an approximately triangular area that should contain the source. The addition of a fourth element in an array, as is illustrated in Figure 54, and the associated time delays can be used to solve the three-dimensional case, providing the altitude of the source or to provide additional data for the two-dimensional case.

A simple validity check on the set of time domain estimates for an infrasonic array can be performed by simply summing the delay time estimates. If the set of measurements is due to a single source and of sufficient accuracy, the sum of the delays will be zero. In the real world, the validity check possible through the coherence function, will ensure that the travel time estimates sum to zero within some small but estimatable error.

A more pictorial way of illustrating the determination of source azimuth is provided in Figure 55 which illustrates the construction of the phase velocity vector for an array having three elements. In the words of *Georges and Young* (1972): "The value of  $\tau$  for each pair of sensors in a network can be interpreted in terms of a trace velocity of a signal along the line joining the pair. To the degree that, when each trace velocity is plotted as a vector from a common origin, the tips of all the vectors align, the analysis is said to yield a single-plane-wave solution with a high degree of confidence".

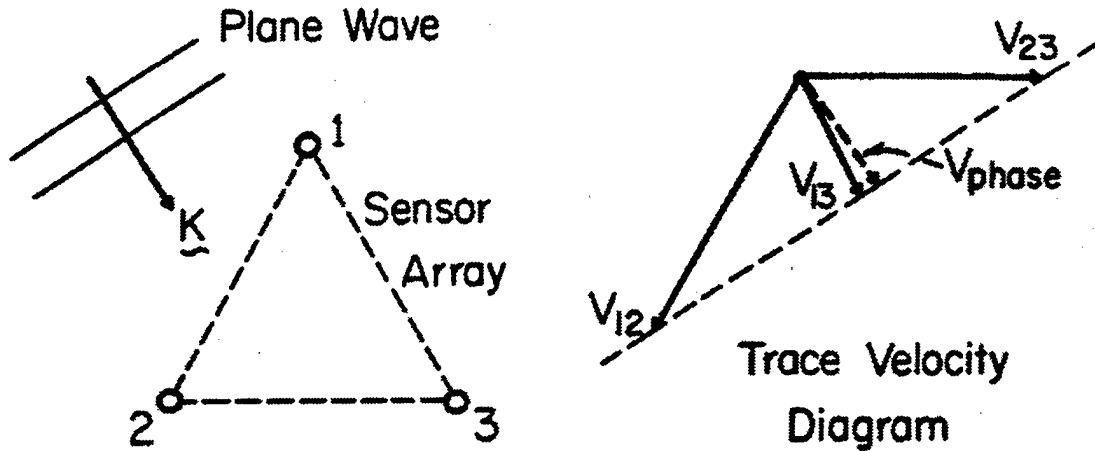


Figure 55. The construction of the phase velocity vector from an array of three sensors utilizing measurements of signal travel time between each pair of sensors in the array. [Figure adopted from *Georges and Young* (1972).]

A very powerful technique which has been used to process infrasonic as well as seismic signals is known as frequency-wavenumber spectral or "f-k" estimation. The methodology has been reviewed by *Burg* (1964) and *Capon, Lacoss and Greenfield* (1969), and has been shown to provide a powerful means for recognizing and separating propagating signals from different sources subject to the limitations of array geometry and other factors. *Smart and Flinn* (1971) developed a high speed algorithm for computing the spectrum and *Smart* (1972) developed an automatic real-time array detector and processor called FKOMB which incorporated a novel f-k filtering technique capable of suppressing powerful interfering or "jamming" signals which would otherwise obscure a signal of interest.

Mathematically, the frequency-wavenumber spectrum of the data from an array of sensors is defined as [*Smart and Flinn* (1971)]

$$P(\omega, k) = \sum_{j=1}^N \sum_{m=1}^N S_{jm}(\omega) e^{ik \cdot (r_j - r_m)} \quad (3.10)$$

where in the above,  $\omega$  is the frequency,  $k$  the two-dimensional wavenumber,  $N$  is the number of sensor elements in the array,  $r_j$  ( $j=1,2,\dots,N$ ) locates the positions of the array elements referenced to an arbitrary origin and  $S_{jm}(\omega)$  is the cross-spectrum between the  $j$ -th and  $m$ -th sensor elements given by

$$S_{jm}(\omega) = A_j(\omega)e^{-i\alpha_j(\omega)}A_m(\omega)e^{i\alpha_m(\omega)} \quad (3.11)$$

and where

$$A_m(\omega)e^{i\alpha_m(\omega)} \quad (3.12)$$

is the Fourier transform of the m-th sensor output over some specified time interval.

Figure 56 provides an illustration of the power of the f-k spectrum estimation procedure to detect a desired signal which would otherwise be undetectable because of the presence of a more dominant interfering signal. The top panel of the figure shows the f-k power spectrum contoured in three-dimensions. As indicated, there are two signals present: a "dominant signal" and a "hidden signal". The time-trace at the bottom of the figure displays the beamformed output from an array of sensors indicating the expected time interval for the arrival of the hidden signal. Without *a priori* knowledge, it is clear that the hidden signal would, indeed, go undetected. The middle panel of the figure exhibits the results using FKCOMB to filter the dominant signal from the record and then to recompute the f-k spectrum. The presence of the hidden signal is clearly shown.

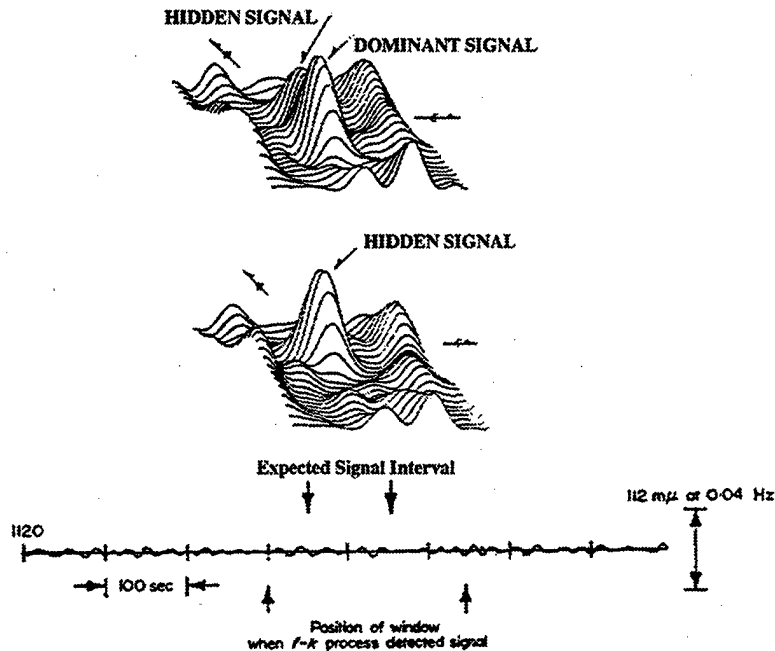


Figure 56. An example of the power of the f-k spectral estimation method to detect a weak signal in the presence of a more dominating one. The figure is based on seismic, rather than infrasound data, but is applicable to either type of signal. [Figure adopted and modified from Mack and Smart (1973).]

## 4.0 EARLY WORK IN INFRASOUND AND ATMOSPHERIC ACOUSTICS

### 1874 - 1949

Most of the early work in atmospheric acoustics revolves around studies of the eruption of the Krakatoa volcano, the impact of the Great Siberian meteorite [cf. *Whipple* (1930)], the oscillations of the earth's atmosphere and the formation of zones of silence and abnormal audibility, observed, for example, in the U.K. and Europe following the large explosion at Oldebroek on October 28, 1922.

The first notices of the effect of atmospheric wind, and wind and temperature variations on the propagation of sound in the atmosphere were made by *Stokes* (1857) and *Osborne Reynolds* (1874). The work of Reynolds demonstrated that refraction explains why sound is heard better to the leeward (facing the wind) of its source than to the windward (away from wind).

The first (or very early) examples of ray paths for atmospheric propagation were provided by *Rayleigh* (1896) and by *Barton* (1901).

*Lindemann and Dobson's* (1922) work on the theory of meteors came to the conclusion that the temperature in the atmosphere increases rather rapidly at a height of 60 km such that the temperature at an altitude of 80 km is about the same as that on the ground.

*Milne* (1921) wrote a fundamental paper on sound propagation in the atmosphere in which ray theory based equations were developed for propagation in an inhomogeneous atmosphere including the effects of wind, and equations were developed for describing the wavefronts in such an atmosphere. In addition, equations were developed to describe propagation from a point source in a horizontally stratified atmosphere and were used to clarify the conditions for limited and unlimited audibility for atmospheric temperature profiles describable by simple analytical forms. Figure 57 reproduces *Milne's* (1921) ray diagram for the formation of a shadow zone.

Total reflexion with limited range of audibility.

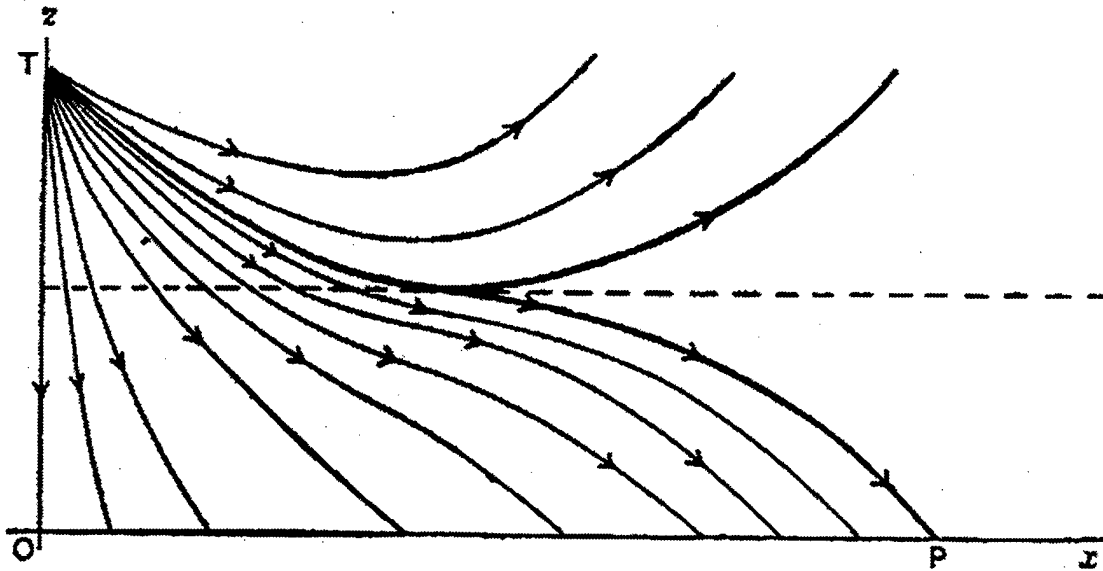


Figure 57. A ray diagram illustrating the formation of a shadow zone. [Figure adopted from *Milne* (1921).]

*Whipple* (1923) pointed out that, if the dependence of temperature with height was as inferred by *Lindemann and Dobson* (1922), i.e., if temperature increased as a function of height in the stratosphere, then the "occurrence of zones of audibility and zones of silence, surrounding the scenes of great explosions" can be explained where, by zones of silence and audibility, is now known to mean concentric regions around a source at different ranges where the sound produced is inaudible and audible, respectively. *Whipple* (1923) also pointed out that the drift trails of meteors imply that there is considerable horizontal wind motion at altitudes near 60 km and that a seasonal horizontal wind variability at these heights might explain the seasonal variability in the direction of audition observed for explosive sources during World War I.

*Gutenberg* (1939) reviewed work conducted in Europe on zones of audibility and presented additional data acquired on Benioff barographs and seismometers deployed at the California Institute of Technology in Pasadena, CA and at other locations in southern California. The source of the pressure waves for the California data was gun fire during target practice by Navy ships off the coast and sources for the European data were



explosions. Figure 58 illustrates the formation of zones of audibility and silence following a 5,000 kg explosion of buried ammunition.

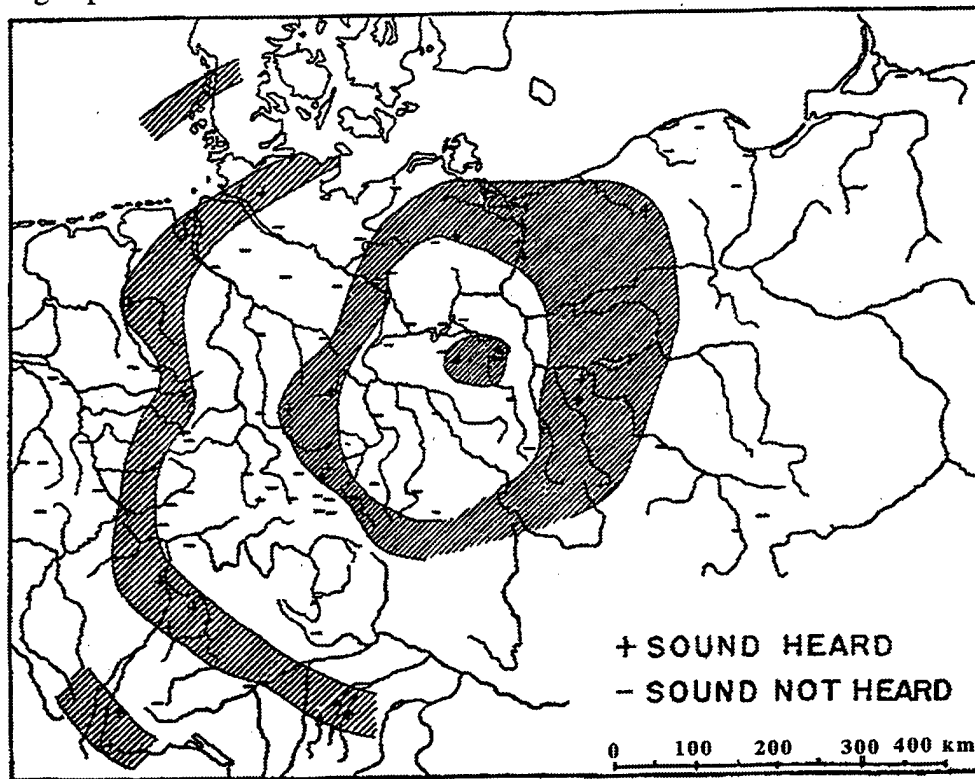


Figure 58. The zones of audibility (shaded regions) and silence which were observed after the detonation of 5,000 kg of buried ammunition. [Figure adopted from *Gutenberg* (1939).]

In discussing the zones of audibility, *Gutenberg* (1939) noted that only in the inner or center zone were direct arrivals detected: in "each successive zone the times are delayed by an amount which increases with zone to zone." In addition, it was noted that in Europe there was a seasonal variability in the location of the inner region of the first zone: 120 km in February and 200 km in August. To account for the delayed arrival times in the non-central zones, it was necessary to conclude that "the sound waves which arrive at the second and succeeding zones have traveled through the stratosphere and that their velocity at the highest point of their path exceeds the velocity of sound near the ground." Figure 59 reproduces the ray paths computed by *Gutenberg* (1939) for propagation in Europe which illustrates the formation of first ring of audibility and the beginning of the second. The beginning of the inner zone is determined by a ray arriving at the shortest distance and, it

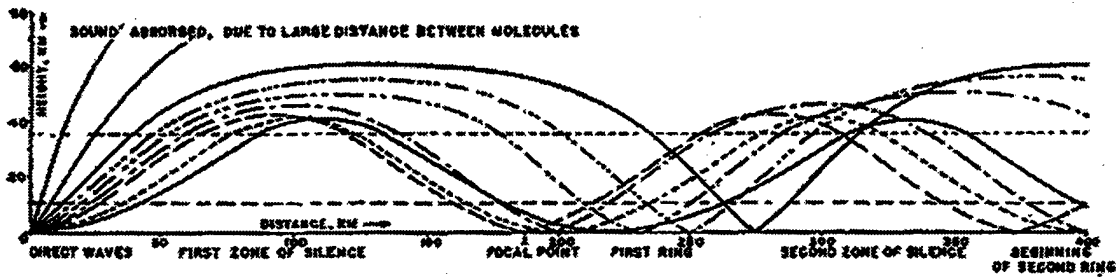


Figure 59. The paths of sound rays which form the first and the beginning of the second zone of audibility. The ray trace is based on European atmospheric data and assumes a range independent atmosphere. [Figure adopted from *Gutenberg (1939)*].

was hypothesized that absorption determined the location of the outer zone.

Based on an analysis of the California data, *Gutenberg (1939)* concluded that travel times exhibited the same behavior as those determined from explosions in Europe and inverted the California data to show that the atmospheres in the two regions were quite similar as is shown in Figure 60.

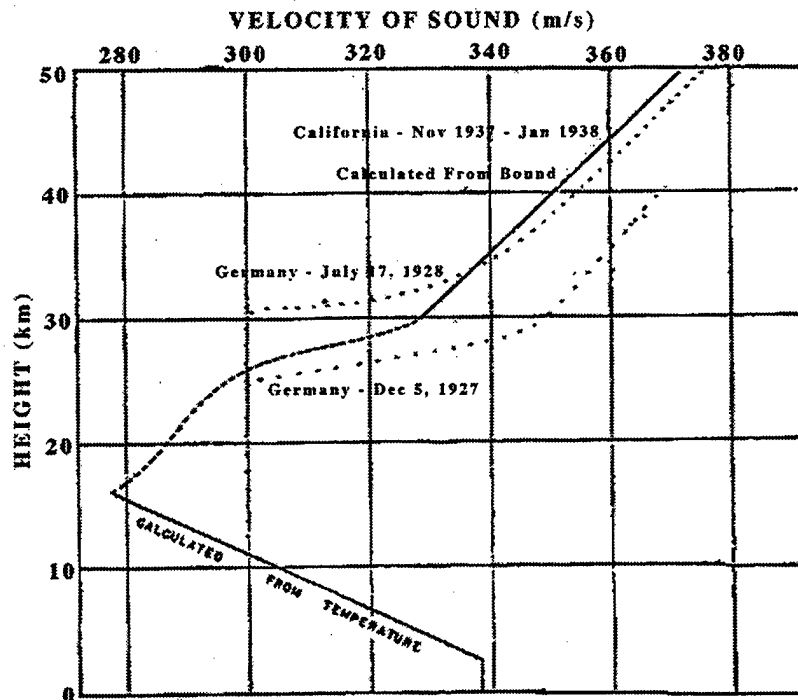


Figure 60. Model atmospheres, or sound speed profiles, estimated from inverting travel time data from explosive sources in California and in Germany. [Figure adopted and modified from *Gutenberg (1939)*.]

In subsequent work, *Gutenberg* (1942) derived expressions for the speed of sound in humid air, the radius of curvature for a ray path propagated in the direction of the wind and demonstrated how the existence of zones of enhanced audibility could be explained if the wind speed, sound speed, or both, became rapidly increasing functions of atmospheric height in the regions reached by the sound rays.

*Saby and Nyborg* (1946) modeled ray propagation in a horizontally stratified atmosphere neglecting winds and incorporating the vertical variability of the sound speed by a number of constant sound speed gradient layers. Under the restriction that the sound rays make small angles with respect to the horizontal, a closed form expression was derived for the range of a ray in terms of the gradients assumed in modeling the atmospheric sound speed profile. The possibility of ray skipping in atmospheric sound propagation, as is illustrated in panel (b) of Figure 61, was also pointed out.

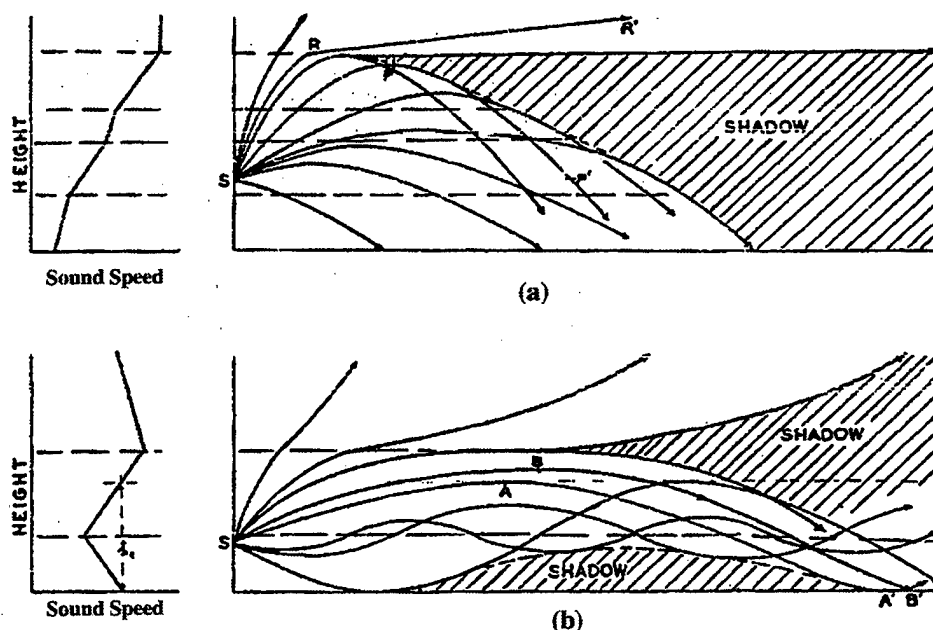


Figure 61. The formation of an acoustic shadow zone corresponding to the inner radius of a zone of silence [Panel (a)] and the acoustic skip phenomenon in which sound rays are ducted in an altitude region having a local minimum in the sound speed [Panel (b)]. [Figure adopted from *Saby and Nyborg* (1946).]

*Blokhintzev* (1946a) derived formal field expressions for the propagation of sound in an inhomogeneous and moving medium, reduced the formal field expressions to ray

theory approximations and extended the results to the propagation of underwater sound. *Blokhintzev* (1946b) applied the theoretical results to an investigation of the absorption of sound caused by scattering due to turbulence and the propagation of sound wave through a shock wave. In the former case, no firm conclusions could be made as to wave attenuation or scattering loss because of a lack of adequate data.

*Cox* (1947) reported the results of microbarographic recordings from a number of chemical explosions conducted during the Army-Navy Explosives Safety Board tests conducted at the Naval Proving Ground test site at Avco, Idaho, during the month of October 1946. The chemical explosions ranged in weight from 3.5 T to 250 T and the associated pressure waves were recorded at portable microbarograph stations at distances from the shot point ranging from 12.9 km to 872 km. Both normal and abnormal signals were observed and Figure 62 presents an example of the waveforms recorded at a range of 182 km as caused by an explosion of 125 T.

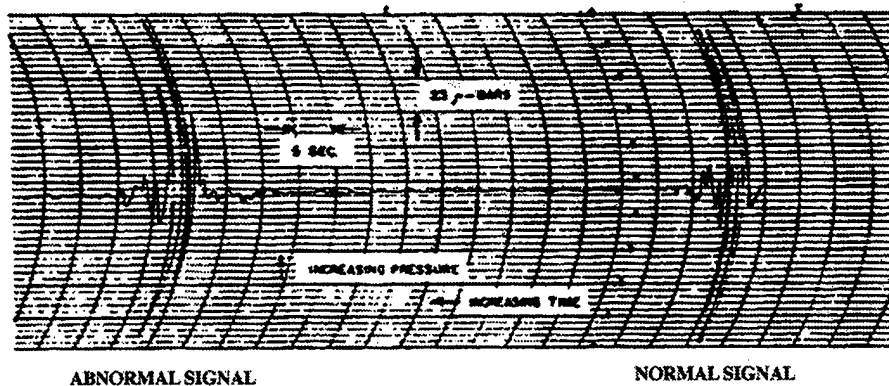


Figure 62. An example of normal and abnormal signals recorded at a range and associated with a 125 T chemical explosion detonated at the Naval Proving Ground near Avco, Idaho on October 16, 1946. [Figure adopted from *Cox* (1947)]

In addition to presenting his data, in which examples of both normal and anomalous signals were presented, *Cox* (1947) presented an excellent survey of the earlier literature on zones of silence and, in particular, on abnormal audibility, summarizing the observations and calculations of *Gutenberg* (1939) which essentially demonstrated that the formation of zones of abnormal audibility was caused by downward refraction of rays from the upper

atmosphere. Cox (1947) also discussed some of the various alternative mechanisms proposed for the formation of zones of enhanced audibility: e.g., a high concentration of hydrogen and helium at high altitudes [von dem Borne (1910)] and effects due to shock wave formation [Wiechert (1925)]; and presented the arguments for rejecting them.

In discussing his results, Cox (1947) noted that the signal-to-noise ratios for his instrumentation were generally higher in the frequency band extending from 1.0 Hz to 20 Hz than in the lower frequency band. It was also mentioned that the largest peak-to-peak pressure recorded for the arrival of a normal wave was 395  $\mu$ bar which resulted from a 250 T explosion at a range of 141 km. The largest abnormal wave arrival had a peak-to-peak amplitude of 220  $\mu$ bar which resulted from a 125 T explosion at a range of 182 km.

Of particular interest to the infrasonic monitoring community are the observations: "Normal signals and abnormal signals received at one station from one blast are not likely to bear much resemblance; neither normal nor abnormal signals originating from a single blast and recorded at adjacent (50 km) stations appear very similar; and signals received at a fixed station from different blasts on different days are of utterly different appearance" [Cox (1947)].

Cox (1949) presented additional data on abnormal signals and, based on the data, was led to propose a theory for the outer edge of a zone of abnormal audibility differing from that proposed by Gutenberg (1939). Rather than absorption limiting the effective widths of the zones, it was proposed that the location of the outer boundary results from the establishment of a critical angle which, in turn, is established by the maximum temperature in the altitude region extending from 30 km to 70 km.

The data leading to the foregoing proposal was acquired in an experiment conducted in 1947 in which a 5 T explosion was detonated on Helgoland island, located off the north-west coast of Germany. The explosion was designed to destroy British fortifications which had been established on the island presumably during WW II. The pressure waves resulting from the explosion were recorded at 10 microbarograph stations located along an

approximate straight line with respect to the island as shown in Figure 63. The closest station to the explosion is Spieka, Germany at a range of 66 km and the most distant is Sorizia, Italy at a range of 1000 km from the shot point. The primary frequency response of the instruments was in the band extending from .05 Hz to 5 Hz.

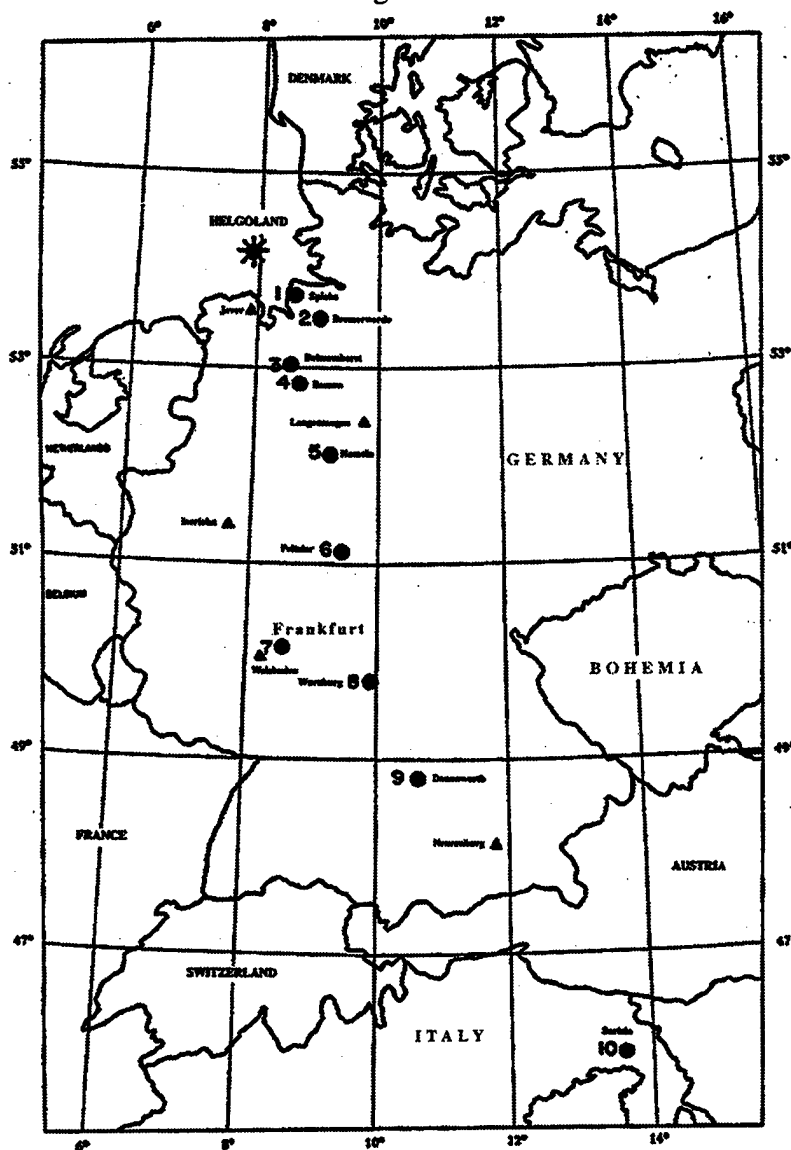


Figure 63. Locations of the microbarograph stations (circles) and meteorological stations (triangles) deployed to monitor the Helgoland island 5 T explosion of April 18, 1947. [Figure adopted from Cox (1949).]

In the paper, Cox (1949) only discussed the results obtained at stations 5, 6, 7, 8, 9 and Table 2 provides a listing of some of the measured signal parameters. Figure 64

illustrates the first arriving components of the abnormal signals recorded in the first abnormal zone.

Table 2. Measured parameters of selected signals from the Helgoland island explosion of April 18, 1947. The numbers in the parentheses denote estimated peak-to-peak amplitudes in  $\mu\text{bar}$  and the listed periods are for dominant periods and do not imply that other frequency components were not present. [Data adopted from Cox (1949).]

Station	Range (km)	Travel Time (s)	Maximum Peak-Peak Pressure	Prominent Periods (s)
5 Hameln	252.1	843.4	(43)	1.6, 0.2
6 Fritzlar	353.0	1146.2	(47)	1.4
7 Frankfurt	441.0	1435.9 1513.3	(13) (76)	0.3 1.8, 0.5
8 Wurzburg	509.3	1631.7 1713.4	4 54	0.3 1.6, 0.5
9 Donauworth	629.9	(2061.5)	?	1.8, 2.4

Inspection of the waveform examples exhibited in Figure 64 shows that as the distance between the shot point and the recording site increases, the low frequency content of the records actually decreases: a circumstance at odds with arguments put forward by *Gutenberg* (1939) that absorption controls the location of the outer zone boundary in the zone of abnormal audibility. Under the absorption hypothesis, the rays that arrive at the outer zone boundary have the highest turning points:  $\sim 60$  km (cf. Figure 59) and it is known that absorption increases with height for a given frequency, and with frequency for a given height. Accordingly, as distance increases within a zone of abnormal audibility, the frequency content of the waveforms should move to lower and lower frequencies.

For completeness, Figure 65 provides a summary of calculations made by *Schrodinger* (1917) for the absorption of sound propagating through rarefied gas. The curves plot absorption per kilometer of propagation and show, for example, that at 0.1 Hz, only 0.01% of a sound wave will be attenuated per kilometer of propagation at an

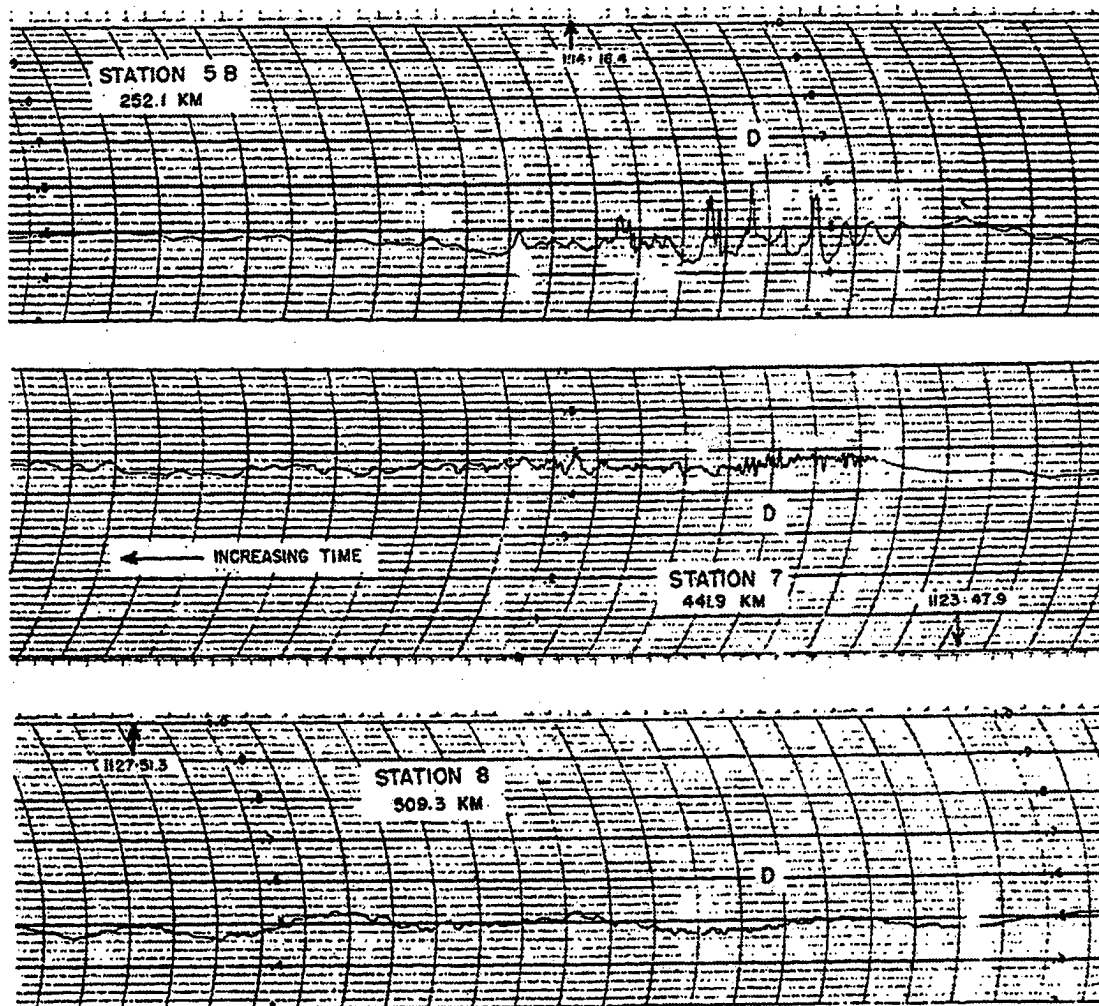


Figure 64. Examples of first arrival signals in the first zone of abnormal zone of audibility recorded at stations 5, 7 and 8 from the 5 T explosion detonated at Helgoland island on April 18, 1947. It is important to note that the low frequency content of the records decreases with increasing distance from the shot point. [Figure adopted from Cox (1949).]

altitude of 20 km, whereas at an altitude of 60 km, 100 times more or 1 % will be attenuated per kilometer. At a frequency of 1 Hz, only .01% of the wave amplitude is attenuated at an altitude of 60 km. The increase in sound attenuation with altitude is due to the fact that as altitude increases, the mean free path between molecular collisions increases and sound is strongly attenuated when the wavelength becomes comparable to the mean free path length.

Motivated by the discrepancy between the anticipated frequency content of the waveforms and that which was measured, Cox (1949) carried out a careful analysis of



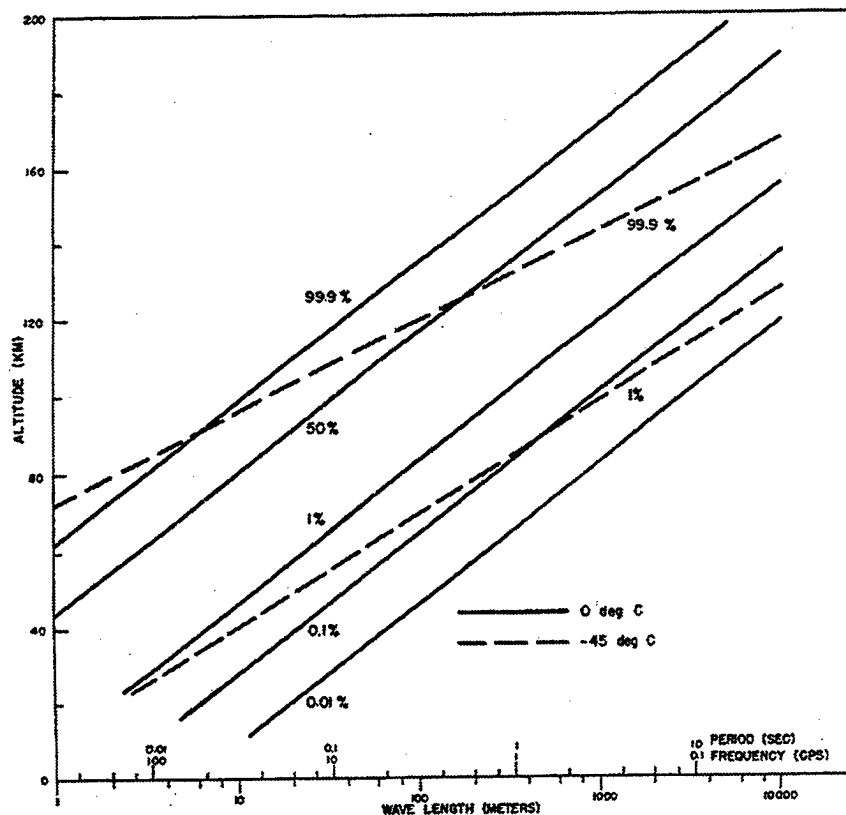


Figure 65. Predicted sound absorption per kilometer of path length as a function of altitude and wavelength (or period or frequency) in an isothermal atmosphere at the indicated temperatures. [Figure adopted from Cox (49) after Schrodinger (1917).]

ray path dispersion utilizing Snell's law and the relationships between group and phase velocity to show that the temperature maximum in the altitude range between 30 km and 70 km establishes a critical angle ray. Dispersion is then such that the high frequency contribution to the early part the received waveform predominates over the low frequency contribution for rays having upper turning points in the vicinity of this ray.

A primary focus of the early work in atmospheric acoustics revolved around the existence of atmospheric tides and whether the driving force was purely gravitational, thermal or both. Two excellent summaries of the subject area were provided in the monograph: Oscillations of the Earth's Atmosphere [Wilkes (1949)] and in the review article by Siebert (1961). The discussion presented herein is based, in part, on both sources

and is included because the work aimed at deriving an understanding of the oscillations of the earth's atmosphere required a concomitant increased understanding of the atmospheric temperature and wind structure as well as the propagation of acoustic-gravity waves.

Observations of the surface pressure variations caused by atmospheric tides are made difficult because of their small magnitude. The first observations of the solar semi-diurnal variation in pressure of the earth's atmosphere was made from a study of barometric records obtained in tropical regions where the daily variations in barometric pressure are significantly smaller than those occurring at higher latitudes. Figure 66 compares barometric records recorded at the tropical site Batavia (now Djakarta) with a corresponding record recorded at Potsdam southwest of Berlin, Germany.

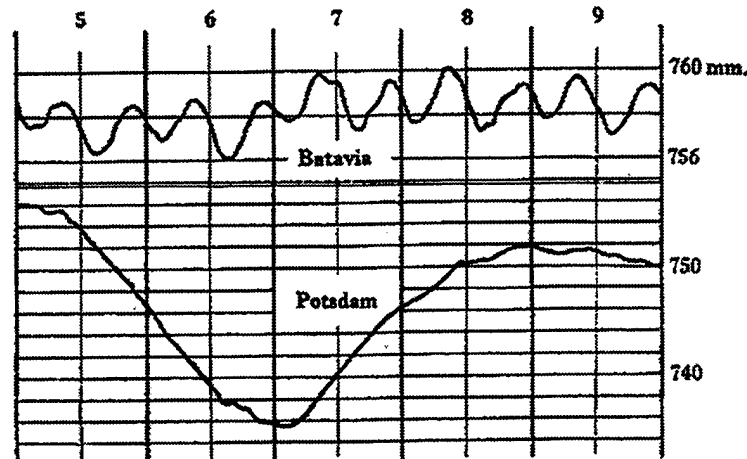


Figure 66. Barometric records recorded at Batavia (now Djakarta) and Potsdam, Germany. [Figure adopted from *Wilkes* (1949).]

As indicated from inspection of the figure, the variability in the Batavia record is  $\pm 2.5$  mm of mercury over the indicated period, whereas the variability at Potsdam is as large as 20 mm of mercury. The peaks in the Batavia record occur near 10 am and 10 pm local solar time and other equatorial semi-diurnal variations have been shown to be the largest of all recorded components of the atmospheric tides.

The first dynamical theory of both the oceanic and atmospheric tides was simultaneously developed by *Laplace* (1778) who also discounted original conjectures that

the atmospheric tides were gravitationally induced, concluding that the atmospheric tidal oscillations were primarily induced by the thermal action of the sun and only secondarily by the gravitational influence of the moon and sun. In developing his tidal theory, *Laplace* (1778) treated the problem as an oscillatory forcing of an isothermal atmosphere and neglected vertical acceleration demonstrating that the equations describing the atmospheric tides obeyed the same equations as those appropriate to an ocean of uniform depth,  $H$ , if that depth were replaced by the atmospheric scale height. *Wilkes* (1949) found the assumption that the oscillations took place isothermally of interest since *Laplace* (1778) had earlier "corrected Newton's value for the velocity of sound by pointing out that changes of volume in sound waves take place adiabatically": a circumstance now known to be true for atmospheric oscillations.

By 1882, significantly more data were available: *Lord Kelvin* (1882) published a table of Fourier tidal coefficients at periods of 8 h, 12 h and 24 h and concluded, with *Laplace* (1778), that thermal forcing was responsible for the barometric tide suggesting that quantitative predictions might be made by replacing the gravitational tide producing forces in *Laplace's* (1778) equations with thermal sources.

At this time, it was also known that at high latitudes the 12 h, or semi-diurnal, tidal component was larger than the 24 h component which, on the surface, would appear to be disagreement with the assumption that the tidal forcing was predominantly due to solar heating since the 24 h variability in solar heating is significantly greater than that which occurs over a 12 h time period.

In the same paper in which the tidal coefficients were published, *Lord Kelvin* (1882) proposed a resolution to the apparent paradox, known as "*resonance theory*", which explained why the semi-diurnal tide was larger than the diurnal by postulating that the earth's atmosphere possessed a free period of oscillation near 12 h. Were such a supposition to be true, the reason for the larger semi-diurnal atmospheric tide would be due to the atmosphere acting as a resonant system. Following *Lamb* (1911) and *Wilkes* (1949),

the actual passage in *Lord Kelvin's* (1882) paper proposing the resonance theory is reproduced:

"The cause of the semi-diurnal variation of barometric pressure cannot be the gravitational tide-generating influence of the sun, because if it were there would be a much larger lunar influence of the same kind, while in reality the lunar barometric tide is insensible, or nearly so. It seems, therefore, certain that the semi-diurnal variation of the barometer is due to temperature. Now the *diurnal* term, in the harmonic analysis of the variation of *temperature*, is undoubtedly much larger in all, or nearly all, places than the *semi-diurnal*. It is then very remarkable that the *semi-diurnal term of the barometric effect* of the variation of temperature should be greater, and so much greater than it is, than the diurnal. The explanation probably is to be found by considering the oscillations of the atmosphere, as a whole, in the light of the very formulas which Laplace gave in his *Mecanique celeste* for the ocean, and which he showed to be also applicable to the atmosphere. When the thermal influence is substituted for gravitational, in the tide-generating force reckoned for, and when the modes of oscillation corresponding respectively to the diurnal and semi-diurnal terms of the thermal influence are investigated, it will be probably found that the period of free oscillation of the former agrees much less nearly with 24 hours than does that of the latter with 12 hours; and that, therefore, with comparatively small magnitude of the tide-generating force, the resulting tide is greater in the semi-diurnal term than in the diurnal."

Following the publication of *Lord Kelvin's* (1882) results, *Margules* (1890, 1892, 1893) extended the theoretical work by investigating both forced and free oscillations based on *Laplace's* (1778) theory considering the influence of friction, the earth's rotation and by providing an overall classification scheme.

*Lamb* (1911), while studying low-frequency wave propagation in the atmosphere, extended *Laplace's* (1778) analysis to an atmosphere in convective equilibrium with adiabatic changes of state or, more generally, an "autobarotropic atmosphere" [*Siebert* (1961)]. In addition to the adiabatic assumption, the atmosphere was modeled more realistically by assuming that the temperature decreased linearly with altitude from the surface to an altitude where the temperature was assumed to vanish. Quite surprisingly, *Lamb* (1911) reached the same essential conclusions as did *Laplace* (1911): that the equivalent ocean depth was equal to the atmospheric scale height.

In investigating atmospheric oscillations in the autobarotropic atmosphere, *Lamb* (1911) reviewed the ideas behind resonance theory citing the analysis of *Hough* (1897) indicating that the free period of the atmosphere could not differ by more than two to three

minutes from 12 h and also developed solutions for three wave types: (1) surface waves, (2) internal gravity waves and (3) Lamb waves [*Lamb* (1909)].

For surface waves, which were characterized as "the most important-type, the motion of the air-particles is mainly horizontal and, independent of the altitude, and waves may be described as 'longitudinal'". The analysis assumed that the wavelengths of the waves were longer than the height of the atmosphere and the phase speed was found to satisfy the condition

$$V = \sqrt{gH}, \quad (4.1)$$

which is the condition appropriate to a surface wave propagating on a fluid of uniform depth,  $H$ .

*Chapman* (1924) provided additional support for the resonance theory based on an analysis of semi-diurnal pressure records recorded at equatorial meteorological stations concluding that resonance theory was both valid and that the observed semi-diurnal signal was made up of two contributions of equal amplitude: one thermal and the other tidal or gravitational. In modeling the thermal source, *Chapman* (1924) assumed that the forcing was due to "that temperature wave which spreads out from the earth's surface into the atmosphere by turbulent mass exchange (*eddy conductivity*)" [*Siebert* (1961)].

*Taylor* (1929) severely called into question resonance theory by showing that the inferred oscillation period as computed from a determination of the scale height from gravity wave propagation in the atmosphere were in disagreement. In his paper, *Taylor* (1929) remarked that "the inherent improbability that the appropriate mode of [free] oscillation should chance to have a period so near to 12 hours" led *Lamb* (1922) to reject the tidal or gravitational explanation for the semi-diurnal pressure signal. He also noted in this connection that "it would be quite fatal to the resonance theory if it could be proved that the free period cannot be as great as 11 hours 56 minutes."

*Taylor* (1929) computed the scale height of the atmosphere by estimating the speed of long wavelength gravity wave propagation in two ways: (1) computing the speed in an

atmosphere in which temperature decreased linearly with height up to a point at which the temperature was taken as constant in such a manner as to render the temperature profile continuous and (2) by utilizing available meteorological station barograph records to measure the phase velocity of the signal from the Krakatoa eruption of August 26, 1883. In so doing it was found that the calculated and measured phase velocities agreed within 2 % and yielded an estimate for the atmospheric scale height of 10 km, whereas a free oscillation period of 11 h and 56 min would require a scale height considerably less: i.e., 7.9 km.

*Taylor* (1936) partially resolved the apparent contradiction raised in his 1929 paper by showing, for a number of model atmospheres, a number of atmospheric oscillations and associated waves are possible, i.e., "when the temperature of the atmosphere is a function only of height above the ground, free oscillations are possible which are identical to those of a sea of uniform depth,  $H$ , except that the amplitude of the oscillations is a function of the height." Thus, there can exist a number of scale heights  $H, H_1, H_2, \dots$  each of which is associated with a wave whose phase speed is governed by Eq. (4.1). Should the real atmosphere support such a large number of oscillations, the aforementioned difficulty with the resonance theory could potentially be resolved. In addition, *Taylor* (1936) also demonstrated that the seemingly fortuitous agreement between the results of *Laplace* (1778) and *Lamb* (1911) was due to the circumstance that *Laplace's* (1778) atmosphere was a special case of *Lamb's* (1911): i.e., under the assumption that  $\gamma=1$ .

*Pekeris* (1937) reviewed work concerned with the resonance theory noting, in particular, the finding of *Taylor* (1929) which cast doubt on the resonance theory. He also noted that *Whipple* (1934) had obtained the same estimate for the speed of the atmospheric wave produced by the Great Siberian Meteor as *Taylor* (1929) obtained for the wave produced by the Krakatoa eruption remarking that the inferred wave speed implies a free period of oscillation of the atmosphere of 10.5 h (or a scale height of 8 km) which is considerably more than 6 minutes from 12 h as required by the resonance theory.

*Pekeris* (1937) was able, however, to save the resonance theory by removing the difficulty with the free period inferred from the estimates of atmospheric gravity wave speeds. This was accomplished, in particular, by demonstrating that the atmosphere has two modes of free oscillation: one mode having a period of 12 h and the other a period of 10.5 h. As a result of the theorem proved by *Taylor* (1936), there is an associated long wave associated with every free period of oscillation. The fact that a second propagating wave associated with the free oscillation period, had not been observed at the time was addressed by *Pekeris* (1939).

In obtaining his results, *Pekeris* (1937) considered a number of atmospheric temperature profiles, reproduced in Figure 67, and found that the existence of two modes of oscillation required a more complicated (and realistic) atmosphere than had been considered before. In particular, and with reference to Figure 67, the profiles I (a linear decrease in temperature as a function altitude) and F (a linear decrease in temperature up to the tropopause and isothermal thereafter) did not support the existence of two modes, whereas any of the other profiles A, B, C, D and E did. The "rise of temperature between about 30 to 60 km, common to all of these atmospheres, has been assumed in accordance with results which were obtained by *Whipple* (1935) from the abnormal propagation of waves from gunfire and which are in agreement with the results of similar experiments carried out in Germany" [*Pekeris*, 1937)].

In addition, *Pekeris* (1937) found that the two oscillatory modes were associated with different atmospheric motions: the motion associated with the 12 h free oscillation period required the pressure variations above and below an altitude of 30 km to be in the opposite phase whereas there was no such "phase reversal" associated with the 10.5 free oscillation period. To add support to his findings, *Pekeris* (1937) noted that in studies of the earth's magnetic field and dynamo effect, *Chapman* (1919) had observed "that the pressure

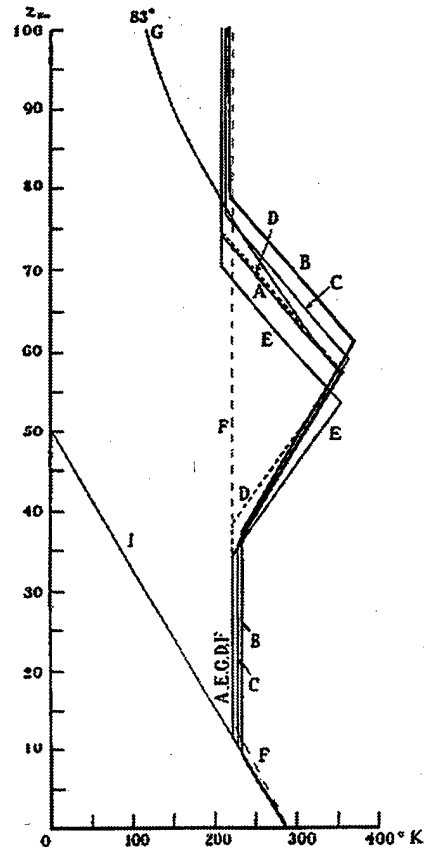


Figure 67. The temperature profiles used to model the propagation of atmospheric waves from the explosion of the Krakatoa volcano of August 26, 1883. [Figure adopted from *Pekeris* (1937).]

oscillations in the upper conducting layer, are nearly  $180^\circ$  out of phase with the observed pressure oscillations at the ground."

To clarify the excitation of free atmospheric oscillations by a point source on the surface of the earth, such as a volcanic eruption, *Pekeris* (1939) considered the propagation of a pulse in an atmosphere with a temperature profile having the form of A, B or I as shown in Figure 67 and the profile considered by *Lamb* (1911): a constant temperature gradient. The point source was modeled as a point vertical velocity impulse utilizing a time function proposed by *Lamb* (1932).

The conclusions of his work were that both modes would, in general, be excited but that the excitation of the wave having the propagation speed corresponding to a free period of oscillation of 10.5 h ("the first mode") would produce a wave having an



amplitude varying from 2.4-to-2.9 times larger than the wave associated with the "second mode", having a 12.5 h period of oscillation, i.e., that the excitation of the first mode would be "favored" over the excitation of the second. It is parenthetically also noted, that of the atmospheres considered, only the realistic atmospheres A & B, produce the cited amplitude amplification for the first mode wave.

In reaching his conclusions, and for theoretical simplification, *Pekeris* (1939) first considered an atmosphere having a constant temperature gradient, and developed the dispersion characteristics for each of the modes finding that the dispersion of the first mode (12 h period) was greater than the second. Because the degree of dispersion depends on the length of the eruptive pulse, the explosive yield was estimated and, depending on the area occupied by the explosion (i.e., area of the caldera or significant fraction of the island, etc.), obtained source durations ranging "from a few seconds to a few minutes." From this time estimate, together with the implied dispersion, amplitude calculations based on the model atmospheres A and B were used to conclude that the first mode should be observable in at least the first passage of the wave. Figure 68, which reproduces a barographic record from a meteorological station at Montsoruris, France, shows that this is indeed the case.

*Pekeris* (1948), in what is one of the most fundamental papers on pulse propagation in the atmosphere, extended his work on the Krakatoa wave, which had a period of approximately an hour, to a consideration of the wave produced by the explosion of the Great Siberian Meteor of 1908 [*Whipple*, 1930]: a circumstance requiring the theory to include waves of much shorter periods "of the order of a minute".

In modeling pulse propagation in the atmosphere, *Pekeris* (1948) derived results for two horizontally stratified model atmospheres: an isothermal atmosphere and a two layer atmosphere in which the temperature was taken as linearly decreasing up to a tropospheric height of 10.3 km and as isothermal above (the form of atmosphere F) in Figure 67. Group and phase velocity curves were computed for each atmosphere and both continuous and impulsive vertical velocity and pressure source types were considered.

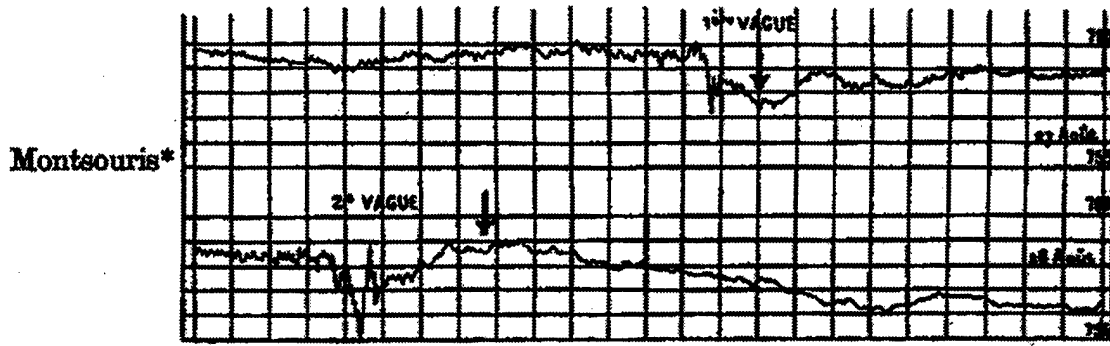


Figure 68. The pressure signature recorded at Montsouris, France, caused by the eruption of the Krakatoa volcano. The arrows locate the position of the second mode and are to the right of the clearly evident first mode locations. The top panel is the pressure signature corresponding to the first passage of the wave and the lower panel is that associated with the second. [Figure adopted from *Pekeris* (1939)]

Figure 69 presents the phase (V) and group (U) velocity curves normalized to the speed of sound ( $C_0$ ) computed for the two atmospheres. The curves labeled by I and II correspond to the isothermal atmosphere and the curve labeled by III corresponds to the two layered atmosphere. The isothermal atmosphere is seen to support two modes, I and II and that mode II exists only at periods below 3.5 minutes which turns out to be the free period of oscillation for purely vertical motions. The phase and group velocity curves for mode III are seen to be flat throughout the indicated period range and to cut-off at a period of two minutes.

For the case of the two-layered atmosphere, *Pekeris* (1948) developed expressions for the far-field pressure radiated by a point source on the ground, assuming a point vertical velocity source having a uniform frequency spectrum and, also for a point source pressure source having a uniform frequency spectrum. The expression obtained for the vertical velocity source is given in Eq. (4.2)

$$p(r,t) = A \frac{1}{\sqrt{r}} e^{i(\omega t - k_1 r + \frac{3\pi}{4})} \left[ \tau^{1/2} \frac{\partial R}{\partial x} \right]^{-1} \quad (4.2)$$

where in the above  $k_1$  is the horizontal wavenumber of the first, or lowest order mode,  $r$  is the horizontal source-to-receiver range and the factor within the square brackets is a term

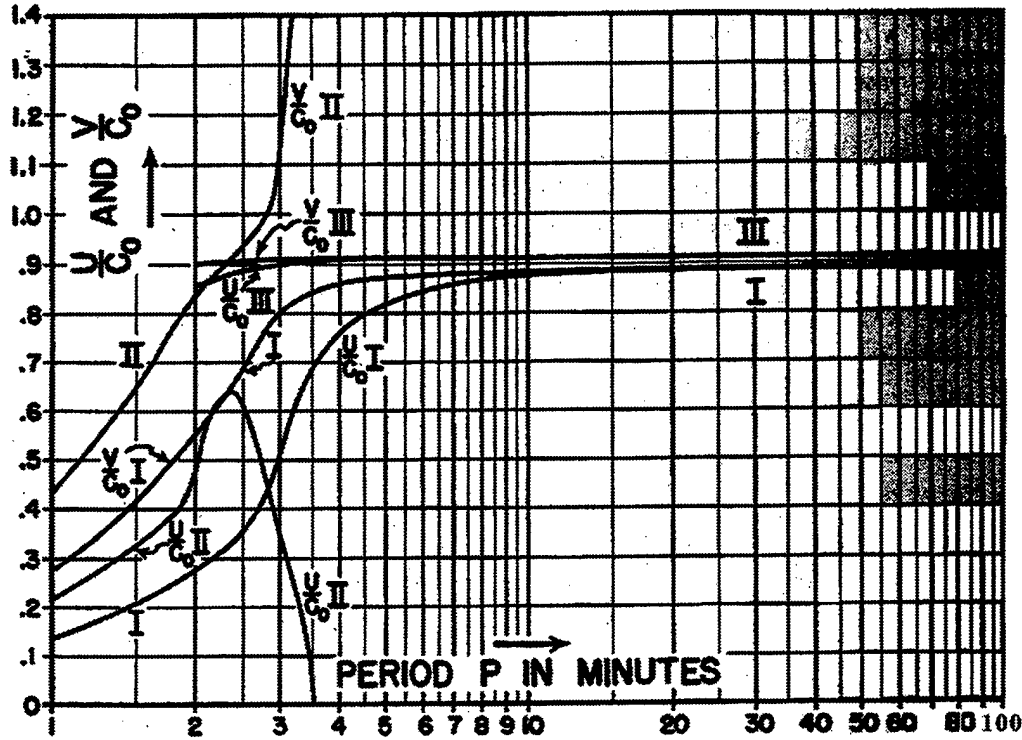


Figure 69. The normalized phase ( $V/C_0$ ) and group ( $U/C_0$ ) velocity curves computed for the isothermal (I and II) and the two layered atmosphere (III). [Figure adopted from *Pekeris (1948)*.]

which determines the relative excitation of the various frequencies which make up the pulse. The corresponding expression for the pressure point source turns out to be slightly different and is given in Eq. (4.3)

$$p(r, t) = A \frac{1}{\sqrt{r}} e^{i(\omega t - k_1 r + \frac{3\pi}{4})} \left[ \tau^{1/2} Q \frac{\partial R}{\partial x} \right]^{-1}. \quad (4.3)$$

Inspection of Eqs. (4.2) and (4.3) shows that they are identical except for the factor of  $Q$  which appears in the latter equation and which vanishes at the Brunt-Vaisala frequency so that the maximum pressure amplitude is predicted to occur near this frequency.

In comparing the theoretical calculations with the composite waveform for the Great Siberian Meteorite constructed by *Whipple (1930)*, it was noted that no periods were recorded shorter than 2 min, the cut-off-period for the two-layered atmosphere. *Pekeris (1948)* did not attempt to synthesize the pulse, however, simply noting that such a construction would require the inclusion of higher order modes.

## 5.0 PROPAGATION AND SOURCE MODELING

In two remarkable papers, *Taylor* (1950a and 1950b) derived expressions for the yield or energy release from an atomic explosion in terms of the radius of the initial explosive shock wave as a function of time. The expressions are believed valid for overpressures  $\geq 10$  atm, and what is remarkable about the papers is that the first was actually written in 1941, some 4 years before the TRINITY test in 1945, and that, as demonstrated in the second paper, the theory agreed so well with experiment. The paper written in 1941 was classified and published with very slight modifications as *Taylor* (1950a).

The key expression derived by *Taylor* (1950a) for the energy release of an atomic explosion is given by

$$E = K(\gamma) \rho_0 R^5 t^{-2} \quad (5.1)$$

where in the above,  $E$  is the non-radiative energy release of the explosion,  $K(\gamma)$  is calculable and solely a function of  $\gamma$ , the ratio of the specific heat at constant pressure to that at constant volume ( $C_p/C_v$ ),  $\rho_0$  is the normal or "unperturbed" density of air ( $\sim 1.25 \times 10^{-3} \text{ g/cm}^3$ ),  $R(t)$  is the radius of the shock front in meters and  $t$  is time as measured from the detonation time of the explosion or from  $t=0$ . [Eq. (5.1) is non-singular at  $t=0$  because  $R=0$  at  $t=0$ .] For a given explosion, the energy release is a constant so that Eq. (5.1) predicts that  $t$  is related to  $R$  as

$$t = (\text{constant}) R^{5/2} . \quad (5.2)$$

In comparing his theoretical expressions with data, *Taylor* (1950b) utilized declassified photographs of the TRINITY test to estimate values of  $R$  and  $t$  and obtained the results exhibited in Figure 70 where it is seen that the predictions of Eq. (5.2) are in excellent agreement with the data. In computing the yield of the TRINITY test, *Taylor* (1950b) emphasized that  $\gamma$  cannot necessarily be taken equal to 1.4 because at high temperatures  $\gamma$  should properly be decreased owing to an increase in  $C_v$  because of

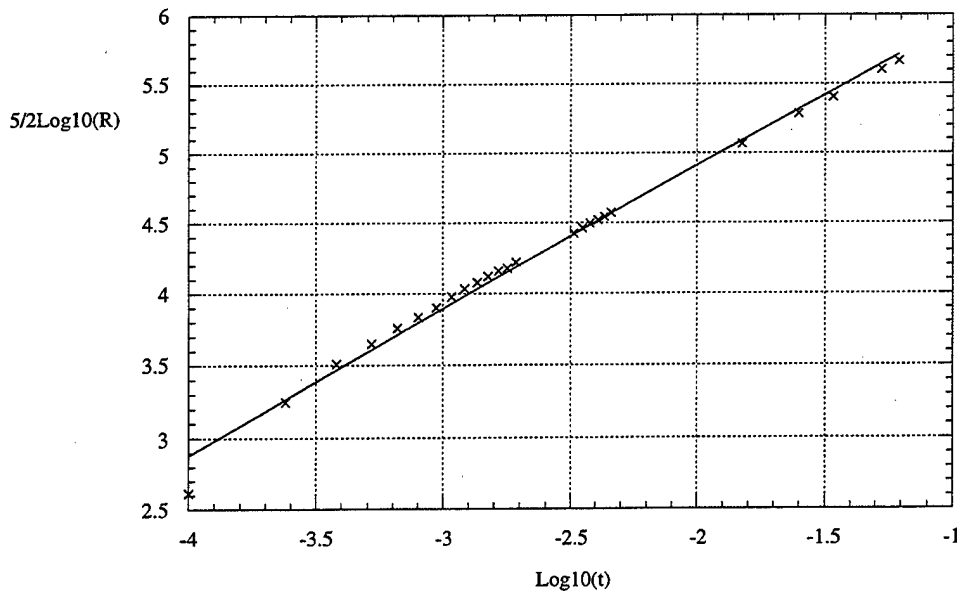


Figure 70. A plot of  $(5/2)\text{Log}_{10}(R)$  vs  $\text{Log}_{10}(t)$ , where  $R$  is the radius of the shock front in meters and  $t$  is the time since detonation in seconds. The X's are the estimates provided by *Taylor* (1950b) and the solid curve is a linear fit to the data.

"energy in the form of vibrations which increases  $C_v$ . On the other hand, the existence of very intense radiation from the centre and absorption in the outer regions may be expected to raise the apparent value of  $\gamma$ ."

Because of this uncertainty in estimating  $\gamma$ ,  $K(\gamma)$  was computed for a range of values and the results of the yield estimations using Eq. (5.1) are shown in Figure 71. As indicated, the predicted yield is a monotonically decreasing function of increasing  $\gamma$  and that for  $\gamma = 1.4$  the predicted explosive yield is 16.8 KT. According to *DOE* (1994), the yield of the TRINITY explosion was 21 KT so that if the *Taylor* (1950a) model is correct, approximately 4.2 KT of energy went into radiation or other sinks.

The first to estimate the pulse shape as a function of range from a large explosion on the ground was *Scorer* (1950). In his paper, *Scorer* (1950) cited the earlier work of *Taylor* (1936) on utilizing gravity waves to model the air waves from the Krakatoa eruption, the work of *Pekeris* (1937) and *Wilkes and Weekes* (1947) on modeling the

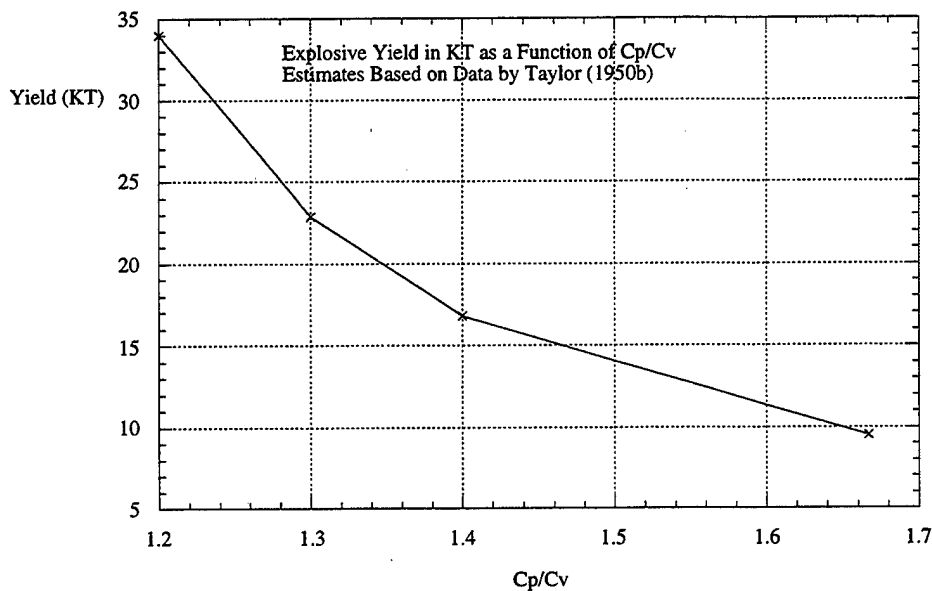


Figure 71. Explosive yield in KT for the TRINITY 1945 test as a function of  $\gamma$  based on estimates provided by *Taylor* (1949b). The yield estimates do not include the amount of energy converted to radiation.

semidirunal pressure variation of the earth's atmosphere in terms of long waves (or gravity waves), and the work of *Pekeris* (1948) who investigated the propagation of a pulse taking into account both acoustic and gravity waves but made no predictions on the specific form of the pulse shape.

In modeling the pulse shape, *Scorer* (1950) included only the gravity wave contribution and assumed a range independent, horizontally stratified atmosphere with no winds. The temperature structure of the atmosphere with height was taken to consist of two layers: a troposphere with a constant lapse rate up to an altitude of 9.61 km followed by an isothermal layer above. The two layer model assumed by *Scorer* (1950) is compared with the U.S. Standard Atmosphere 1976 in Figure 73 where it is seen that the two models are identical up to a height of 9.61 km. The model assumed by *Scorer* (1950) was chosen to allow the development of analytical expressions and is seen to neglect the detailed structure of the upper atmosphere although it provides an "eyeball" average of the latter.

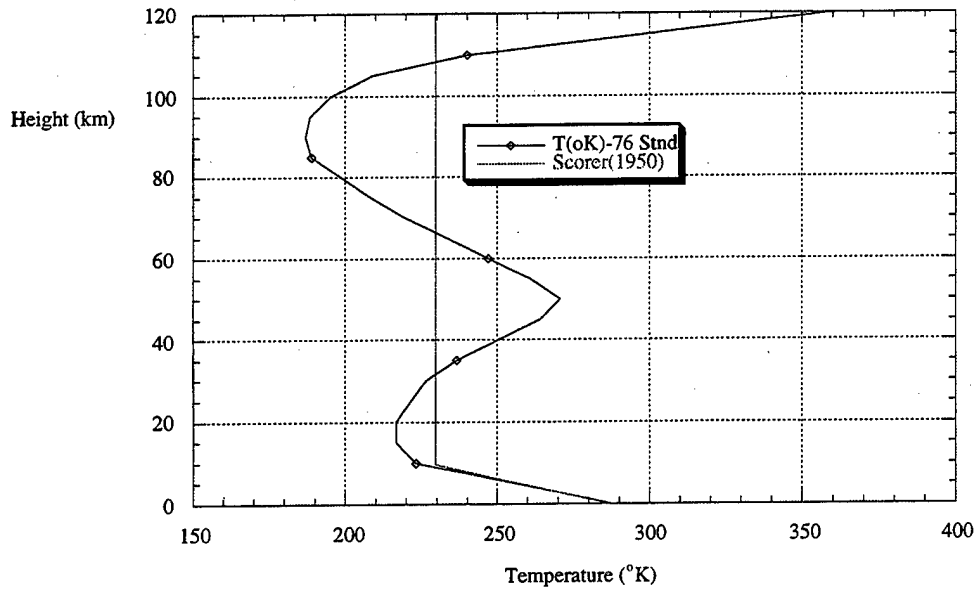


Figure 73. A comparison of the temperature profile used by *Scorer* (1950) and the U.S. Standard Atmosphere 1976 [NOAA, NASA, USAF (1976)].

In deriving the pressure field at the ground due to an explosion on the ground, *Scorer* (1950) followed essentially the same method of approach as did *Pekeris* (1948) except that a quantity referred to as the "modified pressure", defined as,

$$\varpi = \frac{\gamma}{\gamma-1} R \left( \frac{p}{p_{01}} \right)^{\frac{(\gamma-1)}{\gamma}} \quad (5.3)$$

was used as the independent variable, rather than the divergence of the velocity, because it is more closely related to the pressure than is the former. In the above  $\gamma$  is the usual specific heat ratio,  $R$  is the universal gas constant,  $p$  is the pressure and  $p_{01}$  is the pressure at the ground in an unperturbed atmosphere.

*Scorer* (1950) initially considered a harmonic source and used the hydrodynamic equations of motion, adiabatic equation and equation of state to derive two linear differential equations for the modified pressure field in the troposphere and in the isothermal region above. By forcing solution continuity at the interface of the two regions

and matching boundary conditions at the ground and upper atmosphere, *Scorer* (1950) derived an expression for the pressure at the ground, due to an explosion at the ground, given by the Fourier synthesis

$$p_1(r,t) = \frac{1}{4} \pi \rho_{01} B \int_0^{\omega_c} d\omega F(\omega) \left( \frac{2k}{a \sin \theta} \right)^{1/2} e^{i(kr - \frac{\pi}{4})} (e^{i\omega t} + e^{-i\omega t}) \quad (5.4)$$

where in the above  $p_1$  is the pressure at the ground,  $\rho_{01}$  is the density at the ground in the unperturbed atmosphere,  $B$  is related to the volume of material introduced by the source,  $\omega$  is the angular frequency,  $\omega_c$  is the cut-off frequency,  $F(\omega)$  is a function of the frequency,  $k$  is the horizontal wavenumber,  $a$  is the radius of the earth,  $\theta$  is a spherical polar coordinate and it is understood that the real part in Eq. (5.4) is to be taken. Examples of the pulse responses computed from Eq. (5.4) are provided for different ranges in Figure 74.

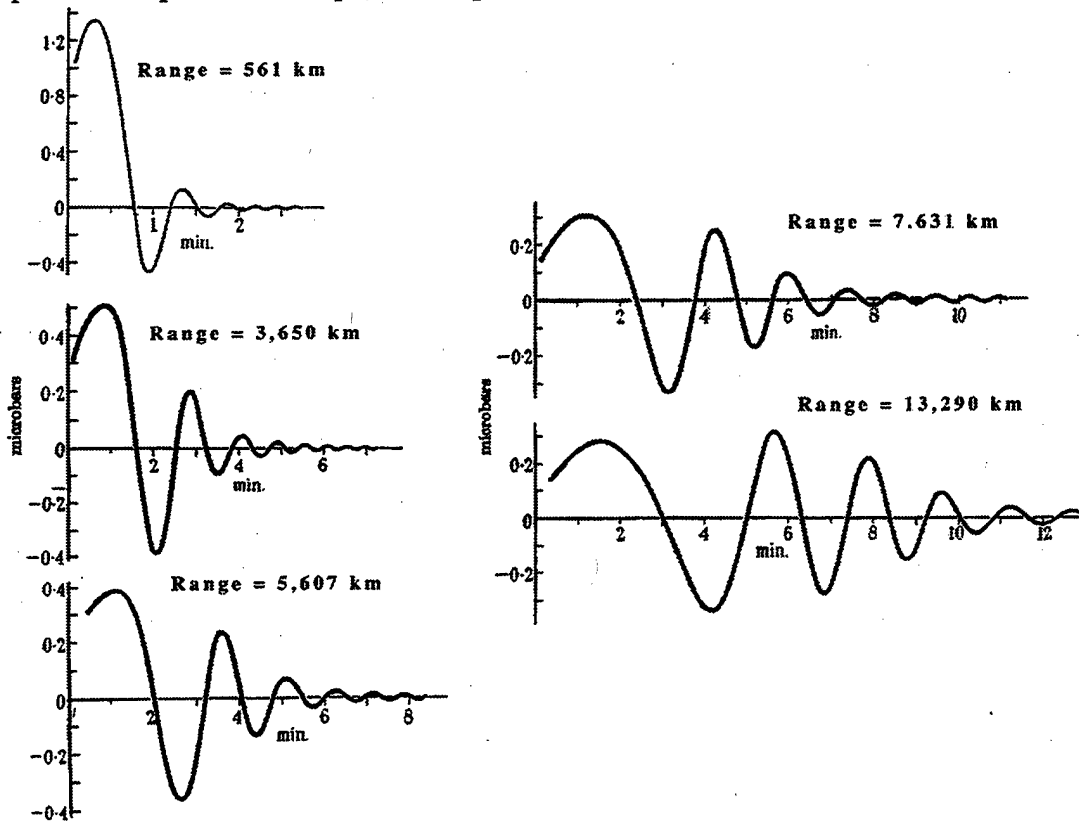


Figure 74. Pulse shapes as a function of range along great circle paths. [Figure adopted from *Scorer* (1950).]

Following the work of *Scorer* (1950), *Hunt, Palmer and Penney* (1960) investigated the far field radiated pressure caused by explosions and also developed the theory in terms of the "modified pressure" variable. However, allowance was made for a



stratospheric duct through the utilization of three isothermal layers as indicated in Figure 75. In addition, the atmospheric model considered by *Scorer* (1950) and a two-layer isothermal atmosphere were also considered. An important conclusion of the work is that the simple two layer models are not sufficient to explain the complicated waveforms observed from explosions and natural events such as meteorites.

For the three-layer model atmosphere, the integral expression obtained by *Hunt, Palmer and Penney* (1960) for the far field pressure on the ground, created by an explosion on the ground, is given as

$$p_1(r,t) = \left\{ \frac{\rho_{01} V}{(2\pi r)^{1/2}} \right\} \sum_n \int_{\omega_{cn}}^{\infty} d\omega \Sigma(\omega) F_n(\omega) (k_n)^{1/2} e^{i(\omega t - kr + \frac{\pi}{4})} \quad (5.5)$$

where in the above  $V$  is the volume of material produced by the source,  $\Sigma(\omega)$  is a function determined by the time variation of the source and  $F_n(\omega)$  is a function of the angular frequency  $\omega$  given by

$$F_n(\omega) = - \frac{\omega \beta_n^2}{\nu k} \text{ for } \omega \geq \omega_{cn} \quad (5.6)$$

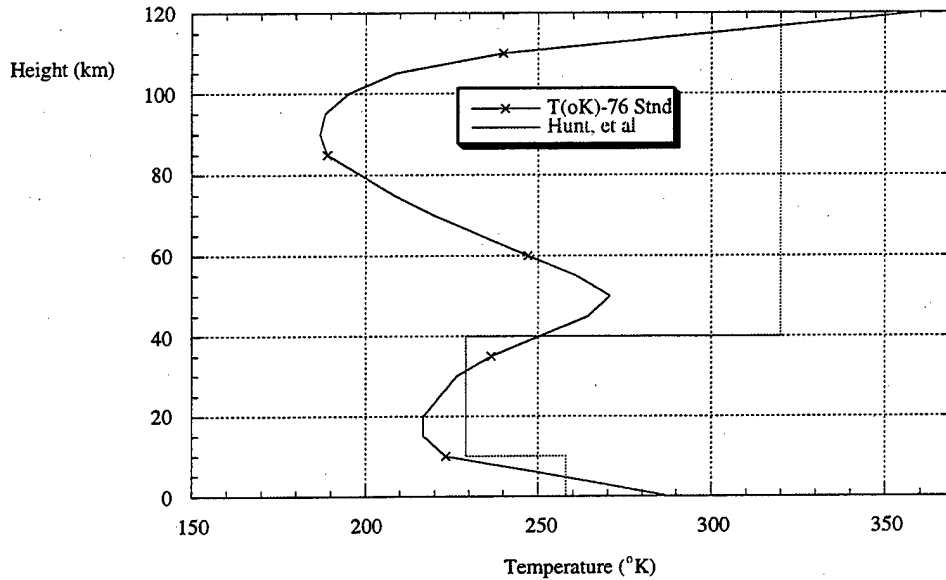


Figure 75. The atmospheric model assumed by *Hunt, Palmer and Penney* (1960) as compared with the U.S. Standard Atmosphere 1976 [NOAA, NASA, USAF (1976)].

where

$$v = \frac{(2 - \gamma)g}{2c_1^2}, \quad (5.7)$$

$$\beta_n^2 = \left\{ \omega^2 - \frac{(\gamma - 1)g^2}{c_1^2} \right\} \left\{ \frac{1}{c_1^2} - \frac{k^2}{\omega^2} \right\} - v^2, \quad (5.8)$$

and the summation is over the number of branches.

*Hunt, Palmer and Penney* (1960) discuss two source functions, or rate of volume insertion ( $=2Vf(t)$ ) functions, which are provided below with the corresponding  $\Sigma(\omega)$  functions:

$$f(t) = \frac{2T}{\pi(T^2 + t^2)} \quad \text{and} \quad \Sigma(\omega) = \left( \frac{2}{\pi} \right) e^{-\omega T} \quad (5.9)$$

where  $T$  is some fraction of the explosion duration and

$$f(t) = \frac{4Tt^2}{\pi(T^2 + t^2)^2} \quad \text{and} \quad \Sigma(\omega) = \left( \frac{2}{\pi} \right) (1 - \omega T) e^{-\omega T}. \quad (5.10)$$

Figure 76 provides the results of the evaluation of Eq. (5.6) for the  $n=0$  and  $n=1$  gravity wave modes from a 5 MT explosion recorded at a range of 6400 km using the source function defined in Eq. (5.10)

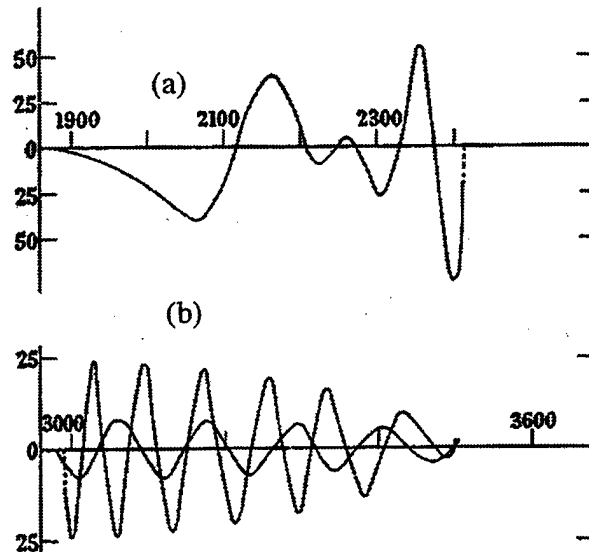


Figure 76. The predicted pressure pulse on the ground in  $\mu\text{bar}$  due to a 5 MT explosion at a range of 6400 km. (a) shows the oscillations due to the  $n=0$  branch and (b) shows the oscillations due to the  $n=1$  branch for periods greater than 70 s. [Figure adopted from *Hunt, Palmer and Penney* (1960).]

*Gazaryan* (1961) presented the results of numerical calculations of modal phase and group velocity curves as a function of period and modal amplitude distributions as a function of altitude for single and double-channel atmospheres modeled by a small number of isothermal layers and for periods greater than one minute. He found, not surprisingly, that the phase and group velocities for the lowest order gravitational mode were essentially the same for both model atmospheres.

Following *Hunt, Palmer and Penney* (1960), *Weston* (1961) published work concerned with explosive pulse synthesis which again accounted only for the gravity wave portion of the pulse but did account for sources at different altitudes above ground. A range independent atmospheric model was assumed and the effects of winds were neglected. However, a more realistic atmospheric temperature profile was used, at least up to the stratopause. Indeed, two temperature models were considered: I & II and these are shown in Figure 77.

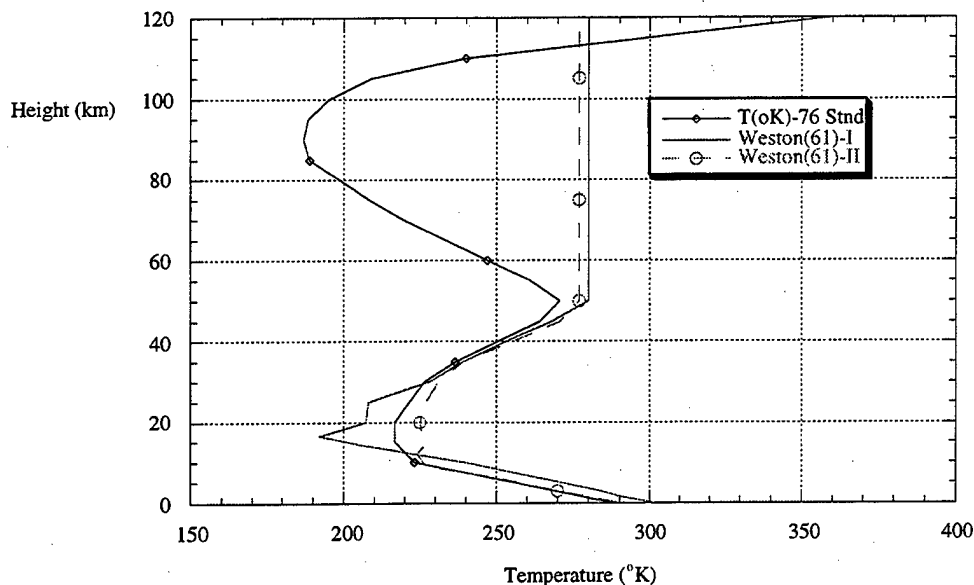


Figure 77. The two temperature profiles considered by *Weston* (1961) compared with the U.S. Standard Atmosphere 1976 [NOAA, NASA and USAF [(1976)].

Starting from the equations of motion, continuity, state and the adiabatic energy equation, *Weston* (1961) derived the following expression for the gravity wave

contribution to the pressure (i.e., the lowest order gravity wave mode)

$$p(a, \theta, t) = \left\{ \frac{\rho_0(R_0)\rho_0(a)}{2\pi a \sin(\theta)} \right\} \frac{V}{\pi} \int_0^\infty d\omega \sqrt{\omega \lambda} Q(\omega) \cos[\omega(t - a\lambda\theta) + \frac{\pi}{4}] \quad (5.11)$$

where in the above  $a$  denotes the radius of the earth and implies that the expression is for a receiver on the ground,  $R_0$  is the height of the explosion ( $R_0 \geq a$ ),  $V$  is the volume of gas injected into the atmosphere by the explosion,  $\lambda$  is the eigenvalue of the gravity wave mode and  $Q(\omega)$  is a function of  $\omega$  determined by the eigenfunctions of the problem.

In addition to deriving the result in Eq. (5.11), *Weston* (1961) cited *Hunt, Palmer and Penny* (1960) as pointing out that *Scorer's* (1950) pulse shapes were in error and computed corrected waveforms for *Scorer's* (1950) assumed atmosphere for a receiver at a range of 3600 km and 6000 km for two heights: ground level and a height of 9.6137 km. *Weston* (1961) found that the pulse shapes were virtually identical but that explosions at higher altitude produce lower amplitude waveforms. Figure 78 illustrates the waveforms.

The waveforms for a range of 7,000 km for atmospheric model I and for two source heights: ground level and a height of 39 km, were also computed. It was found that the waveform amplitude for an explosion detonated at an altitude of 39 km is much reduced in comparison to that of an explosion detonated on the ground.

In a sequel to *Weston* (1961), *Weston* (1962) generalized his previous expression for the pressure to account for several modes of propagation and for an arbitrary point source representation. The specific generalization is given by

$$p(a, t) = \frac{1}{\pi} \left( \frac{\rho_0(R_0)\rho_0(a)}{2\pi a \sin\theta} \right)^{1/2} \int_0^\infty d\omega \sum_j \sqrt{\omega \lambda_j} Q_j \left\{ B_e \cos \left[ \omega(t - a\lambda_j\theta) + \frac{\pi}{4} \right] - iB_o \sin \left[ \omega(t - a\lambda_j\theta) + \frac{\pi}{4} \right] \right\} \quad (5.12)$$

where the summation is over all the modes and the  $B_o$  and  $B_e$  terms are included to incorporate an arbitrary source function. In *Weston* (1961) only one term in the summation

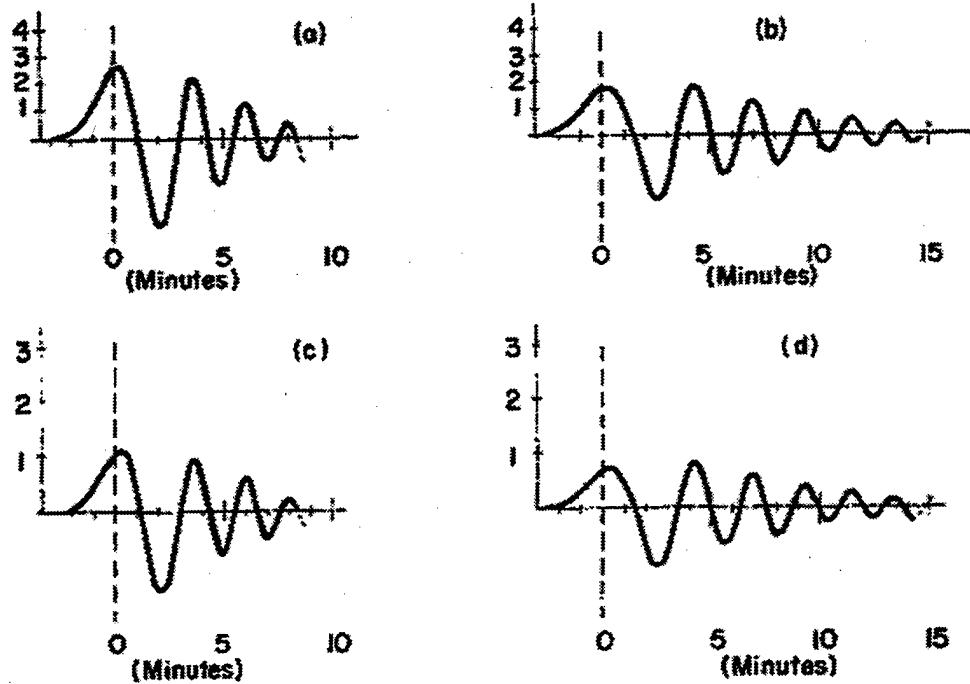


Figure 78. The pressure pulse at the ground at a distance of 3600 km (a) and (c), and at a distance of 6000 km (b) and (d) for Scorer's atmosphere, for an explosion on the ground (a) and (b), and at a height of 9.6137 km (c) and (d). One unit of amplitude corresponds to  $0.614 \mu\text{bar per } 1 \text{ km}^3$  of gas released. [Figure and caption adopted from *Weston* (1961).]

was included (the gravity wave) and a specific volume source representation was assumed: i.e.,  $B_0=V$  and  $B_e=0$ .

For the source function, *Weston* (1962) relied on the work of *Brode* (1956, 1957) and utilized the form

$$p = \frac{\lambda_s}{\lambda} p_1 \left[ 1 - \frac{\lambda_s - \lambda}{L} \right] e^{-\left[ \frac{\lambda_s - \lambda}{L} \right]} \quad (5.13)$$

where in the above  $p_1$  is the peak excess pressure,  $\lambda_s$  is the normalized shock radius given by

$$\lambda_s = \frac{r_s}{\alpha} \quad (5.14)$$

where  $r_s$  is the radius of the shock front and  $\alpha$  is related to the total initial energy in the explosion,  $W$ , by

$$\alpha = \left( \frac{W}{P_0} \right)^{1/3}, \quad (5.15)$$

L is the normalized length of the positive phase and  $\lambda$  is the normalized radius. Equation (5.13) leads to the form

$$\begin{aligned} f(t) &= \alpha \lambda_s p_1 t e^{-t/T} \text{ for } t > 0 \\ &= 0 \quad \text{for } t < 0 \end{aligned} \quad (5.16)$$

where T, the period, is given by

$$T = \frac{\alpha L}{c_0}. \quad (5.17)$$

The form of the source function appropriate for the representation given in Eq. (5.12) is given in terms of  $f(t)$  as

$$B = \frac{4\pi}{\rho_0(R_0)} \int_{-\infty}^{+\infty} dt f(t) e^{i\omega t}$$

where for a source on the ground, the  $4\pi$  is replaced by  $2\pi$ . Substitution of Eq. (5.16) into Eq. (5.18) then gives

$$B = \frac{4\pi T^2 \alpha \lambda_s p_1}{\rho_0(R_0)} \frac{[1 - (\omega T)^2 + 2i\omega T]}{[1 + (\omega T)^2]^2}. \quad (5.19)$$

The forms for the other source time functions given in Eqs. (5.9) and (5.10) can be found by noting that

$$B = \frac{4\pi}{\rho_0(R_0)} \Sigma(\omega). \quad (5.20)$$

By fitting Eq. (5.13) to the data of *Brode*(1957), *Weston* (1962) finds that  $L \sim 0.35$  so that Eq. (5.17) can be used to estimate the characteristic period from nuclear explosions for various yields and heights. The results of the calculations are shown in Figure 79 where it is seen that for a given explosive yield, the period is predicted to increase with increasing height.

*Weston* (1962) utilized Eq. (5.12) to compute synthetic waveforms based on the first three dominant modes which contribute to the leading edge of a pulse at a range of 5500 km and investigated the effect of source altitude. In making the calculations, a very realistic atmosphere was used as is shown in Figure 79. The computed pulse waveforms are shown in Figure 80.

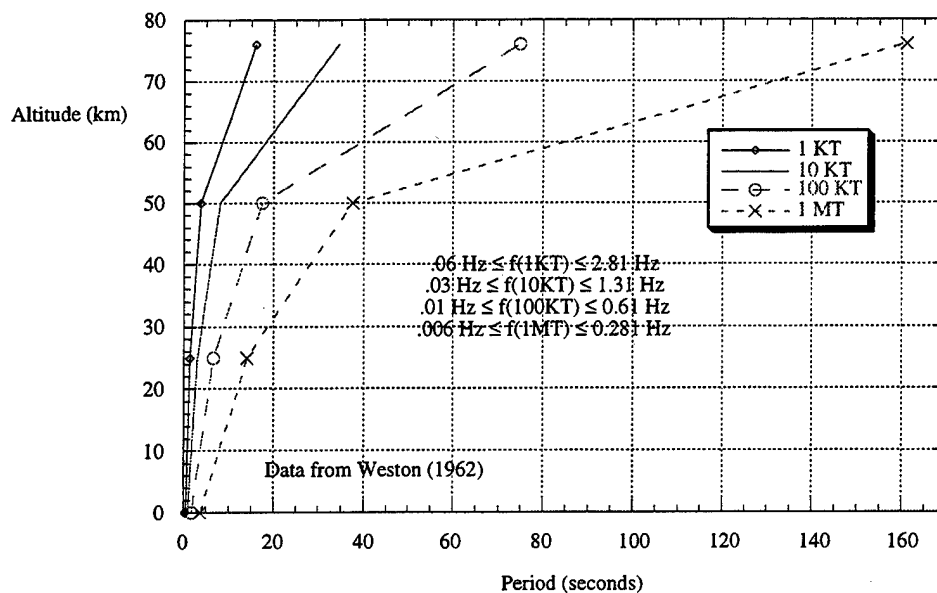


Figure 79. The effect of altitude on the period of infrasound emitted from nuclear explosions of various yields. [Figure based on data provided in *Weston* (1962).] Frequency bounds of the emitted waves are also indicated on the figure and are based on the range of periods which occur over the indicated altitude range.

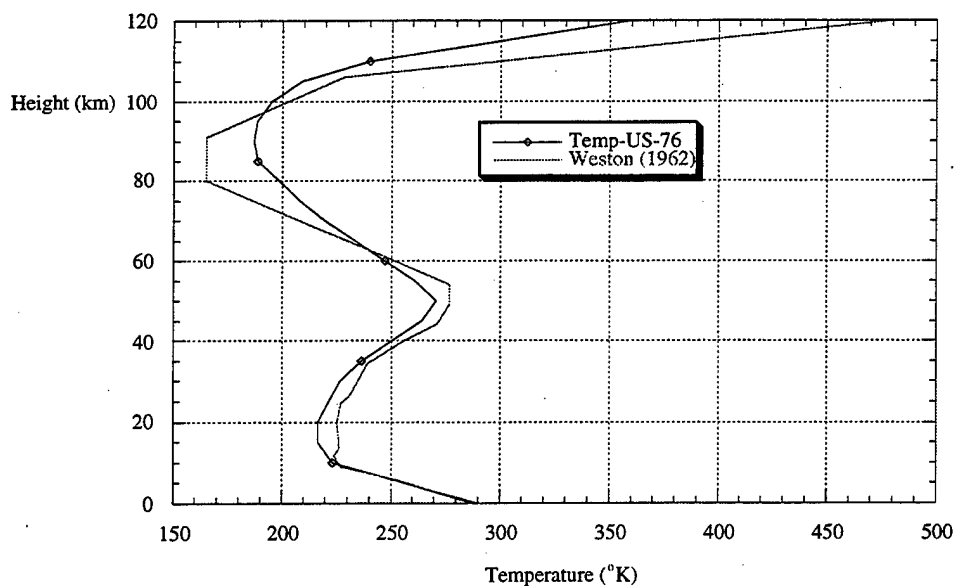


Figure 80. The atmosphere assumed in *Weston* (1962) is compared with the U.S. Standard Atmosphere 1976.

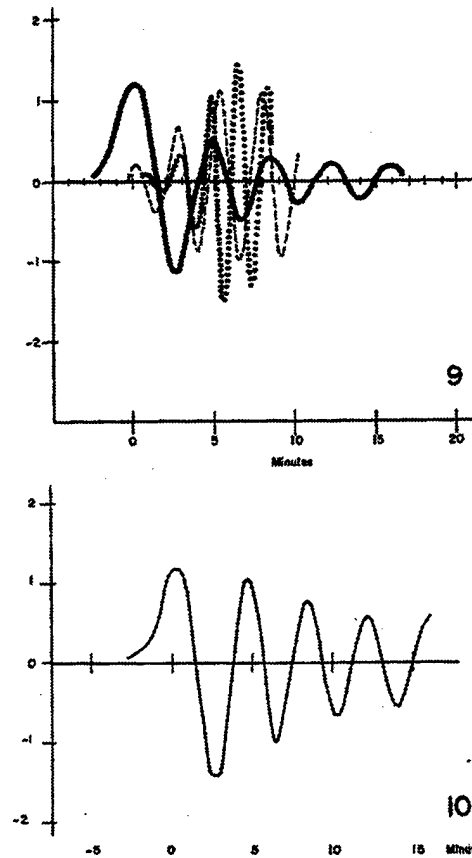


Figure 81. Panel 9: The head of the pressure pulse at ground level at a distance of 5500 km from an explosion on the ground. The solid, dashed and dotted curves correspond to the contributions of modes 0, 1, and 2, respectively. Panel 10: The head of the pressure pulse at the ground for mode 0, at a distance of 5500 km from an explosion at an altitude of 76 km. The amplitude is expressed in units of  $2.9655 \times 10^{-4}$   $\mu$ bars per  $1 \text{ km}^2$  of gas released. [Figure and caption adopted from *Weston* (1962).]

Following publication of the results based on the improved pulse modeling, *Weston and van Hulsteyn* (1962) incorporated the effect of wind into the theory for the propagation of gravity waves by assuming a uniform horizontal wind field. Wind was incorporated into the momentum, continuity and energy equations which were then linearized, combined and solved numerically. The assumed wind speed, temperature and sound speed profiles are shown in Figures 82 and 83. As indicated, the atmosphere was taken to be isothermal above 50 km and the wind profile was terminated at an altitude of 76.5 km. Accordingly, only propagation in the troposphere and stratosphere are adequately modeled. The wind speed profile exhibits a strongly westerly (winds blowing from the west-o-east) trend in the stratospheric region attaining a maximum magnitude of 37 m/s at an altitude of 61 km.



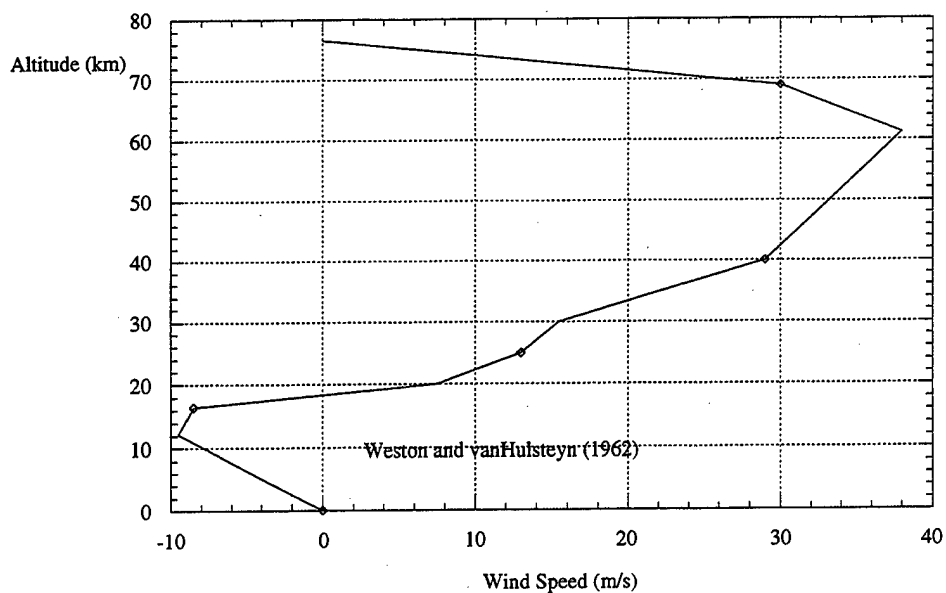


Figure 82. The wind speed profile assumed in the modeling of *Weston and van Hulsteyn* (1962).

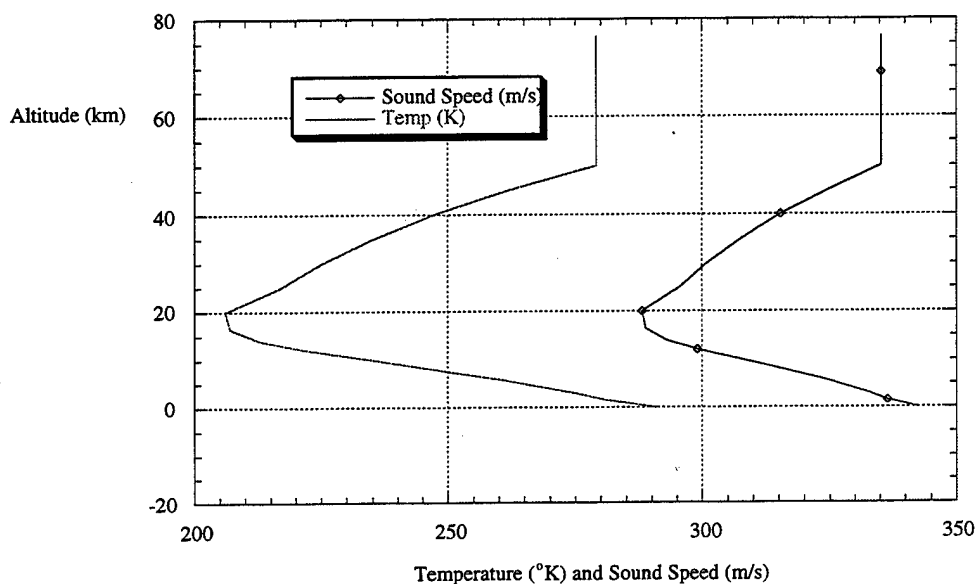


Figure 83. The temperature and sound speed profiles assumed in the modeling of *Weston and van Hulsteyn* (1962).

The key findings of the modeling were that: in downwind propagation, the phase speed and dispersion of the pulse are increased and that the lower frequencies of the pulse are more affected than are the higher frequencies.

*Pridmore-Brown* (1962) emphasized that wind gradients play a role as important as gradients in temperature and sound speed and developed theoretical expressions for the pressure field from a CW point source above a finite impedance ground plane. The relationship of equivalence between temperature and wind speed gradients was provided as

$$\frac{dT}{dz} = \left( \frac{2T}{c} \right) \cos(\phi) \left( \frac{dU}{dz} \right) \quad (5.21)$$

where  $U$  is the horizontal component of the wind speed and  $\phi$  is the angle between the propagation direction and the wind direction. Figure 84 shows the effect of winds on propagation and the formation of a shadow zone in case of a negative lapse rate.

The theoretical expression derived for the pressure field was of the general form

$$p(r, z, t) = e^{-i\omega t} \int_0^\infty d\kappa \kappa \int_0^{2\pi} d\theta e^{i[\kappa r \cos(\theta - \phi)]} \Pi(\kappa, \theta; z) \quad (5.22)$$

where cylindrical polar coordinates are used and  $\Pi(\kappa, \theta; z)$  is a complicated, but analytically known, function of the horizontal wavenumber, angle and height. In the absence of winds, it was shown that Eq. (5.22) reduces to that obtained earlier by *Pekeris* (1946 and 1947) and by *Pridmore-Brown and Ingard* (1955).

*Pridmore-Brown* (1962) derived an approximate evaluation of Eq. (5.22) and an explicit expression for the square of the pressure field in the shadow zone region given by

$$|p|^2 = \left( \frac{B}{r} \right) \exp[-n(f/c_0)^{\frac{1}{3}} g^{\frac{2}{3}} r] \quad (5.23)$$

where in the above,  $g$  is given by the derivatives of the sound and wind speed at the ground plane by the expression

$$g = -(c'_0/c_0 + U'_0 \cos(\phi)/c_0), \quad (5.24)$$

where the primes denote derivatives with respect to the vertical coordinate,  $z$ .

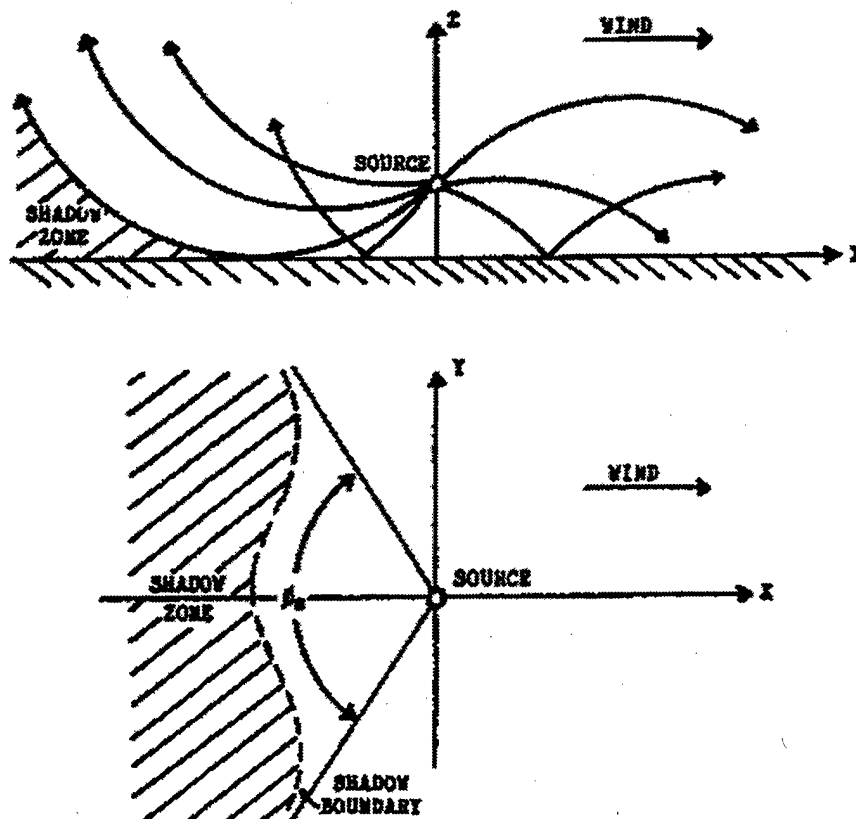


Figure 84. Top Panel: The effect of wind on sound propagation for a point source above a horizontal ground plane. [Figure adopted from *Pridmore-Brown* (1962).]

*Pfeffer* (1962) developed a matrix method for the solution of the linearized hydrodynamic equations such as the one developed by *Thomson* (1950) and *Haskell* (1953) for modeling elastic wave propagation in the earth. The variation in sound speed or temperature with height is modeled by using  $N$  isothermal layers where  $N$  is chosen in such a way as to closely approximate a more continuous variation. *Pfeffer* (1962) tested his method by showing that it yielded identical results for the group and phase velocity curves as obtained by *Pekeris* (1948) for the same atmospheric assumptions.

In a sequel, *Pfeffer and Zarichny* (1962) computed a number of phase and group velocity curves for several model atmospheres utilizing the matrix methodology developed in *Pfeffer* (1962). Figure 85 compares four of the model atmospheres used with the U.S. Standard Atmosphere 1976 and shows that the model atmospheres are not good representations of the standard in the upper atmosphere.

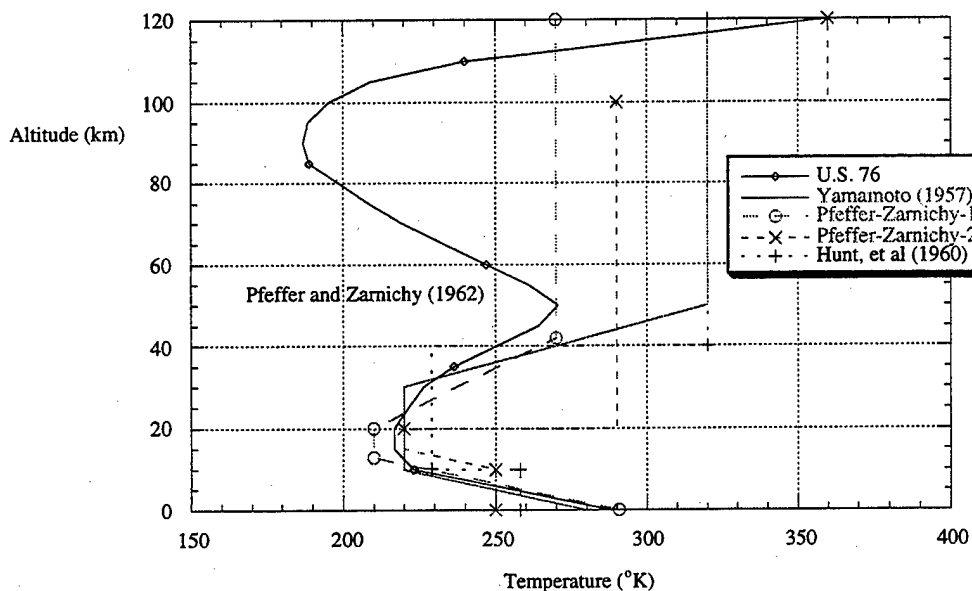


Figure 85. Four of the model atmospheres, utilized by *Pfeffer and Zarichny* (1962) in computing group and phase velocity curves, are compared to the U.S. Standard Atmosphere 1976 [NOAA, NASA, USAF (1976)].

*Pfeffer and Zarichny* (1962) computed phase and group velocity dispersion curves for the fundamental gravity wave mode for the *Yamamoto* (1957), Pfeffer and Zarichny-1 and -2 atmospheres finding that the atmosphere having the highest temperature in the upper layer (Pfeffer and Zarichny -2) produced inverse dispersion: at periods ranging from 360 s to 675 s, the group velocity was found to decrease with increasing period. The other two atmospheres all produced normal dispersion curves. The investigators also studied the behavior of long period fundamental mode cut-off, and minimum and maximum group velocities as a function of temperature in the upper atmosphere. The results of the calculations are shown in Figure 86.

*Pfeffer and Zarichny* (1962) also computed dispersion curves for up to four higher order acoustic modes for the *Yamamoto* (1957) and *Hunt, et al.*, (1960) atmospheres and the results for the *Yamamoto* (1957) model are shown in Figure 87. The curves indicate

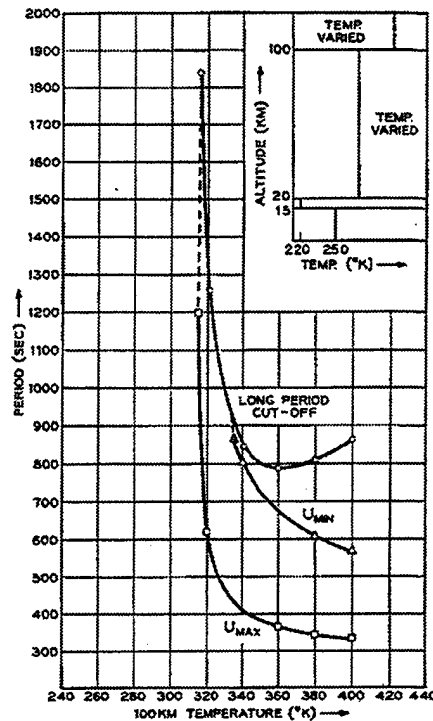


Figure 86. Phase and group velocity dispersion curves for the model atmosphere exhibited in the inset. [Figure adopted from Pfeffer and Zarichny (1962).]

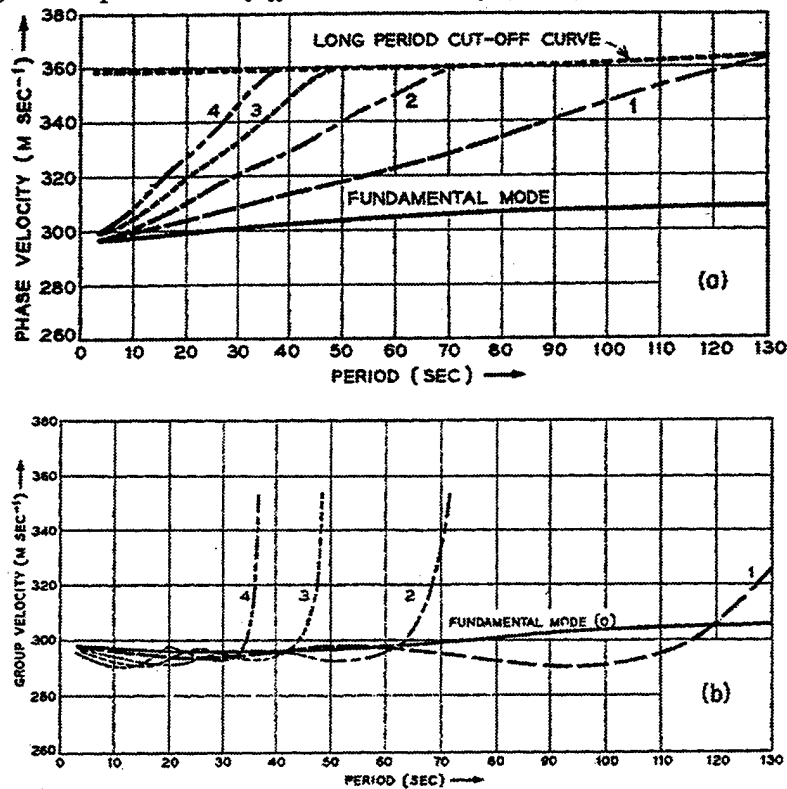


Figure 87. Group and phase velocity curves. [Figure adopted from Pfeffer and Zarichny (1962).]

that several different periods below 130 s have the same group velocity and, for a particular recording station, will arrive simultaneously.

*Donn and Ewing (1962a)* present pressure waveform data, measured dispersion curves and dispersion curves computed from model atmospheres with the goal of using the dispersion curves as a means of studying the atmospheric thermal structure. Section 7.0 presents selected waveform data recorded on Lamont microbarovariographs from U.S. MT tests in the Marshall Islands and Soviet MT tests conducted at Novaya Zemlya, as well as data recorded at Japanese stations from U.S. explosions in the Marshall Islands. Appendix A reproduces the entire Lamont-Doherty waveform collection for atmospheric nuclear explosions. Figures 88 and 89 present group velocity dispersion curves for the Soviet and U.S. tests, respectively.

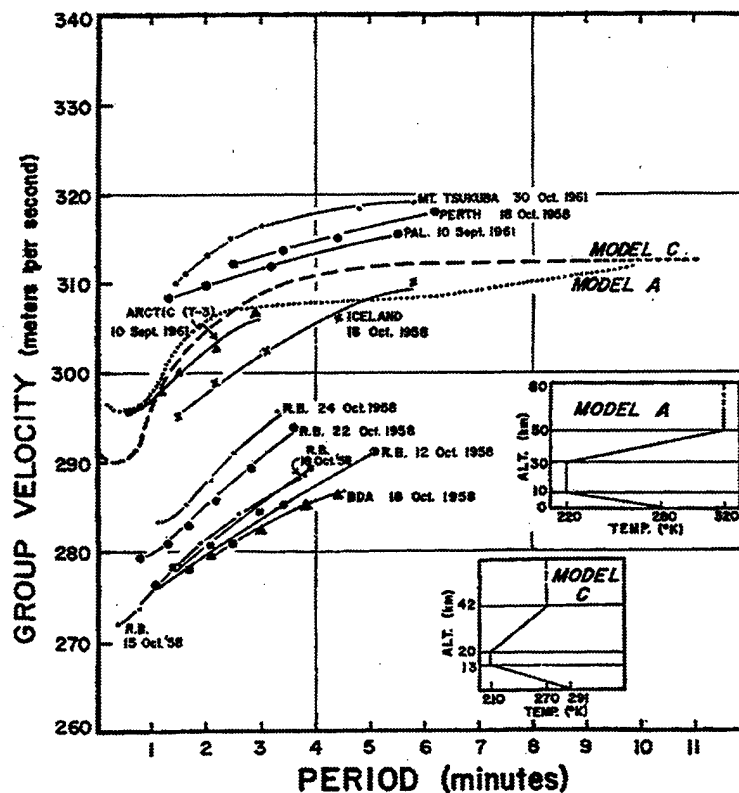


Figure 88. Dispersion curves for U.S. atmospheric nuclear explosions. [Figure adopted from *Donn and Ewing (1962a)*.]

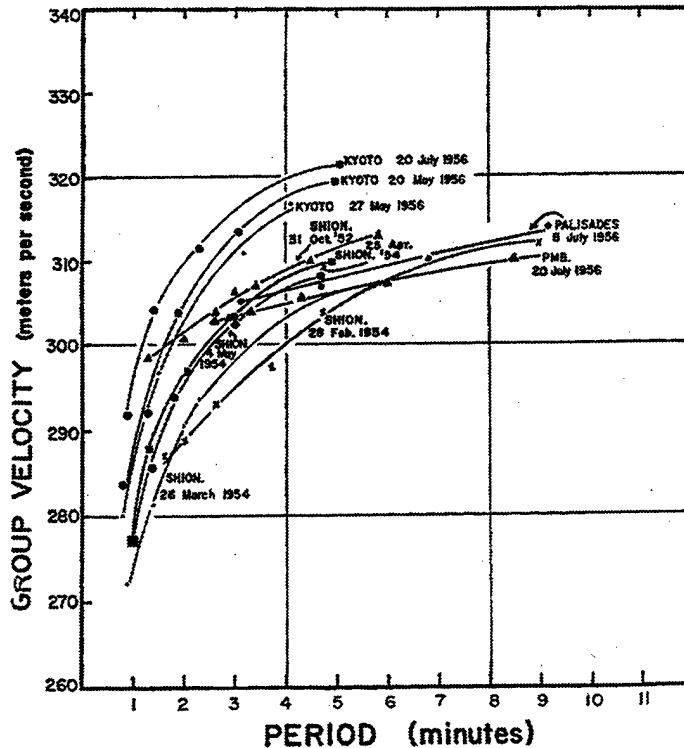


Figure 89. Dispersion curves for Soviet atmospheric nuclear explosions. [Figure adopted from *Donn and Ewing* (1962a)].

Following a detailed discussion of the figures, *Donn and Ewing* (1962a) conclude that: "It would appear from this investigation that the atmospheric structure controlling the dispersive properties of acoustic-gravity waves varies along different paths and probably along different segments of the same path. Those waves travelling the longest routes, or routes which are so disposed as to cancel the varying wind effects in different zones, offer the best means of applying this procedure to the study of average atmospheric structure."

In a sequel, *Donn and Ewing* (1962b) present waveform data, recorded by 9 microbarograph stations distributed world wide, which were produced by October 30, 1961 58 MT Soviet explosion at Novaya Zemlya. Ranges of the stations from the estimated "epicenter" extended from 3547 km for the Foulness, England station to 12,888 km for the Suva, Fiji station. The waveform data are included in Section 7.0 of this report and only the dispersion curves are discussed herein. The waveform data include direct arrivals (referred to as  $A_1$ ), first antipodal arrivals (referred to as  $A_2$ ) and second antipodal arrivals (referred to as  $A_3$ ). All of the records were found to begin with a normally dispersed train

of waves which appeared to be superposed on a longer period wave train showing inverse dispersion. Figure 90 provides the measured group velocity dispersion curves and a comparison of model predictions for two different assumed atmospheric models.

As in *Donn and Ewing* (1962a), the main scientific interest in computing group velocity dispersion curves was to learn about atmospheric structure in much the same manner as had been used in seismology where surface wave dispersion curves were used to constrain models of the earth's interior. In the case of the atmosphere, significant temporal and path dependence was noted for the  $A_1$  arrivals, whereas the higher order arrivals,  $A_2$  and  $A_3$  were more stable owing to the fact that the propagation distances were long enough to average out a significant amount of atmospheric variability.

*Press and Harkrider* (1962) were evidently the first to compute realistic barograms which compared quite favorably with experimental data and which used several realistic

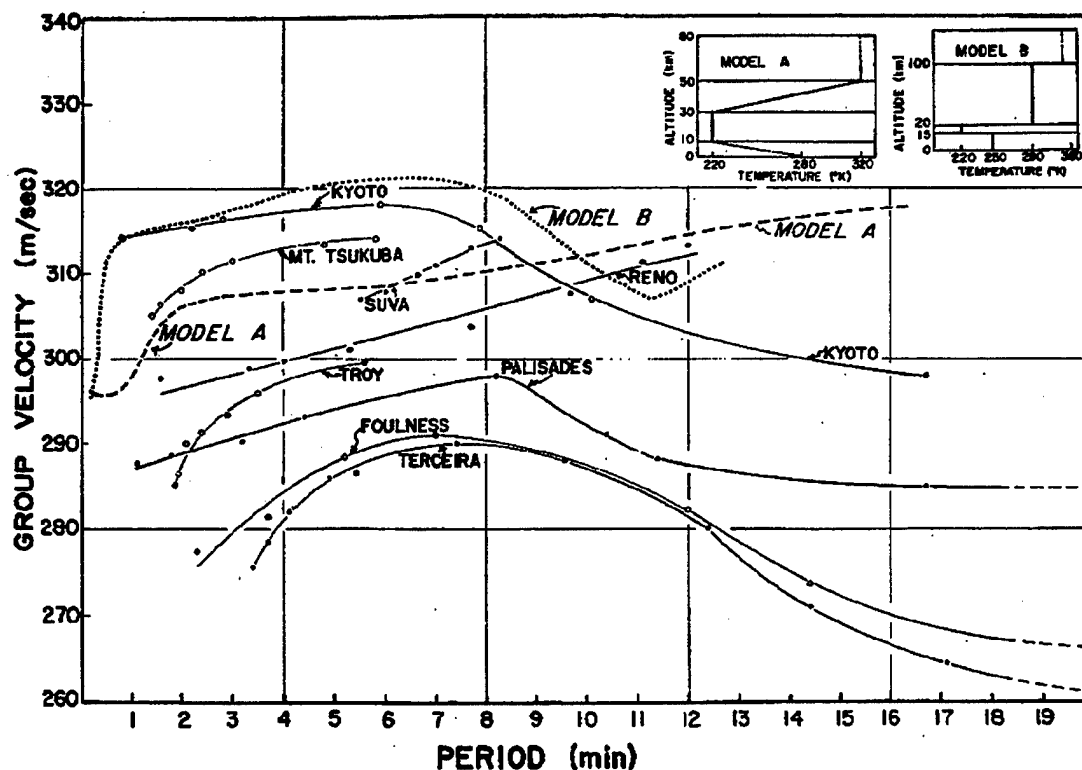


Figure 90. Group velocity dispersion curves for the  $A_1$  waves created by the Soviet explosion of October 30, 1961. [Figure adopted from *Donn and Ewing* (1961).]



models of the atmosphere without winds. Their method is a homogeneous waveguide theory (source function and excitation functions were not included) based on the linearized or characteristic equations developed by *Pekeris* (1948). These equations and boundary conditions were cast in the matrix form proposed by *Haskell* (1953) in much the same manner as was done by *Pfeffer and Zarichny* (1962). In this formulation, the continuous variation of atmospheric properties with height is modeled by a number (typically 20 to 40) of isothermal layers and the matrix approach allows the pressure and particle velocity on the ground to be related to those at any height through a product of matrices appropriate to each of the layers.

*Press and Harkrider* (1962) considered a number of model atmospheres, upper terminations (free and rigid surfaces at 220 km, isothermal half-spaces beginning at 108 km and 220 km) and seasons (Arctic summer and winter, and tropical) in addition to an atmosphere having no gravity so that only acoustic modes could propagate. For each atmosphere, the first two gravity waves ( $GR_0$  and  $GR_1$ ) and acoustic modes ( $S_0$  and  $S_1$ ) were computed. By comparing all of the dispersion curves so computed, *Press and Harkrider* (1962) were able to deduce that the first arriving waves in a barogram are controlled by properties of the lower atmosphere and to develop group velocity curves for the modes which were common to all atmospheres and these curves are shown in Figure 91. In the words of the authors: "We would expect that most of the energy excited by near-surface explosions propagates according to these values of phase and group velocity. The first-arriving waves would correspond to the region of flat group velocity curves for the  $S_0$  and  $GR_0$  modes. Thus, a transient containing periods of 3 to 10 minutes would arrive at a time corresponding to a propagation velocity of 312 m/s. This would be followed by waves of gradually decreasing period."

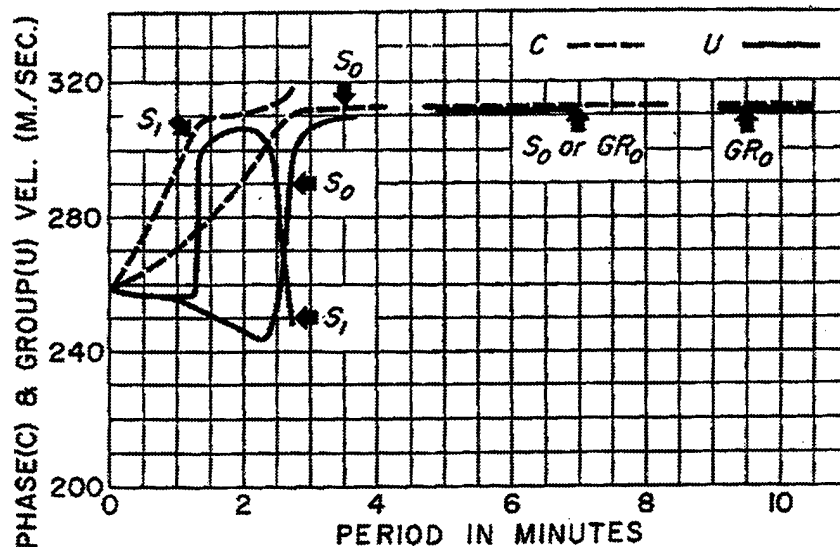


Figure 91. Invariant segments of phase (C) and group (U) velocity dispersion curves as computed from several ARDC model atmospheres. [Figure adopted from *Press and Harkrider* (1962).]

In addition to the foregoing, *Press and Harkrider* (1962) computed synthetic barograms as superpositions of acoustic and gravity wave modes and compared the theoretical waveforms with microbarogram records of Soviet atmospheric explosions. An example of one of the comparisons so made is provided in Figure 92 where it is seen that the theoretical and experimental records are quite similar. The experimental group velocity

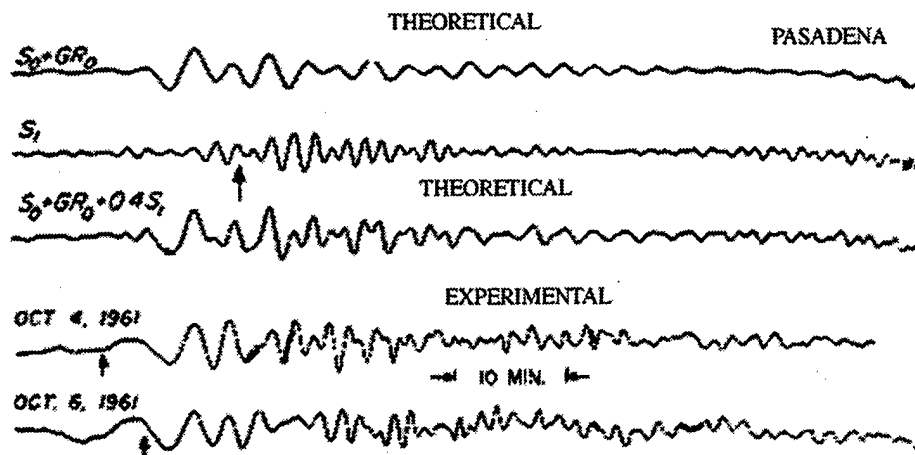


Figure 92. A comparison of theoretical and measured microbarograms for two atmospheric nuclear explosions as recorded on microbarographs located at Pasadena, CA. As indicated, a superposition of the fundamental gravity wave mode ( $GR_0$ ) and the first two acoustic modes ( $S_0$  and  $S_1$ ) is required to fit the data. [Figure adopted from *Press and Harkrider* (1962).]

points for the A<sub>1</sub> arrivals were found to exhibit significant scatter whereas those for the A<sub>2</sub> and A<sub>3</sub> were quite stable, a circumstance which was attributed to changes in the atmosphere.

*Pfeffer and Zarichny* (1963) also computed phase and group velocity curves and synthetic barograms for different and realistic atmospheres in the absence of winds using a modification of the *Thomson* (1950) and *Haskell* (1953) matrix approach which was adopted for propagation in the atmosphere by *Pfeffer* (1962). Some of the model atmospheres were based on the COSPAR (Committee on Space Research) atmosphere and others were based on the ARDC standard atmosphere. Both of these atmospheres appear to be quite similar to the U.S. Standard Atmosphere 1976.

In computing the group velocity dispersion curves, the COSPAR atmosphere was modified by terminating the atmosphere with an isothermal layer at successive heights (52 km, 110 km, 130 km, 200 km, 300 km, and 700 km). The continuous variation of sound speed with height was modeled by approximating the variation with a number of iso-speed layers *N* (26, 47, 49, 56, 66, 76). Dispersion curves were computed for the atmospheres terminated at 52 km, 110 km and 130 km for the fundamental mode, and for the fundamental, the first five acoustic and the first five gravity wave modes for the atmospheres truncated at 52 km and 300 km. The computed phase velocity dispersion curves were found to exhibit a step-like behavior and the group velocity dispersion curves were found to exhibit a plateau-like structure which *Pfeffer and Zarichny* (1963) attributed to the "interference of 'quasi-horizontal' and 'quasi-vertical' modes. The dispersion represented by the 'quasi-horizontal modes' is controlled by the stratospheric and by the higher velocity layers above and below this channel and is therefore insensitive to the atmospheric structure above the ozonosphere. The gross features of the barograms recorded at the ground following nuclear explosions in the lower atmosphere can be accounted for by these modes. The dispersion associated with the 'quasi-vertical modes' is

controlled by the 85 km sound channel and by the higher velocity layers above and below this channel."

*Pierce* (1963a) theoretically considers propagation in a three-layer model atmosphere consisting of single duct formed by sandwiching "a homogeneous fluid layer between two similar half-spaces of the same density but of higher sound speed". The focus is on the propagation of acoustic waves rather than gravity waves and the situation considered is one in which both the source and receiver are located in the same half-space but outside the duct. The theory is developed in terms of a velocity potential and decomposes the field into a direct, reflected and secondary field, where by reflected field is meant that energy reflected from the lower layer of the duct. It is then shown that the secondary field can be decomposed into three contributions: a sum over normal modes, complex modes and a lateral wave. At long ranges it is shown that the normal mode terms dominate and that a major effect of locating the source and receiver outside of the waveguide is to "accentuate lower order modes and the lower frequency portion of the source spectrum."

*Pierce* (1963b) considers the problem of acoustic-gravity wave propagation from a point source in an isothermal atmosphere under free field conditions and when the source is located above a ground plane. The basic method of approach in both cases is to begin with the linearized equations of hydrodynamics, develop a Green's function satisfying the conditions of causality and the required boundary conditions and to use Green's theorem to find the pressure field at any point in the medium in the limit of an infinitesimal source. In the case of free field conditions, *Pierce* (1963b) corrects earlier work on the same problem carried out by *Stretenskii* (1954) and finds that there are two frequency pass bands between which waves will not propagate. These bands are given as:

$$\frac{(\gamma-1)^{1/2}g}{c} < \omega < \frac{\gamma g}{2c} \quad (5.25)$$

and as:

$$0 < \omega < \frac{(\gamma - 1)^{1/2} g \cos(\theta)}{c} \quad (5.26)$$

where  $\theta$  is the angle measured from the vertical. Numerically, and for  $c=344$  m/s, the first condition is  $0.018 \text{ rad/s} \leq \omega \leq .020 \text{ rad/s}$ .

When the presence of the ground is taken into account, *Pierce* (1963b) derived an integral expression for the pressure field which could be explicitly evaluated at zero range, and asymptotically by methods of stationary phase or steepest descent. In the stationary phase approximation, it was demonstrated that the received pressure field could be decomposed into direct, reflected and surface wave components with the latter dominating at long ranges. In the frequency range given in Eq. (5.26), it was found, through a calculation of the acoustic intensity, that the energy flowing from the source tends to concentrate in the lower regions of the atmosphere: a circumstance which is shown in Figure 93 which exhibits the relative magnitude of acoustic intensity and propagation direction as functions of source height and source-to-receiver range.

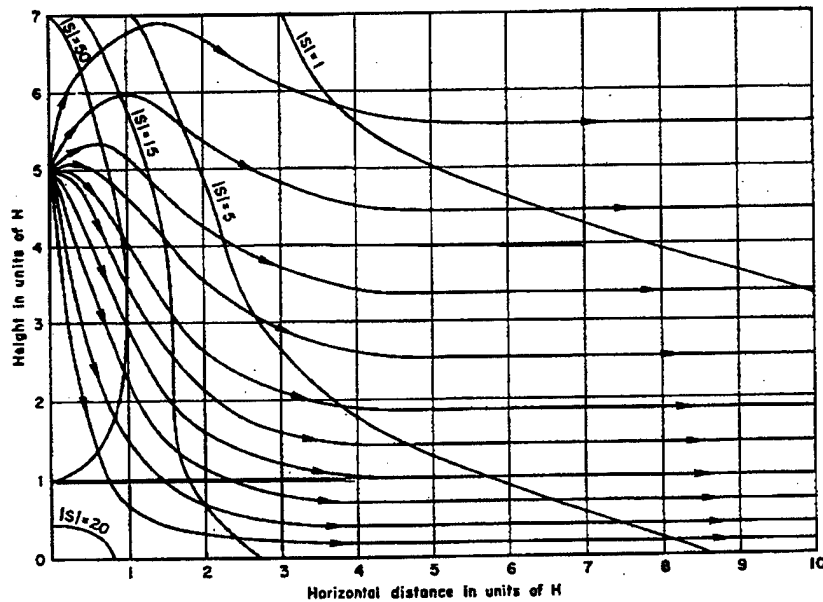


Figure 93. The propagation direction and relative magnitude of the acoustic intensity,  $|S|$ , as a function of height and horizontal source-to-receiver range in an isothermal atmosphere over a ground plane. Quantities are plotted in units of atmospheric scale height,  $H (=c^2/\gamma g)$ , for a source frequency corresponding to  $\omega=0.48$  and a source height of  $5H$ . [Figure and caption adopted from *Pierce* (1963b)].

*Harkrider* (1964) extended the work and model of *Press and Harkrider* (1962) to include the modeling of an explosive source on the ground and at various altitudes above the ground. The basic method of approach was based on the *Haskell* (1953) matrix method and utilized the ARDC standard atmosphere modeled by 39 isothermal layers as shown in Figure 94. However, wind effects were not included in the modeling.

The source was introduced into the model in the frequency domain so that the variation of pressure with time was in agreement with observations acquired near the source of an actual nuclear explosion.

Utilizing the improved model, *Harkrider* (1964) computed numerous group and phase velocity dispersion curves, primarily for the A<sub>1</sub> arrival, for various source altitudes and propagating acoustic-gravity wave modes. In addition, numerous theoretical barograms were computed in the time domain to assess the contributions of the various propagating modes and the frequency content of barograms for a fixed height as a function of yield. In general, it was found that only the lowest order gravity wave mode (GR<sub>0</sub>) and

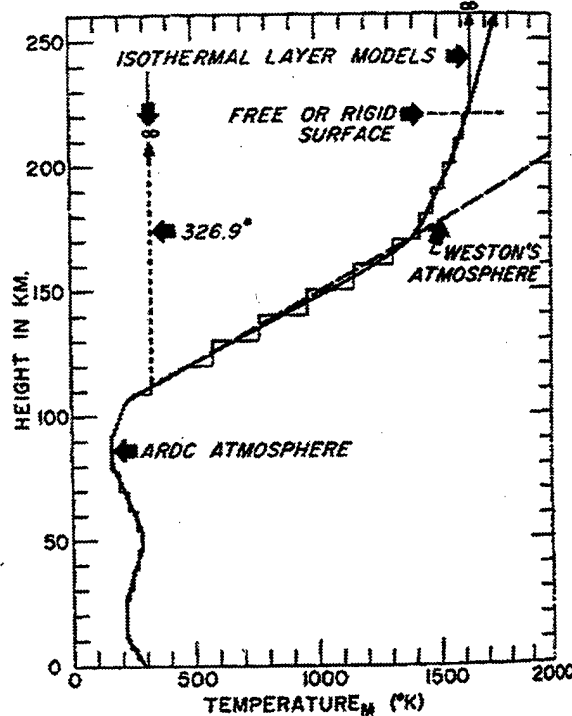


Figure 94. The ARDC standard atmosphere and its approximation by 39 isothermal layers. The atmosphere used by *Weston* is provided for comparison. [Figure adopted from *Harkrider* (1964).]

the first three acoustic modes ( $S_0$ ,  $S_1$  and  $S_2$ ) were required to synthesize a barogram and that increasing the explosive yield for a fixed explosive height produced waveforms having decreasing high frequency content.

Harkrider (1964) computed synthetic barograms for yields and source heights appropriate to a number of Soviet explosions in the 5 MT to 60 MT range and compared them with data acquired on a barograph at the California Institute of Technology Seismological Laboratory and found generally satisfactory results. A comparison of computed and observed waveforms for 8 MT and 9 MT Soviet nuclear explosions is provided in Figure 95.

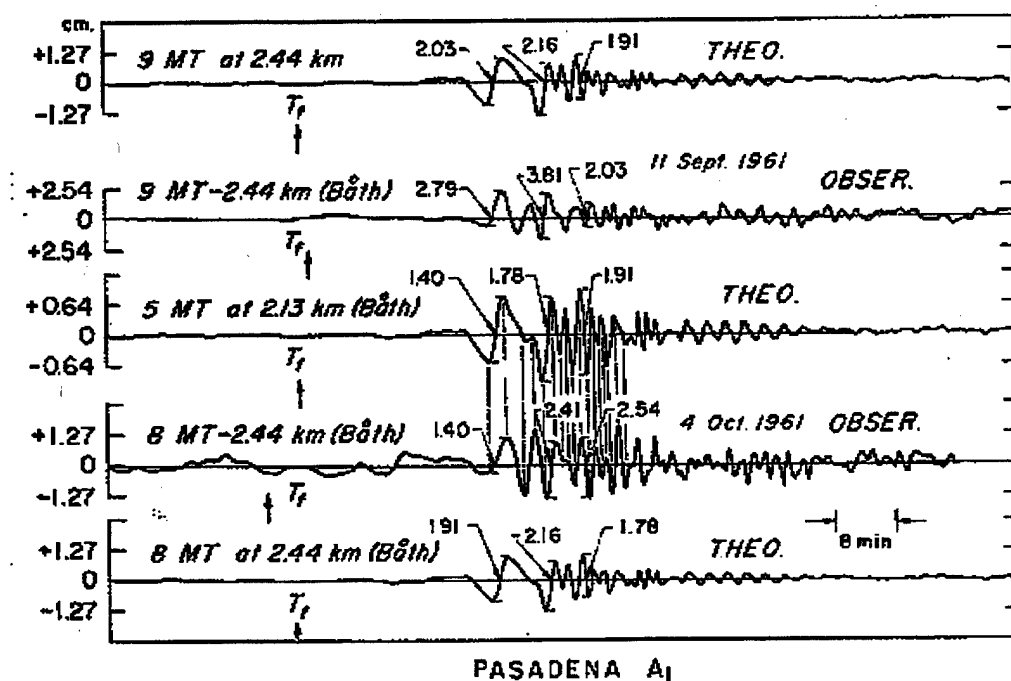


Figure 95. A comparison of theoretical and observed barograms from 8 MT and 9 MT explosions detonated at Novaya Zemlya in September and October of 1961. The waveforms were recorded at the Cal Tech Seismological Laboratory in Pasadena, CA. The waveforms are for the direct, or  $A_1$ , arrival. [Figure adopted from Harkrider (1964).]

Additional conclusions of the modeling results included:

- "A scaled point source is sufficient to model thermonuclear explosions."
- "Different parts of the vertical temperature structure of the atmosphere control the excitation of these modes [ $GR_0$ ,  $S_0$ ,  $S_1$ ,  $S_2$ ]. The zone with a velocity minimum near 20-

km controls the early-arriving acoustic modes. The region with a velocity maximum at about 50 km controls the early-arriving gravity modes. The minimum velocity region at about 85 km controls the short-period acoustic modes which travel at a group velocity equal to the acoustic velocity of this channel. The upper atmosphere controls the late-arriving long-period waves of each mode."

- "The observed shift in dominance of certain frequencies with yield and altitude can generally be explained by means of the empirical scaling laws derived from the direct wave near the explosion."

*van Hulsteyn* (1964, 1965a and 1965b) considers the form of the atmospheric pressure wave observed at a large distance from a low altitude nuclear explosion that would be received by an observer located on the ground. The basic method of approach is quite similar to that of *Weston* (1961 & 1962) but differs in that an isothermal atmosphere is assumed and only the gravity wave mode is retained. In addition, the source modeling is different although the same source function as that given in Eq. (5.13) is utilized. In *Weston* (1962), a surface  $S_0$  is taken to surround the source location and to be of radius  $R_0$  sufficiently large so that the pressure field is acoustic or of finite amplitude. It is assumed that the pressure field is specified on  $S_0$  and that the linear equations of hydrodynamics hold outside of this surface. *Weston* (1962) developed an equivalent source at  $R=0$  which yields the desired pressure field on  $S_0$  and, in the process, the surface is shrunk to zero radius. *van Hulsteyn* (1964) simply specifies the field on  $S_0$  and treats the problem utilizing a form of Huygen's principle.

For the source function, *van Hulsteyn* (1965b) utilizes the approximate expression "obtained by *Brode* (1956) and used by *Weston* (1962)" and which agrees with *Glasstone* (1962) given by

$$p(R, t) = p_1 \frac{R_0}{R} \left[ 1 + \frac{R - c_0 t}{\alpha L} \right] \exp\left(\frac{R - c_0 t}{\alpha L}\right) \text{ for } R < R_0 \text{ and } T > \frac{R_0}{c_0} \quad (5.27)$$

$$= 0 \text{ otherwise}$$



where in the above  $R_0$  is the radius of a sphere surrounding the explosion,  $p_1$  is the peak overpressure on  $S_0$ ,  $\alpha$  is a scaling factor characteristic of the explosion, and  $L$  is "the dimensionless length of the positive phase" and  $T$  is the time duration of the positive phase.

The formal expression for the pressure field derived by *van Hulsteyn* (1965b) is given by

$$p(a,t) = 7.2797 \frac{\delta \epsilon}{(\sin \theta)^{1/2}} I(t) H(t) \mu\text{bars} \quad (5.28)$$

where in the above  $p(a,t)$  is the pressure field for a receiver on the ground,  $t$  is the time since the detonation of the explosion,  $\epsilon$  is the explosive yield in kilotons,  $\delta$  is the fraction of yield that goes into the atmospheric pressure disturbance,  $\theta$  is the angular separation of the source and receiver,  $H(t)$  is the Heaviside step function and  $I(t)$  is the integral expression given by

$$I(t) = \frac{1}{\pi} \int_0^{\omega_c} d\omega \frac{(1 + \frac{\beta^2 T^2 \omega^2}{3} + \frac{\beta^4 T^4 \omega^4}{9})^{1/2}}{(1 + T^2 \omega^2)} \cos[\omega \tau - \psi(\beta, \alpha) + \frac{\pi}{4}] \quad (5.29)$$

where in the above  $\beta = (R_0/c_0 T)$ ,  $\alpha = (T/c_0 L)$ ,  $\psi(\beta, \alpha)$  is a known function of  $\alpha$  and  $\beta$ ,  $T$  is the ,  $\tau$  is the observer's time ( $=t-t_a$  where  $t_a$  is the total time for the pulse to reach the observer),  $c_0$  is the speed of sound and  $\omega_c$  is the cut-off frequency.

Estimates the parameters  $R_0$ ,  $T$  and  $\beta$  were obtained from tables presented in *Glasstone* (1962) [pps 135 and 143] and values of  $\delta \epsilon$  from the waveform data presented by *Rose, Oksman and Kataja* (1961), *Araskog, Ericsson and Wagner* (1961) and *Wexler and Hass* (1962). Through the calculation of synthetic barograms for 1 KT and 15 MT explosions, *van Hulsteyn* (1965b) concludes that "the period of the gravity wave is unaffected by the yield of the explosion." Figure 96 reproduces the synthetic waveform for a 1 KT explosion at various ranges from the explosion for a receiver located on the ground.

*Pierce* (1965) extended the theories of *Weston and van Hulsteyn* (1962) and *Pridmore-Brown* (1962) to the propagation of infrasonic waves from a point source having an arbitrary time variation,  $f(t)$ , and for an atmosphere having arbitrary temperature and wind speed profiles with height but uniform in one direction. The basic method of

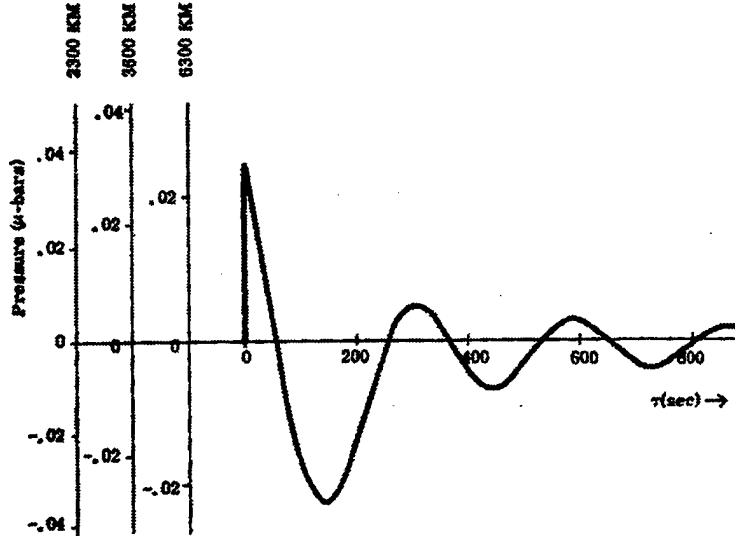


Figure 96. A synthetic pressure pulse as a function of time for receivers located at distances of 2300, 3600 and 6300 km from a 1 KT explosion. A low altitude air burst corresponding to  $\delta=0.5$  has been assumed. [Figure adopted from *van Hulsteyn* (1965b).]

approach was that adopted by *Pridmore-Brown* (1962) in which the fundamental equations of hydrodynamics are linearized and then Fourier transformed and combined to produce a linear second-order differential equation for the Green's function of the pressure field.

The essential expression derived for the pressure field is given by

$$p(r, t) = \sqrt{\frac{\rho_0(z)}{\rho_0(z_0)}} \int_{-\infty}^{+\infty} d\omega e^{-i\omega t} g(\omega) P(r, \omega) \quad (5.30)$$

where  $\rho_0(z)$  is the density of the unperturbed atmosphere at the observation point,  $\rho_0(z_0)$  is the density of the unperturbed atmosphere at the source height,  $z_0$ ,  $g(\omega)$  is the Fourier transform of the source time function,  $f(t)$  and  $P(r, \omega)$  is defined as

$$P(r, \omega) = \iint d^2k e^{ik \cdot (r - r_0)} Z(z, z_0, \omega, k) \quad (5.31)$$

where  $Z(z, z_0, \omega, k)$  is an auxilliary or Green's function which satisfies causality and the boundary conditions of the problem: e.g., the vertical component of particle velocity vanishes at the ground. In the above,  $\omega$  is the angular frequency,  $r$  is the vector observation coordinate and  $r_0$  is the source location.

Given the above representations, *Pierce* (1965) develops a normal mode decomposition of the form

$$P(r, \omega) = \sum_{n=1} A_n(\omega, \theta) R_T^{-1/2} e^{i\beta_n(\omega, \theta) R_T} \quad (5.32)$$

where in the above  $R_T$  is the magnitude of the horizontal (or ground) projection of  $\mathbf{r}-\mathbf{r}_0$ ,  $\theta$  is the angle between the propagation direction,  $A_n(\omega, \theta)$  is the modal amplitude,  $\beta_n(\omega, \theta)$  is the modal phase and the summation is over the normal modes.

*Pierce* (1965) shows how to obtain expressions for the group velocity of the normal modes and demonstrates that the effective horizontal group velocity for a given mode depends on the direction of propagation and is not necessarily in the same direction as the horizontal wavevector. In addition, a number of integral theorems are derived, one of which is utilized to develop a perturbation theory for computing the effects of wind on dispersion for an isothermal atmosphere and which utilizes the eigenfunctions computed in a model which does not include the effects of winds.

*Meecham* (1965) developed a simplified normal mode method for modeling propagation of long period acoustic-gravity waves. The focus of the work was on an investigation of the effects of geometric dispersion as opposed to geometric spreading and the method of approach was based, in part, on the phase and group velocity results obtained by *Pfeffer and Zarichny* (1963) and the modeling results of *Harkrider* (1964).

In modeling atmospheric propagation, it was found convenient to consider a received pulse as being composed of three parts: "low-frequency gravity wave modes, intermediate [period] signals and acoustic signals." It was argued that modal solutions are applicable for the gravity wave and intermediate period contributions but that ray theory is probably more applicable to the higher frequency parts of the signals due to the large number of modes which must be summed to synthesize a waveform. Stationary phase methods were used to derive explicit pressure formulae for single mode gravity wave and intermediate period waveforms. In addition, it was found that dispersion generally "causes a reduction in signal amplitude proportional to the square root of the range, regardless of the portion of the signal considered. This is in addition to the reduction due to simple geometric spreading. The additional range dependence is sufficient to give the observed reduction in signal level over that expected from ordinary cylindrical spreading."

In a sequel, *Meecham* (1966) discussed the propagation of intermediate- (periods ~ one minute) and short-period (periods less than one minute) infrasound from nuclear explosions in an attempt to understand the duration of the observed signals in both period ranges. Utilizing known meteorological data and simple ray theory calculations it was argued that in the intermediate period range, the signal duration is enhanced by large scale weather fronts which, through horizontal refraction, serves to increase signal duration. For the propagation of short periods, it was argued that increased signal duration is caused by upper atmosphere wind ducts which lead to ray splitting and a multiple pulse arrival structure.

In a paper published in 1965, *Hines* (1965) questioned the use of isothermal layers to model acoustic propagation in a realistic atmosphere as was done, for example, in the work of *Pfeffer and Zarichny* (1962) and *Press and Harkrider* (1962). *Hines's* (1965) concerns were based on the observation that the differential equations derived to describe propagation involved coefficients dependent on derivatives of the atmospheric scale height with respect to altitude. One year later, *Pierce* (1966a) provided a rigorous justification for the use of isothermal layers by reformulating the problem in terms of two coupled first order differential equations whose coefficients were explicitly independent of derivatives of scale height or, equivalently, on sound speed as a function of altitude.

*Balachandran* (1968) studied the propagation of free acoustic-gravity waves in a temperature and wind stratified atmosphere using a method of approach which can be considered an extension to that used by *Pfeffer* (1962). Thus, the atmosphere is divided into a number of homogeneous horizontal layers in which the temperature and wind speed are taken as constants. The linearized hydrodynamic equations are developed for the pressure and particle velocity and the *Thomson* (1950) and *Haskell* (1953) matrix approach is used to obtain solutions for the fields and for the group and phase velocity dispersion curves.

The goal of the work was to determine if winds could provide an explanation of the inverse dispersion (group velocity decreasing with increasing period) reported by *Donn and Ewing* (1962). In the modeling, the COSPAR standard atmosphere was employed along with various models of wind profiles and it was demonstrated that winds are indeed capable of explaining the inverse dispersion and, in particular, that winds of the order of 100 m/s at an altitude of 100 km are required to account for inverse dispersion in the period range extending from 5 min (300 s) to 15 min (1500s). Figure 97 shows the modes which are needed to explain the measured dispersion curve for a Soviet nuclear test conducted on August 5, 1962. As indicated, the fundamental and first two gravity waves are required.

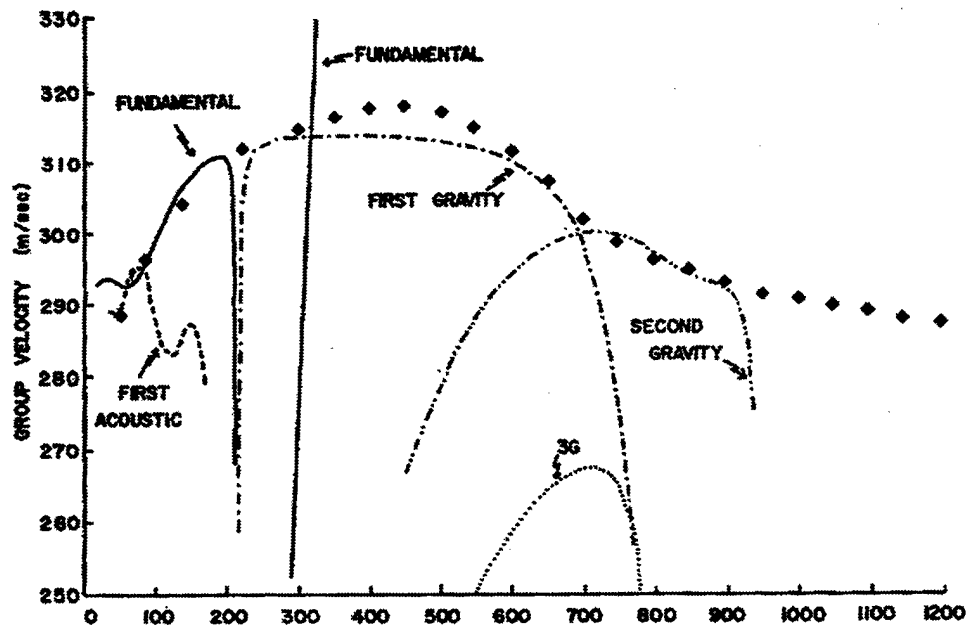


Figure 97. The fundamental and first two gravity wave modes required to explain the group velocity curve measured from the Soviet atmospheric nuclear test conducted on August 5, 1962. [Figure adopted from *Balachandran* (1968).]

*Cole and Greifinger* (1968a and 1968b) studied the propagation of acoustic-gravity waves in an isothermal atmosphere with the neglect of winds. The problem of interest was the calculation of the received pressure waveform at ionospheric heights created by a nuclear explosion, modeled as an instantaneous point energy source, on the ground.

The basic method of approach was to linearize the fundamental hydrodynamic equations by expanding the pressure, density and velocity fields in terms of a small parameter defined as

$$\varepsilon = \frac{(\gamma-1)Q_0}{P^* h^3} \quad (5.33)$$

where  $Q_0$  is the energy released by the explosion,  $P^*$  is the ambient pressure on the ground and  $h$  is the atmospheric scale height. For sea level explosions where  $h \sim 10$  km,  $\varepsilon \sim 1.5 \times 10^{-5} Y$ , where  $Y$  is the hydrodynamic yield in KT. Accordingly,  $\varepsilon \ll 1$  for explosions up to a few MT's: e.g., for a 1 MT explosion,  $\varepsilon = 0.01$ .

Given a linearization of the basic hydrodynamic equations, the problem is solved starting from a formal integral representation of the field of the form,

$$p(r,t) = e^{z/2} \frac{1}{\pi} \int_0^\infty dk k J_0(kr) F(k;z,t) \quad (5.34)$$

where  $F(k;z,t)$  can be thought of as a Green's function, and utilizing two asymptotic or stationary phase approximations. The evaluation leads to three contributions to the received pressure field at an arbitrary point in the medium: a non-oscillatory cylindrical "ground wave" ( $P_{GR}$ ) and dispersive acoustic-gravity (or low frequency) ( $P_{AG}$ ) and acoustic (or high frequency) ( $P_A$ ) waves which vanish for a receiver located on the ground. The ground wave field is found to have the particularly simple form:

$$P_{GR}(r,z,t) = -\frac{1}{2\pi} \frac{(2-\gamma)}{\gamma} e^{\frac{(\gamma-1)}{\gamma} z} \frac{t}{(t^2 - r^2)^{3/2}} \quad (5.35)$$

where  $r$  is the source-to-receiver range,  $t$  is the time and  $z$  is the height above the ground plane.

At ionospheric heights, only the dispersive acoustic and acoustic-gravity wave phases contribute to the received pressure waveform and it turns out that the high frequency acoustic waves arrive before the acoustic gravity waves: a circumstance which is not the case for receivers at lower altitudes. Figure 98 shows computed waveforms as a function of ionospheric height above the earth's surface for an assumed scale height of 8 km and a

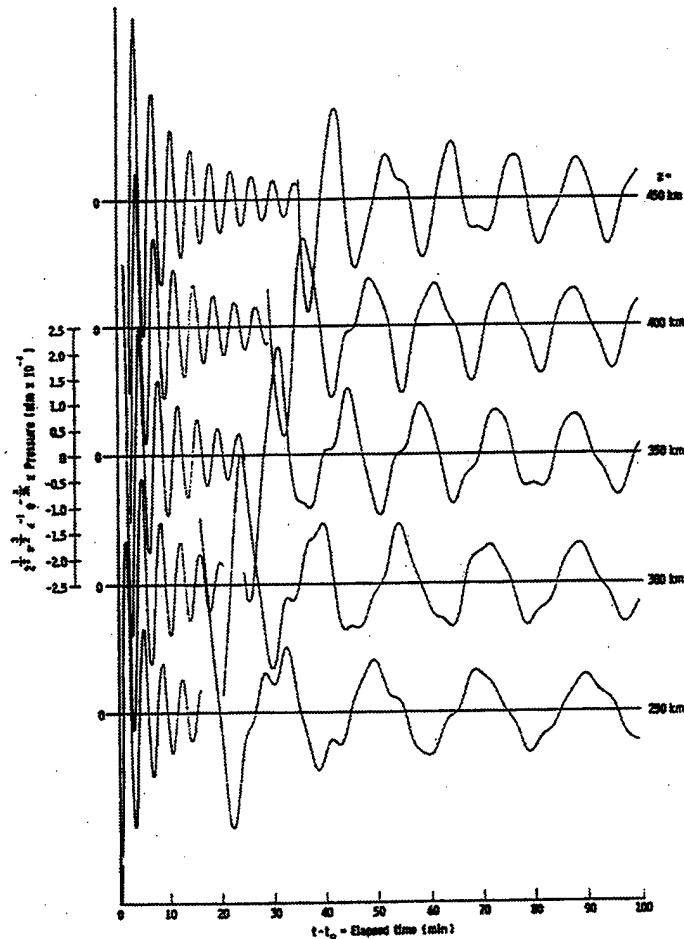


Figure 98. Computed pulse responses for an isothermal atmosphere for an instantaneous point source on the ground. The source to-receiver-range is 1000 km and the assumed scale height for the atmosphere is 8 km. [Figure adopted from *Cole and Greifinger (1968b)*.]

source-to-receiver range of 1000 km. As indicated, the acoustic signals arrive before the lower frequency acoustic-gravity waves.

*MacKINNON* (1968) considered the effects of winds on acoustic-gravity wave propagation from explosions in the atmosphere utilizing a normal mode approach quite similar to *Pierce* (1965) differing primarily "in the order of integration" and for the specific model atmosphere shown in Figure 99.

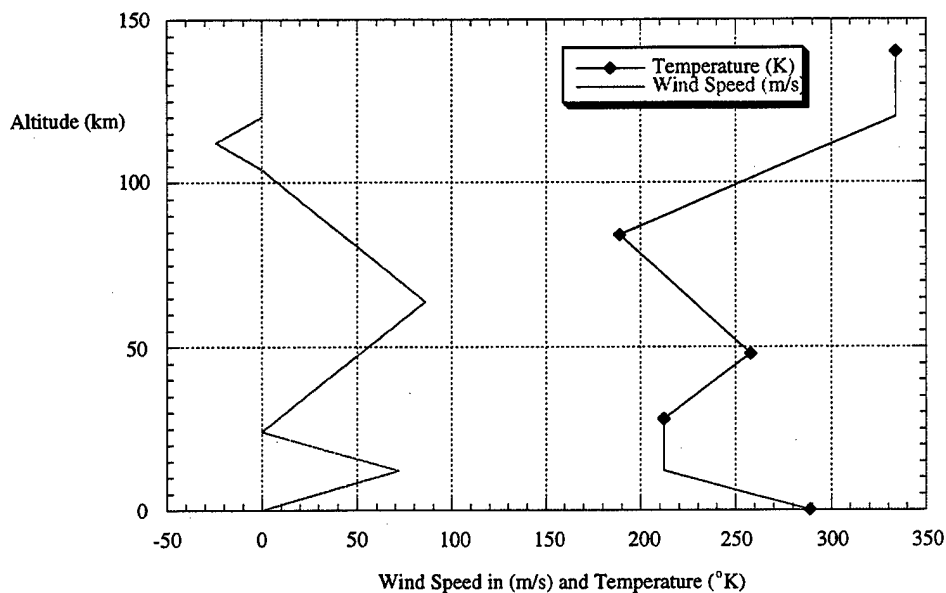


Figure 99. The model atmosphere considered by *MacKINNON* (1968). The curve on the left-hand side provides the assumed wind speed profile and the curve on the right-hand side provides the assumed temperature profile. Both parameters are taken as constants above an altitude of 120 km.

Given the model atmosphere, calculations of group velocity dispersion curves and waveforms were made assuming contributions from the fundamental, first gravity wave and the first five acoustic modes. The modeling utilized the source function of *Hunt, Palmer and Penney* (1960) appropriate for a nuclear explosion having a yield of 2.5 MT and detonated at an altitude of 7 km.

Among the primary findings of work were that: "The action of the wind is to suppress the higher order acoustic modes in the upwind direction and enhance them in the downwind direction. With regards to amplitude, the opposite is true of the first gravity mode. Both normal and inverse dispersion are present at short as well as at long periods" [*MacKINNON* (1968)].

Figure 100 shows the very pronounced effect that the wind has on the group velocity dispersion properties of the first, second, third and fourth acoustic modes. The effect on direction of propagation is seen to effect not only the group speeds but, in the case



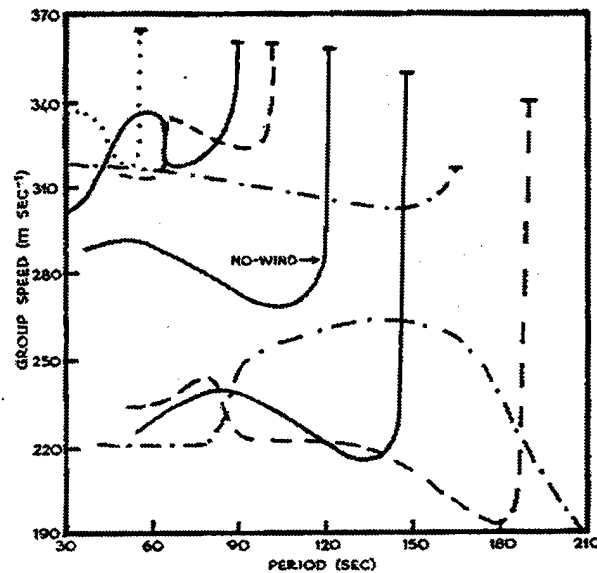


Figure 100. Computed acoustic group velocity curves for the model atmosphere. The notation is: ..... first mode, - - - - second mode, ——— third mode and ····· fourth mode. The upper curves correspond to downwind propagation and the lower curves to upwind propagation. [Figure adopted from *MacKINNON* (1968).]

of the first mode, to change the entire behavior of the group velocity as a function of period. In addition, it is seen that the fourth acoustic mode is entirely suppressed in the upwind direction. The low frequency cut-offs of the individual modes are indicated by the small horizontal lines at the end of the vertical segments of the dispersion curves.

Figure 101 illustrates the dispersion characteristics of the third acoustic mode at a source-to-receiver distance of 4 km for propagation downwind and in a wind-less atmosphere. As indicated, there is both normal and inverse dispersion and the amplitude of the mode for propagation in the downwind direction is significantly enhanced over that for propagation in a wind-less atmosphere. As noted by *MacKINNON* (1968), the fact that modes are suppressed in upwind propagation implies that the total waveforms should be simpler for upwind propagation than downwind propagation because less modes will be effective. Such a circumstance does indeed seem to be the case as a careful inspection, for

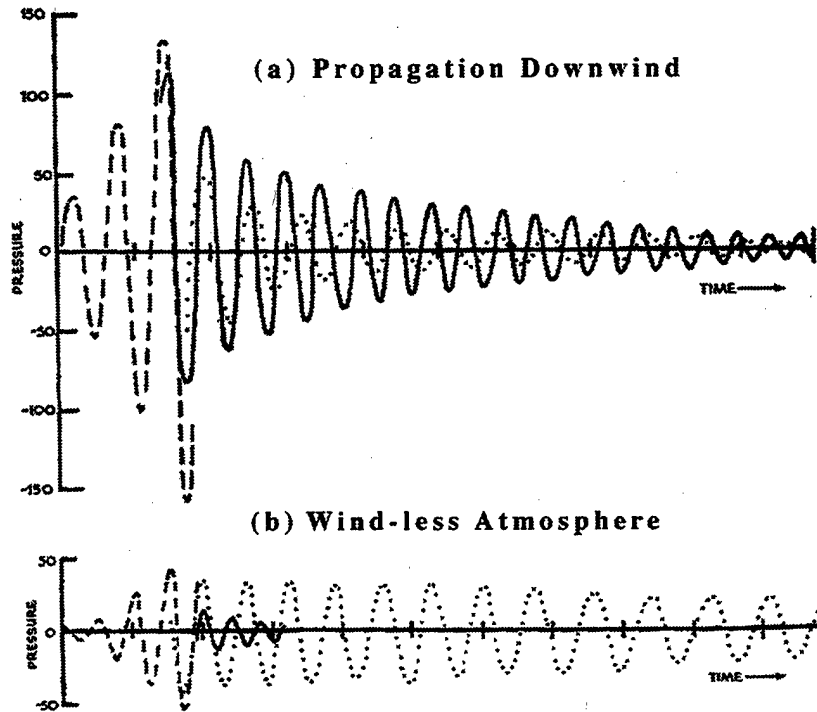


Figure 101. The dispersion characteristics of the third acoustic mode at a source-to-receiver range of 4 km corresponding to propagation downwind and in a wind-less atmosphere. The notation is: - - - - Airy phase, ——— normal dispersion, ····· inverse dispersion. The units of pressure are arbitrary and the time intervals, indicated by the tick marks are separated by 100 s. [Figure adopted from MacKINNON (1968).]

example, of the data of Yamamoto (1957), Donn, Pfeffer and Ewing (1963) and Wexler and Hass (1962) indicates.

In a sequel to Balachandran (1968), which explained the inverse dispersion observed by Donn and Shaw (1967) and Donn, Pfeffer and Ewing (1963) as being due to strong high-altitude winds in the direction of wave propagation, Balachandran (1969) reported the results of more detailed modeling on how winds effect phase and group velocity dispersion curves utilizing the COSPAR 1961 International Reference Atmosphere. Although some modeling was conducted utilizing a 52 km model atmosphere having only a lower atmospheric sound channel, most of the modeling involved the assumption of an atmospheric model 300 km in height which had two sound channels. The boundary condition at the top of the model was taken to be an isothermal semi-infinite half-space having a temperature equal to that of the reference atmosphere at an altitude of 300

km. In the upper half space, the winds were specified to be in the negative direction to allow the computation of dispersion curves to longer periods: i.e., to shift the low frequency or long period modal cutoff to higher values.

The results of the modeling demonstrated that winds close to the ground primarily effect waves having periods less than 400 s, whereas waves having periods longer than 400 s are influenced by both low and high altitude (~100 km) winds. At long periods, inverse dispersion is produced by high altitude winds blowing in the direction of wave propagation and by low altitude winds blowing in a direction opposite to that of wave propagation. Normal dispersion, however, is produced by opposite wind conditions: i.e., when upper atmospheric winds are in the direction opposite to that of wave propagation and when lower atmospheric winds are in the same direction as that of wave propagation.

In addition to studying the effect of wind on phase and group velocity dispersion curves, *Balachandran* (1969) computed vertical profiles of pressure, vertical velocity and kinetic energy density for model atmospheres and used the results, in conjunction with the dispersion curves, to support the conclusions of *Pfeffer and Zarichny* (1963) that the quasi-horizontal portions of the dispersion curves are those portions most relevant to the observation of acoustic-gravity waves by sensors located on the ground.

*Pierce, Posey and Iliff* (1971) reported on a new formulation for the synthesis of theoretical waveforms produced by nuclear explosions. The methodology, valid for pulse propagation in homogeneous but otherwise arbitrarily vertically stratified temperature and wind dependent atmospheres, was used to investigate the effects of wind and wind direction on pulse shape and to quantify the effect of energy yield and height of burst on the pressure waveform received by a microbarograph located at large source-to-receiver ranges. Of particular note in the paper is the very careful attention which was given to source modeling which resulted in a final choice of an energy source time function given by

$$f_E(t) = \frac{1}{4\pi}(\gamma-1)K\left(\frac{E}{c^2}\right)\left(\frac{t}{T_Y^2}\right)e^{-t/T_Y} U(t) \quad (5.36)$$

where  $\gamma$  is the ratio of the specific heats of air,  $K$  is a dimensionless constant,  $E$  is the total energy release in the explosion,  $c$  is the local speed of sound,  $t$  is the time measured from detonation,  $U(t)$  is the Heaviside step function and  $T_Y$  is a characteristic time given by

$$T_Y = \left( \frac{p_{\text{ref}}}{p_o} \right)^{1/3} \left( \frac{c_{\text{ref}}}{c} \right) Y_{\text{KT}}^{1/3} t_{\text{ref}} \quad (5.37)$$

where  $p_{\text{ref}}$  is reference pressure ( $=1$  atm),  $c_{\text{ref}}$  is a reference sound speed ( $= 331$  m/s),  $t_{\text{ref}}$  is the time duration of the blast wave at a reference distance of one mile from an explosion having a yield of 1 KT and where  $Y_{\text{KT}}$  is the ratio of the explosive energy to a reference energy of  $4.2 \times 10^{19}$  ergs.

In the theoretical formulation and notation of *Pierce, Posey and Iliff* (1971), the far-field pressure pulse or waveform is represented by a summation of guided modes as indicated in Eq. (5.38)

$$p(r, z, z_o, t) = \sum_n p_n(r, z, z_o, t) \quad (5.38)$$

where  $r$  is the source-to-receiver range,  $z$  is the receiver height,  $z_o$  is the source height and  $t$  is the time for the signal to propagate from the source to the receiver.

For the direct arrival modes,  $p_n$  is given by

$$p_n(r, z, z_o, t) = \alpha K E \left( \frac{\rho_o(z)}{\rho_o(z_o)} \right)^{1/2} \Psi_n(r, z, z_o, t) \quad (5.39)$$

where  $\alpha$  is a factor which accounts for spreading loss over a spherical surface and is given by

$$\alpha = (\gamma - 1)(2\pi)^{-3/2} [r_e \sin(r / r_e)]^{-1/2}, \quad (5.40)$$

where  $r$  and  $\gamma$  have been defined previously,  $r_e$  is the radius of the earth,  $K$  is a constant ( $\sim 0.5$ ),  $E$  is the total energy released by the explosion,  $\rho_o$  is the ambient density and  $\Psi_n$  is given by

$$\Psi_n(r, z, z_o, t) = \int d\omega k_n^{1/2} S(\omega, T_Y) M_n(\omega, z, z_o) \cos\{\omega t - k_n r + \phi\}. \quad (5.41)$$

In the above,  $k_n(\omega)$  is the horizontal wave number of the n-th guided mode,  $S(\omega, T_Y)$  is proportional to the Fourier transform of the energy source function defined in Eq. (5.36),

$$S(\omega, T_Y) = [1 + (\omega T_Y)^2]^{-1} \quad (5.42)$$

and where the phase,  $\phi$ , is determined by the characteristic time and frequency as

$$\phi = (\pi/4) = -2 \tan^{-1}(\omega T_Y). \quad (5.43)$$

The quantity  $M_n$  is a function of the sound and wind speed profiles assumed for a particular problem and, neglecting the subscript n for notational simplicity, is given by

$$M_n = \left( \frac{-[Z(z_0) + gY(z_0)]Z(z)}{2\Omega(z_0)c^2(z_0)I} \right) \quad (5.44)$$

where  $\Omega = \omega - \mathbf{k} \cdot \mathbf{v}$  is the Doppler shifted frequency, and the integral I is given by

$$I = \int_0^\infty dz \left\{ \Omega \left( \frac{\mathbf{k} \cdot \mathbf{v}}{k} \right) Y^2 + \omega k \Omega^{-3} Z^2 \right\}. \quad (5.45)$$

The functions Y and Z are found to satisfy the equations

$$Y(z) = \Phi_1(z) / c(z) \quad (5.46)$$

and

$$Z(z) = g \frac{\Phi_1(z)}{c(z)} - c(z) \Phi_2(z) \quad (5.47)$$

where the functions  $\Phi_1$  and  $\Phi_2$  satisfy the system of linear, first order and coupled differential equations given by

$$\frac{d\Phi_1(z)}{dz} = A_{11}\Phi_1(z) + A_{12}\Phi_2(z) \quad (5.48)$$

and by

$$\frac{d\Phi_2(z)}{dz} = A_{21}\Phi_1(z) + A_{22}\Phi_2(z) \quad (5.49)$$

where, in Eqs. (5.48) and (5.49), the coefficients are given by

$$A_{11} = \frac{gk^2}{\Omega^2} - \frac{\gamma g}{2c^2}, \quad (5.50)$$

$$A_{12} = 1 - \frac{c^2 k^2}{\Omega^2}, \quad (5.51)$$

and

$$A_{21} = \frac{g^2 k^2}{\Omega^2 c^2} - \frac{\Omega^2}{c^2} \quad (5.52)$$

with  $A_{22} = -A_{11}$ .

The eigenvalues for the problem are determined by requiring that  $\Phi_1$ , which physically represents the vertical particle velocity, vanish at the ground,  $z=0$ , and that both the functions  $\Phi_1$  and  $\Phi_2$  vanish fast enough as  $z \rightarrow \infty$  so that the integral in Eq. (5.45) is convergent. The magnitude of  $k$  which satisfies these conditions is then taken as the horizontal wavenumber for the  $n$ -th guided mode. In actual implementation, the phase, group and propagation directions of each of the  $n$ -modes are determined by finding the zeros of a normal-mode dispersion function,  $F(\omega, k)$  which is constructed from a functional of the  $A_{ij}$ 's [*Pierce* (1967)].

As noted by *Pierce, Posey and Iliff* (1971), formulating the problem as described above yields continuous solutions  $Y(z)$  and  $Z(z)$  even though the sound speed,  $c(z)$ , and wind speed,  $V(z)$ , profiles may have discontinuities. In addition, approximating a continuously stratified atmosphere by a large but finite number of constant wind and sound speed layers, has been rigorously justified [*Pierce* (1966)].

Utilizing the full-wave synthetic barogram model, *Pierce, Posey and Iliff* (1971) used it to investigate the behavior of the pressure amplitude observed by a ground based sensor as a function of explosive yield and height of burst with the results obtained shown in Figure 102. As indicated from inspection of the figure, the pressure amplitude is predicted to be a nonlinear function of the burst height and the magnitude of the variation of the nonlinearity is seen to increase with decreasing yield. The study and quantification of such behavior in any yield range is mathematically intractable and requires the use of a robust and computationally efficient propagation model.

The results presented in Figure 102 corrected previous estimates of height of burst effects. In particular, *Scorer* (1950), *Hunt, Palmer and Penney* (1960) concluded that the earliest part of the pulse received at long range ( $\sim 2,000$  km) should have an amplitude

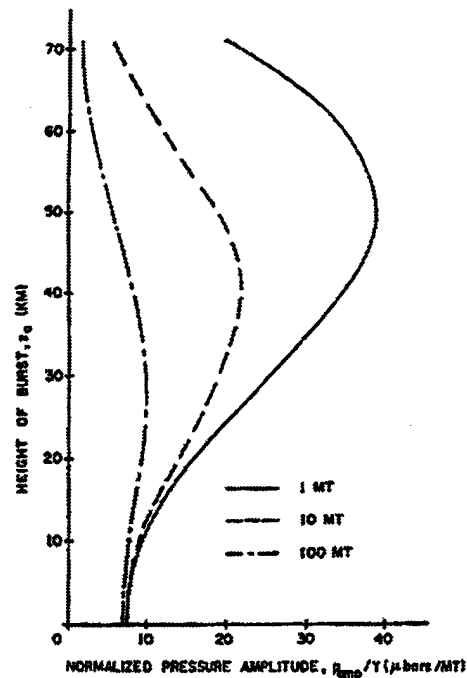


Figure 102. The dependence on height of burst for the pressure amplitude observed on the ground for 1 MT, 10 MT and 100 MT explosions. The source-to-receiver range is 10,000 km. [Figure adopted from *Pierce, Posey and Iliff* (1971).]

which is proportional to the energy yield of the explosion: a circumstance noted earlier by *Pierce* (1968). The results of *Harkrider* (1964), on the other hand, predicted an amplitude scaling of  $Y^{0.6}$  for explosions having yields above 5 MT and *Weston* (1962) predicted that the amplitude of the arriving pulse decreases drastically as the height of the explosion increases, whereas *Harkrider* (1954) found that there was only a 20% amplitude decrease in the altitude range extending from 2 km to 17 km. The essential findings of *Pierce, et al.*, (1971) are that the amplitude of the pulse is proportional to the energy yield, but that the amplitudes increase with increasing burst height up to an altitude of 40 km and then decrease thereafter as indicated in Figure 102. For completeness, Figure 103 shows synthetic waveforms computed for a ground-level 1 MT explosion, at a source-to-receiver range of 10,000 km, for three separate burst heights: 0 km, 50 km and 70 km. Inspection of the figure clearly shows that the explosion detonated at an altitude of 50 km produces the largest pressure amplitude and the figure illustrates the radically different characteristics of the waveforms as a function of altitude.

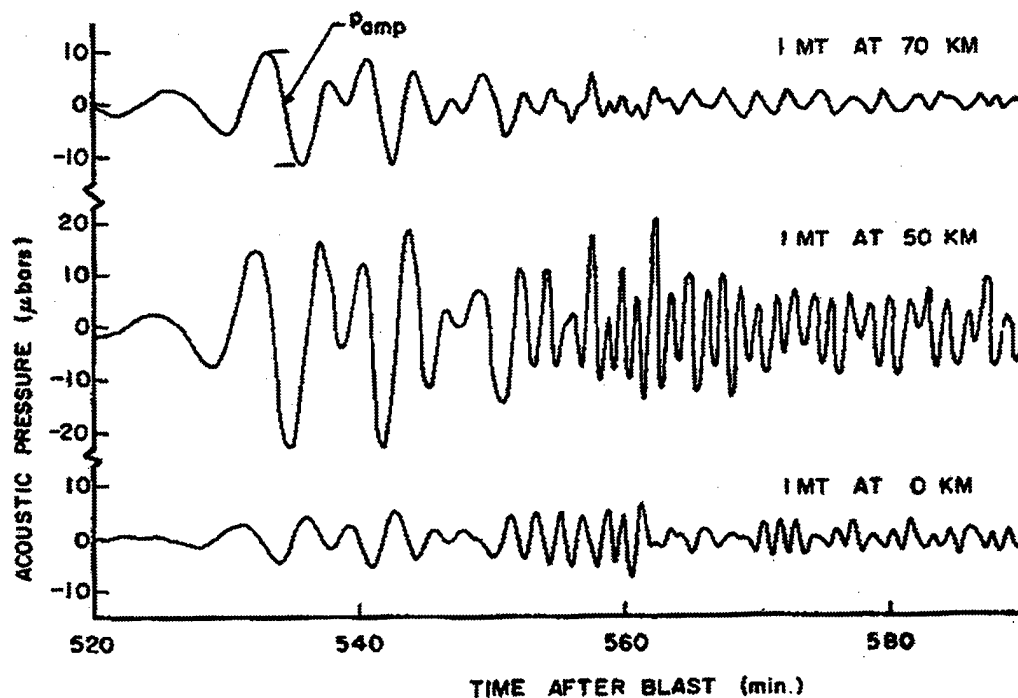


Figure 103. Synthetic barograms computed for a ground level 1 MT explosion appropriate to a source-to-receiver range of 10,000 km. The assumed atmospheric model corresponded to subtropical summer and the calculations were made at the three indicated altitudes. [Figure adopted from *Pierce, Posey and Iliff* (1971).

*Thomas and Craine* (1971) published the results of synthetic waveform modeling based on the methodology of *Pierce* (1966b) for incorporating the effects of winds on the individual modes contributing to the waveform. The modeling was accomplished utilizing a fully realistic atmosphere obtained by averaging meteorological data from a number of meteorological stations. The temperature data were extrapolated to an altitude 240 km utilizing the COSPAR reference atmosphere and the winds were set equal to zero above 66 km since data were evidently unavailable above this altitude. Figure 104 compares computed theoretical waveforms for two assumed point source models with that of a pressure pulse caused by a nuclear explosion on the Island of Mururoa and recorded at an infrasound station located at Moscow, Idaho. The range from the site of the explosion to the recording site was 7,930 km and the predominant winds were in the east-to-west direction. The top trace (a) is the measured waveform, whereas, the middle (b) and lower



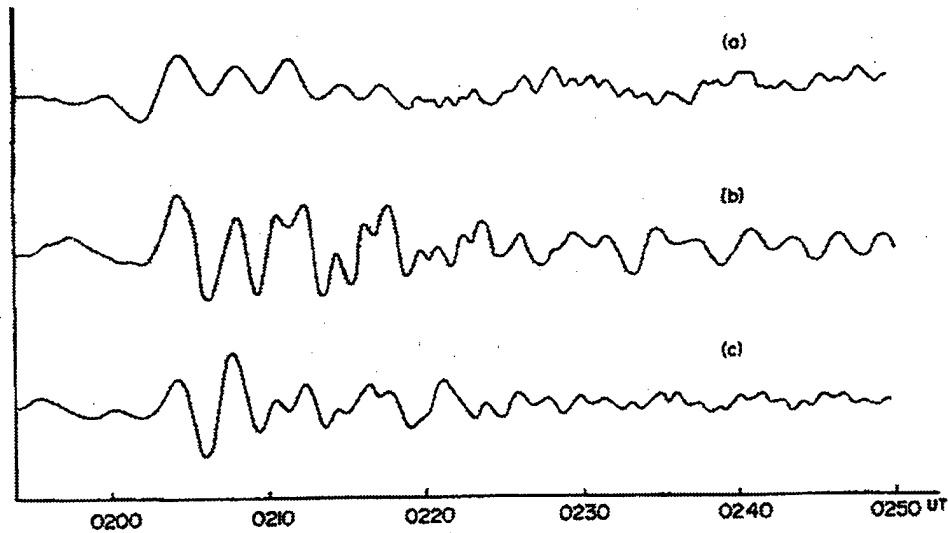


Figure 104. Theoretical and experimental waveforms appropriate to a nuclear explosion at Mururoa Island on September 9, 1968. The top trace (a) is the measured waveform recorded at Mururoa Island; the middle trace (b) is a synthetic modeled using a point source radiating equal energies into all frequencies; and (c) is a synthetic modeled using the point source function in equation (5.53). [Figure adopted from *Thomas and Craine* (1971)].

(c) waveforms are synthetics computed from a point impulsive source radiating equally into all frequencies and from a point source whose time function is taken to be of the form

$$f(t) = t \left( 1 - \frac{t}{2\tau} \right) \exp\left(-\frac{t}{\tau}\right). \quad (5.53)$$

with the parameter  $\tau$  set to 5.5 in order to give "the same zero-crossing time for a 1.5 MT explosion as experimentally observed." During the time of wave propagation from the source-to-receiver, the wind speed was observed to be a small fraction of the sound speed and the theoretical waveforms are seen to reproduce the first few low frequency cycles as observed experimentally but to lack the higher frequency content of the experimental record particularly at times after 0220 UT. In other modeling, it was shown that the variability of winds in an atmospheric model is sufficient to cause variability in the time signature of a synthetic waveform.

*Pierce and Posey* (1971) developed a theory for Lamb wave excitation by an atmospheric nuclear explosion and the subsequent propagation of the wave in a temperature- and wind-stratified atmosphere. The theoretical development was based on previous results obtained by *Bretherton* (1969) and *Garrett* (1969a and 1969b) for the

dispersion and phase velocity of the mode. As first noted by *Press and Harkrider* (1962), it is found that the Lamb mode is properly regarded as a composite mode in the sense indicated in Figure 105 which compares an approximate expression for the dispersion of the mode with predicted dispersion curves of guided gravity and acoustic modes as computed utilizing full wave synthetics [*Pierce, Posey and Iliff* (1971)].

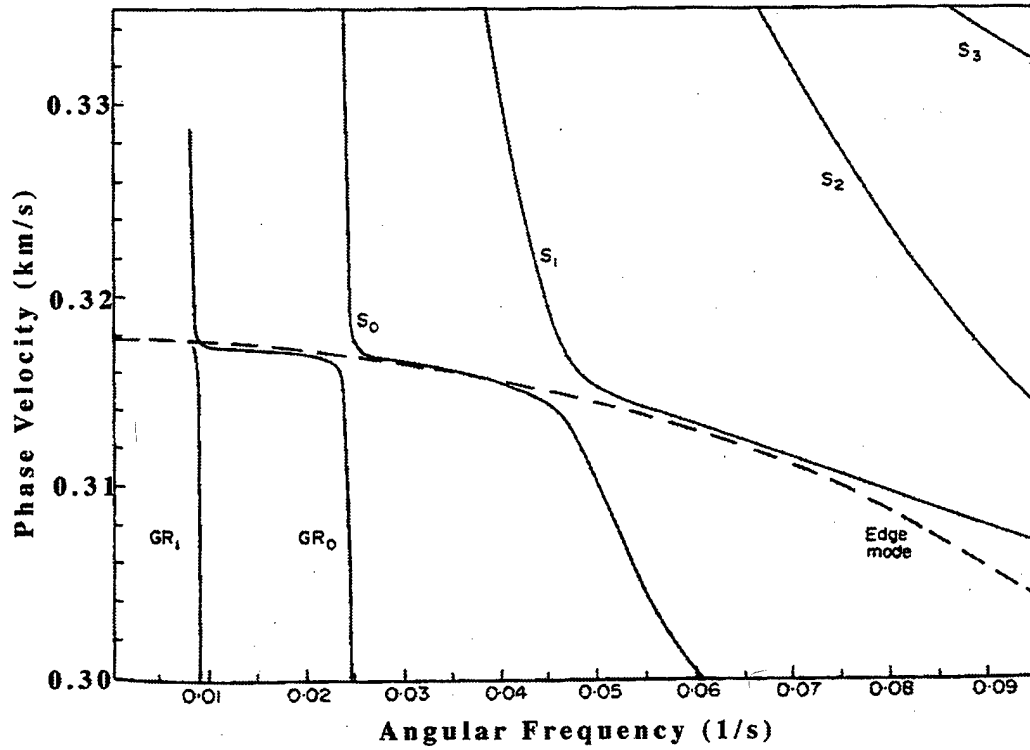


Figure 105. A comparison of an approximate edge mode dispersion curve (dashed line) with guided mode dispersion curves computed using a full wave synthetic barogram model [*Pierce, Posey and Iliff* (1971)].  $GR_0$  and  $GR_1$  denote the first two gravity wave modes and  $S_0$ ,  $S_1$ ,  $S_2$  and  $S_3$  are the first four acoustic modes. [Figure adopted from *Pierce and Posey* (1971).]

As indicated in the figure, the Lamb (or edge) wave dispersion curve is slowly varying over the indicated period range and can be approximately constructed from the horizontal portions of a number of gravity and acoustic wave modes.

At long source-to-receiver ranges, *Pierce and Posey* (1971) were able to develop a closed form expression for the pressure field given by

$$p(x,t) = \left[ \frac{DV(x,x_0)gE}{(c_{L0}T_Y)^{3/2}c_{L0}^2(db/d\theta)^{1/2}} \right] \psi(t,s,\theta) \quad (5.54)$$

where in the above  $D$  is a constant given by ( $K \sim 0.5$ )

$$D = \frac{K(\gamma-1)(2-\gamma)}{4\pi} \approx 0.013, \quad (5.55)$$

$V(\mathbf{x}, \mathbf{x}_0)$  is the dimensionless quantity

$$V(\mathbf{x}, \mathbf{x}_0) = \frac{\Lambda(\mathbf{x})\Lambda(\mathbf{x}_0)c_{L0}^{1/2}(c_L + v_{Lk})_0}{p(\mathbf{x}_0)c_L^{1/2}|c_L \mathbf{e}_k + \mathbf{v}_L|^{1/2}(c_L + v_{Lk})^{1/2}}, \quad (5.56)$$

$g$  is the acceleration due to gravity,  $E$  is the total energy released by the explosion,  $c_L$  is the local Lamb wave phase velocity,  $\mathbf{e}_k$  is a unit vector pointing in the propagation direction,  $v_{LK}$  is the projection of the mean or local wind speed,  $\mathbf{v}_L$ , in the direction of propagation,  $\mathbf{v}_L \cdot \mathbf{e}_k$ , the subscripted-o quantities denote evaluation at the source point and the quantity  $\Lambda(\mathbf{x})$  is given by

$$\Lambda(\mathbf{x}) = \frac{p_o^{1/\gamma}(\mathbf{x})}{p_o(\mathbf{x}_g)^{(1/\gamma-1/2)}} \quad (5.57)$$

where  $\mathbf{x}_0$  is the source location and  $\mathbf{x}_g$  (or  $\mathbf{x}_{0g}$ ) is the point on the ground directly below the observer (or source) and where  $db/d\theta$  is the "ray channel width per unit  $\theta$ ".

As an indication as to just how good the expression for the Lamb mode is, Figure 106 compares an observed waveform from a 10 MT explosion detonated 3 km above Johnson Island in the South Pacific with the predictions of Eq. (5.54) and with the predictions of full wave synthetics. Inspection of the figure shows that the synthetic waveforms are in excellent agreement through the first three cycles except for the earliest part of the records: i.e., in the time interval after blast extending from 285 min to approximately 292 min. In addition, the waveforms are seen to begin with a pressure rise which is supported by the data.

Near the end of their paper, *Pierce and Posey* (1971) noted several implications of the edge wave theory, representative examples of which include:

- The "first period",  $T_{1,2}$ , as measured by the time difference between the first and second peaks in the waveform, should generally increase with source-to-receiver range as  $r^{1/3}$ .

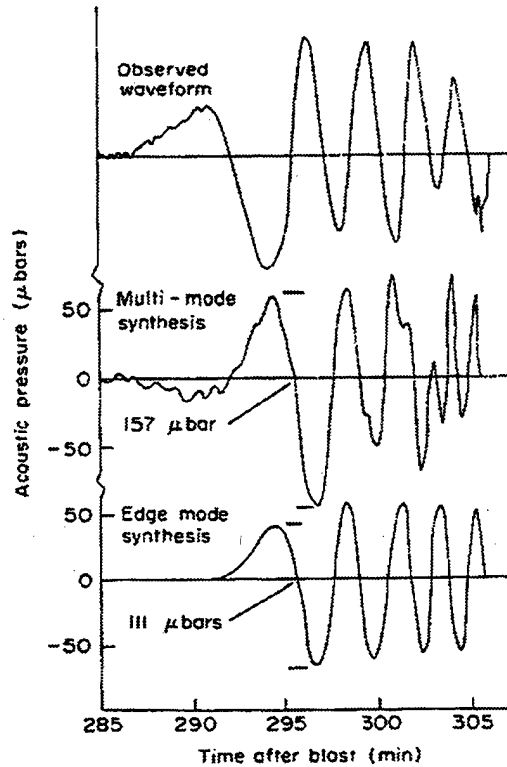


Figure 106. A comparison of an observed pressure waveform (top panel) with a synthetic waveform computed utilizing a full wave pulse propagation model (middle panel) [Pierce, Posey and Iliff (1971)] with that predicted by the edge wave model (lower panel) [Pierce and Posey (1971)]. The theoretical waveform was taken from Donn and Shaw (1967) and was reported to have an estimated peak-to-peak amplitude of 350  $\mu$ bar. The theoretical waveforms assumed an explosive yield of 10 MT. [Figure adopted from Pierce and Posey (1971).]

- The ratio of the first period,  $T_{1,2}$  to that of the "second period",  $T_{2,3}$ , as determined from the time difference between the second and third peaks, should be in the approximate ratio  $\sim 1.5$ .

- There turns out to be a particularly simple expression for estimating the energy release from a nuclear explosion which involves only the source-receiver range, radius of the earth, atmospheric scale height, speed of sound, the first period  $T_{1,2}$  and pressure amplitude of the first peak to trough in the waveform. The mathematical expression is presented in Eq. (7.2) of Section 7.0 where it is compared with data.

Greenfield and Harkrider (1971) derived an exact expression for the acoustic-gravity wave layer matrix and layer derivative matrices appropriate for incorporation into a

synthetic barogram model based on the *Thomson* (1950) and *Haskell* (1953) method for the case in which the sound speed in a layer is represented by a linear gradient rather than a constant. The work was motivated by the insight that the gradient formulation would reduce the number of layers required to represent the truly continuously varying temperature profile of the atmosphere. As noted by the authors, *Friedman and Crawford* (1968) and *Vincent* (1969) had "found that for certain combinations of phase velocity and period, hundreds of (isothermal) layers were needed to get 0.1 per cent accuracy in the layer matrix elements".

Once developed, *Greenfield and Harkrider* (1971) incorporated the gradient layer results into the previously developed computer models of *Press and Harkrider* (1962) and *Harkrider* (1964) and demonstrated that the new formulation was computationally efficient, to be the most useful in those atmospheric regions having a large temperature gradient and, in those situations, to require fewer layers than models utilizing constant sound speed layers.

*Pierce and Kinney* (1976) provide a summary report discussing the results of several papers authored by themselves and other co-workers and, in particular, include the Ph.D. thesis work of *Kinney* (1976) together with a complete listing of the computer program INFRASONIC WAVEFORMS which is used to numerically implement the propagation equations provided at a very high level in Eqs. (5.38) through (5.52).

The work of *Kinney* (1976) was primarily focused on developing methodologies to compute wave forms more accurately at both low and high frequencies. To improve modeling at low frequencies, a methodology for computing the imaginary parts of wave vectors associated with leaky modes was developed for the lowest order gravity-wave modes,  $GR_0$  and  $GR_1$ , and incorporated into the INFRASONIC WAVEFORMS program. To improve waveform modeling at high frequencies, an acoustic eigenray model was developed for a windless atmosphere in which the ambient pressure and density were taken to be constant and the sound speed profile was taken to be a continuous function of height.

The sound speed-altitude points were made continuous through the use of a cubic spline fit and the phase shifts occurring at caustics were explicitly included.

In addition to the foregoing, the problem in the correct ordering of normal modes was studied by utilizing the INFRASONIC WAVEFORM program to compute modal dispersion curves appropriate to the real atmosphere having two sound channels and numerical evaluations of the WKBJ phase integral relationship to compute dispersion curves appropriate to the upper and lower sound channels. As a result of the numerical calculations it was concluded that, for a receiver on the ground and sources below 50 km, it should be quite sufficient to compute and order the propagating modes using only the lower channel for frequencies above 0.2 rad/s, corresponding to a frequency of .032 Hz or a period of 72 s.

Finally, it is noted that *Pierce* (1990) has recently revisited the problem of wave propagation in fluids characterized by unsteady and inhomogeneous flow and has very carefully derived an approximate equation which may have applicability to problems in both atmospheric and underwater acoustics. By unsteady and inhomogeneous is meant flow in which the ambient background properties and flow are allowed to vary both spatially and temporally. In the absence of a source, the equation is given by

$$\frac{1}{\rho} \nabla \cdot (\rho \nabla \Phi) - D_t \left( \frac{1}{c^2} D_t \Phi \right) = 0, \quad (5.58)$$

where in the above  $\rho$  is the fluid density,  $\Phi$  is velocity potential,  $c$  is the sound speed and  $D_t$  is the derivative operator

$$D_t = \frac{\partial}{\partial t} + \mathbf{v} \cdot \nabla. \quad (5.59)$$

*Pierce* (1990) regards Eq. (5.58) as "a possible generalization of the fundamental acoustic wave equation".

## 6.0 NATURAL AND MAN MADE SOURCES OF INFRASOUND

This section reviews a number of the background noise sources which have the potential, under certain circumstances, to degrade the performance of infrasonic monitoring. In addition to the summary presented herein, reviews of various infrasonic sources have been presented by [Georges and Young, (1972) [sensing techniques, signal processing, microbaroms, earthquakes, auroral waves, volcanoes, meteorites, convective storms, sensor proximity to the jet stream, passing weather fronts and mountain associated waves]; Gossard and Hooke (1975) [mountain lee waves, auroral waves, severe weather, microbaroms, nuclear explosions, volcanoes]; McIntosh (1982) [Chinese 4MT explosion of 11/18/76, chemical explosion, satellite re-entry]; Kulichkov (1992) [auroras, microbaroms, sonic booms, thunderstorms, volcanic eruptions, explosions] and by Wilson, Olson and Spell (1995) [auroral infrasonic waves (AIWs), microbaroms, volcanic infrasound, earthquake infrasound and mountain associated waves (MAWs)].

### A. Aurora

The *AFGL Handbook of Geophysics and the Space Environment* (1985) describes the characteristics of the aurora as "the light resulting from the precipitation of electrons and protons from the magnetosphere into the earth's atmosphere. This light consists of atomic line spectra and molecular band spectra characteristic principally of oxygen and nitrogen, the chief constituents of the upper atmosphere ionized or excited by collisions with these precipitating particles. Associated with auroral precipitation and ionization, currents called auroral electrojet currents produce magnetic fields detectable at ground level by magnetometers and form the basis for magnetic indicators of auroral activity."

Chrzanowski, Greene, Lemmon and Young (1961) report the observation of propagating waves associated with high geomagnetic activity (or "magnetic substorms") as measured by the magnetic index  $K_p$  or auroral sources. The data were acquired on a four-element array of microbarographs located near Washington, D.C. and arranged in quadrilateral pattern of 7.5 km average spacing on a side.

Two types of infrasonic signals were reported. The first, referred to as acoustic waves, were found to occur when  $K_p$  rose to a value of approximately 5, to have periods extending from 20 s to 80 s, amplitudes ranging from 1  $\mu$ bar to 8  $\mu$ bar and to have trace velocities in the range of 552 m/s to 775 m/s indicating a source or disturbance at high altitude. The second type of waves were referred to as "slow travelling" and were characterized by periods in the range of 100 s to 300 s, trace velocities ranging from 10 m/s to 100 m/s and amplitudes up to 100  $\mu$ bars. The latter waves appeared to have propagation directions corresponding to the 500 mb winds over Washington, D.C.

In reporting their observations of auroral infrasound, *Campbell and Young* (1963) trace auroral acoustic effects back to 1770 [*Hearne* (1911)]. Early work in the area involved observations of high frequency audible sounds (hissing, crackling, etc.) and includes the work of *Jelstrup and Stormer* (1927); *Beals* (1933) and *Stormer* (1938). The early work served to establish that: periods of high visible auroral activity were necessary but not sufficient for the observation of the associated acoustic signals and that aurorally generated infrasound occurred when sunspot or solar activity was at its maximum.

*Campbell and Young* (1963) acquired their infrasound measurements utilizing two microphone arrays positioned within the auroral zone at Ft. Yukon, Alaska ( $66^{\circ}34'N$ ,  $145^{\circ}$ ,  $15'W$ ) and separated along a 2.37 km baseline oriented in a west-to-east direction. To measure geomagnetic and cosmic absorption activity associated with the production of infrasound, a magnetometer and riometer were located at College, Alaska ( $64^{\circ}52'N$ ,  $147^{\circ}50'W$ ) and a second riometer was positioned at Ft. Yukon. *Campbell and Young* (1963) observed that, in general, "whenever the incoherent noise of local winds was low, every night of bright visual aurora, or ionospheric evidence of aurora, was associated with 10- 110-sec (0.1 Hz to .009 Hz) period pressure oscillations of about 1- 10-dynes/cm<sup>2</sup> (1- 10  $\mu$ bar) amplitude. Correspondingly, nights of no auroral activity showed no infrasonics with the exception of a remarkable event of a unique type...". The event of unique type will



not be discussed herein except to note that its origin was ascribed to the presence of "turbulence events within the electrojet."

The signals associated with auroral activity were observed to propagate from east-to-west before midnight with the arrival of the waves preceding the measured increased geomagnetic levels on the magnetometer and riometer sensors. Following the midnight hours, the propagation of the infrasound signals was observed to be from the west-to-east, and the increased geomagnetic signals were observed to precede the acoustic arrivals. The first circumstance was noted to be "consistent with the westward progression of maximum aurora activity." An example of the aurora infra sound detected by the two microphone stations is provided in Figure 107.

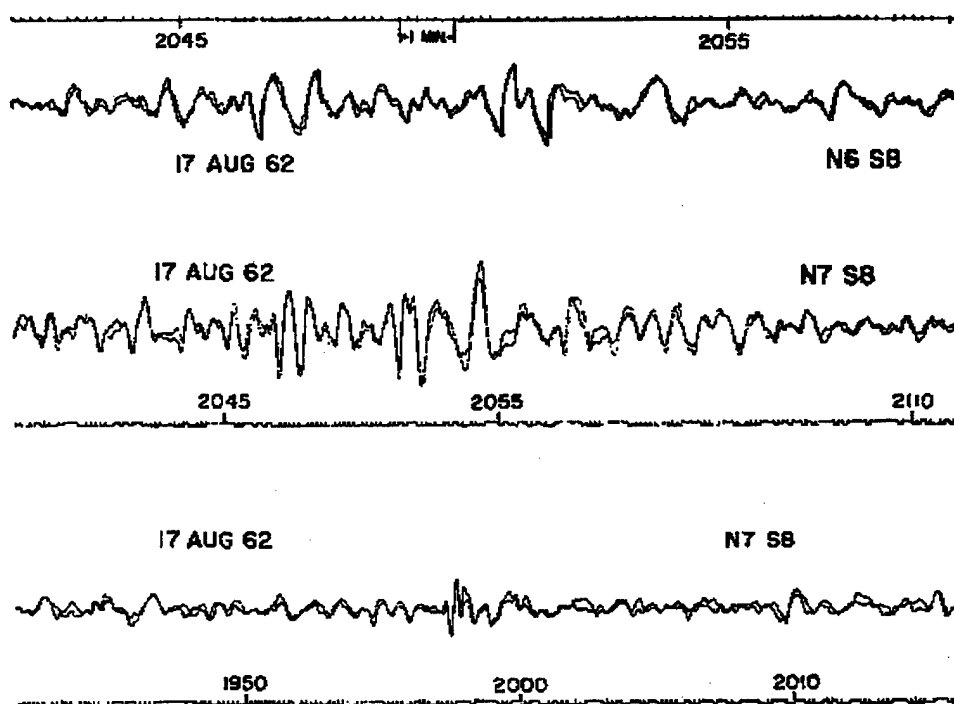


Figure 107. Examples of aurally produced infrasound. [Figure adopted from *Campbell and Young* (1963).]

*Campbell and Young* (1963) also cited the work of *Maeda and Watanabe* (1963) who estimated that a  $1 \text{ dyne/cm}^2$  (or  $1 \mu\text{bar}$ ) pressure level at the surface of the earth would require an ionospheric energy flux of approximately  $100 \text{ ergs/cm}^2$ . In attempting to

mechanisms: (1) periodic ionospheric heating by the bombarding particles responsible for the production of the aurora itself; (2) ionospheric heating by hydromagnetic wave generation and (3) the direct effect of hydromagnetic wave penetration of the ionosphere; and concluded that only the first mechanism could supply the requisite energy.

*Procunier* (1971) cites a review of sound associated with auroral sources [*Silverman and Tuan* (1971)] attributing the first association to the year 1729, and attributes the first infrasonic observations to *Chrzanowski, et al.* (1961) and presents data on aurorally produced infrasound in the high frequency range extending from 1 Hz to 16 Hz.

The high frequency range data were recorded utilizing 5 Helmholtz resonators located at Barrow, Alaska and equipped with front-end noise filters. The frequency response of each resonator was chosen differently so that the entire frequency band was covered: i.e., at the octave spacing of 1 Hz, 2 Hz, 4 Hz, 8 Hz and 16 Hz. Data were acquired during the month of January 1970 over a 10-hr period "at times of auroral interest" and over 100 events were observed.

A typical event recorded by the 4 Hz detector is shown in Figure 108 and Figure 109 compares the characteristics of the auroral signal in the low-frequency region and in the high-frequency region. Inspection of Figure 108 shows that the acoustic event occurs during a time when the horizontal component of the earth's magnetic field is rapidly changing. The events were observed to be impulsive and "of one to two cycles in duration and occurred at times of disrupted magnetic activity. In addition, the events seemed to be quasi-repetitive - that is, when events were occurring they would be at 30- to 60-s intervals. This wave-train nature was observed on several occasions and always during times of magnetic disturbance."

Figure 109 compares waveforms recorded at the same period of time as recorded on a long period microbarograph (.001 Hz-to-1 Hz) located at College, Alaska, and on the Helmholtz resonators located at Barrow, Alaska and the signal characteristics are seen to be

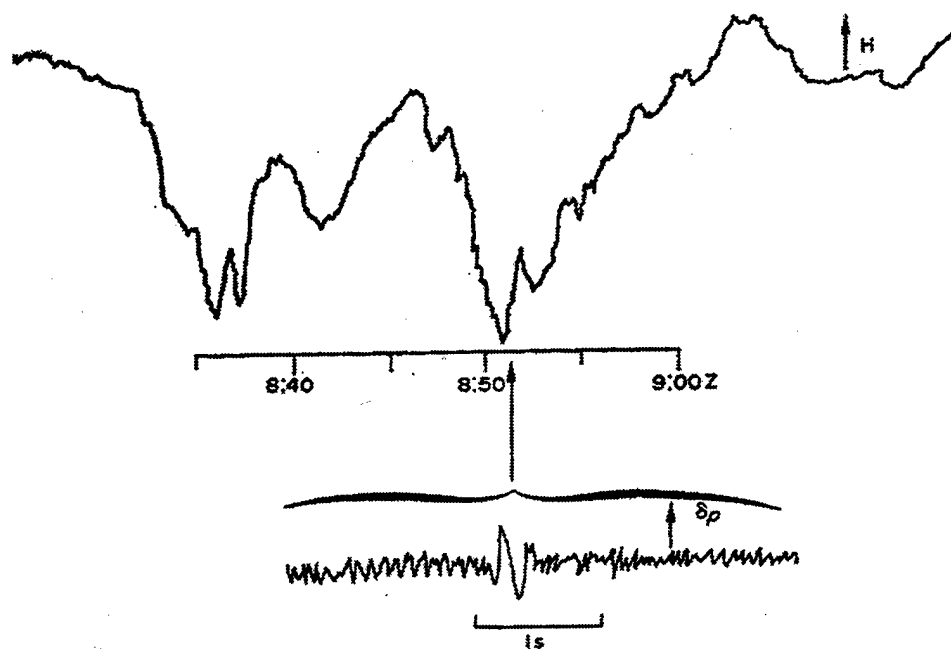


Figure 108. A "typical" auroral event recorded at Barrow Alaska on the 4 Hz Helmholtz resonator. The upper part of the figure plots the horizontal component of the earth's magnetic field and the lower part of the figure shows the associated acoustic waveform. [Figure adopted from *Procunier* (1971).]

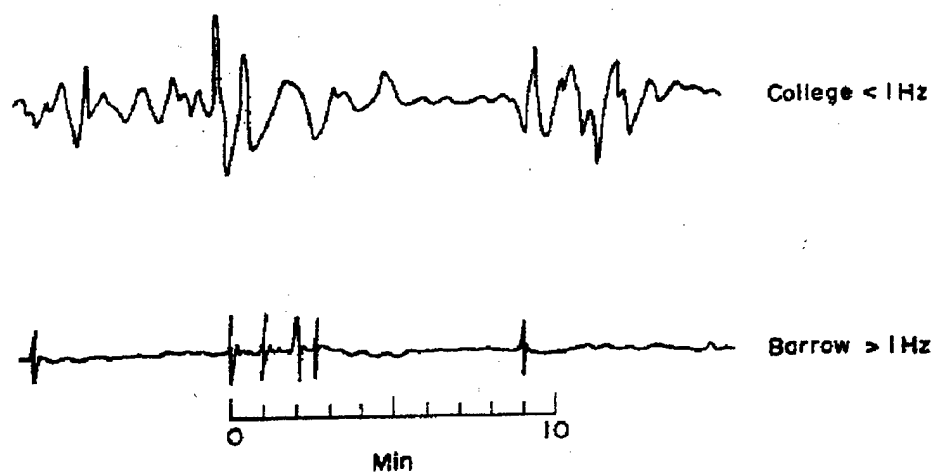


Figure 109. A comparison of aurally produced infrasound signatures recorded on a long period (.001 Hz to 1 Hz) microbarograph array at College, Alaska and on the "short period" Helmholtz resonators located at Barrow, Alaska. [Figure adopted from *Procunier* (1971).]

completely different with the higher frequency recording exhibiting a quasi-periodic pulse like structure.

*Wilson* (1971) reviews past work aimed at determining the morphology and source mechanisms of auroral infrasonic substorms noting, in particular, the work of *Wilson and Nichparenko* (1967), who found that the production of auroral infrasonic waves required a "supersonic motion of large scale auroral forms in a direction transverse to the long axis of auroral arcs.." a circumstance "which led to the development of a 'shock wave' model to explain the directional and amplification properties of the radiation of infrasonic waves by auroral arcs in supersonic translation" [*Wilson* (1967)].

In addition, *Wilson* (1971) auroral observations obtained at Inuvik, N.W.T., Canada during 1969 to 1970 are discussed in some detail which have served to demonstrate basic asymmetric generation mechanism in the auroral production of infrasound: supersonic motions of auroral arcs that sweep across the zenith from north-to-south (equatorward motions) are observed to produce infrasound whereas poleward motions (south-to-north) do not.

*Wilson* (1975) reviews the production of AIW (auroral infrasonic waves) as of 1975 focusing the discussion in five areas: (1) AIW characteristics and substorm morphology, (2) AIW source arcs, (3) AIW generation asymmetry and mechanisms, (4) AIW propagation and (5) high frequency auroral infrasound as observed: for example, by *Procunier* (1971) and *Liszka and Westin* (1972).

As of 1970, microbarographic observations of AIWs had been made in the frequency passband extending from 0.01 Hz to 0.1 Hz and observations at high latitude stations had observed that the generation of AIWs was characterized by the supersonic motions of auroral arcs moving perpendicular to their long axes. A "typical AIW" observed on a microbarograph array located at Stevens Village, Alaska on April 2, 1973 arrived with a horizontal trace velocity of 400 m/s and exhibited a peak-to-peak amplitude of 10 mbar and a duration of approximately 2 minutes.

By 1972, the asymmetric nature of the AIW source generation mechanism noted above had been established [Wilson (1971) and Wilson (1972)] and this circumstance led to the theoretical work of *Feder and Banks* (1972) and *Swift* (1973) attempting "to explain the observed asymmetry by a cancellation of the Lorentz force and Joule heat source terms for auroral motions that are poleward in the opposite direction to ( $\mathbf{J} \times \mathbf{B}$ ) the Lorentz force." Graphic illustration of the asymmetry in the AIW source generation mechanism is provided in Figure 110 showing microbarograph data acquired at Inuvik, Canada on select days in

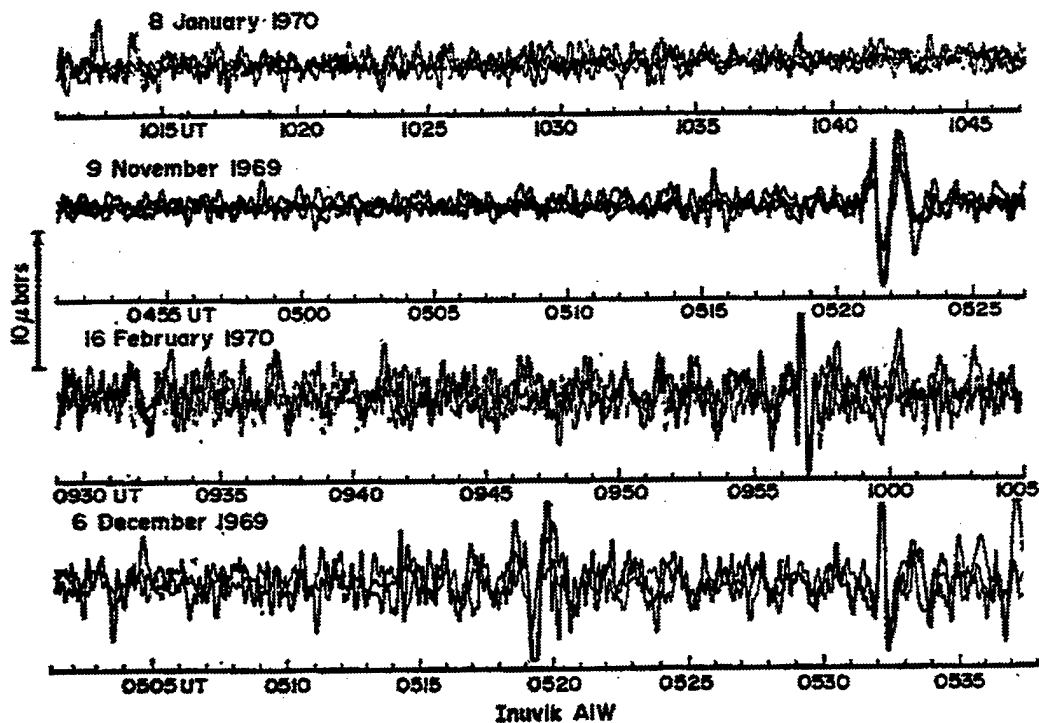


Figure 110. Infrasonic data acquired during 1969 and 1970 on a four-element microbarograph array deployed at Inuvik, Canada. The labels on the horizontal axes are UT. [Figure adopted from Wilson (1972 and 1975).]

1969 and 1970. For each day, approximately 30-minute time records are provided following poleward auroral arc motions crossing the Inuvik zenith moving poleward (from the south-to-north. On January 8, 1970, the poleward expansion crossed Inuvik at 1024 UT and the microbarograph records indicate no AIW arrivals. On November 9, 1969 the poleward expansion occurred at 0507 UT and was followed by an equatorward motion at 0521 which is associated with the AIW arrival at virtually the same time. On February 16,

1970, the poleward motion occurred at 0833 UT and was followed by an equatorward motion at 0957 which was associated with the AIW arrival occurring at the same time. Finally, on December 6, 1969 the poleward motion occurred at 0500 UT and a following equatorward motion at 0519 which produced the observed AIW signal.

In addition to the foregoing, *Wilson* (1975) cites the AIW observations of *Goerke and Woodward* (1967) at Boulder, CO having horizontal trace velocities of 400 m/s, the observations of *Johnson* (1972) utilizing a network of infrasound stations (Pullman, WA, Boulder, CO and Washington, D.C.) which established that AIWs can propagate to ranges of at least 1800 km and still have a recognizable form.

*Wilson* (1975) also discusses the 1 Hz to 16 Hz "high frequency" AIW observations of *Prokunier* (1971) and the 2 Hz observations of *Liszka and Westin* (1972) and attributes the observations to different source mechanisms than those which produce the lower frequency observations because the high frequency signals appear to have different characteristics than their lower frequency counterparts: e.g., the 2 Hz signals appear to be more continuous in nature than those recorded by *Prokunier* (1971) and the 2 Hz signals are observed to propagate from south-to-north. *Wilson* (1975) concludes his review by emphasizing the need for further research on AIW source mechanisms.

*Wilson, Olson and Spell* (1995) present a very succinct and high level review of AIW (auroral infrasonic wave) measurements conducted during the time period from 1965 to 1985 by University of Alaska investigators. The authors note, in particular, that AIWs have been observed at all infrasonic auroral zone stations: Alaska (Fairbanks, Palmer, and Steven's Village); Canada (Inuvik, N.W.T.); Sweden (Kiruna); Antarctica (Windless Bight on the Ross Ice Shelf).

In summarizing a large body of work on AIWs, *Wilson, Olson and Spell* (1995) note that a generally agreed upon and detailed physical explanation for the source mechanism of AIWs is not extant. It is emphasized, however, that enough is known about AIWs and associated processes within the aurora to constrain the source mechanism to be

"a momentum source that is electromagnetic in origin": a Lorentz-force coupling or an ion-collision process.

Several observational facts serve to constrain possible AIW source mechanisms:

- "Only supersonic motions of large scale auroral arcs produce AIW" [*Nichparenko* (1967); and *Wilson* (1969a)].

- "AIW are only produced by supersonic westward- and eastward-propagating surges or by equatorward-moving supersonic westward electrojet arcs. The source motions are thus westward in the evening, southward around midnight, or eastward in the morning. No AIW have ever been observed at Palmer, College or Inuvik from poleward-moving supersonic westward electrojet auroral arcs. No AIW at these stations have ever been observed propagating south-to-north from any kind of auroral source."

- The "assumption of line-current approximation [for the form of the source] will allow the speed, direction of motion and zenith crossing time of electrojets to be determined from the surface magnetic perturbations."

- "The average trace velocity of AIW is 510 m/s, giving an angle  $\alpha$  between the wave normal and horizontal of about  $50^\circ$ . The average period (duration of the first pulse) of AIW is about 20 sec... The phase of the pressure pulse can be either positive or negative for AIW that are due to southward-moving supersonic auroral arcs that contain a westward electrojet."

- A postulated shock wave theory for the source mechanism [e.g., *Wilson* (1969b)] yields an expression for the time delay,  $\Delta t$ , between the passage of aural arc and the arrival of the acoustic signal given by

$$\Delta t = \frac{h}{c} \left[ 1 - \left( \frac{c}{V_A} \right)^2 \right]^{1/2} \quad (6.1)$$

where  $h$  is the atmospheric height of the auroral arc,  $c$  is the speed of sound in an isothermal atmosphere and  $V_A$  is the speed of the auroral jet. For an assumed altitude of

130 km,  $V_A = 1300$  m/s and  $c = 330$  m/s, the predicted delay time is 381.04 s or 6.35 min.

## 6.2 Avalanches

*Bedard, Greene, Intrieri, and Rodriguez* (1988) have reported the association of infrasonic waves with avalanches in and around the area of Boulder Colorado. The signals were recorded on an array of six microbarographs equipped with noise-reducing front end wind filters. The signals are characterized by very low amplitude: 2  $\mu$ bar peak-to-peak at the maximum; and by the fact that the acoustic spectra are concentrated in frequency: typically in the range from 1 Hz to 3 Hz. The signals appear to last for a period of at least 20 sec.

*Bedard, et al.*, (1988) utilized a model of an avalanche given by *Hopfinger* (1983) to develop an expression for estimating the frequency radiated by an avalanche. Figure 111 provides a cross-sectional view of an avalanche indicating what are thought to be the important regions and processes and, in particular, the formation of leading edge "roll waves" which are a candidate for a source mechanism as they provide a possible means for the production of "monochromatic" radiated acoustic energy.

In deriving their theoretical expression for the radiated frequency,  $f$ , *Bedard, et al.*, (1988) set

$$f = \frac{U}{\lambda} \quad (6.2)$$

where  $U$  is the speed of motion of the avalanche and  $\lambda$  is the wavelength of the rolls. The roll wavelength is taken to be equal to an average roll wavelength and equal to  $18h$ , where  $h$  is the height of the avalanche as defined in Figure 111. By setting

$$U = F_r \left( \frac{\Delta \rho}{\rho g h} \right)^{1/2} \quad (6.3)$$



where  $F_r$  is the Froude number,  $g$  is the acceleration of gravity, and  $\Delta\rho$  is the difference in density between the medium density,  $\rho_m$ , and the avalanche density,  $\rho_a$ . Combining Eqs. (6.2) and (6.3) then leads to the expression

$$f = \frac{F_r(\Delta\rho/\rho_g)^{1/2}}{18h^{1/2}} \quad (6.4)$$

*Bedard, et al.*, take  $F_r = 1$ ,  $\Delta\rho = 0.1 \text{ g/cm}^3$  and find that Eq. (4.4) predicts radiated frequencies in the range from 1 Hz to 3 Hz for values of  $h$  in the range:  $0 \text{ m} \leq h \leq 2.8 \text{ m}$ ; and for values of avalanche speed in the range:  $2 \text{ m/s} \leq U \leq 49 \text{ m/s}$ . Figure 112 shows that the measured spectral content of the avalanche signal is quite close to that predicted.

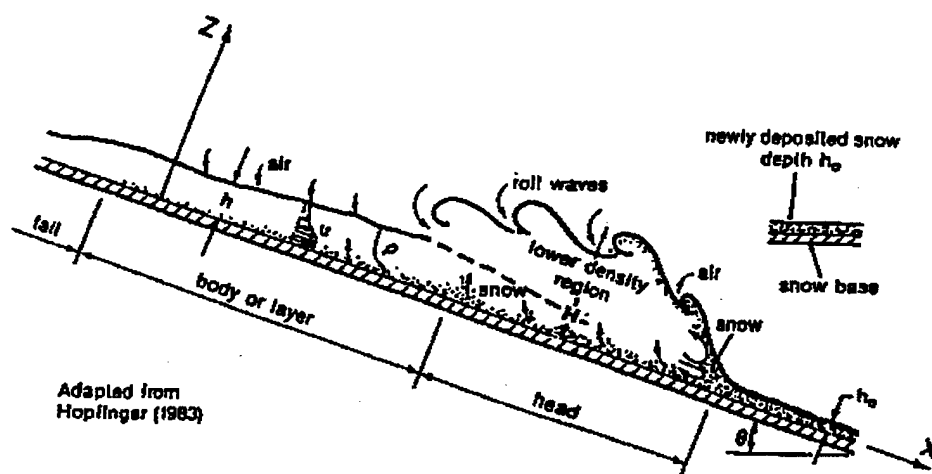


Figure 111. A cross-section view of an avalanche after Hopfinger (1983) and Bedard, et al., (1988). The cross section exhibits the important mechanisms involved, defines parameters used in the text to estimate a source mechanism and, in particular, the presence of roll waves.

Although the theoretical estimates for the radiated frequency are quite close to those observed, *Bedard, et al.* (1988) note that specific source generation mechanisms for avalanche noise generation remain to be explained. It is hypothesized, however, that "water vapor and water droplets rapidly cooled as the avalanche terminates produce regions of heating from the release of latent heat of condensation or fusion. The surface frictional

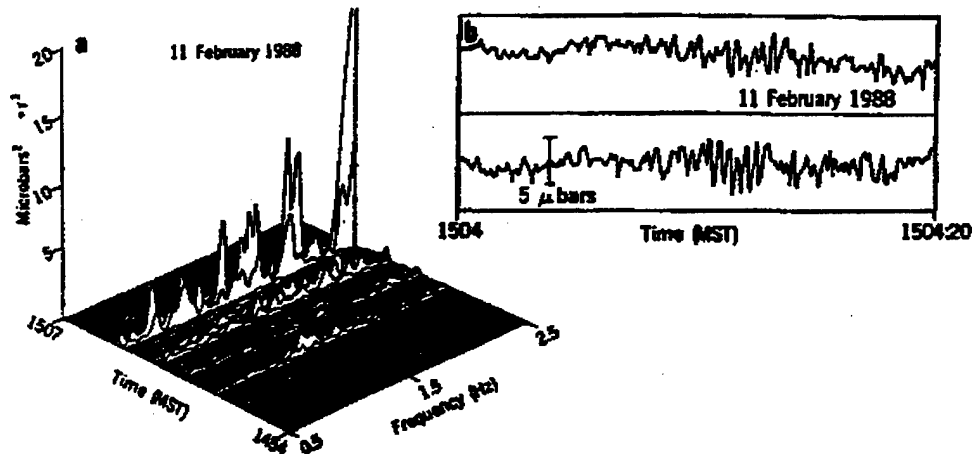


Figure 112. Spectral amplitudes and waveforms of infrasonic signals recorded on February 11, 1988 by an infrasonic array at Boulder, CO. The spectrum is quite "peaky" in the band extending from 0.5 Hz to 2.5 Hz and the peak-to-peak signal amplitude is 2  $\mu$ bar. [Figure adopted from *Bedard, et al.*, (1988).

heating would be an important component of the process warming air that is entrained in the rolls. Subsequently, the warmed air in the rolls containing a mixture of water vapor and water droplets could be rapidly cooled by mixing with the ambient air after the lower region h stopped moving. The rolls could act as a series of monopole acoustic sources."

### C. Bolides or Meteorites

The classic paper on the production of infrasound by meteors is the discussion by *Whipple* (1930) of the Great Siberian Meteor which fell in Siberia on June 30, 1908. Data are presented on both air wave arrivals and seismic arrivals produced after the meteor struck ground. Barograph data were presented from six stations in England: Petersfield, Reading, London [South Kensington, Westminster, Shepard's Bush] and Cambridge. The distance from the centroid of the English stations to the impact point of the meteor was 5,720 km. From the data taken at five of the stations [Shepard's Bush was not used], a composite microbarogram was formed "in which the pen movements due to local and gradual changes in the meteorological conditions have been eliminated." The data from the individual stations and the composite waveform are displayed in Figure 113.

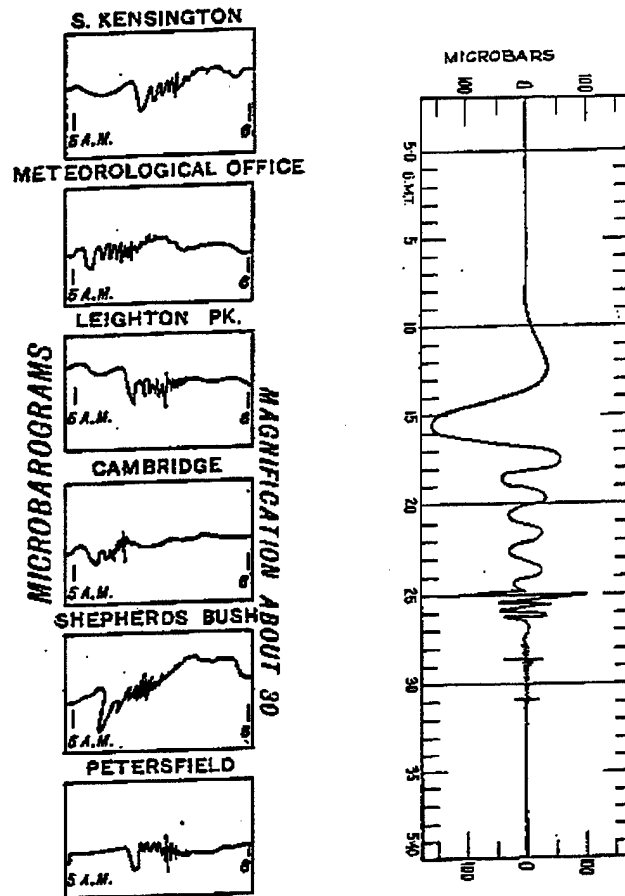


Figure 113. The panel to the left displays the measured microbarograms recorded at the indicated stations and the panel to the right presents the "composite microbarogram". [Figure adopted from *Whipple* (1930).]

Assuming a plane wave arrival, *Whipple* (1930) estimated the energy of the air wave to be

$$E(\text{Air Wave}) = 3.2 \times 10^{22} \text{ ergs} = 3.2 \times 10^{13} \text{ Joules}$$

or, assuming a conversion relation of  $1 \text{ MT} = 4.22 \times 10^{22} \text{ ergs}$ , an explosive yield of 0.76 MT.

*Groves* (1957) develops a solution for the velocity of a body falling from a height outside the earth's atmosphere, through the atmosphere and to the ground. The propagation of the shock wave which is produced is also considered including the effects of a refracting atmosphere. The results of the investigation are presented in terms of curves of velocity and

maximum distances from impact points at which sound can be heard. The effects of the atmosphere on a vertically falling body were shown to imply that only part of the shock wave would reach the ground for a body falling from an altitude of 120 km or greater. However, a body falling from a shallower altitude an additional part of the shock wave will propagate to the ground.

The velocity and maximum distance impact points results are presented in terms of the variable  $p^*$  which is defined by the relation

$$p^* = \frac{mg \sin(\theta)}{SC_D} \quad (6.5)$$

where  $m$  is the mass of the body,  $g$  is the acceleration due to gravity,  $\theta$  is the trajectory inclination from the horizontal,  $S$  is the cross-sectional area of the body and  $C_D$  is the drag coefficient. Figure 114 reproduces the computed range curves as a function of height for different values of  $p^*$  referred to as the "modified ballistic entry parameter" by *Revelle* (1976).

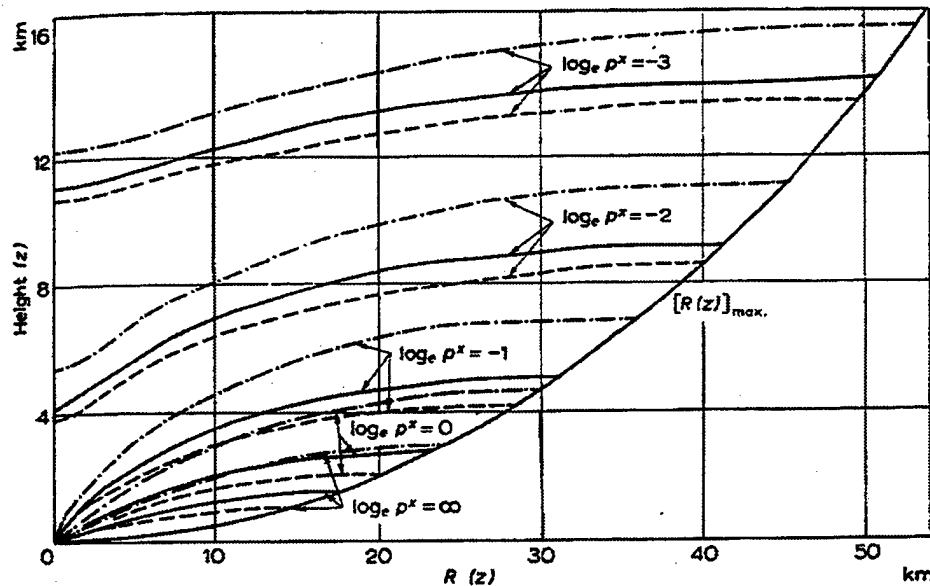


Figure 114. The distance from the impact point to the point at which a shock wave originating at height  $z$  reaches the ground. ---  $Z = 100$  km; —  $Z = 200$  km; - - -  $Z = 300$  km;  $p^*$  in units of atmospheres. [Figure adopted from *Groves* (1957).]

*Donn and Balachandran* (1974) report on the observations of infrasound which they associate with a meteor event which occurred at 9:27 AM on October 20 (1973) and describe the Lamont-Doherty infrasound system as consisting "of two tripartite arrays of capacitor microphones at the same location operating in the passbands 0.1 to 1 hertz and 1 to 10 hertz, respectively." At the time the paper was submitted to Science, only the data from low frequency tripartite array had evidently been processed: the one operating in the frequency passband extending from 0.1 Hz to 1 Hz (see the discussion below).

Figure 115 reproduces the recorded wave forms where Panel A shows a portion of the 24-hour drum record from one of the microphones in the array and Panel B shows the records from each of the three microphones making up the tripartite array. The lines labeled with the numbered circles on the figure are meant to correlate the identical waves recorded by the individual array sensors. As indicated from inspection of the figure, the slopes of the lines show a rapidly decreasing and then increasing time delay: a circumstance that is attributed to a rapidly moving source. *Donn and Balachandran* (1974) rule out an airplane as a source as the data would require an airplane flying at 10 km to have a Mach number of 3 which would produce a classic N-wave from a sonic boom rather than the signals that are observed.

Utilizing the results of *Krilov* (1960) which indicate that no meteor shock wave would be generated until a meteor penetrates to an elevation of 60 km-to-80 km and the results of *Hawkins* (1964) which imply that meteors decelerate to subsonic speeds below ~ 20 km to assign an altitude of 55 km for the source of wave 10 and an altitude of 25 km for the source of wave 1, *Donn and Balachandran* (1974) use measured values of the trace velocity to construct an estimate of the actual meteor trajectory which predicts a time difference between the wave 1 and wave 10 arrivals of 27 s which is in close agreement with the measured value of 26 s.

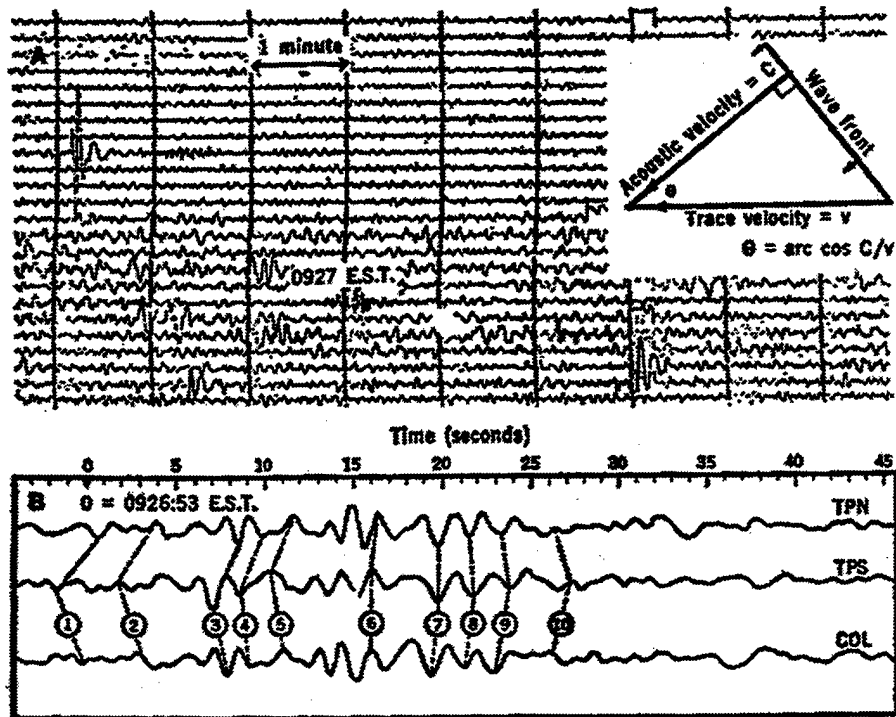


Figure 115. Panel (A) provides a portion of the 24-hr drum record for October 20, 1973 and shows the assumed meteorite event at 9:26:53 E.S.T. Panel (B) shows the tape playback to a high-speed recorder of the meteorite signal in Panel A for each of the three instruments making up the low-frequency tripartite array. The lines correlate the same phases for identical waves labeled 1 through 10 in the figure. The pressure amplitude of the meteorite signatures are about  $1 \mu\text{bar}$ . [Figure adopted from *Donn and Balachandran* (1974).]

*ReVelle* (1975) suggested that the conclusions reached by *Donn and Balachandran* (1974) about the detection of infrasound from meteors was not conclusive as there was no photographic or radar (or other) "ground truth" data to support a one-to-one association with a meteor event and the production of infrasound. *ReVelle's* (1975) other main concern with the *Donn and Balachandran* (1974) association was based on what was assumed to be the reported infrasound frequency of 0.3 Hz. Based on a cylindrical line-source model of meteoritic sound generation [*ReVelle* (1974)] and a reasonable assumption of meteor size as  $\sim 1$  kg, the predominant meteor produced infrasonic frequency that should be near 3 Hz. *Donn and Balachandran* (1975) responded that, while they did indeed have no corroborating evidence from other sensors, they had done the best they could to rule out other sources. In addition, they pointed out that *ReVelle* (1975) had erred in interpreting

*Donn and Balachandran* (1975) responded that, while they did indeed have no corroborating evidence from other sensors, they had done the best they could to rule out other sources. In addition, they pointed out that *ReVelle* (1975) had erred in interpreting their paper as associating the frequency of the meteor event to be 0.3 Hz noting that the last paragraph of their paper suggested a dominant energy of the event as being between 0.3 Hz and 3 Hz. In addition, they provided data on the event which was recorded on another microbarograph array designed for higher frequency recording which placed the frequency of the dominant energy at 2.5 Hz.

*McIntosh, Watson and ReVelle* (1976) report the observation of an infrasonic event associated with the entry of a meteor into the earth's atmosphere on December 14, 1974. The entry of the meteor was also recorded by a ground based radar which indicated that the meteor was composed of multiple components at slant ranges from 240 km to 280 km from the radar site. The reported head echo from the meteor was 140 s in duration. It was noted that, in principle, both the meteor velocity and mass can be estimated from the duration of the head echo [*McIntosh* (1976)]. However, the record quality was only sufficient to estimate the mass as  $\sim 1$  kg. The velocity had to be assigned a "reasonable guess" value of 35 km/s.

The infrasound from the meteor was presumably produced through the generation of a shock wave which was detected on the ground. The associated infrasonic signature was recorded on each of four elements of a microbarograph array located at the Springhill Meteorological Observatory in Canada. The sensor spacing of the array ranged from 136 m to 238 m which is approximately half-wavelength spacing (150 m) at a frequency of 1 Hz. The basic sensor elements were ceramic microphones attached to a backing volume with contact to the atmosphere via a fine orifice or needle valve. Two of the array sensors were connected to Daniels pipe arrays of 29 m length which were constructed of garden hose in which hypodermic needles were inserted at 0.94 m intervals. The other two sensors

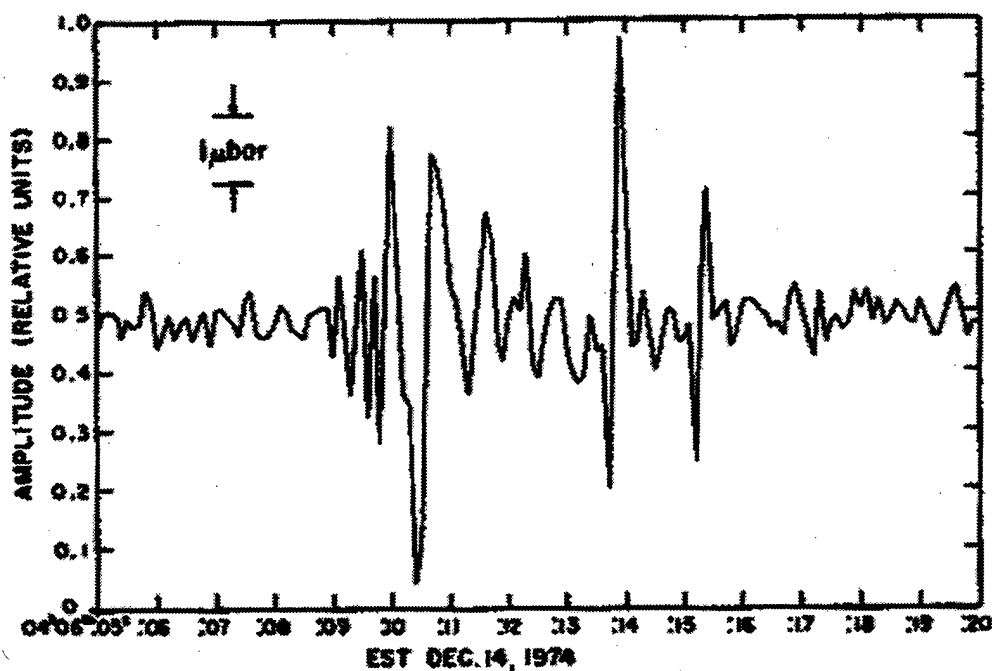


Figure 116. Infrasonic signal produced by a meteor as recorded on one of the microphones making up the microbarographic array at the Springhill Meteor Observatory. [Figure adopted from *McIntosh, Watson and ReVelle (1976)*.]

to 16 s). The maximum peak-to-peak amplitude is seen to be approximately  $7\mu\text{bar}$ . The spectrum of the signal was reported to be "characterized by a broad peak between 1 and 2 Hz and a secondary peak about 2.4 Hz.

The association between the radar observations and the infrasonic signature was made stronger by demonstrating that the time interval between the radar echo and the time of arrival of the infrasound was consistent with acoustic propagation speeds and that the radar estimation of the meteor's mass was consistent with a meteor blast-wave theory developed by *ReVelle (1974)*.

*Revelle (1976)* presents a thorough analysis of the generation and propagation of infrasonic waves excited by the entrance of a meteor into the earth's atmosphere and, in particular, develops a line-source cylindrical blast wave source model for the propagating acoustic wave. The results are valid for propagation in a continuum gas and the analysis incorporates the effects of atmospheric refraction within the geometric acoustics



approximation and the attenuation of the blast wave. In addition, earlier experimental observations published by investigators such as: *Goerke* (1966), *Bayer and Jordan* (1967), *Woodward and Goerke* (1967), *Shoemaker and Lowery* (1967), *Millman* (1970) and *Opik* (1970), are noted.

Utilizing the developed theory and various observed parameters associated with known meteorite events, *Revelle* (1976) computed other meteorite parameters such as meteorite mass, diameter and kinetic energy at the source height. Table 3 shows, for example, the theoretical estimates of meteor kinetic energy for various known meteorite events.

Table 3. Observed, assumed and computed meteorite parameters for four known meteorite events.  $\tau_g$  is the observed period at maximum amplitude in s,  $t_d$  is the total duration of the wavetrain,  $\Delta p_{op}$  is the observed zero-peak pressure amplitude on the ground in  $\mu\text{bar}$ ,  $Z_z$  is the assumed height of the meteorite event and  $E_s$  is the computed kinetic energy of the meteor at the source height in ergs. [Data adopted from *Revelle* (1976).]

Event	$\tau_g(\text{s})$	$t_d$	$\Delta p_{op}$	$Z_z(\text{km})$	$E_z$
Revelstoke	16.5	20 min	4.0	34	$2.9 \times 10^{21}$
Holbrook-1	2.5	10 s	1.1	27	$3.5 \times 10^{17}$ - $3.5 \times 10^{18}$
Holbrook-2	4.0	12 s	0.25	57	$1.3 \times 10^{19}$ - $1.3 \times 10^{20}$
Kincardine	54	34 min	1.25	64	$1.2 \times 10^{22}$ - $1.2 \times 10^{23}$
Alaskan Fireball	12	.....	2.3	61	$2.0 \times 10^{20}$ - $2.0 \times 10^{21}$

*Golitsyn, Grigor'yev and Dokuchayev* (1977) derive expressions for the total energy radiated into internal and infrasonic waves by meteors in flight between the altitudes of 50 km and 120 km and in the mass range  $10^{-4} \text{ kg} \leq m_0 \leq 10 \text{ kg}$ . The theoretical development proceeds from the basic hydrodynamic equations of motion which incorporates mass, energy and momentum source terms and models the meteor source as a cylindrical tube of radius  $a$  and length  $L$ . The analysis shows that the energy (or heat) source term is dominant and separate expressions are derived for the total energy converted

into infrasonic and gravity waves. The expression for the source energy radiated into acoustic waves,  $E_A$ , is given by

$$E_A = \frac{(\gamma-1)^2 E_o^2}{2(2\pi)^{3/2} \rho_{oo} c^2 a^2 L} \quad (6.7)$$

where  $E_o$  is the initial energy of the meteorite ( $=0.5m_o V_o^2$ ),  $c$  is the sound speed,  $\rho_{oo}$  is the atmospheric density at the ground. In addition, a particularly simple expression is derived for the amplitude of the pressure wave recorded on the ground in the far field given by

$$p \approx (\gamma-1)E_o / 2\pi^{3/2} r a^2 \approx 25 \mu\text{bar} \quad (6.8)$$

where  $r$  is the horizontal range from the observation point to the meteor location. In providing the estimate in Eq. (6.8), it has been assumed that the meteor is at a height of 87 km and that the initial mass and speed are 1 kg and 60 km/s 60 km, respectively. The estimate of 25  $\mu\text{bar}$  is seen to be an order of magnitude higher than the measured values provided in Table 3.

*Bedard and Greene* (1981) presented data on the infrasonic detection of a meteor which passed over the Boulder Colorado area on April 22, 1975 and which produced signals recorded on microbarograph arrays at Boulder and Frazer, Colorado. The investigators mention the work of *Wylie* (1932), who proposed two mechanisms for the radiation of sound from meteors: the emission of a cylindrical shock wave along the meteor's path or with air turbulence produced by the meteor at low altitudes, and that of *Koroberikov, et al.*, (1972) who postulated an explosive mechanism.

In analyzing their data, *Bedard and Greene* (1981) used ray tracing to rule out the cylindrical shock mechanism in favor of an explosive type of source as the latter mechanism was consistent with the observation of two arrivals, separated by 240 s, which were observed on the microbarograph array at Frazer, Colorado. To fit the data, the explosive event would have had to take place at an altitude of 25 km. Of interest to investigators interested in utilizing infrasound to study meteorites, is the conclusion by

*Bedard and Greene* (1981) that: "Although our acoustic detection of this meteorite event was fortuitous, we feel that we have demonstrated that multi-array acoustic sound ranging for meteors and meteorites [as suggested by *Donn and Balachandran* (1974a)] is feasible."

Figure 117 shows the waveform of the event as recorded on the Boulder, CO array.

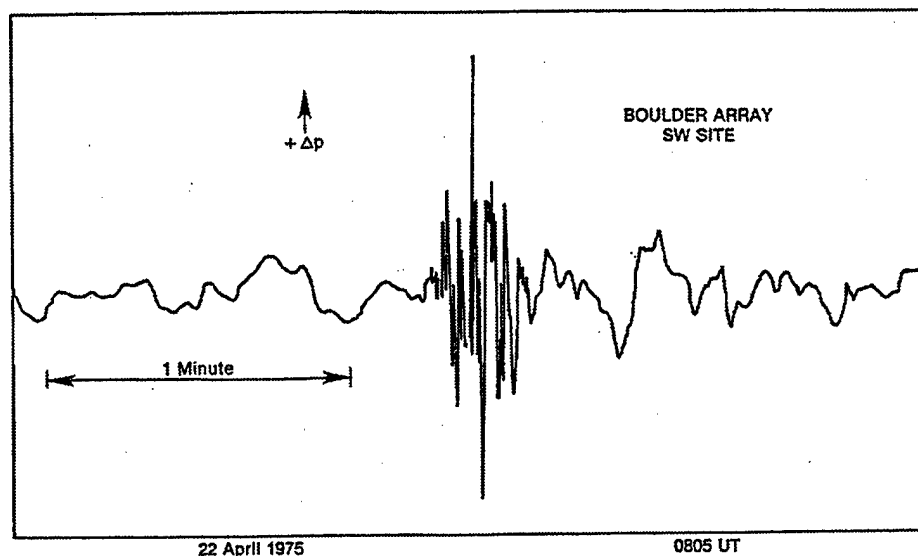


Figure 117. The acoustic signal recorded at the Boulder, CO array site from a fireball which passed over Boulder on April 22, 1975. [Figure adopted from *Bedard and Greene* (1975).]

*Revelle and Delinger* (1981) mention numerous sources of naturally occurring infrasound (defined as propagating energy in the frequency band extending from 0.01 Hz to 20 Hz) but focus particularly on infrasound due to meteor-fireballs and cite four source mechanisms: cylindrical blast wave, line source model; finite length line source model; point source; spherical blast wave model and combined line and point source model. In addition, the authors allude to the installation of two infrasonic arrays near Flagstaff, Arizona for infrasonic monitoring.

The atmospheric infrasonic monitoring program conducted by AFTAC during the period extending from 1960 to 1974 is also briefly discussed, and mention is made of 10 meteor-fireball events recorded by the program having yields in the energy range extending from 0.1 KT to 150 KT. A high frequency extrapolation of earlier low frequency Lamb wave results [*Pierce and Posey* (1971)] was reported and is given by the equation

$$\frac{\Delta p r^{1/2}}{E} = 2.34 \times 10^3 T^{-1.50} \quad (6.9)$$

where  $\Delta p$  is the peak-to-peak amplitude of the first cycle of the waveform in  $\mu\text{bar}$ ,  $r$  is the horizontal range from the source-to-receiver points,  $E$  is total energy release of the explosion in KT [with 50% of this value assumed to have been lost due to radiation] and  $T$  is the period (in seconds) as measured from the first to the second identifiable peak in the arriving wave. Using the AFTAC meteor data, *ReVelle and Delinger* (1981) derived the analog to the above given by

$$\frac{\Delta p r^{1/2}}{E} = 1.50 \times 10^3 T^{-2.00} \quad \text{with } r^2 = 0.58 \quad (6.10)$$

where  $r^2$  is the correlation coefficient and concluded that "the data substantiates the high frequency extrapolation of the Pierce-Posey result within the observational errors." In both cases, the energy release was determined from AFTAC's empirical regression fit to atmospheric nuclear explosions and is given by

$$\text{Log}_{10}(E) = 3.34 \text{Log}_{10}(T^*) - 2.58 \quad \text{for } E \leq 100 \text{ KT} \quad (6.11)$$

where  $T^*$  is the wave period at the maximum of the received waveform. The foregoing relations lead to a relationship between the Lamb wave period,  $T$ , and  $T^*$  given by

$$\text{Log}_{10}(T^*) = 0.45 \text{Log}_{10}(T) + 0.41 \quad \text{with } T^* \leq T \quad (6.12)$$

*Kraemer and Bartman* (1981) report the observation of infrasound from a meteor entering the atmosphere over South Dakota on May 24, 1975. The infrasonic signals were recorded on a four element microbarograph array arranged in a quadrangle pattern with element spacing ranging from 465.75 m to 773.19 m. The basic sensor was a Globe microphone equipped with front-end noise filters of 600 ft (182.9 m) to 800 ft (243.84 m) in length. The noise filters were constructed from water hose with hypodermic needles inserted every 5 ft (1.52 m) along the hose length.

In addition to the infrasound arrivals, the meteor was photographically tracked by two ground stations which were formerly part of the Prairie Network meteor camera system. Figure 118 provides the waveforms measured by the four microbarographs in the

array and the signature is seen to consist of two parts: an early arriving signal, labeled A, which was shown by ray tracing to arrive from a height of  $\sim 66.5$  km, and a later arrival, labeled D, which was shown to arrive from a height of  $\sim 54$  km.

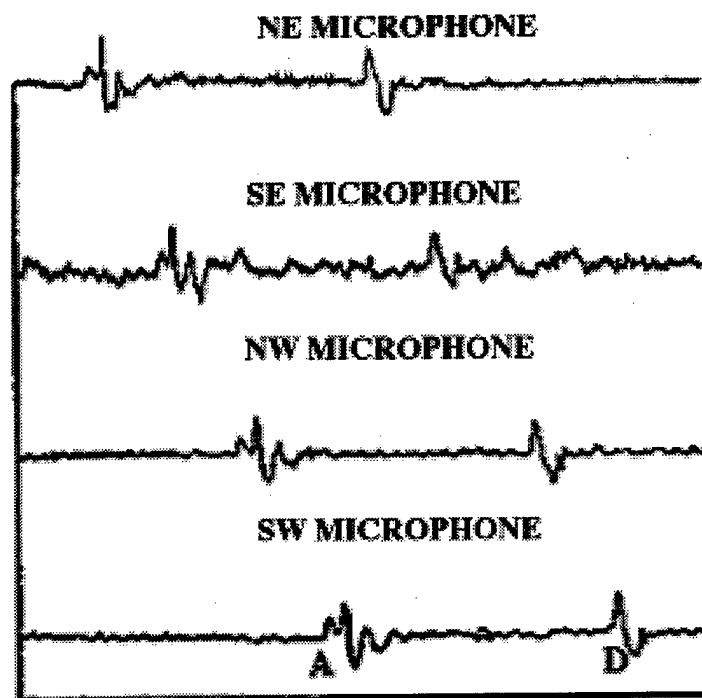


Figure 118. Measured waveforms associated with a meteor observation over South Dakota on May 24, 1975. [Figure adopted from *Kraemer and Bartman* (1981).]

The reported velocity, elevation angle, amplitude (peak-to-peak) and period of the two arrivals were reported as  $380.433 \pm 1.247$  m/s,  $27.02^\circ \pm .119$ ,  $1.38 \mu\text{bar}$  and  $.211 \pm .008$  s for the A-wave arrival and as  $359.259 \pm 0.193$  m/s,  $19.35^\circ \pm .012$ ,  $2.26 \mu\text{bar}$  and  $.222 \pm .008$  s for the D-wave arrival.

The data were used to evaluate the cylindrical blast wave meteor source model proposed by *Revelle* (1976) and the measured waveform properties were found to generally agree with the predictions of the model. In particular, the predicted amplitudes were within a factor of two of those measured, and the predicted mass of the meteor was in close agreement with the 320 grams estimated by photometric means.

*Bedard* (1988) reports on the detection at Boulder, CO of infrasound which was excited by the passage of a fireball over central Oregon on August 12, 1985: a range of

approximately 1220 km. As it passed over Oregon, nearby observers related that the event produced a "swishing sound". The period of the observed infrasound was predominantly in frequency passband extending from 0.7 Hz-to-1.4 Hz.

#### **6.4 Bridges**

*Donn, Balachandran and Kaschak* (1974) reported the observation of infrasound radiated by vibration of the Tappan Zee Bridge which crosses the Hudson River, north of Columbia University's Lamont Doherty Geological Observatory and, quite possibly, by a similar vibration of the George Washington Bridge which lies to the south of the laboratory. The sound radiated from the Tappan Zee Bridge was characterized by a frequency of 8.5 Hz, whereas the sound radiated from the George Washington Bridge was observed to have predominant frequency of 5 Hz. Peak-to-peak signal levels were observed to be 2  $\mu$ bar. The source of the vibrations was attributed to the motion of the bridge roadbed caused by vehicular traffic and the signal duration was observed to be essentially continuous.

In establishing the source mechanism, a fixed tripartite array (approximately 15 m on a side) of capacitor microphones was installed at a site adjacent to the laboratory. A mobile tripartite array was then located at other sites for triangulation purposes. In addition, three geophones were mounted on the bridge and the vibrational spectra of the geophones were found to closely match that recorded by the microphones. The most efficient propagation was observed to occur when a temperature inversion was present (temperature increasing with height immediately above the ground) or when winds were present having a direction from the source which increased with height above the ground.

#### **6.5 Earthquakes**

*Donn and Posmentier* (1964) reported the observation of infrasonic waves as a result of the Alaskan earthquake of March 27, 1964 at three "microbarovariograph" stations

located at: Palisades, NY, Berkeley, CA and Honolulu, HI. The instrumentation was reported to have a flat response out to periods of 300 sec and to have a dynamic range extending from a few  $\mu$ bars to a few hundred  $\mu$ bars. In addition, seismometers were co-located with the infrasonic sensors at all observing stations.

In relating the observed pressure measurements to the earthquake source, *Donn and Posmentier* (1964) discuss three possible mechanisms for the production of the waves: (1) local generation from a region around the infrasonic station due to the vertical displacement of air above the surface seismic waves, (2) distant generation by the earthquake source and propagation to the infrasound sensor through the atmosphere [a mechanism first proposed by *Cook* (1962) and first verified by *Bolt* (1964)] and (3) generation by resonant coupling which can occur when the group velocity of the short period Rayleigh waves are equal to the sound speed in the air [a mechanism observed by *Benioff, et al.*, (1951)].

Of the three possible mechanisms, it was concluded that the first is operative at all three stations and that infrasound produced by the second mechanism was only observed at the Berkeley, CA station. The local Rayleigh wave mechanism was demonstrated by the fact that the arrival times and periods of the infrasonic and Rayleigh wave arrivals were the same, that the magnitude of the pressure signal could be accounted for by the well known relation between pressure and particle velocity:  $p = \rho cv$ , and through the computation of dispersion curves for the infrasonic arrivals. The computed dispersion curves were compared with a summary of Rayleigh wave dispersion curves prepared by *Oliver* (1962) and it was found that the Berkeley, CA and Palisades, NY curves compared well with known continental Rayleigh wave dispersion curves and, in addition, that the Honolulu, HI infrasonic dispersion curve compared well with the known oceanic Rayleigh wave dispersion curve. The possible movement of the infrasonic sensors by the ground motion was considered and ruled out. Figure 119 shows the records recorded at the three stations and the arrival of the direct wave from the earthquake is clearly evident on the Berkeley record.

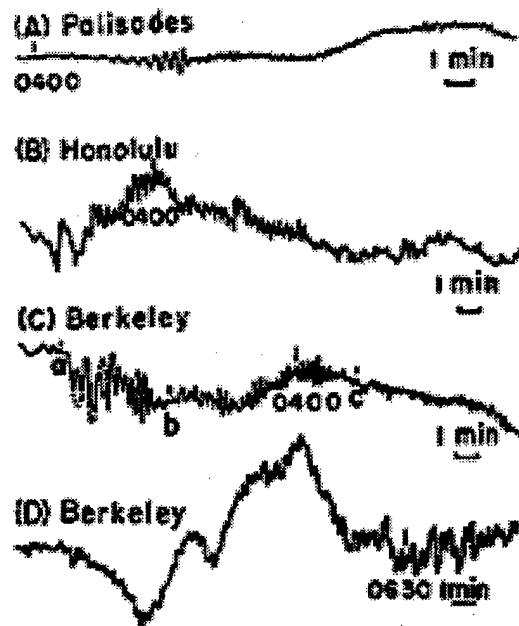


Figure 119. Waveforms recorded at Palisades, NY, Honolulu, HI and Berkeley, CA which are associated with the Alaskan earthquake of March 27, 1964. [Figure adopted from *Donn, Balachandran and Kaschak (1974).*]

*Row (1967)* briefly reviewed the early work of *Lamb (1932)*, *Taylor (1929 and 1936)* and *Pekeris (1939 and 1948)* which was directed toward understanding the atmospheric waves produced by the eruption of the Krakatoa volcano in 1883 and applied the methodology of *Weston (1961)* to derive pulse waveforms which were associated with ionospheric disturbances caused by the great Alaskan earthquake of 1964 and the large Soviet nuclear explosion at Novaya Zemlya on October 30, 1961. The ionospheric disturbances of both events were observed to propagate at sonic velocities above an atmospheric height of 100 km and to be characterized by an abrupt onset and a "long period tail". Under the assumptions of an unbounded, isothermal and dissipationless atmosphere, *Row (1967)* was able to derive a closed form expression for the pulse shape which agreed in form with the observed ionospheric pulse shapes and with the numerical results obtained earlier by *Kohl (1954)*. The ionospheric disturbances were observed by backscattering radio waves from the ionosphere and the Doppler shift of the initial part of the pulse was



observed to be negative in agreement for an upward displacement of the ground in the case of the Alaskan earthquake and with the outgoing pressure pulse from the explosion.

*Cook* (1971) discusses the mechanisms of infrasound generation by earthquakes and specifically reports on infrasonic observations of the Montana earthquake which occurred on August 18, 1959. In addition to the work of *Donn and Posmentier* (1964), the infrasonic observations of the Gobi-Altai earthquake of December 4, 1957 is cited [*Passechink* (1959)] as well as the generation of infrasound from a tsunami in the Pacific Ocean which was produced by the great earthquake in Chile which occurred on May 21, 1960 [*Ecollan and Rocard* (1960)].

Three earthquake mechanisms for the generation of infrasound are discussed: local infrasound, epicentral infrasound and diffracted infrasound. The case of local infrasound corresponds to waves produced by seismic waves which propagate through the geographical region in which the infrasound observing station is located. In this case, *Cook* (1971) shows that a rather significant region is responsible for producing the observed infrasound signal. In particular, some 70% of the observed infrasound is produced from a circular region of radius  $4\lambda_0$  so that for a seismic wavelength of 20 km, an area of 20,000 km<sup>2</sup> is involved.

Epicentral infrasound is taken as sound which is created over the epicenter of the earthquake and which propagates to long range in the atmosphere. Diffracted infrasound is similar to that of epicentral infrasound except that it arrives preferentially from the horizontal direction owing to diffraction caused by mountains and valleys.

Figure 120 presents the waveforms recorded on a four element microbarograph array located at Washington, D.C. Sensor separation in the array was stated to be 8 km.

Inspection of the figure shows that the signal was quite coherent over the array aperture and that there are several different arrival phases. The portion of the records from A-to-B represent typical infrasonic noise. The arrival phase labeled B is associated with the

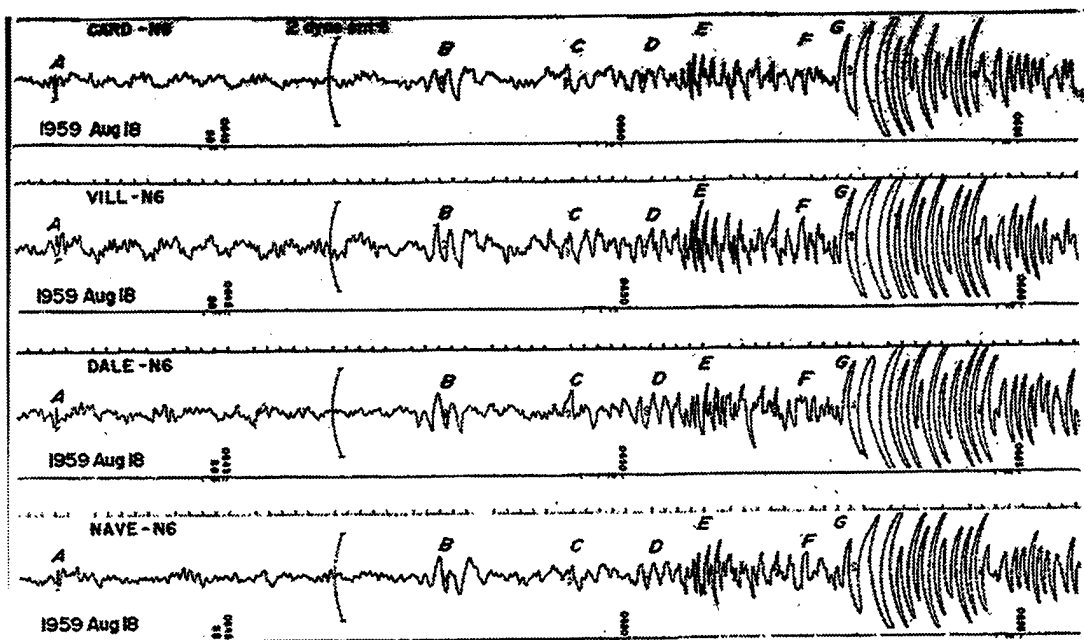


Figure 120. Graphic recordings of "local infrasound" radiated by seismic waves from the Montana Earthquake of 1959 and recorded on a four element microbarograph array located at Washington D.C. [Figure adopted from *Cook (1971)*.]

arrival of shear waves from the earthquake, the phase G with Rayleigh waves and E with the seismic  $L_g$  surface wave. The phases C and D are assumed to be continuations of the phase associated with the B phase. Peak-to-peak signal levels were reported as 0.8, 0.8 and 5.7  $\mu\text{bar}$  for the B, E and G phases respectively, with corresponding oscillation periods corresponding to 11 s, 6 s and 16 s.

*McIntosh (1982)* reports on the infrasonic observation of a magnitude 7.6 earthquake with an epicenter near the coast of Guerrero, Mexico (Lat 17.82°N and Long. 101.26°W) on a microbarograph array located at Saskatoon, Saskatchewan, Canada. The signal, a pressure wave driven by the motion of the earth such as a Rayleigh wave, traveled a distance of 3,850 km in 22 minutes implying a seismic group velocity of 3 km/s. The wave period was observed to be  $T=15$  s but the amplitude of the signals was not reported.

## 6.6 Industrial Sources

*Liszka* (1974) reported on the observation of a number of industrial infrasonic sources detected in Sweden from the three infrasonic stations located at: Kiruna ( $67^{\circ}8'N$ ,  $20^{\circ}4'E$ ), Jamton ( $65^{\circ}8'N$ ,  $22^{\circ}5'E$ ) and Lychsele ( $64^{\circ}6'N$ ,  $13^{\circ}7'E$ ). Each station consisted of a tripartite array of sensors (microphones) which, under favorable conditions, had a sensitivity of 77 dB below 1  $\mu$ bar. The predominant frequency recorded at all stations is 2 Hz with the Kiruna station also recording at 4 Hz and 8 Hz. Interelement sensor spacing was reported as less than one wavelength.

One of the primary sources of infrasonic sound identified was hydroelectric power plants and, in particular one located at Tuggen, Sweden, having a rating of 105 MW. The recorded infrasound levels were reported as 2  $\mu$ bar at Jamton and 0.5  $\mu$ bar at Kiruna. The radiated acoustic power was estimated to be in the range extending from 1 MW to 10 MW. Figure 121 provides an example of amplitude recordings from the Kiruna and Jamton infrasonic stations which were associated with the operation of the Tuggen hydroelectric power plant.

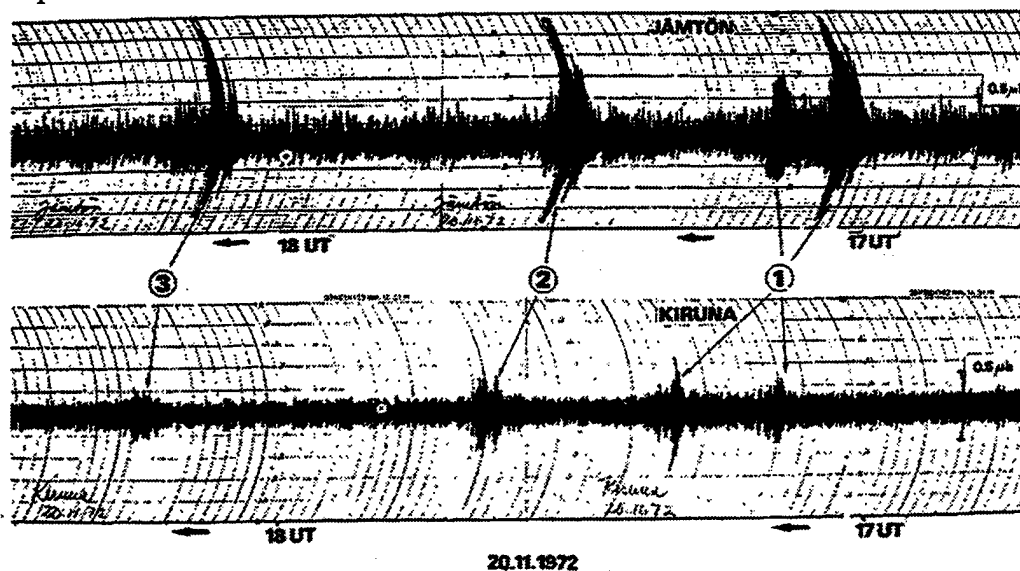


Figure 121. Infrasonic amplitude recordings at Kiruna and Jamton for a series of events associated with a hydroelectric power plant located at Tuggen, Sweden. [Figure adopted from *Liszka* (1974).]

Other quoted industrial sources of infrasound were: industrial plants emitting steam or gases, oil field gas exhausts, and oil derricks in the North Sea. In addition, it was speculated that "infra-acoustic energy is probably generated and radiated by oscillating water masses in the dam, headrace or tailrace tunnels."

In addition to identifying sources of industrial infrasound, *Liszka* (1974) summarizes an analysis procedure utilized by *Cowling, Webb and Yeh* (1970) to estimate the arrival angle and phase velocity of gravity wave arrivals utilizing a tripartite array of sensors located at the positions  $(x_1, y_1)$ ,  $(x_2, y_2)$  and  $(x_3, y_3)$ . The procedure involves knowing the frequency of the arrival,  $f$ , the positions of the microphones and the measurement of the phase difference between the microphone pairs 1 and 2 ( $\Delta\phi_{12}$ ) and the microphone pairs 1 and 3 ( $\Delta\phi_{13}$ ). In terms of these quantities, the arrival angle ( $A$ ) is given by

$$A = -\tan^{-1} \left[ \frac{y_1 - y_2 - P(y_1 - y_3)}{x_1 - x_2 - P(x_1 - x_3)} \right] \quad (6.13)$$

where  $P$  is the phase difference ratio given by

$$P = \frac{\Delta\phi_{12}}{\Delta\phi_{13}} \quad (6.14)$$

and the expression for the phase velocity is given by

$$V_p = \frac{2\pi f}{\Delta\phi_{12}} [(y_1 - y_2)\cos(A) - (x_1 - x_2)\sin(A)] \quad (6.15)$$

## 6.7 Jet Stream

*Claerbout* (1967) suggested in his Ph.D. thesis that the jet stream generates internal gravity waves. *Herron and Tolstoy* (1969a) postulated that perturbations in the jet stream were the cause of a fairly continuous, but low level background of pressure fluctuations in the mesoscale range observed on microbarograph arrays deployed around the general area of Columbia University's Hudson Laboratory at Dobbs Ferry, New York. By mesoscale is meant pressure wavelengths in the range extending from 1 km to  $10^3$  km or in the period range extending from several minutes to several hours.

*Herron, Tolstoy and Kraft* (1969) present data acquired on large (~ 250 km sensor spacing) and small (~ 2 km to 5 km) microbarograph arrays which provided the impetus for the *Herron and Tolstoy* (1969a) postulate. The data evidenced "a correlation of seasonal pressure spectrum levels with horizontal distance to the core of the jet stream winds." The observed pressure waves "correlate in velocity and direction with the jet stream winds over the array." In addition, it was observed that much of the noise in the 20 min to 90 min period range moved across the array at speeds comparable to those of the jet stream: 10 m/s to 50 m/s. Figure 122 provides an example of pressure fluctuations associated with jet stream winds as recorded on various stations in the Hudson Laboratory network as recorded on October 14, 1967. The Nevis and BT1 stations are the farthest apart at a distance of ~ 7 km and records evidence a high signal correlation over this sensor separation.

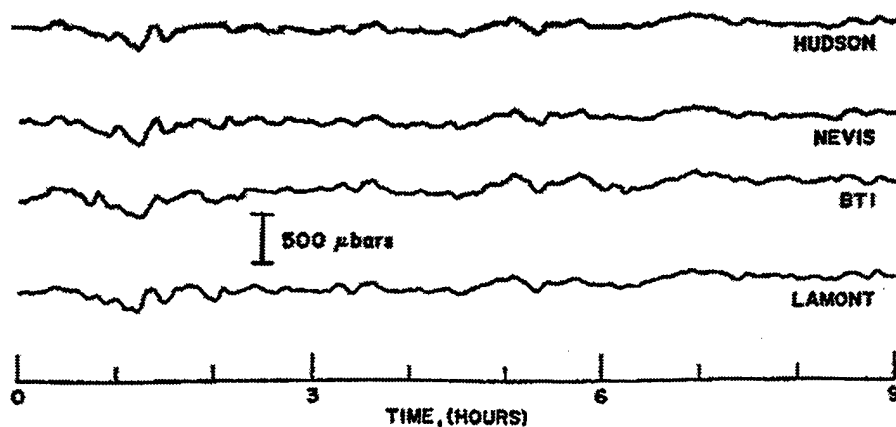


Figure 122. Waveforms recorded on selected microbarographs in two infrasonic arrays near the Hudson Laboratory and which are associated with perturbations in the jet stream. [Figure adopted from *Herron, Tolstoy and Kraft* (1969).]

Figure 123 presents the mean monthly pressure spectra based on 24-hour data samples measured at the Hudson infrasonic station in 1967. The spectral levels are seen to exhibit a seasonal or monthly variability and the dashed lines which bracket the monthly spectra represent the extremes in the measured data. The dotted curve which lies in the high frequency region extending from approximately 10 cph to 800 cph is the average profile for July. The dashed curve at the bottom is a wind velocity spectrum due to *Van der Hoven*

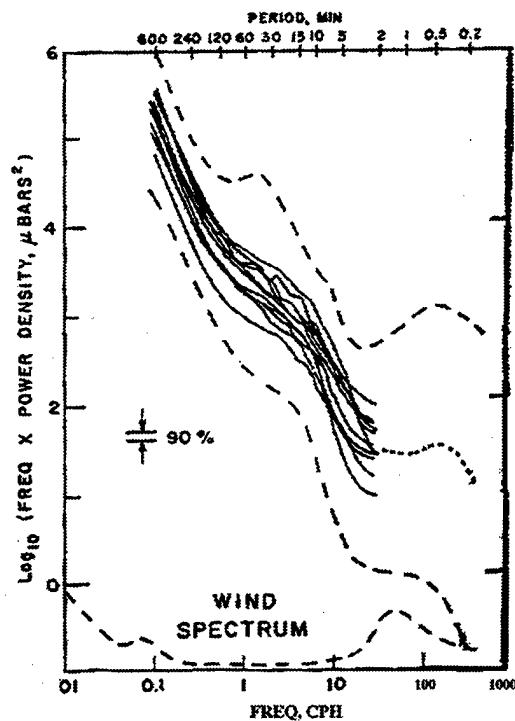


Figure 123. Average monthly pressure spectra recorded at 24 hour intervals on a microbarograph located at the Hudson Laboratories. The spectra are associated with perturbations in the motion of the jet stream. [Figure adopted from *Herron, Tolstoy and Kraft* (1969).]

(1957). The short period peak in the spectra near 100 cph is due to turbulence effects near the earth's surface and has been found to correlate with a peak in *Van der Hoven's* (1957) spectrum [*Gossard*, 1960]. The peak or "knee" in the spectra in the frequency band extending from 1 cph to 10 cph was postulated to represent input to ground based pressure fluctuations due to variability in the jet stream.

*Herron and Tolstoy* (1969) presented additional data showing a strong correlation of the direction of movement of the observed low-frequency pressure disturbances and the direction of high altitude tropospheric winds which can persist for weeks. Graphic illustration of the correlation of direction of movement of high altitude tropospheric winds and the direction of movement of low-frequency pressure disturbances is provided in Figure 124.

In theoretical calculations, *Herron and Tolstoy* (1969b) compute the pressure fluctuations observed at the ground which would be produced by a simple harmonic wave

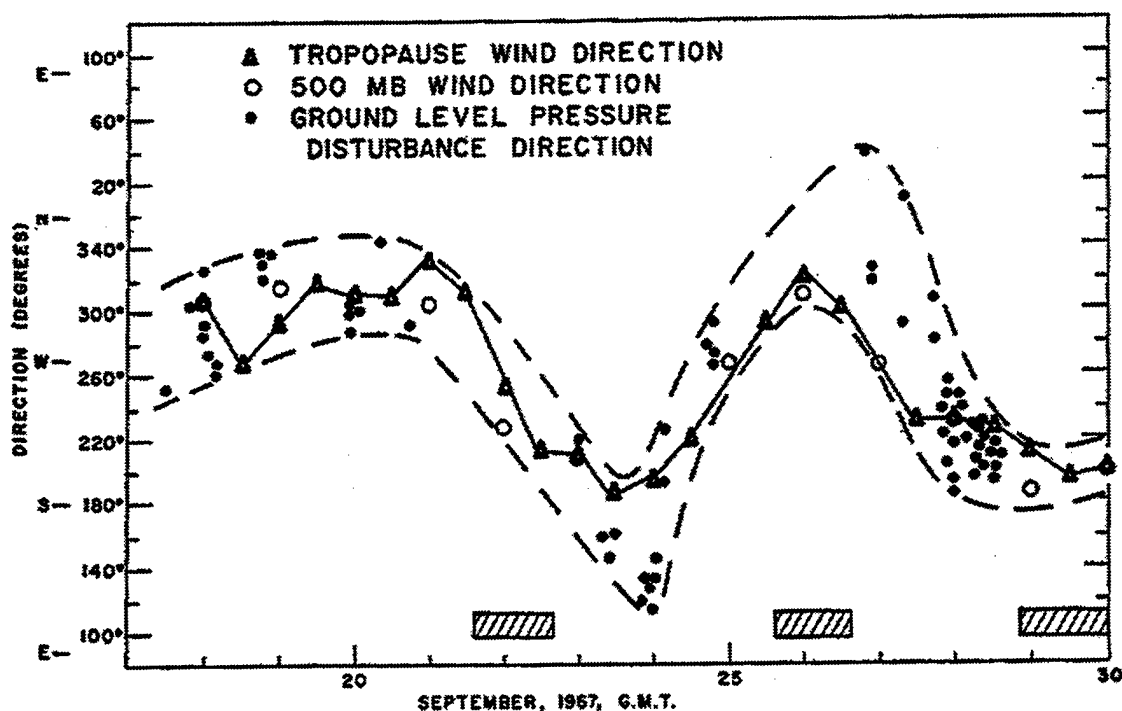


Figure 124. The measured correlation between the direction of high altitude (500 mb) and tropospheric winds, with the ground level pressure wave disturbance direction. The dashed curves indicate extreme values and the cross hatched regions correspond to those time intervals in which pressure data is absent. [Figure adopted from *Herron and Tolstoy* (1969).]

at the height of the tropospheric jet stream and propagating with a phase velocity equal the average speed of the jet stream core. Utilizing linear gravity wave theory, measured jet stream wind velocity power spectra [*Kao and Woods* (1964)], and the assumptions that spectra are "frozen in" and stationary, *Herron and Tolstoy* (1969b) show that the simple model provides an estimate of the ground level pressure fluctuations which is in reasonable agreement with experiment. The theoretical expression derived for the power spectrum of the pressure fluctuations,  $\Pi$ , is given by

$$\Pi \equiv 0.2c^2k \frac{\gamma}{\gamma_0} E_{ss}(k), \quad (6.16)$$

where  $c$  is the speed of sound,  $k$  is the wavenumber in cycles/km,  $E_{ss}(k)$  is the *Kao and Woods* (1964) longitudinal power spectrum for longitudinal wind velocity fluctuations,  $\gamma_0$

is the gravity-wave vertical wavenumber at the height of the jet stream, and  $\gamma$  is the same quantity evaluated at the ground surface. A comparison of the predictions of Eq. (6.16) with measured power spectra is given in Figure 125. As is evident from inspection of the figure, the predictions of Eq. (6.16) are in general accord with the observations.

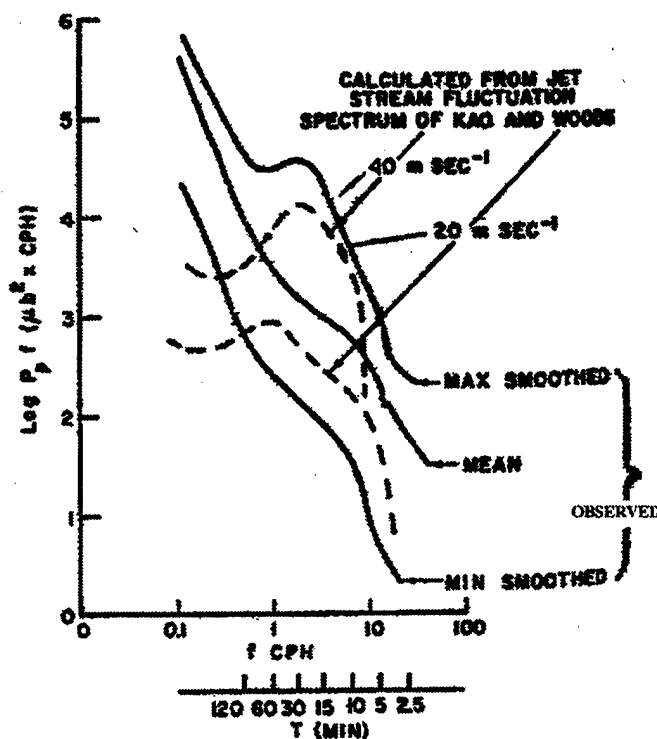


Figure 125. A comparison of mean pressure power spectra observed at the ground by Herron and Tolstoy (1969) with the calculated spectra which assumes perturbations in the jet stream radiate internal gravity waves. [Figure adopted and modified from Tolstoy and Herron (1969).]

## 6.8 Microbaroms

Microbaroms are infrasonic pressure waves having a period of from 5 seconds to 8 seconds and amplitudes of a few  $\mu\text{bar}$  and are the atmospheric analogs of "microseisms" which have been observed on land based seismometers. Donn and Posmentier (1967) indicate that the signals were first observed by Benioff and Gutenberg (1939), Gutenberg and Benioff (1941) and by Baird and Banwell (1940).



*Daniels* (1962) briefly summarizes the work of *Benioff and Gutenberg* (1939) who observed microbaroms in the period range extending from 0.5 s to 5 s at Pasadena, CA, the work of *Baird and Banwell* (1940) who independently observed microbaroms in the period range extending from 4 s to 10 s in measurements conducted at New Zealand and who also reported that simultaneously recorded microseisms had the same period although an exact matching between the two signatures was rarely possible. *Daniels* (1962) also refers to his own earlier observations [*Daniels* (1952, 1953 and 1959)] and the work of *Saxer* (1954) who reported "a high degree of correlation between the amplitudes of ocean waves in the north Atlantic and microbaroms observed in Freiburg, Switzerland. Furthermore, almost perfect correlation was found over an interval of about one month between periods of microseisms recorded at Strassburg and microbaroms recorded in Freiburg."

*Daniels* (1962) also rejected his earlier hypothesis that the source generation mechanism was due to "transient groups of standing waves" [*Daniels* (1953)] because such a source is multipole in nature and too weak to produce the observed effects. In place of this mechanism, one proposed by *Nanda* (1960) for the explanation of microseisms was suggested as a possible source for microbaroms as well. In the latter mechanism, the periodically varying amplitude of sea waves produces an oscillatory wind drag which, when the mean ocean surface is tilted, can produce a vertical component leading to the production of microseisms. *Daniels* (1962) notes, in this context, that both a level and tilted surface will produce oscillatory atmospheric pressure waves.

*Donn and Posmentier* (1967) present data on microbaroms which were recorded on a tripartite array of microbarographs located near Lamont Geological Observatory on April 7, 1966 when a severe storm was present in the North Atlantic. The array consisted of three condenser microphones equipped with *Daniels* pipe wind noise filters 1,000 ft in length. In addition to data from the microbarographs, concomitant microseism data was presented which was gathered on a seismometer. The spectra of the acoustic and seismic data were found to be very similar with only a slight shift in the spectral peaks: "the

microbarogram peaks at 5.8 and 6.3 sec and the microseism peaks at 5.9 and 6.5 sec." However, a lack of correlation between the microseism and microbarom amplitude fluctuations was observed. It was argued that the similarity of spectra implied a common source but that the lack of correlation between the microbarom and microseism amplitude fluctuations implied that the microbaroms were not produced by microseisms, i.e., by the motion of the ground.

Following the publication of this data set, *Posmentier* (1967) published a theory of microbaroms which was based on the work of *Longuet-Higgins* (1950) and on an investigation of two source generation mechanisms associated with marine storms: (1) "an ocean whose surface is moving in randomly related patches of standing waves", referred to as "center of gravity coupling"; and (2) "an ocean whose surface is moving in randomly related patches of progressive wave trains", referred to as "off resonant coupling". Numerical modeling was used to demonstrate that center of gravity coupling was the generation mechanism which best fit the data: microbarom periods equal to one-half that of the ocean waves and microbarom amplitudes of a few  $\mu$ bars. The theoretical expression obtained by *Posmentier* (1967) for the pressure due to a patch of standing waves is

$$p = \frac{\rho a^2 \omega^2 K S}{\pi r} \quad (6.17)$$

where in the above,  $\omega$  is the angular frequency of the ocean waves,  $a$  is the wave amplitude,  $\rho$  is the air density,  $K$  is the acoustic wavenumber,  $S$  is the patch area and  $r$  is the range to the receiver.

In his review of previous experimental work, *Posmentier* (1967) mentions the observations by *Baird and Banwell* (1940) in New Zeland who reported that the periods of both microbaroms and microseisms were in the period range of from 4 s to 10 s and that the amplitudes of the microbaroms and microseisms generally "wax and wane" together and that microbarom amplitudes are generally larger at night: in contrast to microseism amplitudes which are invariant to a daily cycle.

In work conducted at Fribourg, Switzerland, *Saxer* (1945) made simultaneous measurements of ocean wave heights, microseisms and microbaroms and demonstrated a strong correlation between all three with microbarom pressure levels reported to be "sometimes greater than 1 $\mu$ bar". *Saxer* (1945) also explained the observed diurnal and annual variation of microbarom amplitudes as being due to "changes in the layer of air at 50 km up" [now known to correspond to the height of the stratopause] and "suggested that reflection of microbaroms takes place in this 50 km layer." In support of this conjecture, *Dessauer, Graffunder and Schaffhauser* (1951) reported microbarom phase velocity measurements, also obtained at Freiburg, of approximately 400 m/s.

In reviewing previous theoretical work on microbaroms, *Posmentier* (1967) mentions a number of works by *Daniels* (1952, 1953, and 1962) in which a variety of microbarom source mechanisms are proposed based on the: (1) " 'piston effect' of ocean waves, radiating in patches 40m square, and with random phase relations;" (2) "transient groups of standing waves;" and (3) oscillatory wind drag over the periodically varying surface of the ocean. The first proposed mechanism was shown to lead to microbarom amplitudes which were too high, the second proposed mechanism was found to be equivalent to a multipole source and, accordingly, too inefficient and the third proposed mechanism has evidently not been reduced to a form which can be compared to experiment.

In other theoretical developments, *Posmentier* (1967) reviews the work of *Cook* (1962a) who demonstrated that microseisms can't produce the observed microbarom levels observed on microbarographs and, conversely, microbaroms can't produce microseisms. *Cook* (1962a) also proposed and discarded a theory of microbarom generation based on infinite propagating wave trains because such waves were shown not to radiate acoustic energy. In later work, *Cook* (1962b) demonstrated that "a semi-infinite wave train has a non-zero energy radiation, and that the pressure field produced by such a source can account for the observed microbaroms."

*Donn and Rind* (1971 and 1972) report on additional observations of microbaroms and, in particular, on their potential use as a technique to monitor upper atmospheric wind and temperature changes utilizing known properties of the atmosphere in conjunction with acoustic ray tracing techniques.

Figure 126 provides typical microbarom signatures as recorded on three elements

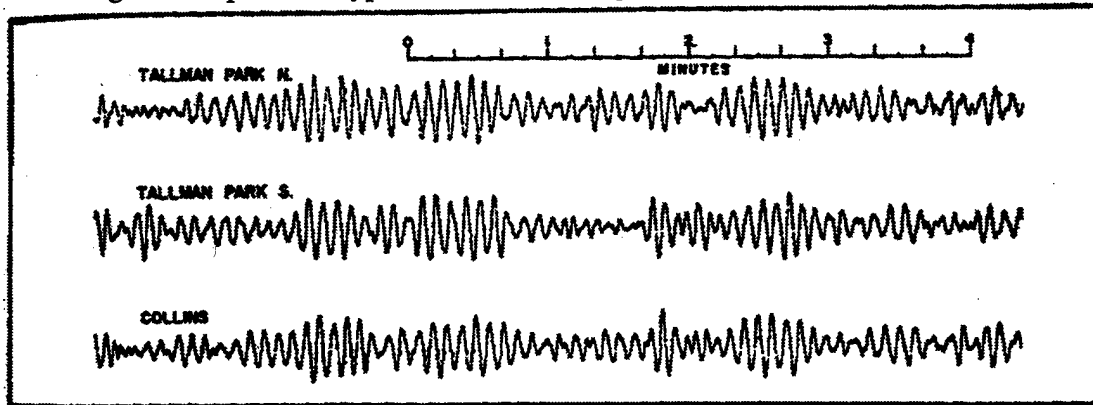


Figure 126. Microbaroms recorded on April 7, 1966 on three elements of the Lamont-Doherty tripartite microbarograph array located near Palisades, NY. [Figure adopted from *Donn and Rind* (1972).]

of the Lamont-Doherty tripartite microbarograph array located near Palisades, NY. The predominant period of the waves is 5 sec and the amplitudes are a few  $\mu$ bars. The records are highly coherent at a level of 0.8 and the source of the particular signals shown was demonstrated to be a marine storm east of Newfoundland, Canada.

In the absence of other interfering signals, the predominant variability in microbarom levels observed at Lamont occurred in the fall, winter and early spring is semi-diurnal and a typical example of this variability is shown in Figure 127. The data were acquired in October of 1967 and the periods of high amplitude occurring at the hours of 1200 and 2400 are clearly in evidence. Although this semi-diurnal variability is the most characteristic, *Donn and Rind* (1971 and 1972) were able to demonstrate that there are diurnal and seasonal variations in microbarom amplitudes which can be associated with, for example, tidal and seasonal wind variations and stratospheric warmings.

Figure 128 illustrates the seasonal (or monthly) variability in microbarom amplitudes for the months of January, April, May, July and October. Inspection of the

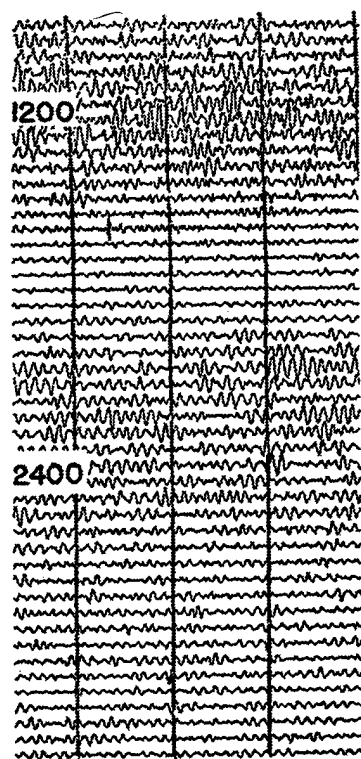


Figure 127. Portions of microbarograph drum records acquired on October 6 to October 6, 1969. In the figure each horizontal trace represents 30 minutes of data. The semi-diurnal variation in microbarom amplitude is clearly in evidence. [Figure adopted from *Donn and Rind (1971)*.]

upper panel of the figure indicates the two semi-diurnal peaks occurring near 2100 and 1100 but also indicates the presence of variability on other time scales as indicated by the broadening of the peak near 2100 in comparison to that at 1100. The broadening of the peak near 2100 is due to averaging over a "less-frequent third peak at 0400." The fact that the minima in the January curve were less pronounced than in the other months was determined to be due to a stratospheric warming which effectively created a reflecting layer at 50 km producing enhanced microbarom signals.

Inspection of the lower panel of Figure 128 shows that microbarom amplitude magnitudes and their variability are low in the summer (July) and that the amplitude magnitudes and their variability are distinctly different in the month of May for the two years shown. The higher levels in May of 1968 were argued to be due to the prolongation of winter propagation conditions caused by the stratospheric warming.

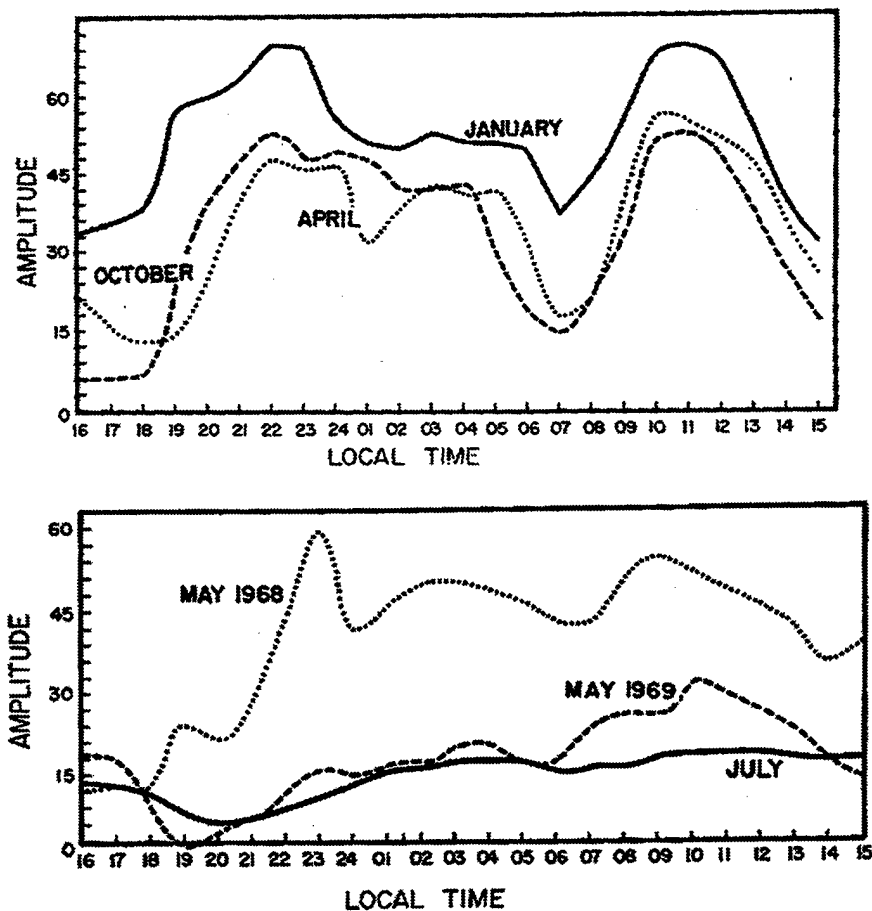


Figure 128. The upper panel shows average hourly amplitudes of microbaroms for January (solid curve), April (dotted curve) and October (dashed curve). The curves for January and October are based on three years of data and the curve for April on two years of data. The lower panel shows similar data for the months of May 1968 and May 1969 and July based on two years of data. In both panels, the amplitude scale is arbitrary. [Figure and caption adopted from *Donn and Rind (1972)*.]

## I. Microbursts

*Zuckerwar (1986)* has reported on the possibility of using infrasonic monitoring to detect the occurrence of a microburst or severe wind shear event located close to the ground. A three element array of microphones arranged in the geometry of an isosceles triangle having short sides of 800 ft (243.84 m) and a long side equal to 1,385 ft (422.34

m) was utilized. The sensors utilized were Globe 100C capacitance microphones which were equipped with wind screens and enclosed in wooden boxes and the array was deployed at the NASA Langley Research Center. Data from the microphones were filtered into the 2 Hz to 16 Hz band as wind noise was found to be high at frequencies below 2 Hz and, at frequencies above 20 Hz, man-made sources of background were quite significant.

To associate specific source signatures with recorded signals, *Zuckerwar* (1986) computed the auto- and cross-spectra of those signals which could be unambiguously associated with a single source and utilized meteorological support data available from the National Weather Service (reports of storms and atmospheric turbulence), LLP's (lightning locator plots) available from three stations in Virginia and air weather service - surface weather observations (local cloud cover, pressure, wind speed, etc.).

From an analysis of data acquired on 72 days during the time period of June 6, 1984 to December 5, 1984, it was determined that the great bulk of the data could be grouped into four spectral classes:

- Class 1: Signals having auto- and cross-spectra which "are characterized by a broad peak and high coherence. These are believed to originate from man-made sources", e.g., sonic booms or aircraft noise. These signals were found to comprise 15% of the total data set.

- Class 2: Signals believed to be associated with machinery noise and having spectra which "show one or more prominent discrete frequencies, which are believed to control the convergence of the adaptive filter. The prominent frequencies are usually in the vicinity of 10 Hz --but on rare occasion as low as 4 Hz, have a high coherence and high amplitude (at least 20 dB above the background), and occur according to no identifiable pattern." These signals were found to comprise 62% of the data set.

- Class 3: Signals of unknown origin having "spectra containing one or more narrow peaks, about 5 components wide, have a high coherence across the peak." These signals were found to comprise 7.6% of the data set.

- Class D: Signals thought to be associated with meteorological events and having spectra which exhibit "two distinguishing features: (1) a good fit to a power law with a negative slope but (2) low coherence ( $<0.4$ ) at nearly all frequencies." This class of spectra comprised the remaining 15% of the data set and representative auto-spectra of the signals are presented in Figure 129.

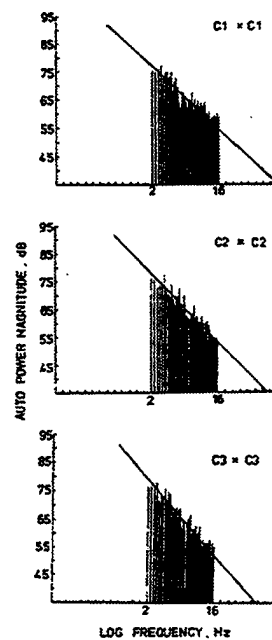


Figure 129. Spectra assumed to be associated with microburst phenomena. [Figure adopted from Zuckerwar (1986).]

Although Zuckerwar (1986) was unable to unambiguously associate a particular Class D waveform with a microburst event owing to the latter's unknown signal characteristics, it proved possible to make an association with several meteorological events such as distant and severe thunderstorms, hurricanes, gales and tropical storms and depressions. In addition, and of possible interest for the use of infrasound to monitor wind shear, 9 signals were observed over a three day period in November of 1984 during a period in which severe turbulence was in existence over the eastern part of the U.S. and reported to be "due to strong low level winds with possible low level wind shear."

In reviewing possible additions to the FAA's LLWSAS (Low-Level Wind Shear Alert System), Bedard (1984) summarizes what was then known about the microburst



phenomenon in addition to discussing larger scale thunderstorm outflows. The primary interest, however, was on developing methodologies to provide advanced microburst warning time utilizing additional conventional pressure sensors and anemometers which could be incorporated within to the existing LLWSAS. No mention was made, however, of using infrasonic monitoring at significant distances from the thunderstorm activity.

*Bedard* (1988) provided evidence of infrasonic emission from a microburst once it reached the ground. The event occurred on August 5th, 1985 and the "outflow passed through the meteorological tower of the Boulder Acoustic Observatory." The dominant frequency content of the received acoustic energy was in the 1 Hz to 2 Hz frequency band. *Bedard* (1988) indicated that the power spectral time plot of the microburst event was quite different from other natural events such as meteor and avalanche produced infrasound.

*Bedard's* (1988) observation appears to be in accord with the theoretical modeling results of *Hardin and Pope* (1988) who estimated the spectrum which might be expected from a microburst event close to the ground by utilizing predictions of aerodynamic noise generated by flow in the presence of an infinite plane [*Powell* (1960)] and a numerical simulation of the microburst flow field [*Proctor* (1987)]. The results of the calculations for the power spectral density of microburst noise is provided in Figure 130. The spectrum is observed to peak at 2.5 Hz.

## **6.10 Missile Launches**

*Fehr* (1967a) presented infrasonic records obtained from the launchings of Atlas-Agena and Scout rockets and, in addition, measurements of background noise in the frequency band extending from 0.5 Hz-to-20 Hz. The data were recorded on a four-element microbarograph array with each element equipped with a front-end noise filter. The work demonstrated that "signals from rockets igniting in the upper atmosphere and ionosphere travel long distances and can be detected by ground sensors."

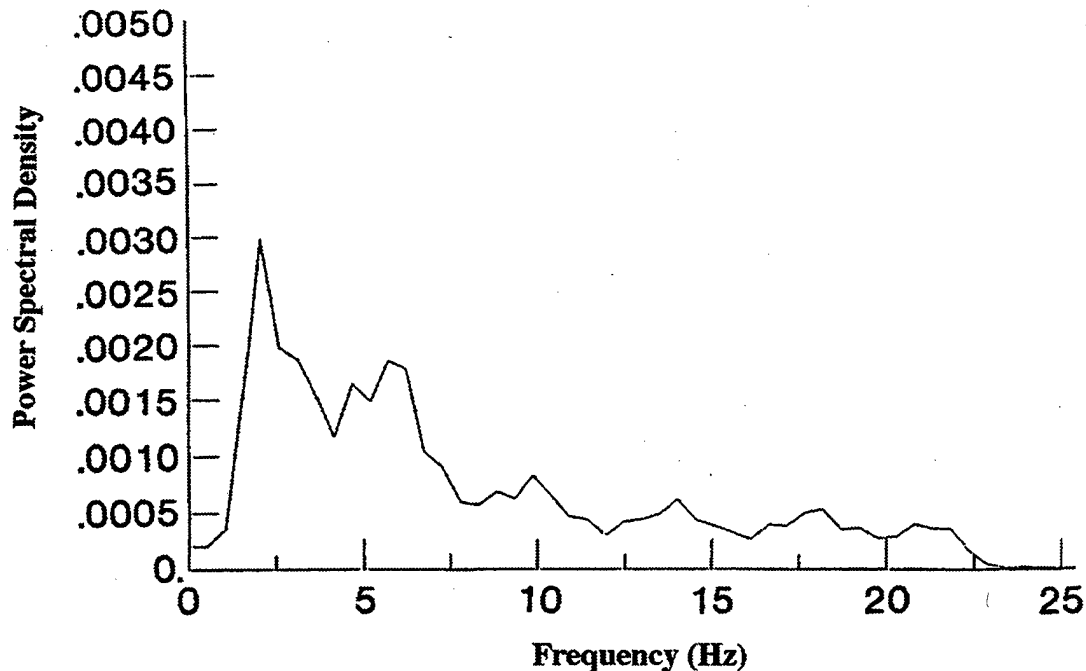


Figure 130. The predicted acoustic power spectrum for a microburst near or on the ground. [Figure adopted from *Hardin and Pope* (1988).]

The noise data were found to exhibit peaks near 1.5 Hz, 0.63 Hz and 0.83 Hz which were associated with atmospheric turbulence: an association which is in agreement with the work of *Wescott and Kushner* (1963) who concluded that sound radiation from upper air turbulence produced pressure signatures in the frequency range extending from 0.5 Hz to 1.5 Hz and having peak-to-peak pressure levels in the range extending from 0.1  $\mu$ bar to 3  $\mu$ bar peak-to-peak. In addition, a peak was measured at 16 Hz which was associated with waves breaking on the shore and subsidiary peaks were observed at 0.1 Hz 0.16 Hz which were associated with other ocean wave phenomena.

The recorded infrasonic rocket signals are thought to be created during the ignition phase of the various rocket stages and caused by turbulence [e.g., *Lighthill* (1954)] in the exhaust stream. The signals from both the Scout and Atlas-Agena rockets are characterized by an initial high intensity low-frequency phase due to rocket motor ignition which is followed by a higher-frequency phase of longer duration due to rocket exhaust. Figure 131 shows the records measured at four microbarographs due to an Atlas-Agena launch on November 8, 1965. The background noise levels are evidently quite different on the

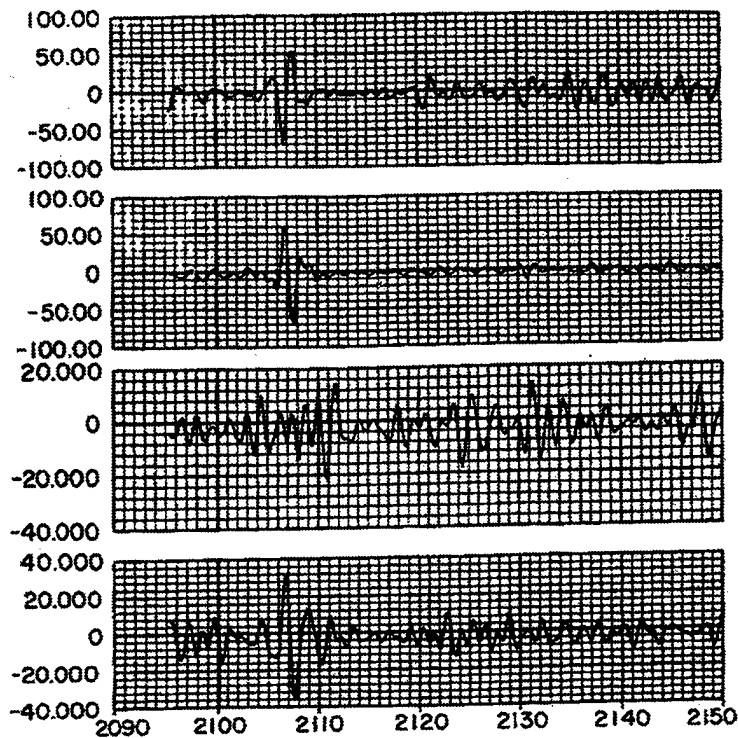


Figure 131. Four records which represent the arrival of infrasonic pressure waves from an Atlas-Agena launch at Vandenberg AFB on November 8, 1965. The noise levels on each of the four sensors making up the microbarograph array are seen to be quite different. [Figure adopted from *Fehr* (1967a).]

individual sensors making up the microbarograph array. The Atlas-Agena ignition signal arrives after T+2100 seconds.

*Kaschak* (1969) published observations on the long-range propagation and detection of subsonic, normal and supersonic signals produced during missile launches at Cape Kennedy, FL, and Vandenberg AFB, FL. The data were acquired on U.S. Army microbarograph arrays arranged in a square 457.5 m on a side and having a signal passband extending from 0.4 Hz to 15 Hz. The subsonic signals were the most infrequently observed and had group velocities in the range extending from 190 m/s to 240 m/s whereas the supersonic exhibited group velocities in the range extending from 500 m/s to 1000 m/s and were associated with missile launches in which the thrust was greater than 200,000 lbs.

The frequency range of the signals was observed to have a center frequency of 1.0 Hz and a bandwidth extending from 0.5 Hz to 3.0 Hz. Signal durations from the launches

at Vandenberg AFB, as measured by arrays located in California, Oregon and Washington, D.C. were observed to increase with increasing source-to-receiver range and had durations extending from 108 s to 320 s with the normal signals exhibiting longer durations than the supersonic arrivals. *Kaschak* (1969) did not publish source levels nor did he postulate a source mechanism.

*Balachandran and Donn* (1971b) discuss the characteristics of infrasonic signals associated with the launches of the Saturn V, Apollo 4 and Apollo 14 launches from Cape Kennedy on November 9, 1967 and January 13, 1971, respectively and summarize similar observations obtained in earlier work: *Donn et al.*, (1968), *Kaschak* (1969), *Kaschak, Donn and Fehr* (1970) and *Balachandran and Donn* (1971a). Figure 132 provides the infrasonic signal recorded on one of the Lamont-Doherty microbarograph arrays associated with the Apollo 4 launch.

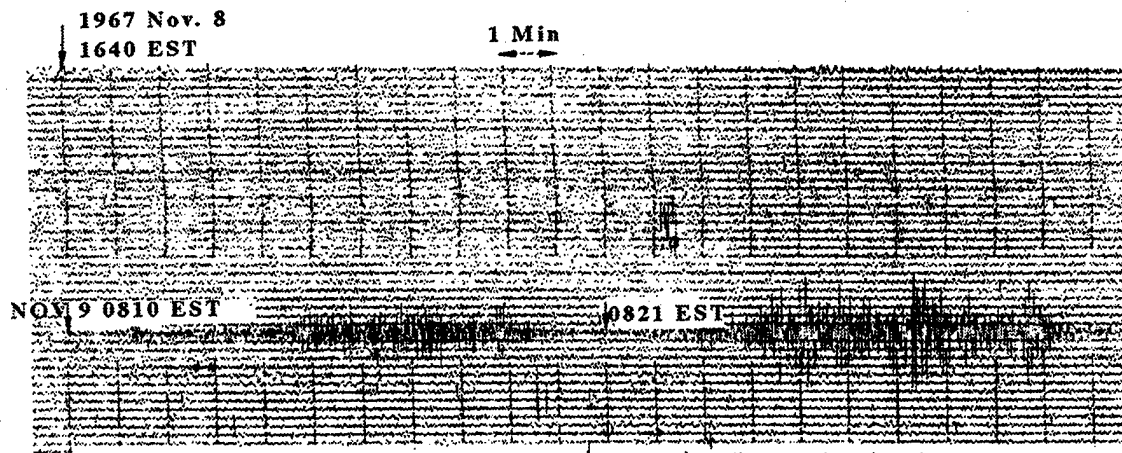


Figure 132. The infrasonic signal received at a Lamont-Doherty microbarograph array associated with the launch of the Saturn V Apollo 4 spacecraft. The maximum amplitude of the signal is 20  $\mu$ bar and the first arriving pulse is associated with the first stage re-entry signal and the second with the launch. [Figure adopted from *Balachandran and Donn* (1971b).]

In summarizing the earlier work, it is noted that the infrasonic signals associated with rockets vary from fractions of a Hz to a few hertz and are detected at long ranges (~1,000 km): a circumstance consistent with an aerodynamic source for the propagating energy rather than that of the rocket motor. In addition, received signal amplitudes exhibit

seasonal variations in the amplitude of the detected signals which can be explained by the variation of the stratospheric winds.

Inspection of the signal in Figure 132 shows that each of the pulses making up the total waveform last for several minutes and that there is a gradual build up in signal amplitude to a maximum and then a gradual decay in amplitude for each of the pulses making up the total waveform. *Balachandran and Donn* (1971b) were able to explain both the pulse length and amplitude behavior of the pulses utilizing ray theory. The time spread was found to be due to the arrival times of the particular contributing rays and the amplitude behavior due to constructive or destructive interference. Because of meteorological uncertainties, the individual rays contributing to each time element of the pulses could not be determined. The characteristics of the Apollo 14 signal were found to be different from those of the Apollo 4 signal and to have a lower maximum amplitude of 10  $\mu$ bar. In particular, the Apollo 14 signal did not consist of separate re-entry and launch pulses but exhibited an essentially continuous waveform owing to pulse overlap: a circumstance attributable to different environmental conditions.

*Posmentier* (1971) presented preliminary observations of natural background infrasound in the frequency band extending from 1 Hz to 16 Hz and presented waveforms in this band associated with the launch of the Apollo 14 rocket and with a source attributed to a local aircraft. The array consisted of four microbarograph sensors described as "Fehr and Fisk 'Aerophones', which employ thermistors to measure the flow in a tube connecting a reference volume to the environment [*Fehr* (1967b)]". The sensors making up the array were separated by a distance of 9 m and arranged in a "star pattern" (i.e., an equilateral triangle with a sensor at the geometric center) which has been shown to be the optimum configuration [*Haubrich* (1968)] and, it is noted parenthetically, is the array configuration selected for the international array of stations to be deployed to monitor compliance to a CTBT. Figure 133 presents examples of the waveforms recorded.

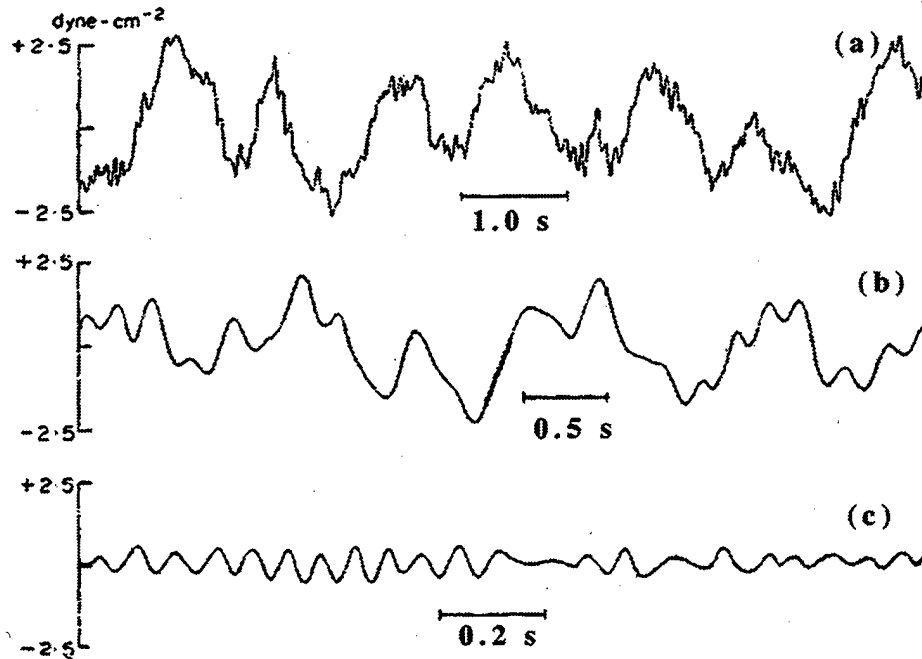


Figure 133. Examples of signals recorded on a four element microbarograph array installed at Sterling Forest, NY, a rural area about 50 km from New York City. Panel (a) is the waveform associated with the Apollo 14 launch; Panel (b) is the waveform associated with a local airplane and Panel (c) is a sample of the natural background noise in the frequency band extending from 1 Hz to 16 Hz. [Figure adopted from *Posmentier* (1971).]

A segment of the signal recorded from the launch of the Apollo 14 is shown in the top panel of Figure 133. A spectral analysis of the signal indicated that the frequency associated with the maximum variations of the waveform was 1 Hz. The total duration of the signal was reported to be 11 min and, as in the observations of *Balachandran and Donn* (1971b), did not consist of a waveform made up of two sub-pulses corresponding to the arrival of the re-entry and launch phases but, rather, was essentially continuous in nature. In addition to meteorological conditions, *Posmentier* (1971) noted that the flight path of the launch was more southern than earlier launches: a circumstance leading to the temporal overlap of the re-entry and launch waveforms.

The aircraft signature shown in the middle panel of Figure 133 was found to be highly coherent between the sensors making up the array, to have a duration of 30 s, to have a peak-to-peak amplitude of 5  $\mu$ bar, and primary energy in the frequency band

extending from 3 Hz to 16 Hz. The background noise, a sample of which is shown in the lower panel of Figure 133, was associated with microbaroms.

*Hilton and Henderson* (1974) present measurements of sonic-boom overpressures associated with the launchings of the Apollo 15 and 16 moon explorations. The pressure sensors were reported to be sensitive broadband condenser-type microphones equipped with wind screens located at various places on ships at sea. During the launch or ascent phase, pressure data were recorded at ranges of 68 km, 87 km, 92 km, 129 km and 970 km and during the re-entry or descent phase data were acquired at ranges of 9 km, 13 km, 55 km, 185 km and 500 km. Figure 134 provides records of measured sonic-boom signatures recorded during the re-entry phase of the Apollo 15 mission on three ships located in the Pacific Ocean and Figure 135 provides a comparison of measured aircraft and spacecraft overpressures associated with descent phases with those predicted by theory [i.e., *Carlson* (1964) and *Seebass* (1967)]. The agreement between theory and experiment is seen to be quite good.

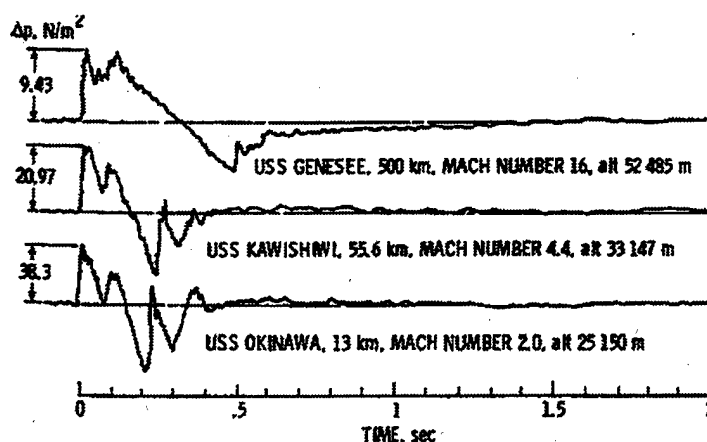


Figure 134. Examples of measured sonic-boom signatures recorded during the descent of the Appollo 15 space capsule as recorded on ships deployed at the indicated locations. [Figure adopted from *Hilton and Henderson* (1974).]

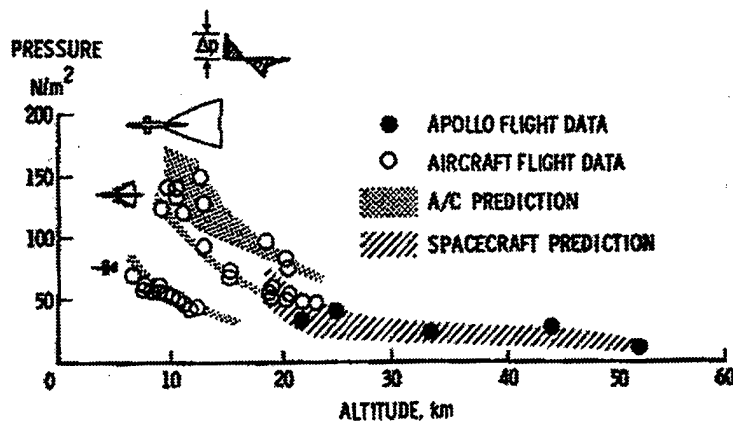


Figure 135. A comparison of measured spacecraft and aircraft peak overpressures with predictions made based on available theory. [Figure adopted from *Hilton and Henderson (1974)*.]

### 6.11 Mountain Associated Waves (MAWs)

*Jordan (1972)* reports the observation of slowly moving gravity waves, or MAWs, produced by the wind on the leeward side of the Continental Divide. The observations were acquired utilizing a four-element microbarograph array comprised of sensors spaced at distances extending from 1 km to 2 km and located at the University of Denver 50 km from the Continental Divide. The basic sensor was the T21B infrasonic microphone which was not equipped with a Daniels front-end noise filter.

The MAW associated gravity waves were found to have periods in the range extending from 2.5 min to 15 min, amplitudes in the range extending from 70  $\mu$ bar to 320  $\mu$ bar and propagation speeds in the range extending from 5.2 m/s to 50 m/s. Three source mechanisms were postulated for the waves: (1) wind shear near the axis of the jet stream for those waves traveling with speeds near the higher end of the speed range and propagating in the same direction as the jet stream; (2) turbulent air flow produced by winds blowing over the mountain tops and (3) by the interaction of downslope winds, produced by winds blowing perpendicular to the general orientation of the mountain tops, and inversion layers. With respect to the second source mechanism, it was observed that the ACSL (altocumulus, standing wave lenticular clouds) had wavelengths of  $\sim 5$  km which were the same as the observed 10 min period gravity waves.



*Larson, Craine, Thomas and Wilson* (1971) present data on MAWs as recorded on microbarograph stations located at Pullman, WA, Boulder, CO and College, Alaska focusing, in particular, on an event occurring November 28-30 in 1968. The authors characterize MAWs as having a period range extending from 10 s to 100 s, zero-to-peak amplitudes in the range from 0.5 mbar to 7 mbar, trace velocities corresponding to acoustic and higher, and durations lasting from a few hours to a few days. Figure 136 exhibits the signal or correlation of records from the four microbarograph sensors located at Pullman, WA on November 28, 1968 at 1430 UT. The peak-to-peak signal amplitude is 6.5  $\mu$ bar and the average period of the wavetrain was measured to be 50 s.

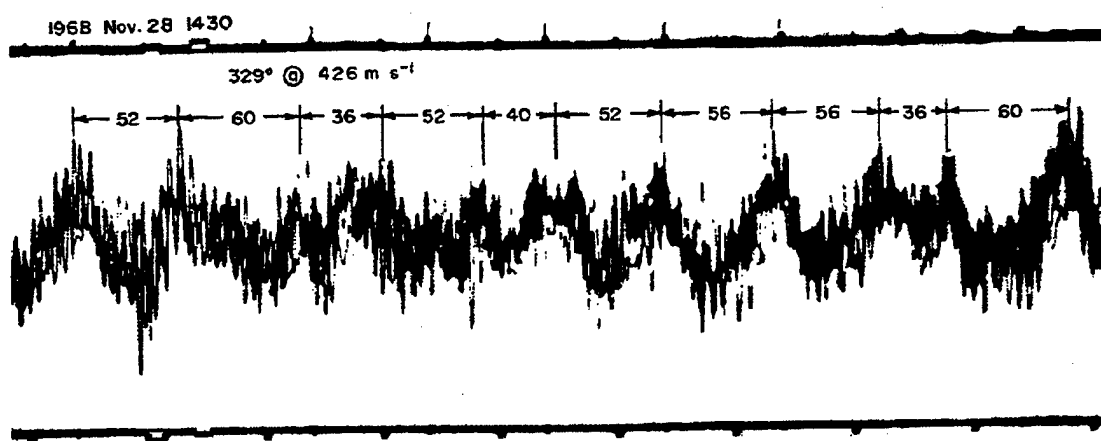


Figure 136. The correlation MAW signals recorded on a four element microbarograph array located at Pullman, WA at 1430 UT on November 28, 1968. The periods of selected segments of the wavetrain are as indicated with the average period of the total wavetrain measured as 50 s. The approximate peak-to-peak signal amplitude is 6.5  $\mu$ bar and the measured trace velocity was 426 m/s. [Figure adopted from *Larson, Craine, Thomas and Wilson* (1971).]

The association of the received signals with mountains was accomplished by using the three microbarograph stations for triangulation to show that the principal source areas were "along the coast of British Columbia and in the inland Rocky Mountains of the British Columbia-Alberta border. In addition, the investigators proposed that some of the observed events were associated with aerodynamic sound generation associated with the wind blowing over mountain ranges with, perhaps, the formation of Karman vortices which

create a dipole acoustic source radiating perpendicular to the direction of flow over an obstruction such as a mountain [e.g., *Abernathy and Kronauer* (1962)]. In support of this mechanism, *Larson, et al.*, (1971) noted the existence of satellite pictures distinctly showing vortex shedding by mountains [NASA (1967)] and established a strong correlation between the month-to-month variation of the amplitude of MAWs recorded at Boulder, CO with the annual variation of wind zonal and eddy kinetic energy in the 850-to-500 mb layer.

*Rockway, Hower, Craine and Thomas* (1974) investigate the seasonal variability of MAWs using a three-dimensional ray tracing computer program developed by *Dickenson* (1971) and *Dickenson, et al.*, (1972). The earlier work of *Larson, et al.*, (1971) is cited in which MAWs were observed in the period range of from 10 s to 100 s, to travel with acoustic velocity or higher and to have zero-to-peak amplitude variations extending from 0.5  $\mu$ bar to 7.0  $\mu$ bar. Average temperature and wind speed profiles appropriate to the winter and summer were used to illustrate the extreme variability in propagation due, primarily, to winds. It was concluded that atmospheric variability is such as to make it impossible to clarify the source generation mechanism.

*Rockway, et al.*, (1974) summarize infrasonic observations of MAWs and discuss possible source mechanisms for their generation. The signals are characterized as having very small amplitudes, normally less than 1  $\mu$ bar peak-to-peak, and to have very long durations: 24 hours or longer. Usually, but not always, MAWs are produced when the winds at 500 mbar exceed 20 m/s.

MAW observations are discussed based on data gathered at two infrasound stations located in Moscow, Idaho and at Edson, Alberta, Canada and it is shown that some of the primary source areas for the signals "are along the western Canadian coast and the mountain range running from Canada through Montana, Idaho, Wyoming and Colorado."

The source mechanisms for the MAWs are postulated to be associated with three classes of turbulent flows: isotropic turbulence, mean shear turbulence or a combination of

the two. For the case of sound generation by isotropic turbulence, the acoustic spectrum is predicted to have a  $f^{-7/2}$  frequency dependence for frequencies much greater than the ratio:  $C_0 M/L$ , where  $C_0$  is the speed of sound in the fluid,  $M$  is the mach number and  $L$  is the size of the largest turbulent eddy size [Meecham and Ford (1958)]. For the case of sound produced by mean shear turbulence, the acoustic spectra is predicted to have a frequency dependence of the form  $f^{-2}$  [Meecham (1971)].

From inspection of the acoustic power spectra derived from 8 MAW events, it is concluded that the spectral behavior most often associated with the observations is of the form  $f^{-3}$  and, accordingly, associated with isotropic turbulence. For specific mechanisms, Thomas, et al., (1974) consider three specific source mechanisms: the jet stream, breaking lee waves and wake turbulence, and conclude that wake turbulence is the most likely source as the former two sources would be expected to produce flatter spectra than those observed.

Greene and Howard (1975) review the infrasonic data collected on eight NOAA infrasound stations during a one year period extending from July 1, 1972 to June 30, 1973 and identify three major sources of natural infrasound: magnetic storm activity, severe weather and MAWs. A map of the NOAA station locations and microphone array geometry for each station is provided in Figure 137. As indicated, the typical infrasound station consisted of an array of four or five individual microphones. Each microphone was equipped with a front-end Daniels pipe array 1000 ft (304.8 m) in length with inlet ports spaced every 5 ft (1.52m) or, in some cases, every 10 ft (3.05 m). The microphone inter-element spacing varied and extended from 5 km to 10 km.

During the referenced one year period, over two hundred infrasonic events were detected and the stations in the network were used to derive source locations through triangulation. A number of events of high trace velocity were observed at the College, Alaska station and associated with periods of high magnetic storm or auroral activity. A

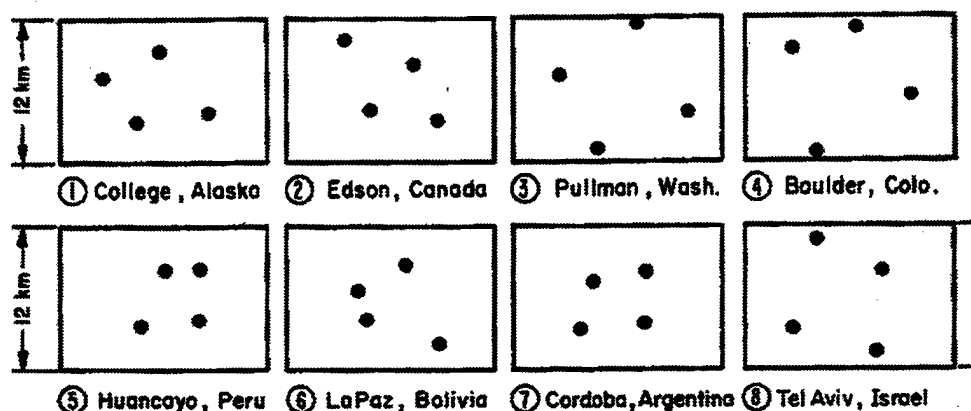
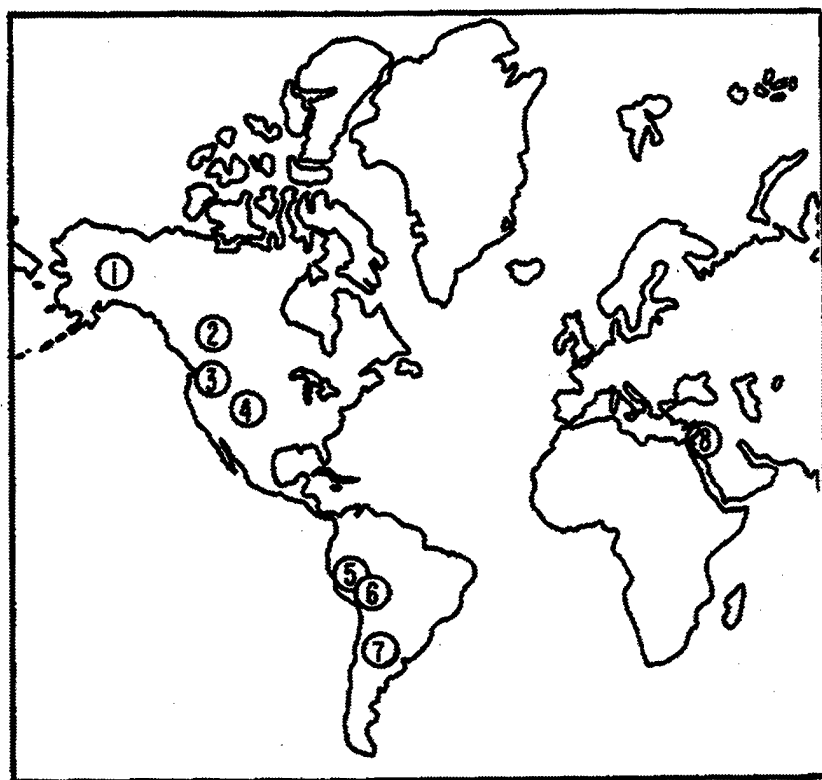


Figure 137. NOAA infrasound stations and array geometry of the NOAA infrasound network. [Figure adopted from *Greene and Howard (1975)*.]

number of other events were observed and associated with severe weather and thunderstorm activity. However, the great bulk of the events were associated with MAWs. Figure 138a shows the locations of MAW sources in the northern hemisphere and Figure 138b shows the source locations in the southern hemisphere. The lack of observed MAWs in the northern section of the Andes was taken as support for the "concept that not all

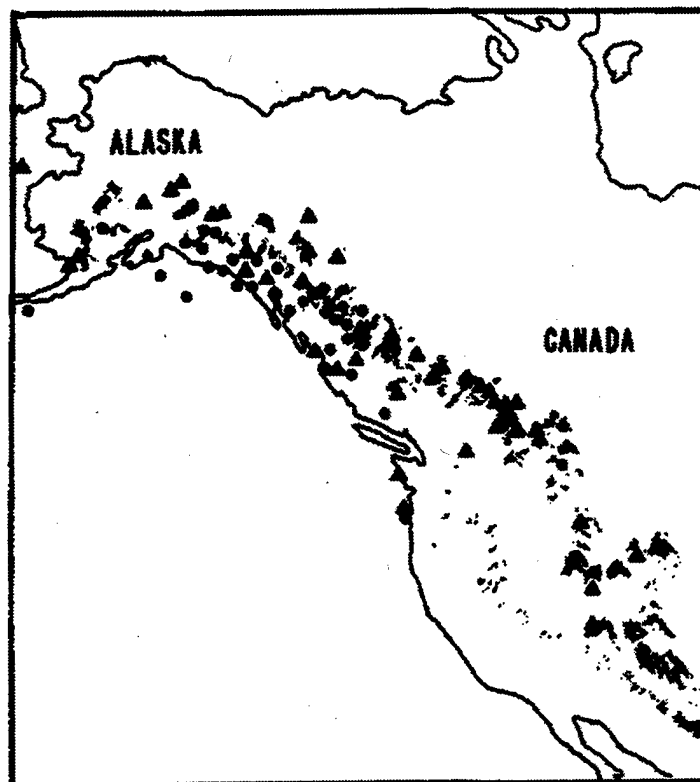


Figure 138a. Microbarograph intersections of infrasound from mountain-associated waves in the Northern Hemisphere. [Figure adopted from *Greene and Howard (1975)*.]

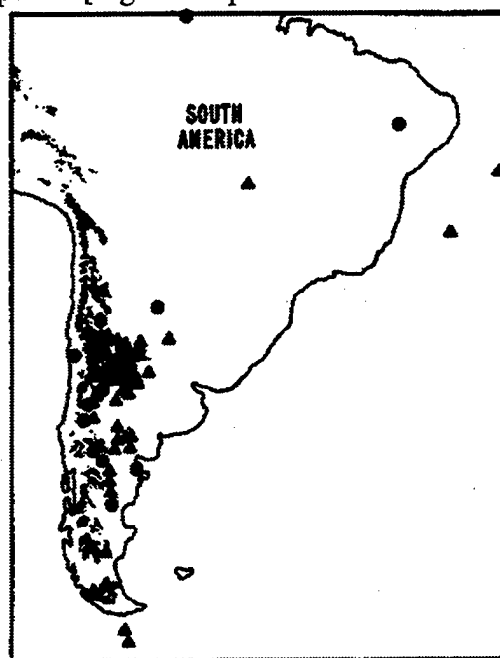


Figure 138b. Microbarograph intersections of infrasound from mountain-associated waves in the Southern Hemisphere. [Figure adopted from *Greene and Howard (1975)*.]

mountains radiate sound and that either some as yet unknown topography or more likely some combination of topography and meteorology is required.

*Hauf, et al.*, (1995) report on the observation of short packets of gravity wavetrains associated with air flow over the Alps and the observation of similar signals before the approach of fronts and thunderstorms. The observations were made with a four-element microbarograph array located in southern Bavaria. The array was designed for the observation short gravity waves with wavelengths in the range extending from 2 km to 30 km and the average array element separation was reported to be 1.2 km. The basic sensor was described as a capacitor microphone exposed to the differential pressure between an internal reservoir and ambient air. An adjustable needle valve was used to control the air flow between the reservoir and the environment. The time resolution is cited as extending from 2 s to 30 min with a resolution of 3  $\mu$ bar. Use is made of wavelet analysis processing for the data acquired on each sensor to isolate the events of interest in time or period from unwanted background noise and sources. Figure 139 displays the pressure variation time series of the four microbarograph elements and the very strong intra-channel coherence is evident.

## **6.12 Satellite Re-Entry**

*McIntosh* (1982) reports on the infrasonic detection of a Soviet satellite re-entry vehicle on August 20, 1979. The re-entry was "seen as a fiery, meteor-like object over much of Ontario and the infrasonic signals were recorded on a four element microbarograph array located at Springhill near Ontario, Canada. Figure 140 shows the waveforms recorded on the infrasonic array. Each microphone was equipped with a 300 m plastic pipe wind noise filter.

The recorded signal level was small  $\pm 1 \mu$ bar and the highest frequency component in the signal was determined to be 1 Hz with the frequency component of the largest wave component measured as 0.33 Hz ( $T = 3$  s). Total signal duration was 6 minutes to 7 minutes.

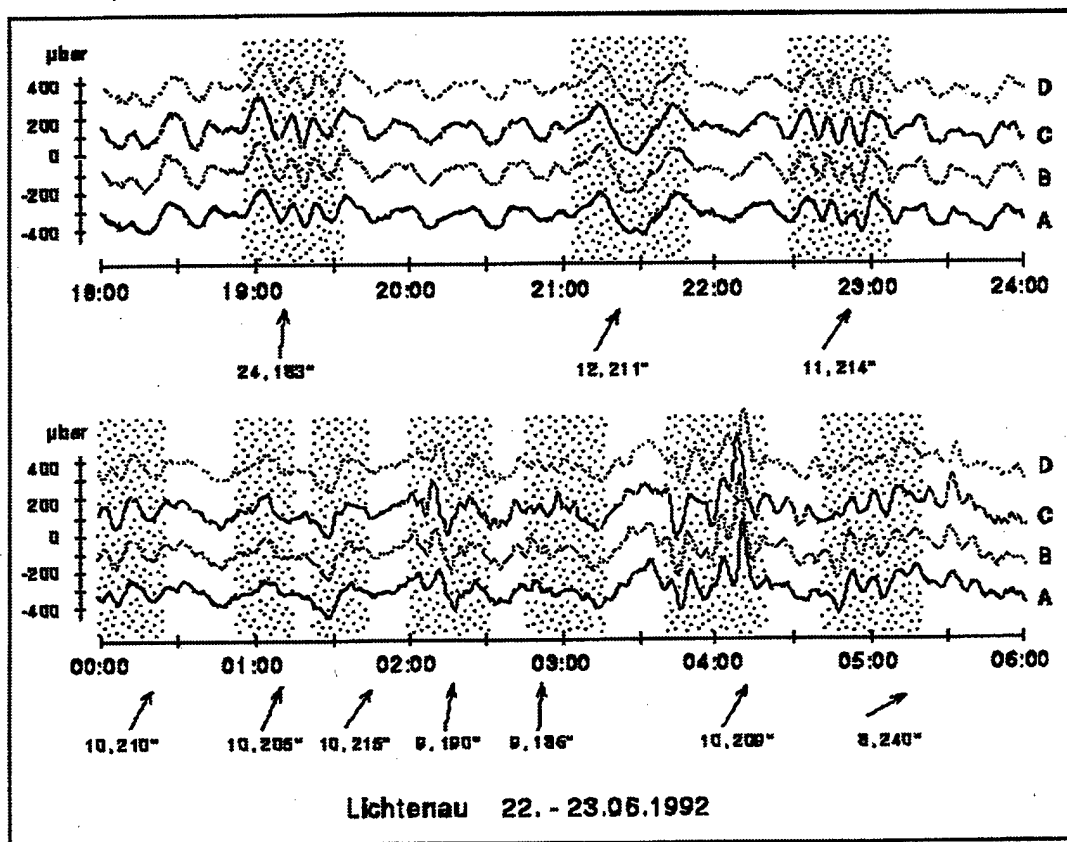


Figure 139. Mountain associated waves (the stippled sections) recorded on a microbarograph array in Bavaria. [Figure adopted from *Hauf, et al. (1995).*]

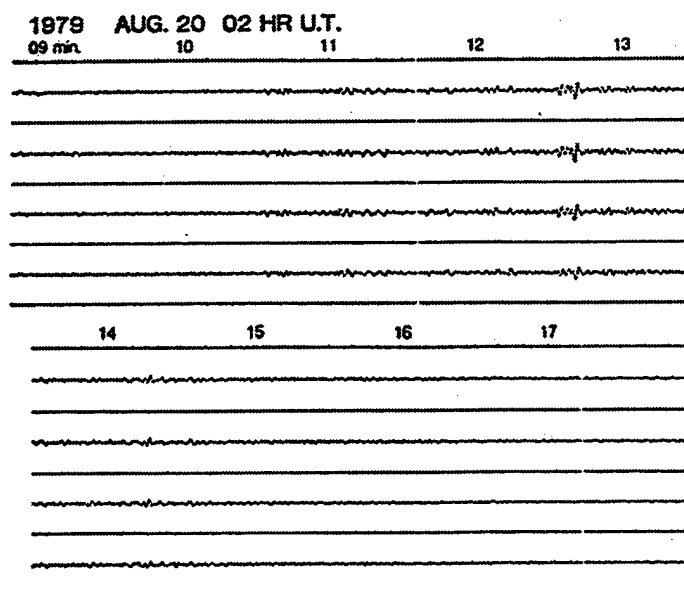


Figure 140. Records from a presumed satellite re-entry observed on the Springhill microbarographs. [Figure adopted from *McIntosh (1982).*]

### 6.13 Severe Storms

*Pierce and Coroniti* (1966) reported on observations of ionospheric disturbances which appeared to be related to thunderstorm activity. In explication of these observations, it was proposed that acoustic-gravity waves are produced by updrafts which are known to occur during the early stages of thunderstorm activity in the troposphere and that these waves can propagate to ionospheric heights. The source mechanism was associated with an equilibrium height "overshoot" of rising unstable air during the initial stages of storm formation and the subsequent oscillations which must occur due to gravity and density stratification at periods near the local Brunt-Vaisala frequency. Such acoustic-gravity wave induced disturbances in the ionosphere can, in turn, produce measurable effects in long range radio wave propagation.

*McDonald* (1974) reviewed some of the evidence for naturally occurring atmospheric infrasonic waves focusing particularly on sources associated with severe weather. The results of an effort aimed at determining the source characteristics of infrasound from that radiated by tornadoes were also presented. The monitoring effort utilized two tripartite arrays of microbarographs located near Dallas, Texas with each array having an element spacing of approximately 5 km. The sensors were not equipped with front end noise filters.

In reviewing past work on infrasound a confusion between, or an inconsistent definition of, acoustic-gravity waves and infrasound is noted. Acoustic-gravity waves are defined as those having periods longer than the natural period of the atmosphere ( $\sim 300$  sec) and infrasound as waves having shorter periods but still below the audible range of human hearing. Reference is made to the view that, of all known sources of infrasound, only 1% have amplitudes above  $1 \mu\text{bar}$  [*Young and Greene* (1972)] and infrasound is accordingly taken to have amplitudes generally less than  $2 \mu\text{bar}$  (whereas acoustic-gravity waves can have amplitudes as high as millibars), periods in the range extending from 20 s to 80 s, detection ranges of up to 1500 km, phase velocities in the range extending from



280 m/s to 350 m/s and wavelengths extending from 5 km to 30 km. Acoustic-gravity waves, on the other hand, are taken to have phase velocities in the range extending from 30 m/s to 100 m/s and wavelength's of several 10's of kms. Phenomena associated with sources of infrasound were listed as: hailstones, high winds, lightning, mountains, storm penetration of the troposphere, tornadoes, wind shear at altitude, visible auroral forms, volcanic explosions, etc.

*McDonald* (1974) reports observations of acoustic-gravity waves from severe storms and forcibly notes the great difficulty in associating a specific mechanism for the source of the waves. A line of tornadoes was also studied infrasonically and no clear association was made except to note that the production of infrasound occurred before the formation of the first tornadoes and, in support of this finding, it was pointed out that the "infamous Lubbock tornado" produced no observable infrasound. The production of infrasound in association with the passage of a front was, however, observed although the specific details about the source mechanism remained elusive: a circumstance that led to the call for continuous infrasonic monitoring with concomitant environmental monitoring.

*McDonald* (1974) also reported that the atmospheric explosion conducted by the French above Mururoa Atoll on July 3, 1970 was recorded on an infrasonic array in Bolivia and on the array located at Grand Saline, Texas. The signal was also detected on a seismometer buried at a depth of 183 m below the ground surface and its signal was found to correlate very well with that recorded by a microbarograph sited on the ground.

*Bowman and Bedard* (1971) review a 10-year study conducted by the Geoacoustics Group of NOAA's Wave Propagation Laboratory which was focused on the observations of propagating infrasound and subsonic disturbances associated with severe weather.

Much of the data involving subsonic waves were acquired utilizing a line of microbarographs located to the west of Washington, D.C., and having separations extending from 25 km to 250 km. In addition, data were acquired utilizing a four-element array arranged in a quadrilateral pattern with individual sensor spacing ranging from 4 km

to 10 km [Bedard, (1966)]. The subsonic waves were associated with severe storm systems and sometimes occurred in association with strong high altitude winds, hailstorms, thunderstorms or snow storms. In one instance, a subsonic disturbance was observed having a period of 18 min, wavelength of 27 km and a maximum peak-to-peak amplitude of 327  $\mu$ bar.

Table 4 summarizes past observations of infrasound related to severe weather.

Table 4. A summary of observations of infrasound related to severe weather conducted by investigators at the NOAA Wave Propagation Laboratory prior to 1971. [Table adopted from *Bowman and Bedard* (1971).]

Observations	Investigators	Location of observation point	Conclusions/Results
First related observations of infrasound to areas of severe weather containing tornadic storms	Chrzanowski <i>et al.</i> (1960) (unpublished)	Washington, D.C.	Infrasound was related to tornadic storms and could be distinguished from magnetic-activity related signals
Attempt to measure infrasound in the immediate vicinity of severe storms	Hass, Hoecker & Matheson (1961) (not documented)	Norman, Oklahoma	Experiment was inconclusive
Reviewed characteristics of infrasonic signals related to severe storms	Cook & Young (1962)	Washington, D.C.	Presented details concerning observations of infrasound attributed to tornadic storms
Observed that the azimuth from which infrasound arrived shifted direction during an interval of locally severe weather	Goerke & Woodward (1966)	Boulder, Colorado	It is possible to track the motion of a severe storm system by monitoring the radiated infrasound
Infrasound was related to local severe thunderstorms and compared with radar	Young, Greene & Bowman (1968) (unpublished)	Washington, D.C.	Storm cells with high elevation for radar returns may be the source of radiated infrasonic energy
Infrasound was related to isolated areas of distant severe weather	Bowman (1969) (unpublished)	Boulder, Colorado, Washington, D.C. (single observatory data)	These isolated storms were severe and were characterized by other investigators as splitting storms with rotation
Infrasound was measured from the same source area at multiple infrasonic stations	Bowman (1969) (unpublished)	Washington, D.C., Boulder, Colorado, Pullman, Wash.	It is feasible to locate the source area using azimuth crossings from several observations
A relation was found between the reported hail size and the dominant period of infrasound from the severe storm area	Bowman (1970) (unpublished)	Washington, D.C., Boulder, Colorado, Pullman, Wash., College, Alaska	A plot of hail diameter as a function of predominant period of infrasound suggests a relationship

As discussed by *Bowman and Bedard* (1971), the first observation of infrasound associated with severe weather, and specifically with tornadic storms, was reported by *Chrzanowski, Young and Marrett* (1960) who reported signals of periods in the range extending from 12 s to 62 s and peak-to-peak amplitudes in the range 0.2  $\mu$ bar to 1.5  $\mu$ bar. *Cook and Young* (1962a) reviewed this work and reported additional measurements from severe weather in Oklahoma: infrasonic signals in the period range extending from 12 s to 50 s and with peak-to-peak amplitudes of 1  $\mu$ bar. *Goerke and Woodward* (1966) reported observing changes in source azimuth from the vicinity of a local squall line and *Young, Greene and Bowman* (1968) reported observations of infrasonic arrivals from severe thunderstorms in the Washington, D.C. area and demonstrated that the regions of

maximum acoustic emission were associated with cloud tops as measured by a weather radar. Figure 141 shows examples of the recorded infrasonic waveforms and Figure 142 forcibly associates the production of maximum acoustic emission with storm cloud tops by comparing weather radar maps of a severe hailstorm with the direction of acoustic emissions. As noted by *Bowman and Bedard* (1971): "Acoustic radiation appears to originate in one storm cell during the first two time intervals, and from another cell after the first one begins to dissipate. The changing direction of the acoustic waves, consistent with the movement of the storm system, is the strongest indication that the storm cells are the origin of the radiated energy."

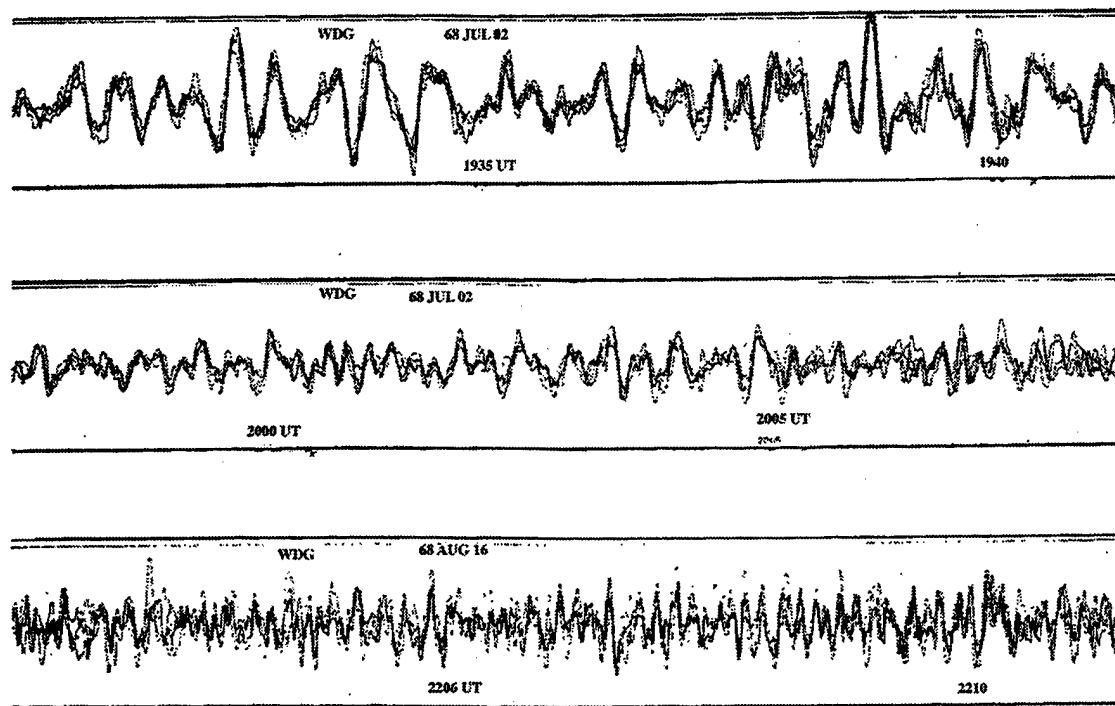


Figure 141. Several examples of infrasonic signals associated with severe storms. The records of July 2, 1968 have periods in the range extending from 5 s to 60s, with maximum amplitudes of 10  $\mu$ bar. The sensors were located in Washington D.C. and the storm was a hailstorm over NW Virginia. [Figure adopted from *Young, Greene and Bowman* (1968).]

Also, as pointed out by *Bowman and Bedard* (1971), infrasound emissions from particularly severe storms could often be observed using several infrasonic stations and, most interestingly, the diameter of the hail aloft, as measured by radar backscatter data, is

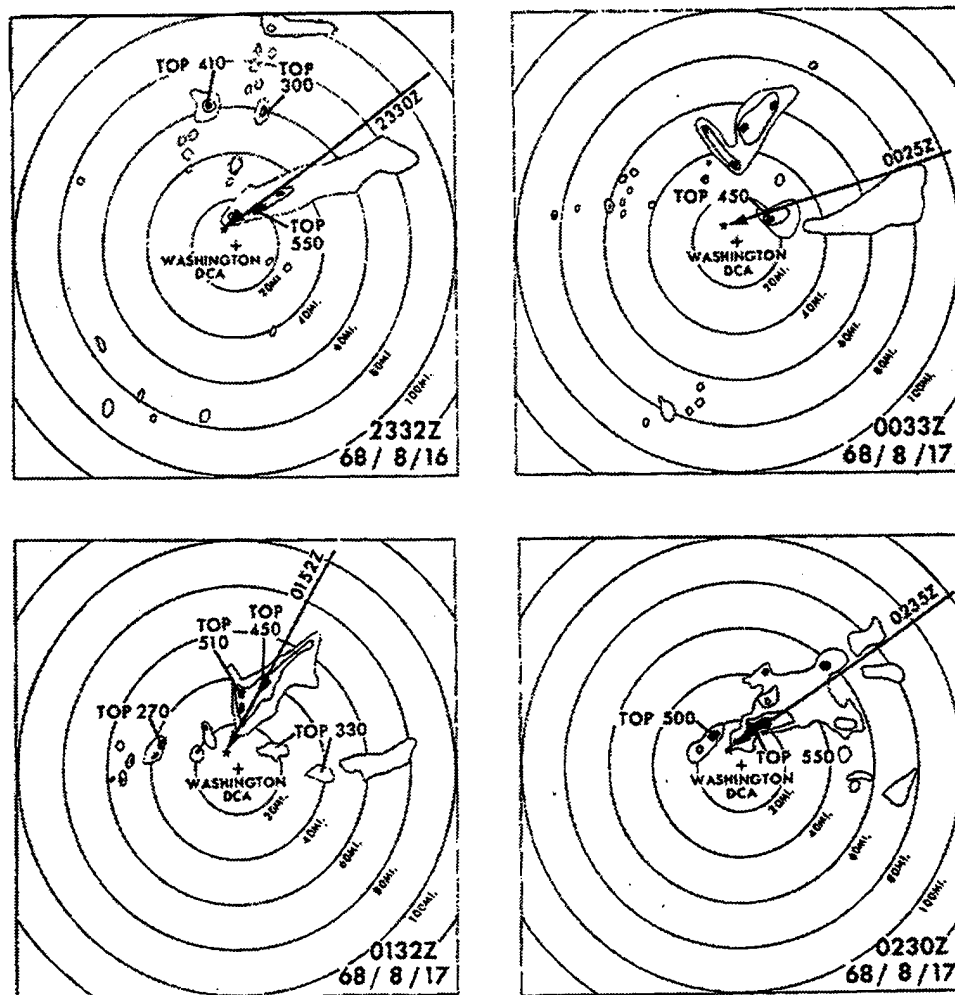


Figure 142. Radar scope photos and the direction of radiated infrasound. The acoustic direction and observation time are indicated by the arrows pointing to the center of the infrasonic monitoring array located to the NW of Washington, D.C. [Figure adopted from *Young, Greene and Bowman (1968)*.]

linearly related to the period of the infrasound emitted by the storm. Figure 143 illustrates the infrasonic tracking of a severe storm from four widely separated infrasonic stations on August 4, 1969 and Figure 144 shows the relationship between hail diameter and period of infrasound emission.

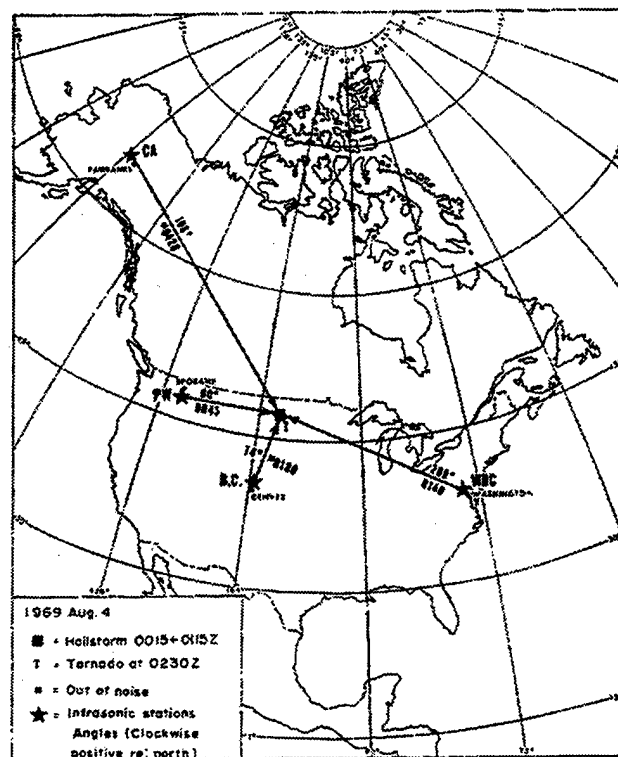


Figure 143. The infrasonic tracking of a severe storm using several infrasonic stations in the central plains on August 4, 1969. [Figure adopted from *Bowman* (1970).]

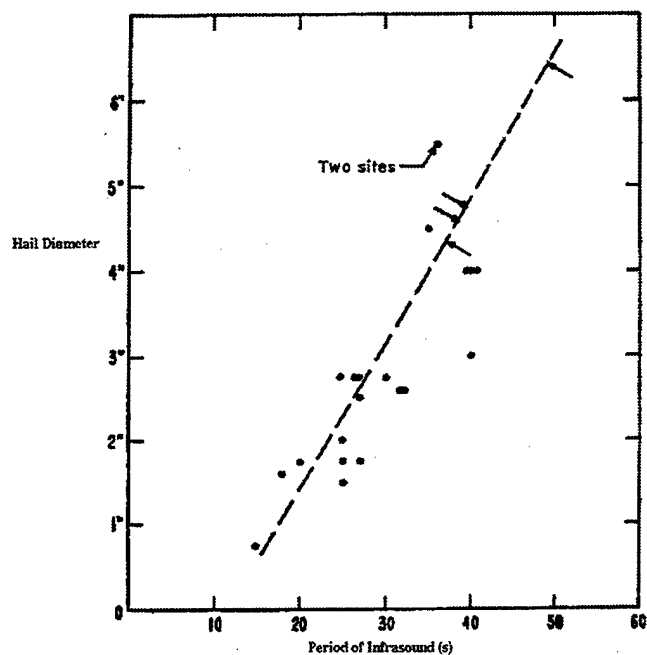


Figure 144. Estimated hail size as a function of predominant infrasound emission from a storm reported to have hail size as large as "gallon jugs." [Figure adopted from *Bowman* (1970).]

*Jordan* (1972) reports on the observation of microbarographic gravity waves associated with summer cold fronts and winds, and with winds associated with thunderstorm cells. The signals due to the latter mechanism were "observed to consist of wave trains initiated by exponential pressure pulses which appear to coincide with the thermodynamic activity when the storm breaks." Figure 145 provides summer microbarograph records extending from 1240 to 2350 MST showing signals from six storm cells as they

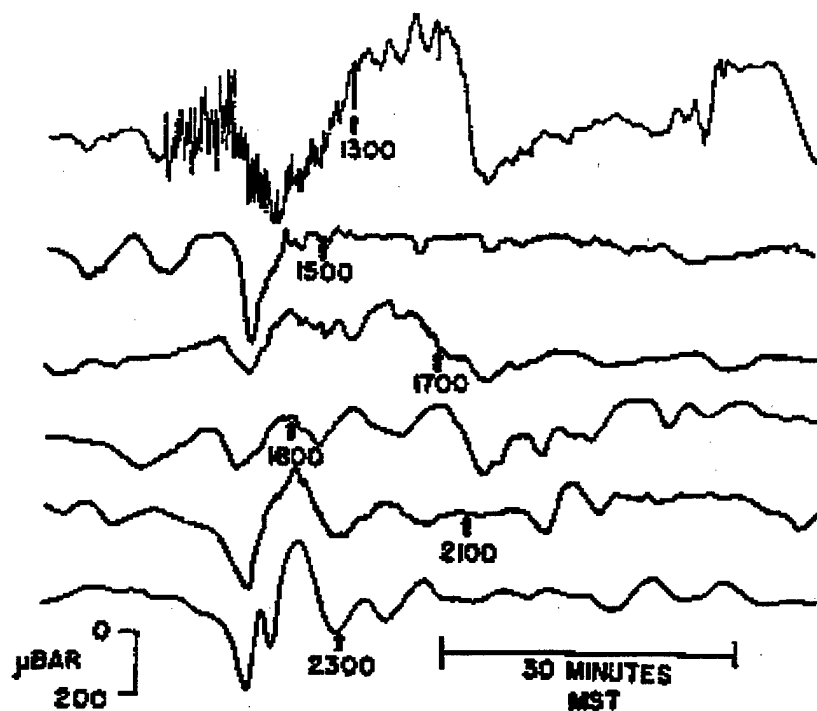


Figure 145. Microbarograph records from a summer thunderstorm exhibiting six storm cells as they reach maturity. In at least four of the events, the exponential shape of the positive pressure pulse (note that pressure is measured positively downward) is apparent. [Figure adopted from *Jordan* (1972).]

reach maturity. The waveforms were acquired on a microbarograph of the T21B type located near Denver, Colorado.

*Georges* (1973a) reviewed the evidence for the production of infrasound by severe storms by comparing and contrasting observations of 3 minute period ionospheric waves as observed by high-frequency (~ 5 MHz) continuous wave Doppler radars with pressure

wave recordings made with micobarographs. In conducting the review a very careful delineation of the observed properties of the ionospheric and acoustic-gravity waves was provided. Based on the results of the review, it was concluded that convective storms do, indeed, provide a common source for the production of both wave types and that the source mechanism, while poorly understood, is likely broadband in nature and capable of producing a total power output of at least  $10^8$  or  $10^9$  W. The wave spectrum observed by the two techniques appears to be quite different: "a narrow band, double-peaked spectrum, always near 2- to 5-min period, appears in the ionosphere, whereas a broad band, highly variable spectrum of wave periods in the tens of seconds characterizes the surface pressure fluctuations". Figure 146 provides a summary hypothesis of how the two sensing techniques might sample different portions of the broadband source spectrum.

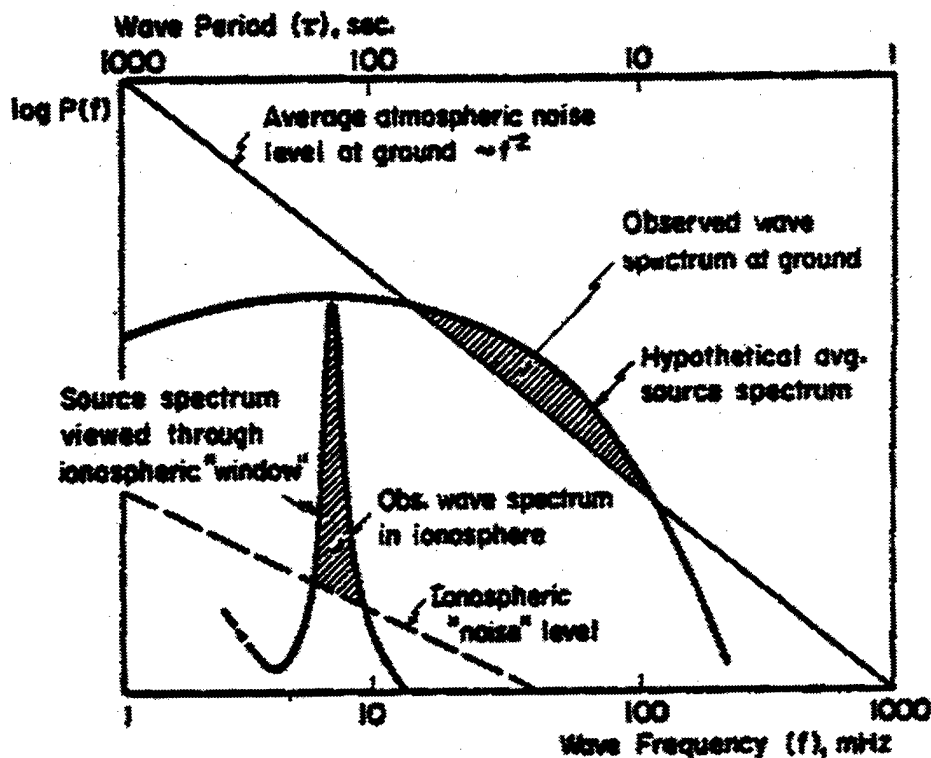


Figure 146. A schematic diagramming a hypothesis of the portion of the severe storm source spectrum sampled by Doppler radars in monitoring ionospheric waves and that sampled by microbarograph arrays detecting propagating pressure waves on the ground. The shaded regions in the figure indicate the observable portions of the source spectrum. [Figure adopted from *Georges (1973a)*.]

In discussing Doppler observations of ionospheric waves which typically have a period near 3 minutes, *Georges* (1973a) cites the theoretical work of *Pierce and Coroniti* (1966) predicting that convective storms would produce acoustic-gravity waves and refers to a number of case studies confirming the existence of a "detailed spatial and temporal relationship" between the presence of convective storm activity and the observation of ionospheric waves. In addition, *Georges* (1973a) derived equations which can be used to estimate the power radiated by a convective storm based on observations of ionospheric waves and microbarograph records. For the case of ionospheric waves, the derived expression for the radiated power,  $P$ , is given by:

$$P = \frac{\pi \rho_o C c_o^2 h^2}{4} \left( \frac{\Delta f}{f_o} \right)^2 \quad (6.18)$$

where  $\rho_o$  is the ambient air density,  $h$  is the ionospheric height,  $C$  is the local sound speed at that height,  $c_o$  is the speed of light in vacuum,  $f_o$  is the center frequency of the Doppler radar and  $\Delta f$  is the measured Doppler shift. For an altitude of 200 km,  $f_o = 5$  MHz,  $\Delta f = 1$  Hz, Eq. (6.18) predicts a radiated power of  $2.8 \times 10^7$  W.

For the case of acoustic waves as observed on the ground, the expression corresponding to Eq. (6.18) can be written as

$$P = \frac{\pi r h p^2}{\rho_o C} \quad (6.19)$$

where  $p$  is the pressure and  $r$  is the horizontal source-to-receiver range. For a measured pressure amplitude of 0.6  $\mu$ bar [the median observed amplitude as reported by *Georges* (1973a)], Eq. (6.19) predicts the radiated power to be  $2.3 \times 10^7$  W which is in excellent agreement for the same quantity computed on the basis of Doppler radar observations of ionospheric waves. The fact that the Doppler and acoustic estimates were so close, and the hypothesized sampling effective for the total storm spectrum (see Figure 145) led to *Georges'* (1973a) estimates of  $10^8$  or  $10^9$  for the total power radiated by a storm.

Of potential importance for better understanding of the source mechanism from convective storms was the infrasonic emissions recorded from a storm system in the



western part of Oklahoma during June 28 and June 29, 1969 which produced signals composed of a number of pulsations of approximately 20 min duration: a circumstance in accord with previous observations of infrasonic waves, but the first such observation for acoustic waves. The observation of the pulse arrival structure led *Georges* (1973a) to hypothesize "a relationship with the observed 15- to 20-min interval between successive emergences of individual cumulus towers in multicellular storms (cf. *Anderson* [1960] and references he cites)".

*Georges* (1973b) reported on the distribution of a number of infrasound events recorded on a microbarograph array located near Boulder, Colorado, during the 1972 storm season. Of a total of 146 events, 13 were identified as being from auroral sources, 27 from South American sources, 20 from waves of unknown origin, 86 from waves associated with convective storms and 45 from waves associated with tornadoes or funnel clouds. Of the sources associated with convective storms, 67 were associated with "severe storms": i.e., those associated with the production of tornadoes, hail, heavy rain and high winds. The waves associated with severe storms can be detected to ranges of 1500 km and "typically have amplitudes of about 1  $\mu$ bar and periods between 10 and 40 sec".

*Georges* (1973b) points out the potential utility of infrasonic arrays "for severe-storm identification and warning purposes"; indeed, "it is reasonable to think of a network of two or three sensor arrays that could identify, locate and possibly track most of the emitting storms between the Mississippi and the Rockies." In addition, and of particular interest to the infrasonic monitoring of atmospheric nuclear testing, is the observation that the false alarms for such a storm warning system "appear to exhibit some property that permits them to be distinguished from storm-associated waves after detailed analysis of wave properties".

*Georges* (1974) reports on the observation of infrasonic signals radiated from thunderstorms in Texas and recorded on four-element microbarograph arrays located at Boulder, Colorado (NOAA) and San Diego, California (NEL). The observations were

actually acquired in 1970 in a program designed to study a number of severe storms occurring in Oklahoma during the time period extending from April 29, 1970 to April 30, 1970.

Based on triangulation, it was concluded that the micobarograph arrays did not detect the thunderstorm activity in Oklahoma but observed strong and persistent arrivals having maximum wave amplitudes of 0.7  $\mu$ bar (Boulder) and 0.6  $\mu$ bar (San Diego). The recorded signal-to-noise ratios recorded at both stations were found to exhibit irregular pulsations which, in light of other similar observations, were postulated to be associated with the source mechanism rather than with propagation or local noise effects.

*Bowman* (1974) pointed out that between the years of 1958 and 1967, 89% of 220 infrasonic signals recorded on microbarograph arrays located in the Washington, DC. area were associated with various severe weather phenomena [*Bowman and Bedard* (1971)], observed that the characteristics of the radiated sound appeared to be stochastic in nature and suggested using narrow band spectral processing techniques to classify various storms. Figure 147 shows the spectral change in infrasound radiated from a hailstorm as a function of time over an eighty minute period.

*Georges and Greene* (1975) reported additional observations of infrasound emitted by convective storms during the 1973 storm season in which data were acquired during the period extending from May 19, 1973 to August 31, 1973. The instrumentation involved three four-element microbarograph arrays: two arrays were located at Rapid City, SD and Escancia, NM and were equipped with noise reducing filters constructed of 200 ft (60.96 m) segments of rubber hose and the third array was located at Boulder, CO with each sensor equipped with a 1000 ft noise reducing filter. The array geometries were "Irregular" and individual sensor spacing ranged from 5 km to 10 km.

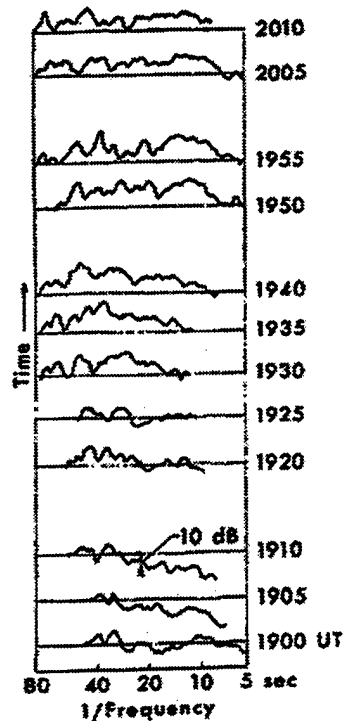


Figure 147. One-tenth octave spectra of infrasound radiated from a hailstorm on July 3, 1968 and recorded on a microbarograph array in Washington, D.C. The spectra are seen to be highly variable and to become of broader bandwidth as time increases. [Figure adopted from *Bowman (1974)* and *Bowman (1968)*.]

The purpose of the experimental work was to determine if monitoring infrasonic emissions from storms could be used to predict severe weather phenomena such as tornadoes and to acoustically track and locate severe storms. As a means of measuring such predictive power, four basic metrics were adopted: false-alarm rate (a measure of how often signals from other sources are misclassified as severe storm sources), detection rate (a measure of how often severe storms are detected), timelines (a measure of how much advanced warning is provided) and location accuracy (a measure of how accurately a storm can be located and tracked). The conclusion of the work was that infrasonic monitoring is a useful technology, in principle, for providing severe weather warnings but that additional work was needed in propagation modeling, sensor technology, noise reduction and cost-trade-off studies for implementing the technology.

In quantifying false alarm rate, *Georges and Greene* (1975) developed various sorting methodologies to eliminate as much as possible the sources other than the storms of interest and, by so doing, were able to reduce the false alarm rate for the three station network to 16%. Utilizing their observations that "virtually all severe storms that radiate infrasound strong enough for detection at ranges of a few hundred kms are in the Midwest," it was possible to remove some of the ambiguity in defining detection rate to estimate a 65% detection rate for tornadic storms (i.e., those that produce tornadoes), a 31% detection rate for tornadoes themselves and a 33% detection rate for storms having radar cloud tops above 50,000 ft. As a result of the focus of the work on the possibilities of forecasting tornadoes, it was observed that "a significant fraction of emissions appeared to be unrelated to the observed tornadoes themselves. The implication is that something in tornadic storms besides tornadoes (larger scale vorticity?) is responsible for the emissions."

In assessing the timeliness of infrasonic monitoring of severe weather phenomena, *Georges and Greene* (1975) were led to remove the propagation delay between source and receiver in comparing the times when tornadoes were formed and when infrasound emissions were received and discovered, thereby, that the infrasonic emissions on average began one hour before the formation of tornadoes: a circumstance providing hope for the use of infrasound as a means of providing tornado warnings in a sufficiently dense network of stations. With respect to location accuracy, it was concluded that measurement and propagation uncertainties precluded a "positive identification and tracking of a particular storm, but we see ways to improve this".

*Beasley, Georges and Evans* (1976) conducted an investigation to test proposed electrical mechanisms (e.g. cloud-to-ground lightning) as a possible source for infrasonic emissions from convective storms. Their work involved the simultaneous recording of atmospheric electromagnetic emissions or "sferics" and infrasound as recorded on an array of microbarographs located at Boulder, CO. The data acquisition took place during the time period extending from May 22, 1972 to August 30, 1992. The conclusion of the

investigation, based on statistical arguments and detailed case studies, was that the infrasound and sferic emissions were non-causally related and, indeed, the emission of infrasound occurs in the early stages of storm formation and precedes the emission of electromagnetic energy.

Figure 148 presents an overall summary of the measured correlation between infrasonic and sferic emissions. As indicated in the figure, there were 64 events for which

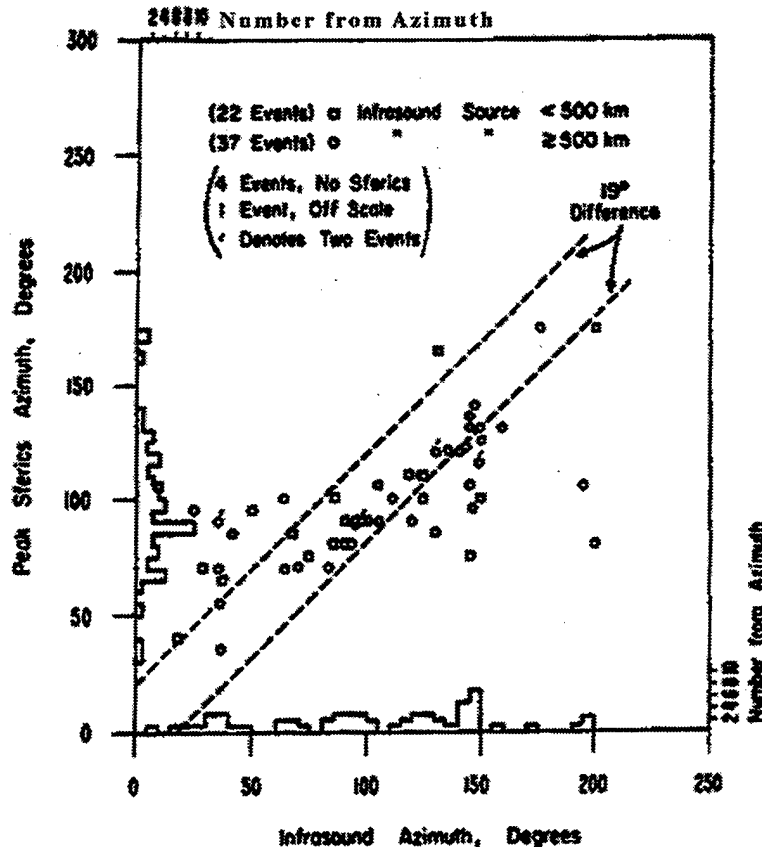


Figure 148. The azimuth of the peak sferics rate (vertical axis) as a function of the azimuthal arrival angle of infrasonic arrivals (horizontal axis). The histograms indicate the number of arrivals in  $5^\circ$  angle sectors and the dashed " $19^\circ$  Difference" lines denote the experimental error bounds in arrival angle estimation. [Figure adopted from *Beasley, Georges and Evans (1976)*.]

simultaneous observations of sferic and infrasonic emissions were made. Twenty-two of the events were from storms closer than 500 km (shown as squares), thirty-seven events were from sources located at ranges greater than or equal to 500 km (shown as circles) and four storm systems emitted no sferic signals. Only 44% of the events fall within the  $19^\circ$

arrival angle range and the histograms suggest different primary arrival angles for the two sources: 80° - 90° for sferic arrivals and a much broader peak for infrasound centered near 140°.

*Georges* (1976) provided a comprehensive review and critique of proposed source mechanisms for the emission of infrasound from severe storms. The review included discussions of convective storm formation and dynamics, as well as detailed and quantitative discussions and assessments of the various source mechanisms listed in Table 5.

Table 5. A listing of candidate source types and mechanisms evaluated for the production of infrasound by convective storms. [Table adopted from *Georges* (1976).]

---

Simple Sources in Cumulus Growth

Latent Heat Release (monopole)  
Cell Circulation (dipole)  
Buoyancy Oscillations (dipole)

Turbulence

Reynolds Stress Viewpoint  
Random Vorticity Viewpoint

Electrical

Discharge Shock (thunder)  
Electrostatic Relaxation  
Pulse lengthening (Nonlinear Effects)

Vortex Sound

Aeolian Tone (Wake Vortices)  
Vortex Instabilities (Multiple Vortices)

Heat-Driven Oscillations

Combustion Oscillations (Periodic Latent Heat Release)  
Condensation in Supersaturated Environment

The conclusion of the review was that "the mechanism most consistent with the observations appears to be a form of vortex radiation, in which instabilities and, ultimately, multiple vortices form about the periphery of a larger mesoscale vortex, and radiate narrow-

band sound as they spin about a common axis." Figure 149 shows a map of horizontal air-velocity vectors at an altitude of 6 km above ground in a thunderstorm in Colorado and clearly supports the multiple vortex viewpoint. Inspection of the figure shows the

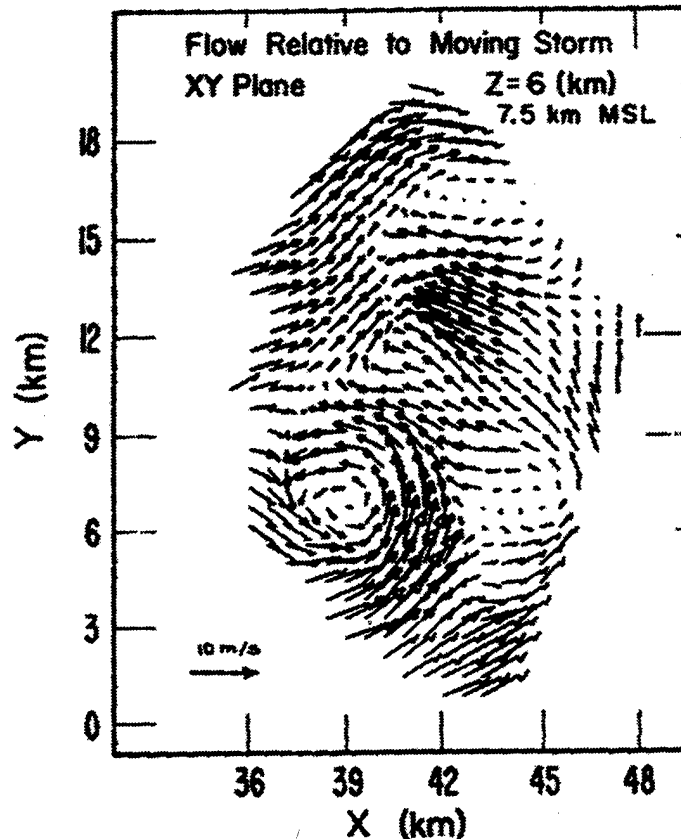


Figure 149. A radar map of horizontal wind velocity vectors at an elevation of 6 km above ground in a thunderstorm over Colorado. The size of each vector is proportional to the wind speed with the maximum speed reaching 10 m/s. [Figure adopted from *Georges* (1976) after *Kropfli and Miller* (1976).]

formation of several vortices within the storm. In particular, a strong and well formed vortex is visible in the lower left of the plot and two weaker and less formed vortices can be seen at the top and lower right.

In reviewing the other candidate source mechanisms listed in Table 5, *Georges* (1976) found that the simple monopole and dipole sources associated with cumulus storm growth produced more radiated acoustic energy than was observed and would produce acoustic signatures of different character than those observed. Radiation by turbulence could not be conclusively rejected because of significant uncertainties in such turbulent

parameters as intensity and Mach-number fluctuations but the mechanism was not favored because the required parameters turned out to be generally too large to produce the required radiated energy. The electrical models were rejected because calculations indicated they were not capable of radiating the required power and lightning, in particular, could be rejected based on the observational fact that it is not typically causally related to infrasound emissions [Beasley, Georges and Evans (1976)]. Finally, the "thermo-mechanical mechanisms appear not to be applicable to severe storms, because the heat-release mechanism (condensation) is always out of phase with wave-associated temperature fluctuations".

The preferred mechanism, radiation by a multi-vortex system leads to the prediction of a radiated power level in agreement with infrasonic and ionospheric observations [Georges (1973a)] based on a theoretical expression derived by Powell (1964) for a corotating vortex pair and given by

$$\Pi = \frac{16}{15\pi} \frac{\rho}{c^5} \left( \frac{\Gamma}{4\pi r} \right)^8 l^2 \quad (6.20)$$

where in the above,  $\Pi$  is the radiated power,  $\rho$  is the density,  $c$  is the speed of sound,  $\Gamma$  is the vortex strength,  $2r$  is the separation distance and  $l$  is the axial length. Figure 150 (Panel a) illustrates the streamline pattern for the vortex pair and shows that the instantaneous source radiation pattern is a rotating quadrupole. Figure 150 (Panel b) provides the geometry for computing the radiated power from the vortex pair where  $u$  is the rotational speed about the common axis of the vortex pair. For  $u = 43$  m/s,  $l = 3$  km and a vortex separation of 820 m, Eq. (6.20) predicts a radiated power of  $10^7$  W in agreement with the inferred value of  $2.3 \times 10^7$  inferred by Georges (1973a) for waves of period 30 s.

Bedard, Intrieri and Greene (1986) have reported infrasonic observations of severe storms in the frequency range 0.5 Hz to 20 Hz and have observed no association of emissions with cloud-to-ground-lightning. Rather, the investigators report a very strong association of infrasound bearings and azimuths with high cloud tops and high radar reflectivity. Such an association had been reported earlier by Georges (1973a) in the



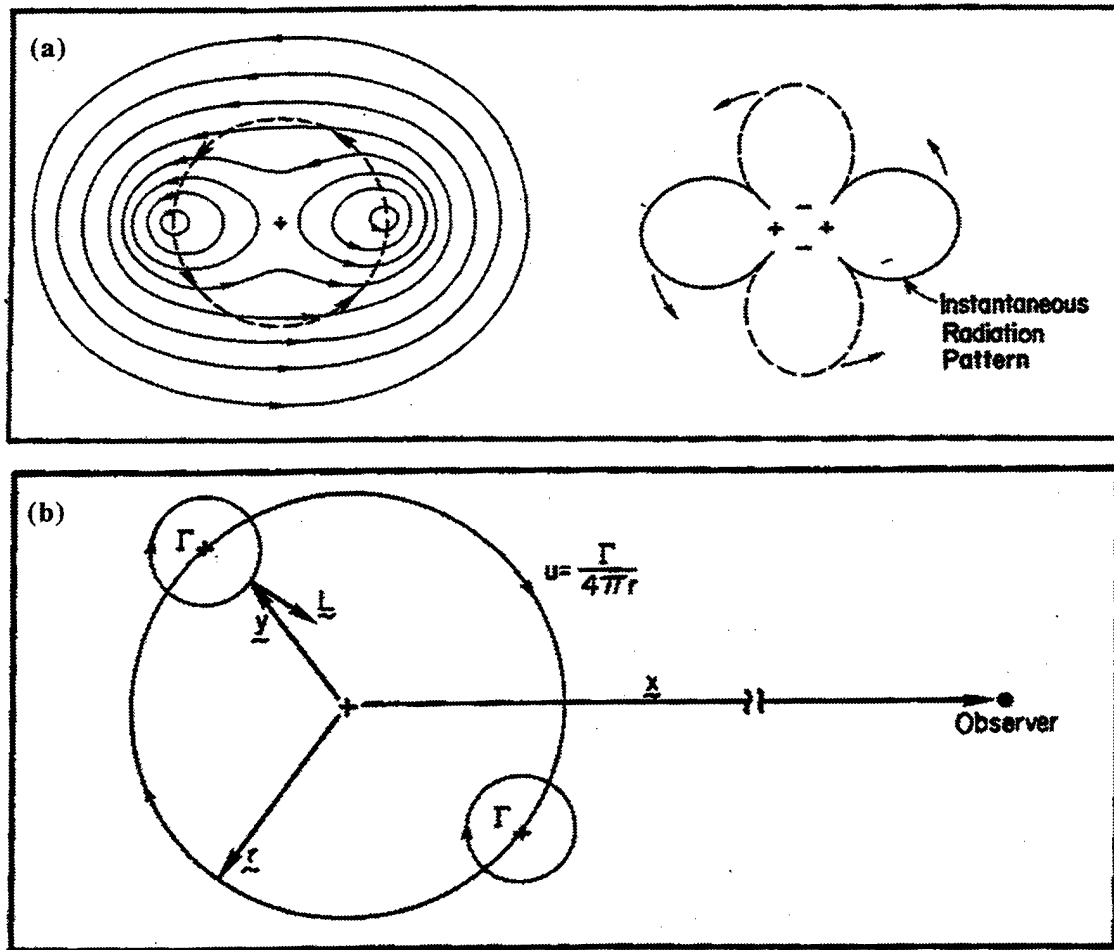


Figure 150. The streamline pattern and instantaneous radiation pattern for a pair of corotating vortex pairs about a common center (Panel a) and the geometry and notational definitions for computing the radiated acoustic power.  $u$  is the velocity that the vortices spin about their common axis. [Figure components adopted from *Georges* (1976).]

frequency region below 0.1 Hz, but the association was found to be much stronger in the higher frequency band. The investigators were also able to track storms out to a range of 800 km where the received signal amplitude was at a level of 0.5  $\mu$ bar peak-to-peak. At shorter ranges, the signal level was as high as 3  $\mu$ bar peak-to-peak and it was observed that the signal amplitude fell off more slowly than  $1/r$ , where  $r$  is the horizontal range from the storm to the microbarograph array. A specific physical mechanism for the production of the

infrasound was not identified although the electrostatic mechanism proposed by *Dessler* (1973) was listed as a possibility.

*Georges* (1987) briefly reviewed the production of infrasound from thunderstorms, again favoring the multi-vortex source mechanism and, as did *Georges* (1976), cited the numerical simulations of *Agee, Snow and Clarke* (1976) indicating that some severe thunderstorms exhibit a transition through a succession of different vortex stages. In addition, *Georges* (1987) presented the infrasonic records associated with a tornado that passed within 27 km of the microbarograph array at Boulder, CO and provided an updated assessment on the utility of infrasound as predictor of severe weather, concluding that the deployment of infrasound stations in an approximate 1,000 km grid could usefully supplement the current storm warning system particularly as a means of providing: precursor signatures for tornadoes, remote monitoring of vorticity concentrations in storms and, more generally, the measurement of other natural sources of infrasound. Figure 151 provides the waveforms associated with the tornado event.

#### **6.14 Solar Eclipse**

*McIntosh and Reville* (1984) reported the observation of travelling pressure waves associated with the solar eclipse which occurred on February 26, 1979. The pressure waves were observed on an array of four infrasonic sensors located 12 miles west of Saskatoon, Saskatchewan, Canada. The geometry of the array was a quadrangle having smaller and larger dimensions of 1.32 km and 3.18 km, respectively. The basic sensor was a ceramic microphone equipped with a front-end wind noise filter of length 300 m.

The strongest of the observed pressure waves were observed at the array approximately 1.5 hr from the time of closest approach of the eclipse and were observed to be in the direction of the heading of the shadow motion at the array site. The waves were found to propagate with a subsonic velocity of 10 m/s, to have a predominant period of 120 s, to have an amplitude of 12 Pa (120  $\mu$ bar) and to have a duration of three hours.

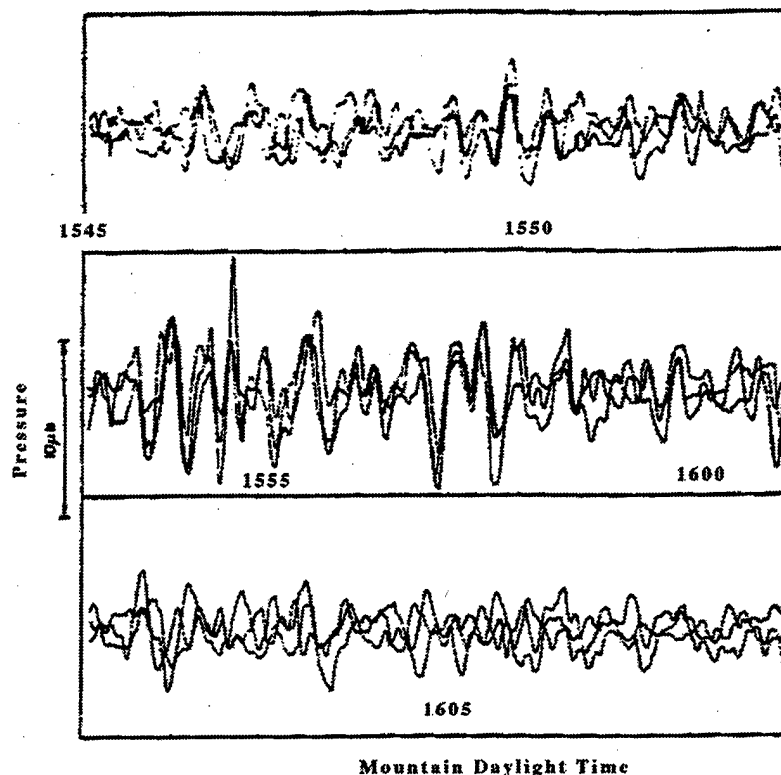


Figure 151. Microbarograph traces associated with the passage of a tornado 27 km to the NE of a microbarograph array located at Boulder, CO. Recordings from the individual sensors have been time shifted to align the traces. The arrow line on the figure legend to the left of the figure denotes 10  $\mu\text{bar}$ . [Figure adopted from *Georges* (1987).]

In arriving at a physical explanation for their observations, *Revelle and McIntosh* (1984) cite the earlier work of *Chimonas* (1970) and *Chimonas and Hines* (1970 and 1971) who postulated the excitation of gravity waves by a solar eclipse due to the generation of bow-waves. The work of *Chimonas* (1973) postulated a similar excitation of gravity waves due to the formation of the Lamb mode. The observations were compared with the predictions of both of these theories and it was concluded that neither mechanism is capable of explaining the observed characteristics of the eclipse associated waves. In particular, the bow-wave theory was shown to predict too large a period for the waves, 400 s in comparison to the 200 s period observed, and to predict a time of arrival one hour before the arrival of the strongest signals. The Lamb mode mechanism cannot explain the data because the mode is known to travel with the local sound speed and not at the measured speed of 10 m/s.

As an alternative physical mechanism, *McIntosh and Revelle* (1984) were led to propose that the eclipse produces a radiative cooling or "perturbation" of a pre-existing low-level (in comparison to the height of the tropopause) jet and that this perturbation leads to the generation of forced gravity waves. The postulated mechanism is consistent with the known existence of a temperature inversion in the area and leads to estimates of propagation speed ( $\sim 1$  m/s) and amplitude ( $\sim 2$  Pa) in rough agreement with the observations.

### 6.15 Solitary Waves

*Christie, Murihead and Hales* (1978) reported the first observations of large amplitude atmospheric waves in the form of isolated solitary waves and wave packets as observed on a five element microbarograph array located near Tennant Creek ( $19^{\circ} 56'S$ ) in the interior of Australia at the Warramunga seismic station. The microbarograph array was arranged in a quadrilateral pattern with one element located near the center with sensor separations providing a net array aperture of 4 km. The microbarometer elements are of NBS design and possess an effective passband extending from 1 s to 1000 s.

The data reported in 1978 presented pressure records corresponding to three distinct types of isolated nonlinear wave activity: "(1) large-scale waves of elevation which belong to the class of classical shallow-fluid internal solitary waves, (2) large-scale internal solitary waves of depression, and (3) solitary waves associated with the atmospheric boundary layer which are described by the deep-fluid nonlinear wave theory of *Benjamin* (1967)."

*Christie, Muirhead and Hales* (1979) reported additional observations of nonlinear propagating infrasonic signals postulated to be generated by intrusive atmospheric density flows in the lower atmosphere. In addition, the authors reviewed an extensive amount of literature which is available on solitary waves, in general, and nonlinear dispersive wave theory, in particular, and provided illustrative examples of the evolution of elevated and long waves together with a listing of other geophysical manifestations of solitary waves (e.g., the wave-like structure in the magnetospheric-solar wind interaction, finite amplitude

Rossby waves as observed in both the atmosphere and oceans, the great red spot on Jupiter, etc.). Figure 152 provides a schematic representation of the temporal evolution of waves of elevation and long waves as predicted nonlinear dispersive wave theory.

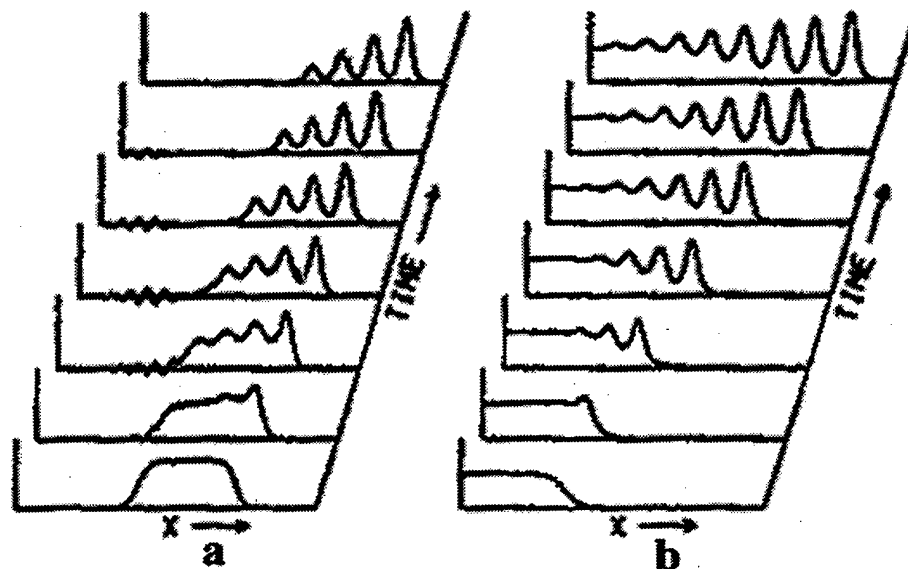


Figure 152. A schematical representation of the evolutionary behavior of a finite length wave of elevation (Panel a) and the leading edge of a long wave (Panel b). The schematics are based on the predictions of nonlinear dispersive wave theory. [Figure adopted from *Christie, Muirhead and Hales (1979)*.]

As discussed by *Christie, et al. (1979)*, the wave of elevation shown in Panel a of Figure 152 "evolves into a supercritical solitary wave family followed by a weak dispersing subcritical oscillatory wave train. Asymptotically, this disturbance is reduced to four solitary waves which are ordered by amplitude." The leading edge of the long wave shown in Panel b of Figure 152 evolves "by the formation of a long train of amplitude-ordered solitary waves along the leading edge of the disturbance."

All of the differing types of propagating nonlinear waves are observed at night when there is a nocturnal radiation inversion and it is thought that the waves propagate along this inversion. Figure 153, by way of illustration, provides waveform records representative of solitary wave formation along the front or leading edge of an intrusive flow and Figure 154 provides surface pressure perturbations corresponding to the passage of "complex solitary-wave-dominated intrusive disturbances." The fact that the amplitudes

of the individual solitary waves are not ordered in time "may indicate that these actively evolving wave forms originate in unusually complex initial disturbances."

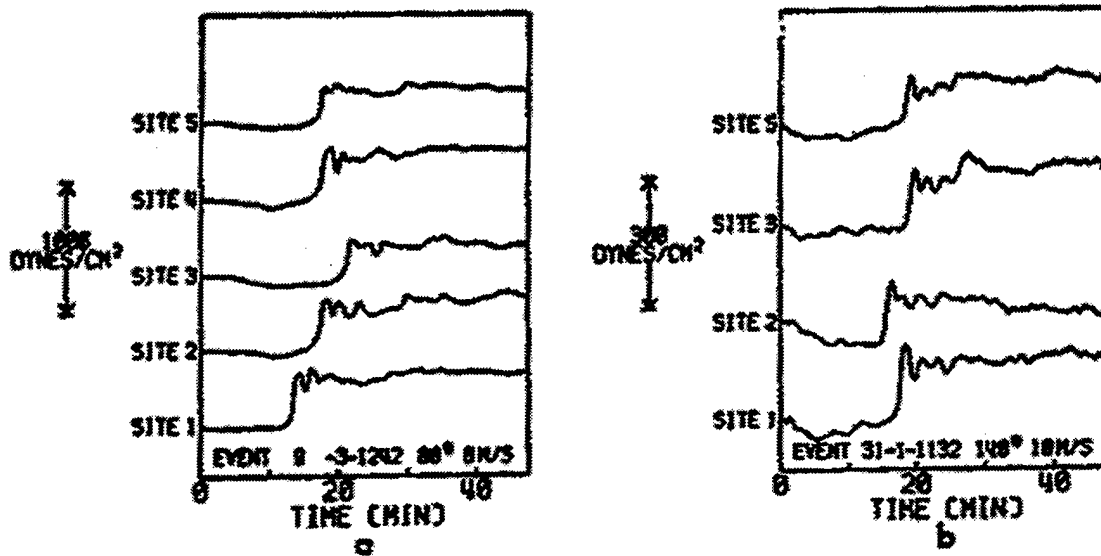


Figure 153. Two different disturbances illustrating the initial formation of solitary waves along the leading edge of intrusive flows. [Figure and caption adopted from *Christie, Muirhead and Hales (1979)*.]

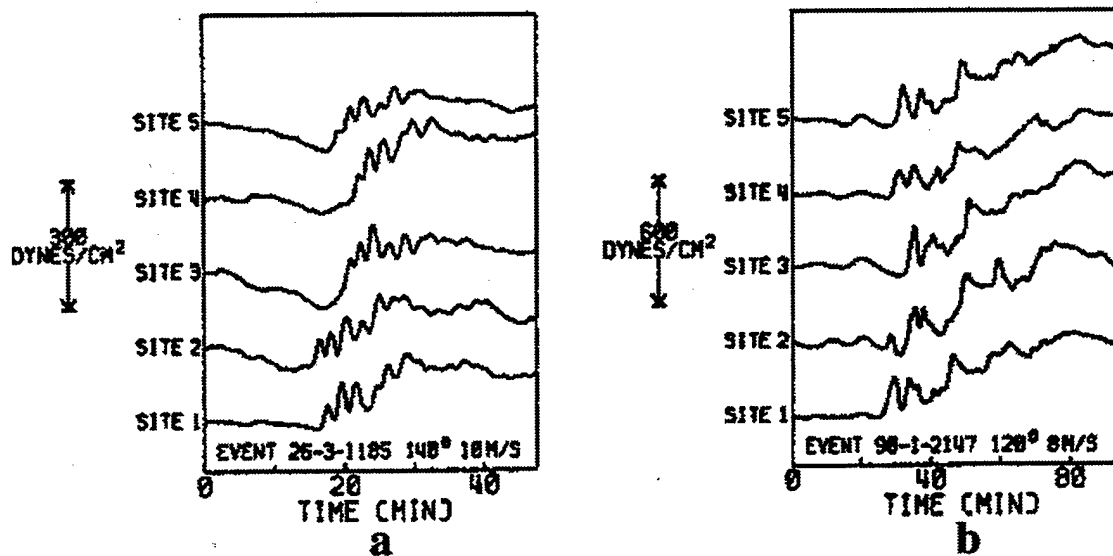


Figure 154. Two examples of complex solitary-wave-dominated intrusive disturbances. [Figure and caption adopted from *Christie, Muirhead and Hales (1979)*.]

Lower tropospheric observations consistent with the nonlinear decay of a propagating internal bore into solitary waves have been reported by *Christie, Muirhead and*

Clarke (1981). The observations were acquired using the five-element Warramunga array of microbarographs and a colocated acoustic monostatic echo sounder. The microbarograph array provided surface measurements of pressure, and the echo sounder provided the detailed structure of the propagating disturbances as a function of time and as a function of height. The echo sounder records indicated the propagation of a "complex internal bore" possessing a solitary wave component associated with the leading edge of the disturbance. The disturbances were observed to extend from the ground to a maximum height of 400 m. Reported pressure levels for the disturbances were 0.8 mbar (80  $\mu$ bar) in one observation and 0.7 mbar (70  $\mu$ bar) in another and the reported durations of the events ranged from 2 h to 3 h. Of potential interest for meteorologists was the observation that these disturbances were possibly associated with the production of "two closely spaced propagating quasicontinuous thin cumulus cloud lines that were observed from the ground in totally clear conditions. The preferred explanation for the production of the propagating cloud lines is "that they represent capping clouds created by the lifting of moist air to the condensation level during the passage of the solitary waves associated with the leading edge of a dissipating finite-length internal bore." The inferred propagation speed and effective wavelengths of the bore-solitary wave systems are  $\sim 10$  m/s and 1.4 km to 2.4 km, respectively.

#### **6.16 Sonic Boom**

Cotten and Donn (1971) reported the observation of sound signals from the Apollo 12 and Apollo 13 spacecrafts utilizing tripartite arrays of infrasonic sensors (capacitance microphones) located on the island of Bermuda. The sensor elements were evidently not equipped with front-end noise filters. The influence of wind noise was mitigated by locating the sensors in small clearings in deep woods and by placing them far enough apart so that the noise would be incoherent in the measurement passband extending from 0.5 Hz (and 0.3 Hz) to 10 Hz.

The recorded signals were found to exhibit high horizontal coherence, a strong impulsive beginning reminiscent of sonic boom N-waves and period contents of 1 s or less. Figure 155 shows tracings of the pressure recordings made on two infrasonic arrays for the Apollo 12 flight on November 14, 1969 and for the Apollo 13 flight on April 11,

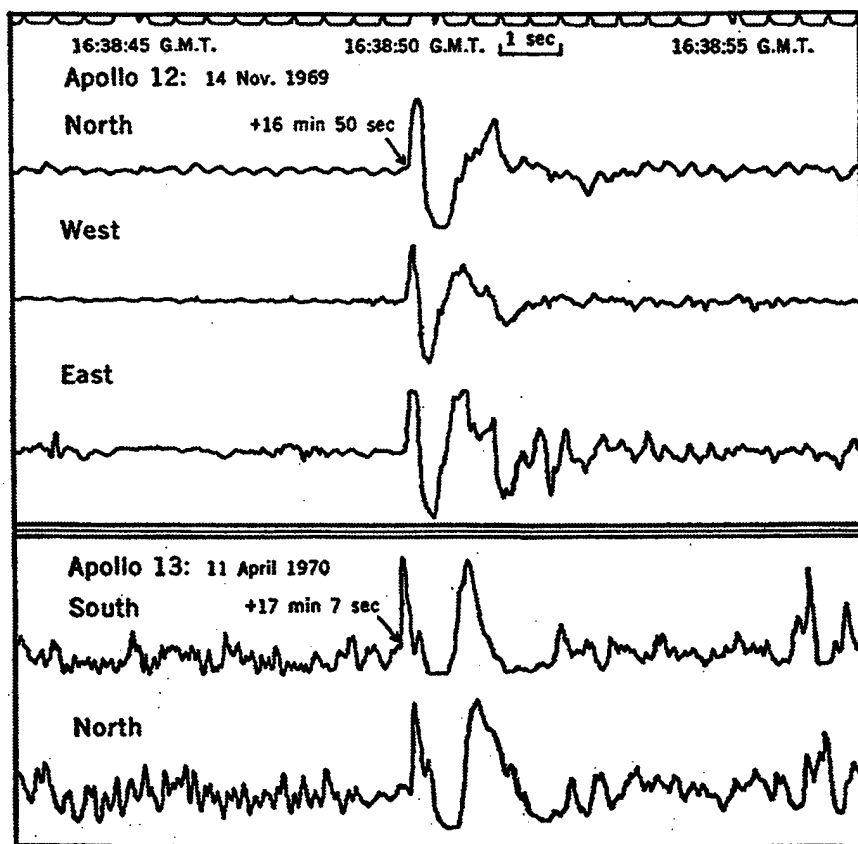


Figure 155. Pressure waveforms recorded at two microbarograph arrays on Bermuda created by the passage of the Apollo 12 and 13 rockets overhead. The maximum variation of the signals is approximately 10  $\mu$ bar. Also included on the figure are the time intervals between the launch of the missiles and the arrival of the infrasound at the Bermuda arrays. [Figure adopted from *Cotten and Donn* (1971).]

1970 and the distinctive N-shape of the initial signal is clearly in evidence. The maximum pressure amplitude variation in the waveforms was reported to be 10  $\mu$ bar.

The observations of the Apollo waveforms were made when the rockets were at an altitude of 188 km and almost directly overhead Bermuda. The fact that any signals were received at all, led *Cotten, Donn and Oppenheim* (1971) to conduct a careful investigation of sonic boom propagation in rarefied atmospheres utilizing then extant acoustic and shock



propagation and attenuation theories for the calculation of shock overpressures. As a result, the authors were able to make a clear distinction between an impulsively produced shock wave at high altitudes and a shock wave created at the same altitude from a source which continuously inputs energy into the wavetrain. Waves of the former kind are very highly attenuated whereas waves of the latter kind are not. In the case of the Apollo signals, "the shock cone does not attenuate because energy is continually resupplied along the shock cone from the vehicle and its plume acting as a piston."

In an excellent survey article, *Donn* (1978) reviews previous work [*Balachandran, Donn and Rind* (1977) and *Rind and Donn* (1975)] utilizing sonic boom signatures radiated from flights of the Concorde to infer upper atmospheric wind profiles in the stratosphere and the thermosphere. The signals were recorded on two three-element microbarograph arrays located near Columbia University's Lamont-Doherty Laboratory. The interelement spacing in one of the arrays was ~ 1 km and monitored the frequency range extending from 0.1 Hz to 1.0 Hz and the second array had an interelement spacing of ~ 67 m so that the frequency range extending from 1 Hz to 10 Hz was monitored.

The central idea of the approach was to utilize the facts that the Concorde's flight path was very well known so that it could serve in some sense as a calibration source and that the acoustic trace velocity measured by the microbarograph arrays is given by

$$V_T = \frac{C}{\sin(\theta)} + W \quad (6.21)$$

where the first term on the right-hand side is the trace velocity, and where  $C$  is the sound speed,  $\theta$  is the wavefront arrival angle as measured from the vertical and  $W$  is the component of the wind in the direction of propagation. Since sound speed is a well known function of temperature, a knowledge of the temperature at the level of reflection, permits a determination of the wind speed at that altitude.

Figure 156 shows the familiar N-wave pressure signature of a sonic boom as recorded in the sonic boom carpet (or directly under the plane) and in the acoustic shadow zone.

Figure 157 presents example far-field waveforms recorded at Lamont for the indicated dates and times and Figure 158 shows the acoustic ray paths associated with the record section. In panel A of Figure 157, for example, the pulse on the far left-hand side

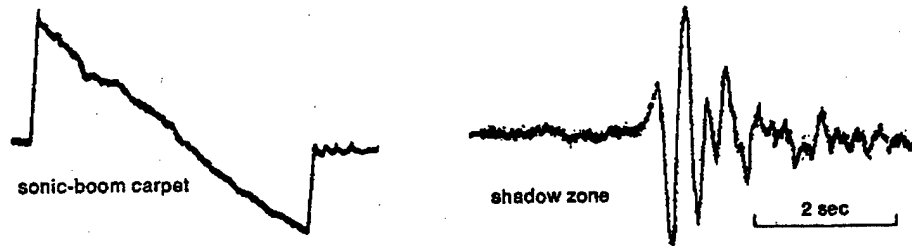


Figure 156. Sonic boom signatures recorded under and in the acoustic shadow zone of a Concorde flight. [Figure adopted from *Donn* (1978).]

represents the received acoustic energy from sound reflected in the stratosphere and which was radiated upward from the Concorde. The pulse to the far right-hand side of the panel is that due to the earth reflected path and the middle pulse of smaller amplitude is an arrival which has reflected at a different stratospheric altitude. Under favorable conditions, acoustic energy also arrives from ionospheric paths some 6 minutes after the arrival of the first stratospheric arrival and this circumstance is shown in Figure 159. When the thermospheric path is present, it is possible to monitor tidal changes in the thermospheric winds.

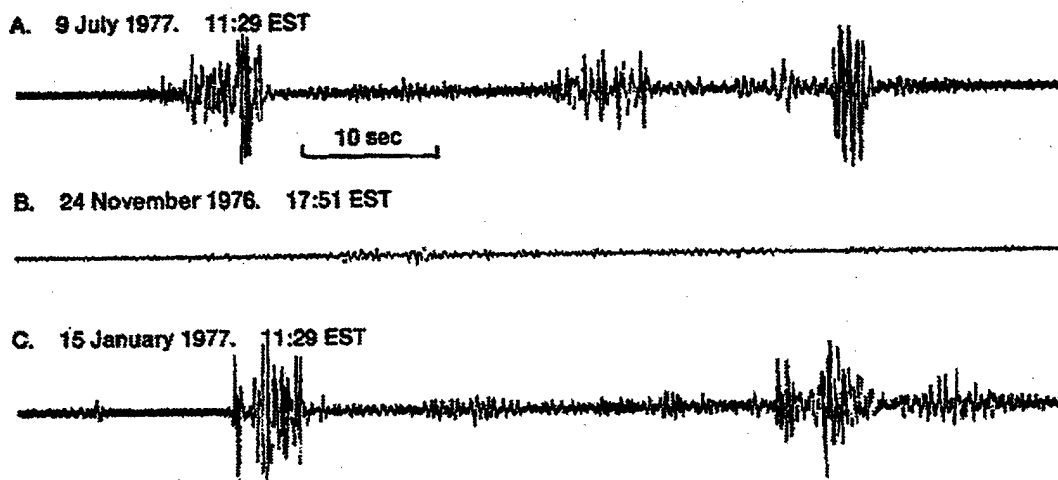


Figure 157. An example of far-field infrasonic waveforms recorded at the Lamont Doherty Laboratory. The total length of the arrival structure is approximately 50 s to 60 s. [Figure adopted from *Donn* (1978).]

When the event shown in Panel A was recorded, there were strong easterly stratospheric winds (winds blowing from the west-to-east) forming an excellent sound

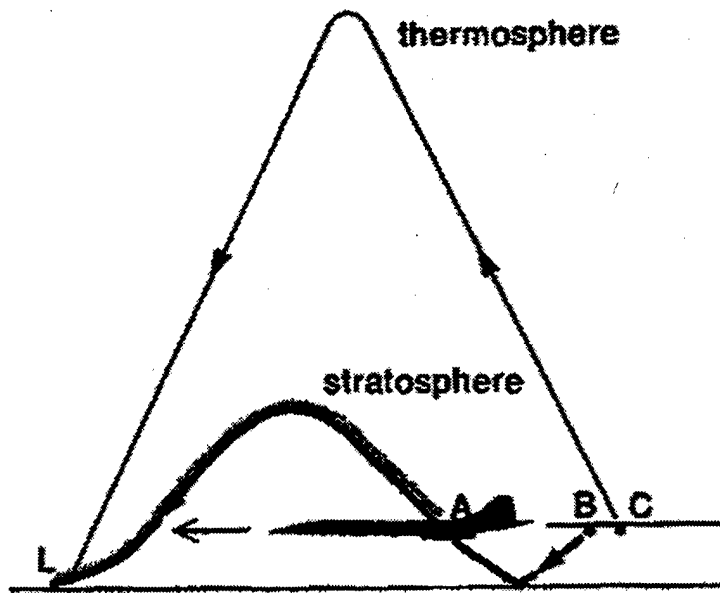


Figure 158. The acoustic ray paths which are associated with the record section shown in Figure 157. [Figure adopted from *Donn* (1978).]

duct. However, when the event shown in Panel B was recorded, the winds were westerly and no signal was recorded. When the event shown in Panel C was recorded there was a stratospheric warming which compensated for the stratospheric wind direction and allowed the formation a stratospheric duct and the propagation of the two stratospheric arrivals.



Figure 159. Infrasonic signals recorded from the Concorde by Lamont microbarographs on September 10, 1977 in the late morning (1020) and afternoon (1620). The signals pulse waveforms on the left-hand-side of the figure correspond to stratospheric arrivals and the pulses arriving at 1026 and 1628 on the right-hand-side of the figure correspond to thermospheric arrivals. The changes in arrival time, amplitude and frequency content of the thermospheric arrivals are caused by semidiurnal atmospheric wind changes. [Figure and material for the caption adopted from *Donn* (1978).]

*McIntosh* (1982) reports the observation of a characteristic N-wave due to a sonic boom and *Liszka and Waldemark* (1995) summarize recordings of infrasound generated by supersonic flights of the Concorde as recorded at stations operated by the Swedish Institute of Space Physics and, in addition, present new data acquired using higher resolution broadband recording equipment installed at the Lulea (65.8°N, 22.5°E) and Uppsala (59.8°N) recording stations.

Past work in the infrasonic monitoring of Concorde flights demonstrated detection ranges out to 4,000 km and that the infrasonic signals arrive in the frequency band extending from 0.5 Hz to 6 Hz. Utilizing the improved instrumentation, it was possible to investigate the "fine structure" of the infrasonic arrivals which demonstrated that in some cases the signal arrived from three different directions: a circumstance attributed to three distinct modes of propagation. Figure 160, for example, plots the azimuth of arrival of Concorde signals as a function reading number during the 21 minute time period extending from 2355 UT to 0018 UT on February 6, 1995. The size of the symbols in the figure are proportional to the spectral amplitude of the maximum signal and the figure clearly illustrates three propagation directions:  $\sim 240^\circ$ ,  $250^\circ$  and  $265^\circ$  with significantly more variability near the  $265^\circ$  azimuth. Figure 161 illustrates the frequency spectra of the Concorde signal corresponding to the azimuth of the flight illustrated in Figure 160.

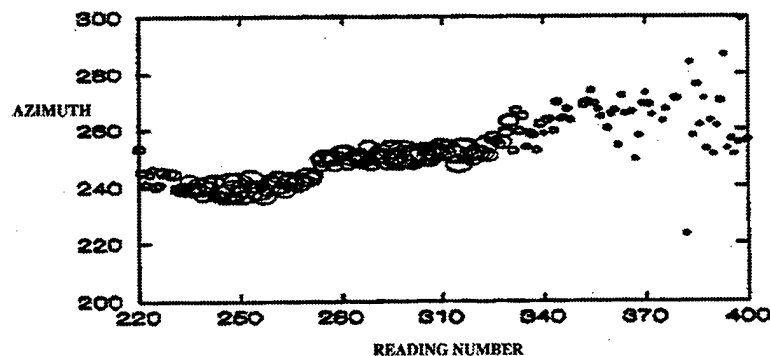


Figure 160. Azimuth of arrival angles of Concorde signals from a British Airways flight from London to New York. The size of the symbols representing azimuths are proportional to the spectral amplitude of the maximum signal. [Figure adopted from *Liszka and Waldemark* (1995).

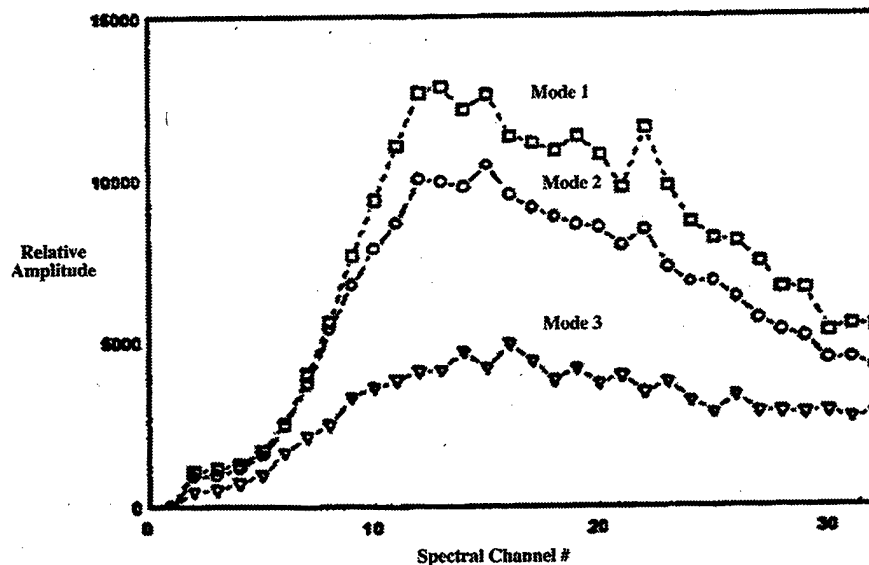


Figure 161. Frequency spectra of a Concorde infrasonic signal to the three observed propagation modes. Spectral channel #32 corresponds to 4.5 Hz. [Figure adopted from *Liszka and Waldemark (1995)*.]

Modes 1 and 2 are seen to have a significantly higher amplitude and character than propagation Mode 3.

Utilizing ray tracing for realistic temperature and wind speed stratified atmospheres, *Liszka and Waldemark (1995)* were able to show that the three propagating modes correspond to three different groups or "clusters" of rays which imply that the observed azimuth of a distant source may be significantly different from the true azimuth. An analysis of the Concorde data indicates that this azimuthal uncertainty may be as large as  $\pm 10^\circ$ . However, not all Concorde data exhibits such a modal propagation.

### 6.17 Thunder and Lightning

*Few, Dessler, Latham and Brook (1967)* reported on experiments designed to investigate the dominant frequency of sound radiated from thunder and presented an approximate theory describing the pressure waveform. In addition to presenting new data, the earlier experimental measurements of *Schmidt (1914)*, *Remillard (1960)*, and *Bhartendu (1964)* are referred to which concluded that the spectrum peaks in the infrasonic range near 1 Hz.

*Few, et al.*, (1967) report the results of separate observations which were made by two different groups: (1) investigators at Rice University who deployed Globe 100-B capacitor microphones for measurements in the frequency range from 0.1 Hz to 400 Hz and (2) investigators at the University of New Mexico, who deployed Bruel and Kajar capacitance microphones for measurements in the frequency range extending from 0.1 Hz to 20 kHz. The conclusions of both groups were that there was no peak in the infrasonic region, but that the dominant spectral peak fell in the range 180 Hz to 260 Hz. Later work by one of the authors [*Few* (1986) and *Few* (1969)] identified errors in this work and concluded that the correct frequency range was lower: ~ 40 Hz to 150 Hz. Figure 162 provides the measured pressure waveform as a function of time from thunder. The dominant frequency of the signal was estimated to be 260 Hz based on the zero crossings.

*Troutman* (1969) reported the results of formally exact numerical calculations on the pressure pulse (shock wave) produced by a lightning stroke modeled as a small cylindrical energy source. Results were presented as curves of overpressure as a function of shock radius for three values of energy release along the source length:  $3.5 \times 10^{11}$  ergs/m,  $3.5 \times$

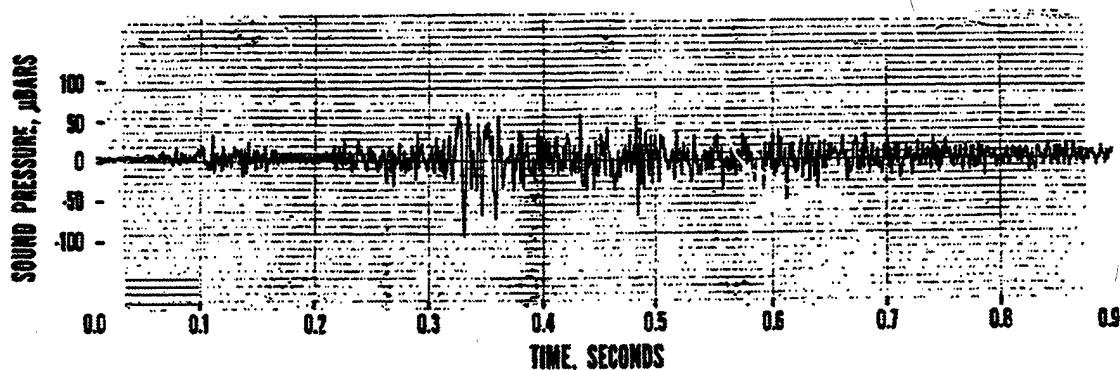


Figure 162. An example pressure waveform attributed to thunder. The dominant frequency content was estimated to be 260 Hz based on the zero crossings. [Figure adopted from *Few, Dessler, Latham and Brook* (1967).]

$10^{12}$  ergs/m and  $3.5 \times 10^{13}$  ergs/m. For an energy release of  $3.5 \times 10^{11}$  ergs/m, the calculations predicted an overpressure of 1 mbar (1,000  $\mu$ bar) at a range of 1 km which

was claimed to be consistent with measurements although it was noted that *Bhartendu* (1968) measured values below 0.1 mb (100  $\mu$ bar) at ranges of "a few kilometers".

*Bhartendu* (1968) also measured pressure waves associated with thunder and, in particular, refers to the work of *Schmidt* (1914) as presenting the first recordings of thunder induced pressure waves and in which two acoustic devices were used in the measurements: one device for measurements of infrasound below 5 Hz and a second device for measurements in the audio frequency range extending from 15 Hz to 200 Hz. *Schmidt* (1914) reportedly found that most of the energy in the spectra associated with thunder was rarefractive in nature peaking at 1.85 Hz in the infrasonic region, and in the frequency band between 15 Hz and 40 Hz in the audible band. On the other hand, *Arabakji* (1952) reported that the signals associated with thunder peaked at 0.5 Hz and were compressive in nature.

Like *Schmidt* (1914), *Bhartendu* (1968) utilized two different sensors to record data in the infrasonic and audible frequency bands. For infrasound measurements, a tripartite array of hot-wire microphones were used with the sensor output connected to a woofer speaker. The sensors were arranged in the geometry of a right triangle with a sensor separation  $\sim$  400 m. Data were acquired in the audible frequency range between 30 Hz and 13 kHz utilizing a crystal microphone.

*Bhartendu* (1968) reported that the overpressures recorded on the crystal microphone ranged between 7  $\mu$ bar and 71  $\mu$ bar. In addition, his measurements in the infrasonic range indicated that the highest levels occurred in the frequency range 1 Hz to 3 Hz and that, although the spectra were complex, they could be classified as one of three kinds depending on whether there was no intense primary maximum, one primary maximum or more than one infrasonic maximum. In the audible frequency range, the most common frequencies were observed to be in the ranges 22 Hz to 28 Hz, 52 Hz to 56 Hz, 66 Hz to 78 Hz with less commonly observed peaks in the frequency ranges: 34 Hz to 40 Hz, 88 Hz to 90 Hz, at 122 Hz and between 202 Hz and 204 Hz. Figure 163 illustrates a thunder record from a ground flash recorded at Saskatoon, Saskatchewan, Canada.

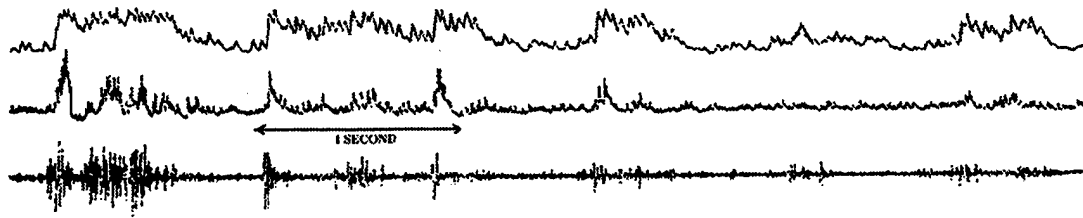


Figure 163. A thunder record from a ground flash. The upper trace is the record from the hot-wire microphone, the middle panel is the record from the crystal microphone and the bottom trace is the signal from the woofer. [Figure adopted from *Bhartendu* (1968).]

*Few* (1969) proposed a so-called "string-of-pearls" model for the production of sound by thunder in which a tortuous lightning channel is modeled as a spherical source in the far-field and as a cylindrical source in the near-field or in the region of wave formation. The work provides a justification of the earlier approximate model proposed by *Few*, *Dessler*, *Latham* and *Brock* (1967).

The string-of-pearls model predicts that the frequency at the peak in the radiated acoustic power spectrum,  $f_m$ , is related to the energy per unit length of the lightning channel,  $E_l$ , according to the relationship:

$$f_m = (0.63)C_o(P_o / E_l)^{1/2} \quad (6.22)$$

where  $C_o$  is the sound speed and  $P_o$  is the ambient pressure. The predicted form of the acoustic power spectrum and sound wave for a short line source is shown in Figure 164. As indicated in the figure, the predicted frequency at the peak of the power spectrum is  $\sim 60$  Hz for the assumed energy deposition per unit length. For comparison purposes, Figure 165 provides the measured acoustic power spectrum from a single thunder event.

Comparing the predicted and measured spectra shows that the two are in qualitative agreement except that the measured frequencies at the spectral peaks appear to be slightly lower than 60 Hz (e.g., in the upper panel of Figure 165 the measured peak is at 40 Hz). Equation (6.22) indicates that for this frequency, the energy deposition per unit length must be  $2 \times 10^6$  J/m which, however, is an order of magnitude larger than the measurements of *Krider, et al.* (1968).



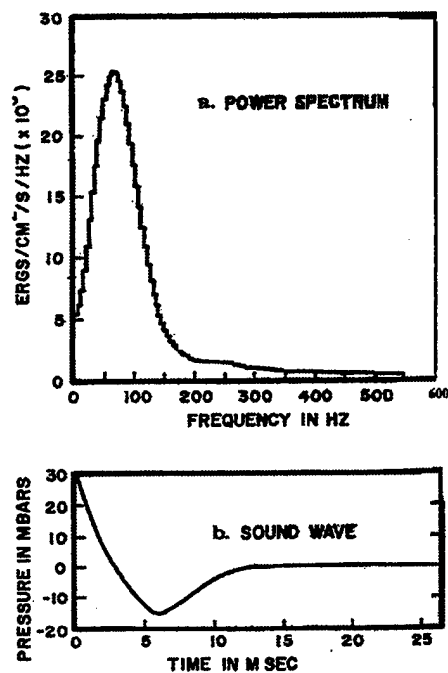


Figure 164. The predicted acoustic power spectrum and radiated sound wave for a short line source under the assumption of  $E_1 = 10^9 \text{ J/m}$  based on the string-of-pearls model. [Figure adopted from *Few* (1969).]

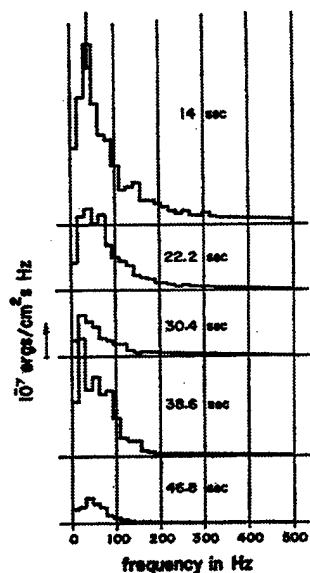


Figure 165. Measured acoustic power spectra for a single thunder event: a long lightning channel of  $\sim 16 \text{ km}$  estimated length. The spectra are computed from sequential data windows approximately 8.2 seconds in duration; the times indicated on the spectra give the lag between the flash and the beginning of the data window. [Figure and caption adopted from *Few* (1969).]

*Bohannon, Few and Dessler* (1977) report observations of infrasonic emissions from thunderclouds in experiments conducted in 1975 near Socorro, New Mexico and during 1976 at the Kennedy Space Center (KSC) in Florida. An analysis of the data show the existence of infrasonic pulses of period 0.5 s (or a frequency of 2 Hz) and of amplitude  $0.1 \text{ N/m}^2$  ( $1 \mu\text{bar}$ ).

The Socorro data were acquired utilizing an array of four Globe 100-B capacitor microphones arranged in a square having sides of length 40 m whereas the experiments conducted at the KSC utilized three arrays of four elements. Figure 166 provides example waveforms of one infrasonic event recorded on the microphone array located near Socorro, NM.

The infrasonic pulse is characterized by a strong compressive phase over the first half cycle followed by a rarefractive phase lasting about one-quarter second before its amplitude decays into the noise. Similar phases were observed in the experiments conducted at the KSC except that additional oscillations were often observed. Indeed, one event lasting 2.5 s was observed on all of the arrays. Acoustic source reconstruction indicates that the sources of the pulses are co-located with the regions containing horizontal lightning channels and the pulses arrive at the microphone array from directly overhead.

The observations are generally consistent with an electrostatic collapse source mechanism proposed by *Dessler* (1973): the predicted frequency, source location and amplitude agree with the observations. However, the initial part of the signal is observed to begin with a compressive rather than a rarefractive phase as predicted by the electrostatic collapse model so that additional source modeling is required.

*Balachandran* (1979) reported on the detection of infrasound radiated from a number of severe thunderstorms near a tripartite array located near the Lamont-Doherty Geological Laboratory of Columbia University. The data were gathered during the time periods: July 24 -25, 1975 and August 26-27, 1976. The signals were found, in general, to be "dominated by sharp rarefaction pulses with periods in the range of 0.4 - 1.0 s and

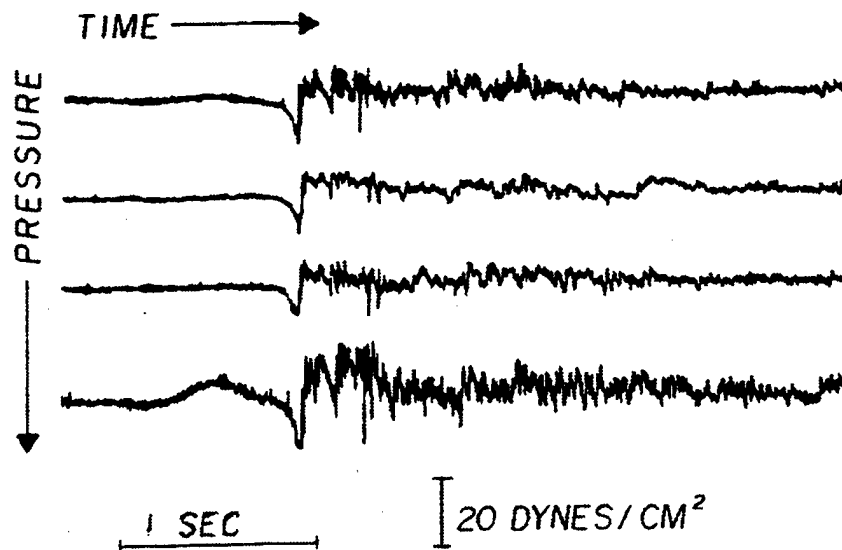


Figure 166. An example of an infrasonic pulse recorded by a four element microphone array located near Socorro, NM. Note that positive pressure is increasing downward. For this event, the infrasonic pulse arrives just prior to the thunder. [Figure adopted from *Bohannon, Few and Dessler (1977)*.]

peak-to-peak amplitudes up to  $10 \text{ dynes/cm}^2$  ( $1 \text{ N/m}^2$ ). The signals were found to be highly directional traveling almost vertically downward." The durations of the pulses were found to extend from a few seconds up to a maximum duration of some 30 seconds.

In interpreting the recorded signals, *Balachandran (1979)* utilized the theoretical model proposed by *Wilson (1920)*, and extended by *Dessler (1973)*, and found that the waveforms were in general agreement with the models. In the *Wilson (1920)* model, "the sudden reduction of the electrostatic field in a thundercloud following the lightning discharge is the source mechanism for the infrasonic component of the acoustic energy radiated by the thunder." Associated with this discharge, there is an implosion in a volume region of the thunderstorm which produces a pulse like signal. The source mechanism is such that the radiation of infrasound is highly directional being almost entirely in the upward and downward directions. Accordingly, the infrasonic signals from thunder will not, in general, be detected from thunderstorms unless the storm is almost directly

overhead. In this connection, *Balachandran* (1979) finds that all of the pulses associated with thunder arrived at the infrasonic array at angles less than or equal to  $45^\circ$ .

In the storms that were observed in August of 1976, *Balachandran* (1979) notes the "most important characteristic of the infrasound signal is that it is predominantly a rarefaction pulse with a roughly V-shape. This is true for the vast majority of the signals, with few exceptions. The duration of the main pulse is about 1 s (frequency of 1.0 Hz), and the peak-to-peak amplitude of the largest of the pulses is about  $10 \text{ dynes/cm}^2$  ( $10 \text{ }\mu\text{bars}$ ). A low-frequency tail (frequency of 0.25 Hz-0.125 Hz) at the end of the main pulse is observed occasionally."

However, in the storms that were observed in July of 1975, some pulses were found to initially be characterized by a compression phase so that there may be an additional source mechanism for the production of infrasound [*Bohannon, et al.*, (1977)].

*McIntosh* (1982) reported the observation of thunder in the winter on a four element microbarograph array located at Springhill, near Ontario, Canada. The signal arrival structure was found to be consistent with an acoustic source at a fixed altitude moving toward the infrasonic array. The frequency spectrum of the signals was found to be strongly peaked near 1 Hz. Signal durations were approximately 5 minutes. Figure 167 provides examples of the frequency spectra obtained.

## 6.18 Volcanoes

Perhaps the most widely studied volcanic event from the perspective of infrasound monitoring was the eruption of the Krakatoa volcano which occurred on August 26, 1883 and which was of such a magnitude to produce a gravity wave which traveled around the world three times [*Proc. Roy. Soc.* (1888)]. In the words of *Taylor* (1929): "In the years succeeding this event all available barograph records were collected by Lt.. Gen. Strachey and examined for traces of the wave. It was found that the velocity of the wave during its first passage outwards from the source was very constant. Using barograph records from

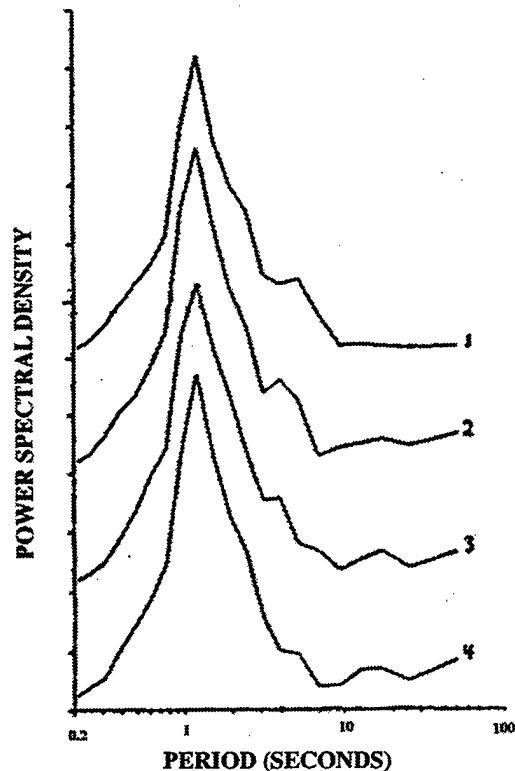


Figure 167. The frequency spectra of thunder signatures obtained in microbarograph observations at the Springhill near Ontario, Canada. The spectra are evidently displaced for easier interpretation. [Figure adopted from *McIntosh* (1982).]

the six nearest stations - viz., Calcutta, Shanghai, Bombay, Melbourne, Mauritius, Sydney - General Strachey found the mean velocity of the wave to be 713 mph, or 1046 feet per second, with a probable error of  $\pm 9$  feet /second." or, in metric units,  $318.82 \pm 2.74$  m/s.

- *McIntosh* (1982) reports observation of infrasound from Mount St. Helens on a four-element microbarograph array located at Saskatoon, Saskatchewan, Canada. Use was made of the *Posey and Pierce* (1971) relation and the records of the 4 MT Chinese nuclear test of 11/18/97 to estimate an equivalent explosive yield of 2 MT to 4 MT.

*Reed* (1987) has also estimated the equivalent explosive yield of the Mount St. Helens eruption also to be a few MTs based on an very careful analysis of 21 available NWS (National Weather Station) barograms near the volcano, other more distant microbarograph reports, comparisons with other large explosions, tree damage estimates,

audibility patterns and with known peak-to-peak pressure vs range scaling curves [e.g., ANSI (1983)].

Figure 168 shows the barogram recorded at the NWS station located at Toledo, Washington, on May 18, 1980. The signature is characterized by an initial very sharp compression "spike" of amplitude 373 Pa, followed by a pause and then a 13 min negative phase of amplitude 394 Pa followed by a second compressional wave peak which lasts a period of approximately one hour. The analysis indicates that the two latter phases are "both probably caused by ejecta dynamics rather than standard explosion wave phenomenology." The microbarograph stations reporting observations of pressure waves due to the volcanic eruption were those listed in Table 6.

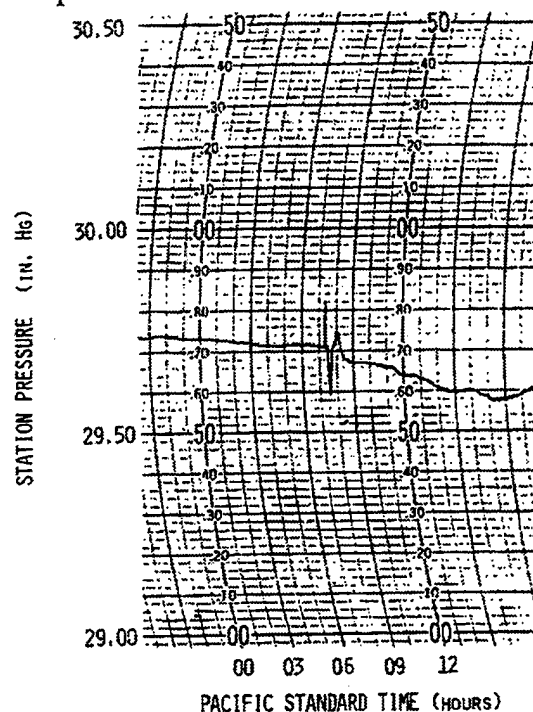


Figure 168. A barogram recorded at the Toledo, WA, NWS station due to the eruption of Mount St. Helens on May 18, 1980. [Figure adopted from Reed (1987).]

Delclos, *et al.*, (1990) report on the processing and interpretation of microbarograph records generated by the eruption of Mt. St. Helens on May 18, 1980. The eruption has been estimated to have an explosive yield of from 10 MT to 30 MT [Ritsema (1980; and Donn and Balachandran (1981)]. Data were recorded on an "array" of twelve microbarograph stations located at ranges of from 7,260 km to 30,940 km from the site of

Table 6. Microbarograph stations and recorded pressure amplitudes from the Mount St. Helens volcanic eruption of May 18, 1980. [Table adopted from *Reed* (1987).]

<u>Location</u>	<u>Latitude</u>	<u>Longitude</u>	<u>Distance (km)</u> <u>&amp; Emission Direction</u>	<u>Amplitude (Pa)</u>
Berkeley, CA	37.9°N	122.3°W	925 - South 39,106 - North	35
				13
Honolulu, HI	21.3°N	157.6°W	4,156 - West	17
DeBilt, Netherlands	52.2°N	5.3°E	7,982 - East	40
			- West	3
Washington, D.C.	39.0°N	77.1°W	3,700 - East	21
Boulder, CO	40.0°N	105.2°W	1,530 - SEast	50
Palisades, NY	41.4°N	73.9°W	3,950 - East	20
Hamburg, FRG	53.5°N	10.1°E	8,000 - East	14.2
Buchholz, FRG	53.4°N	9.0°E	8,010 - East	14.7
Kushiro, Japan	43.0°N	144.4°E	6,945 - West	14
Akita, Japan	39.7°N	140.1°E	7,453 - West	3
Tokyo, Japan	35.7°N	139.8°E	7,778 - West	10
Wajima, Japan	37.4°N	136.9°E	7,833 - West	11
Tonago, Japan	35.4°N	133.4°E	8,211 - West	11

the eruption. Table 7 provides the latitude and longitude coordinates for the station locations and their respective distances from Mt. St. Helens and Figure 169 provides a station map. As indicated, three stations were in French Polynesia, eight stations were in France, and one station in the Ivory Coast.

The microbarographs were developed by the Laboratoire de Detection et de Geophysique (LDG) and are of an inductance bridge type which produce an amplitude modulation on a carrier frequency of 1500 Hz. The sensors are made up of two chambers separated by a diaphragm. One volume is connected to the atmosphere by a 1.5 cm diameter pipe of length 3 m which presumably functions like a Daniel's pipe array to reduce wind noise. The first chamber is also connected to the first by a capillary tube. Instrument sensitivity is quoted as 1μbar to "several hundreds of μbars.

Figure 170 provides record sections of the pressure wave from the eruption for each of the stations in the "network" and Figure 171 provides computed spectra for six of

Table 7. Locations of the microbarographs deployed by *Delclos, et al.*, (1990) and which recorded the infrasonic signals emanating from the eruption of Mt. St. Helens.

<u>Station</u>	<u>Latitude</u>	<u>Longitude</u>	<u>Source/Station Distance (km)</u>
Polynesia			
TPT (Tiputa)	14.98°S	147.62°W	7,260
HAO (Hao)	18.17°S	140.80°W	7,400
PPT (Pamatai)	17.57°S	149.58°W	7,600
Northern France			
GRA (Granville)	48.85°N	1.57°W	7,990
POL (Polders)	48.62°N	1.58°W	8,010
FLE (Flers)	48.76°N	0.48°W	8,050
AUB (St. Aubin)	49.04°N	1.22°E	8,100
BRU (Bryyeres)	48.60°N	2.20°E	8,180
HAU (Haudompre)	48.01°N	6.35°E	8,410
Southern France			
VAL (Valensole)	43.83°N	6.01°E	8,785
AJA 2 (Ajaccio)	41.92°N	8.79°E	30,940
Ivory Coast			
LAM (Lamito)	6.22°N	5.03°W	11,520

the stations illustrating how the spectral content changes with propagation direction with N-S denoting north-to-south propagation, E-W denoting east-to-west propagation and W-E denoting west-to-east propagation. The waveform data show that the signals stand out well above the noise and that the peak-to-peak amplitudes range from slightly over 100  $\mu$ bar down to peak-to-peak levels of 60  $\mu$ bar.

The spectra indicate the presence of perhaps two propagating modes. One, referred to as "low-frequency" is more energetic at frequencies below 3 mHz (period greater than 5.5 min); the other, referred to as "high frequency" has significant energy content at frequencies higher than 4.5 mHz (period shorter than 3.7 min). Whereas, the first mode appears to be always present, the presence of the second would seem to



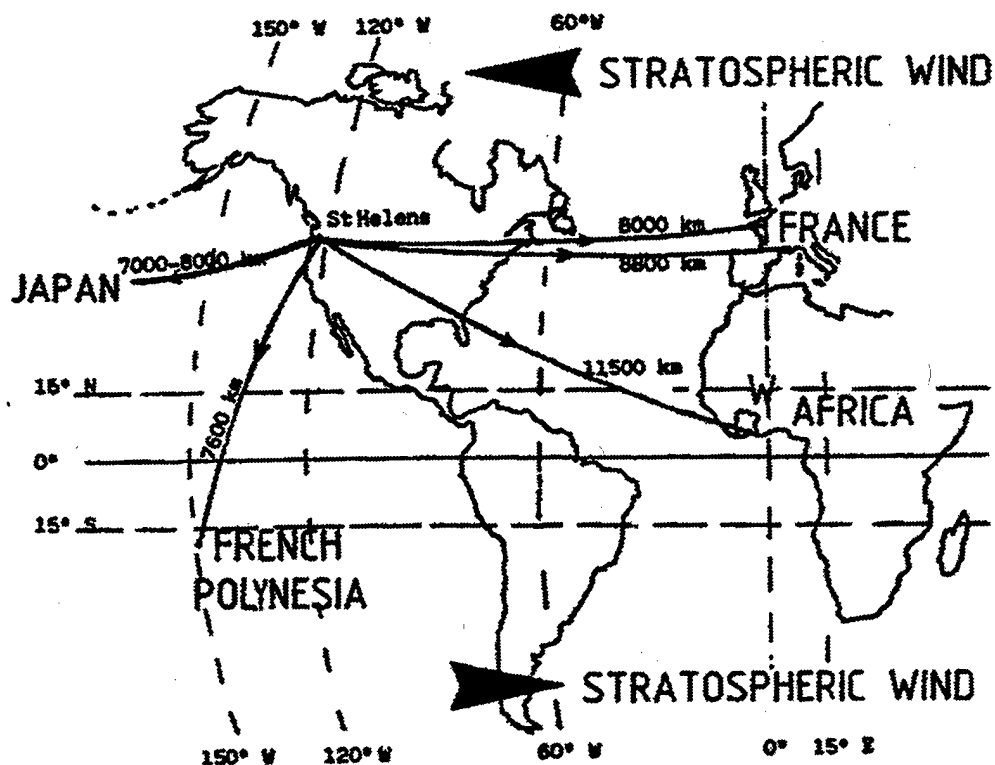


Figure 169. The French microbarograph station network which detected the air wave arrivals from the eruption of Mount St. Helens. [Figure adopted from *Delclos* (1990).]

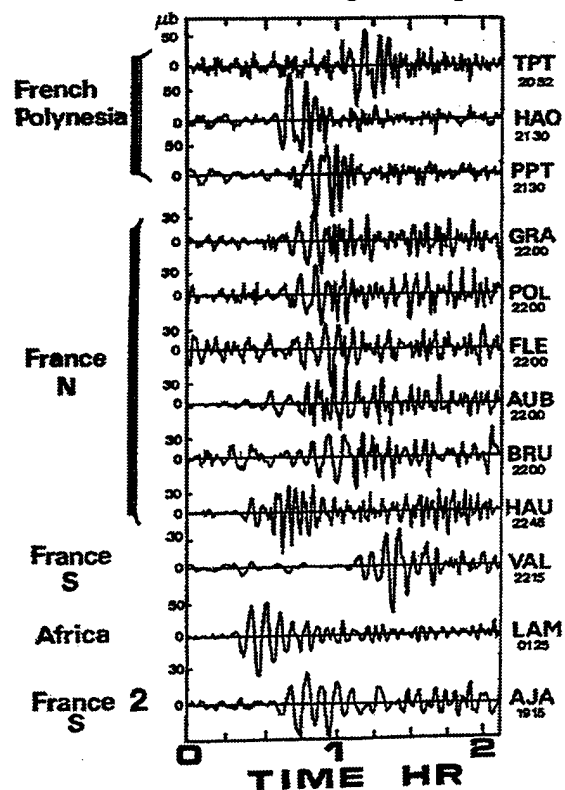


Figure 170. Record sections recorded at the indicated French stations from the Mount St. Helens volcanic eruption. [Figure adopted from *Delclos, et al.,* (1990).]

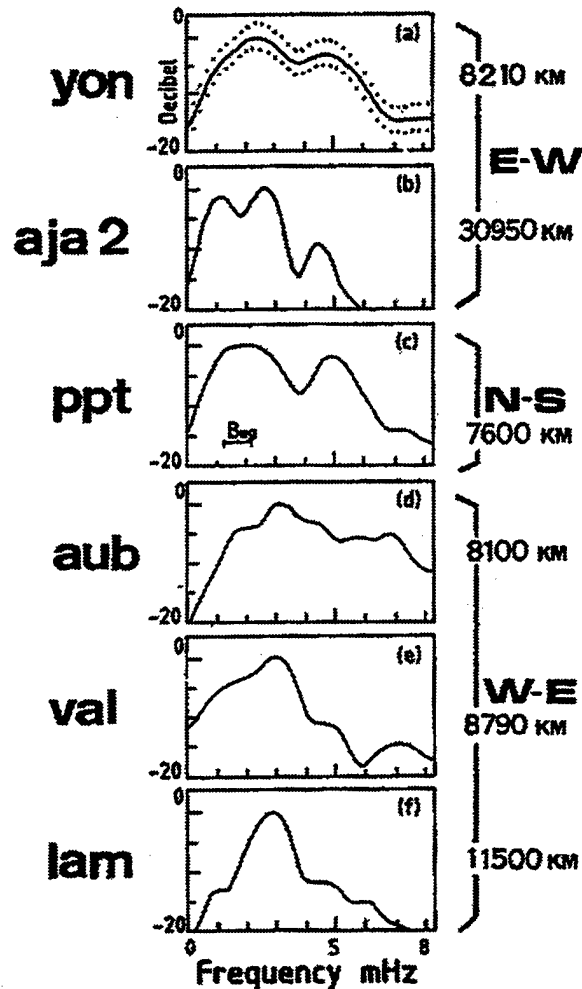


Figure 171. Computed single channel autospectra plotted in terms of decibels. The labels on the left-hand part of the figure denote the individual stations listed in Table 6.5. The propagation direction from Mount St. Helens to the station is indicated on the right-hand part of the figure along with the source-to-receiver distance.

depend on the propagation direction: present in E-W and N-S propagation, but absent in W-E propagation. *Delclos, et al.*, (1990) attribute the low-frequency mode to the Lamb mode, whereas the high-frequency mode is associated with an acoustic mode ( $A_2'$ ).

*Kanamori, Mori and Harkrider* (1994) analyzed the excitation of atmospheric oscillations excited by various volcanic eruptions where observations were available from both pressure and seismic sensors. Table 8 summarizes some of the observations.

*Kanamori and Mori* (1992) and *Widmer and Zurn* (1992) both reported the observation of long Rayleigh wave trains on a seismometers located 30 km from the site of the Pinatubo eruption which were found to be characterized by two predominant spectral

Table 8. Atmospheric oscillations excited by various volcanic eruptions [Table adapted from *Kanamori, Mori and Harkrider (1994)*]

Eruption	Period	Amplitude	References
1991 Pinatubo	270 s, 230 s	3000 $\mu$ bar at 30 km	<i>Kanamori and Mori (1992)</i> <i>Widmer and Zurn (1992)</i>
1982 El Chichon	195 s, 266 s		<i>Widmer and Zurn (1992)</i>
1980 Mt St. Helens	~ 300 s	300 $\mu$ bar at 67 km	<i>Kanamori, et al., (1994)</i>
1883 Krakatoa	~ 300 s	> 2000 $\mu$ bar at 200 km	<i>Kanamori, et al., (1994)</i>

peaks at 270 s and 230 s. *Widmer and Zurn (1992)* also reported similar observations following the El Chichon, Mexico eruption from data gathered on IDA (International Deployment of Accelerometers) stations and on a gravity meter located at the Black Forest Observatory in Germany. As indicated in the table, two spectral peaks were again observed at periods of 195 s and 266 s. The presence of a spectral peak at 300 s following the Mount St. Helens eruption was deduced following a reanalysis by *Kanamori, Mori and Harkrider (1994)* of a GDSN (Global Digital Seismic Network) data at a station 67 km from the volcano, and the presence of the peak at 300 s following the Krakatoa eruption of 1883 was deduced from a previously published barograph record recorded some 200 km from the volcano.

*Kanamori and Mori (1992)* postulated that the observed peaks were due to Rayleigh wave excitation near the source region due to atmospheric oscillations caused by the eruption, whereas *Widmer and Zurn (1992)* postulated a feedback process occurring between the atmospheric oscillations and the eruptive process.

*Kanamori, Mori and Harkrider (1994)* provided a careful theoretical analysis, briefly highlighted in Section 2.0, which, although valid for an isothermal atmosphere, rather convincingly demonstrated that the observed spectral peaks are associated with the

excitation of both gravity and acoustic wave modes which locally couple to the ground near the volcanic source and which excite Rayleigh waves which propagate radially away from the source.

By way of illustration, Figure 172 illustrates pressure waveforms and their

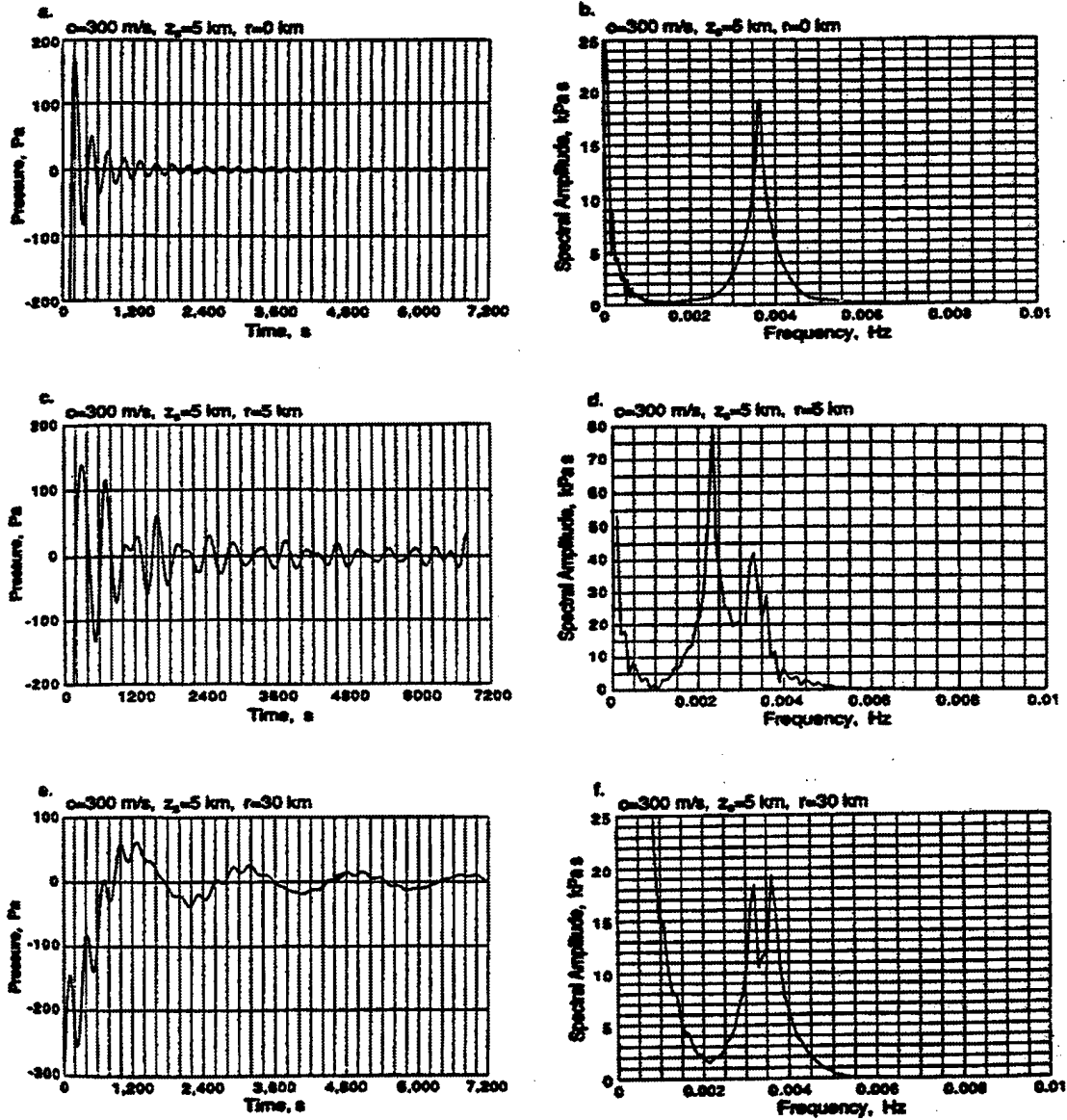


Figure 172. Computed pressure waveforms and their associated spectra as a function of range. Panels a and b are at zero range, Panels c and d are a range of 5 km and Panels e and f are at range of 30 km. In all cases, the source was taken to be at an altitude of 5 km and to be a mass injection source with a constant rate of mass input of  $10^9$  kg/s. [Figure and caption adopted from *Kanamori, Mori and Harkrider (1994)*.]

associated spectra as a function of range. Panels a and b in the figure correspond to zero range with the pressure waveform computed from Eq. (2.42). The signature and spectra are seen to be of a single frequency which corresponds to the acoustic frequency  $\omega_a$ . At a range of 5 km (Panels c and d) the signal is more complex and there are two spectral peaks where the dominant spectral peak occurs at a frequency of  $\omega_c$  defined previously in Eq. (2.45). Accordingly, at this range gravity-wave excitation is dominant: a circumstance not unexpected as the phase and group velocity vectors are perpendicular and the group velocity is in the direction of the pressure oscillation. At a range of 30 km, there are two spectral peaks: one at the acoustic frequency,  $\omega_a$ , and the other at the Brunt-Vaisala frequency,  $N$ . For a realistic atmosphere ( $c=300$  m/s and  $H = 6.6$  km) the acoustic and gravity wave periods are expected to be 275 s and 304 s, respectively whereas the observed periods are, from Table 8, 230 s and 270 s. The pressure waveforms presented in Panels c and e of Figure 172 are computed from a numerical evaluation of Eq. (2.43)

## 7.0 WAVEFORM DATA PRODUCED BY NUCLEAR AND CHEMICAL ATMOSPHERIC EXPLOSIONS

This section provides a "waveform zoo" for selected atmospheric nuclear and chemical waveforms recorded as a consequence of nuclear and chemical explosions conducted in the atmosphere and encountered during the conduct of the literature review.

*Yamamoto (1956)* analyzed barographic records from 14 stations surrounding the U.S. test sites in the Marshall Islands (Bikini and Eniwetok) and published four waveforms recorded at the Rongerik, Majuro, Wake, and Midway stations for February 28, 1954 and two records recorded at Kusaie and Majuro on May 4, 1964. Figure 173 shows the station locations in reference to the U.S. test site. In discussing his results, *Yamamoto (1956)* noted the poor acoustic propagation to the stations to the west of the test site and that wave propagation was generally 50 m/s faster to the east of the test site than to

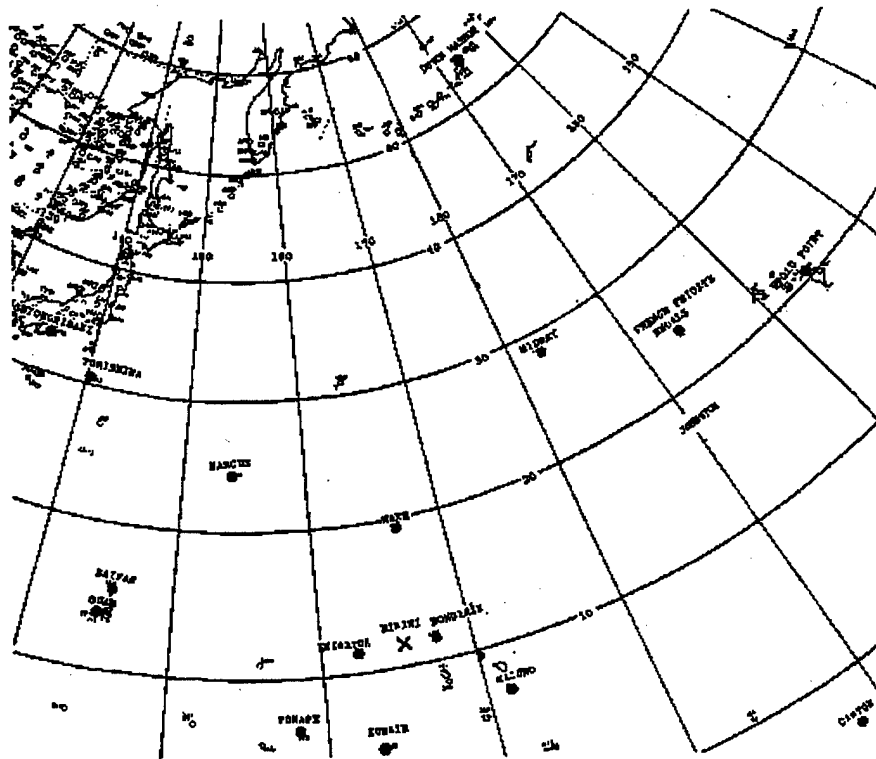


Figure 173. Barograph stations used in the analysis of U.S. atmospheric explosions conducted in the Marshall Islands. [Figure adopted from *Yamamoto (1956)*.]

the west. Figure 174 presents example barographic records.

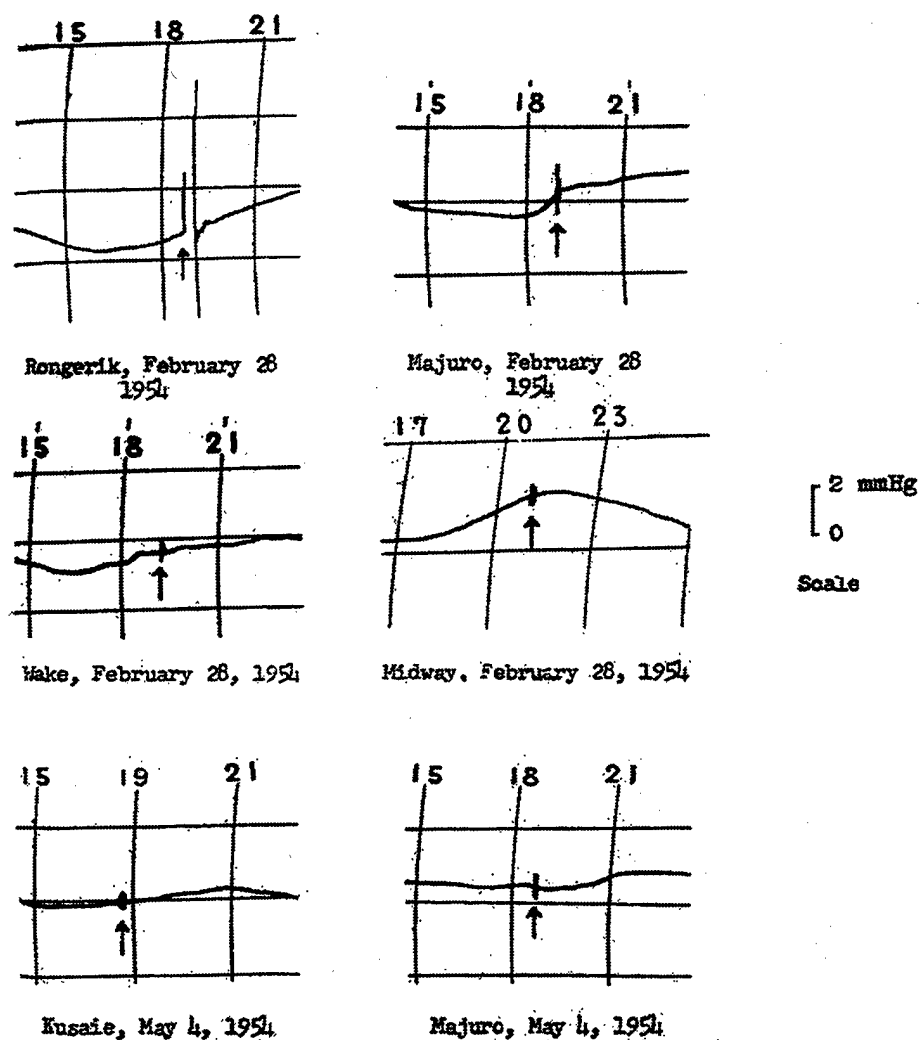


Figure 174. Example barograph records of U.S. explosions detonated in the South Pacific. The "Bravo" explosion of February 28, 1954 was a surface explosion having a yield of 15 MT. The "Yankee" explosion of May 4, 1954 was detonated in a barge and had a yield of 13.5 MT. [Figure adopted from Yamamoto (1956).]

Rose, Oksman and Kataja (1961) present microbarograph records of the October 30, 1961 Soviet 58 MT test which were recorded at Sodankyla, Finland. The peak-to-peak amplitude of the direct wave arrival was reported as  $\pm 1,000$  mbar. Waveforms of the antipodal and direct arrival-second transit were also provided, but the recorded peak-to-peak amplitudes were not. Figure 175 provides tracings of the arrival records.

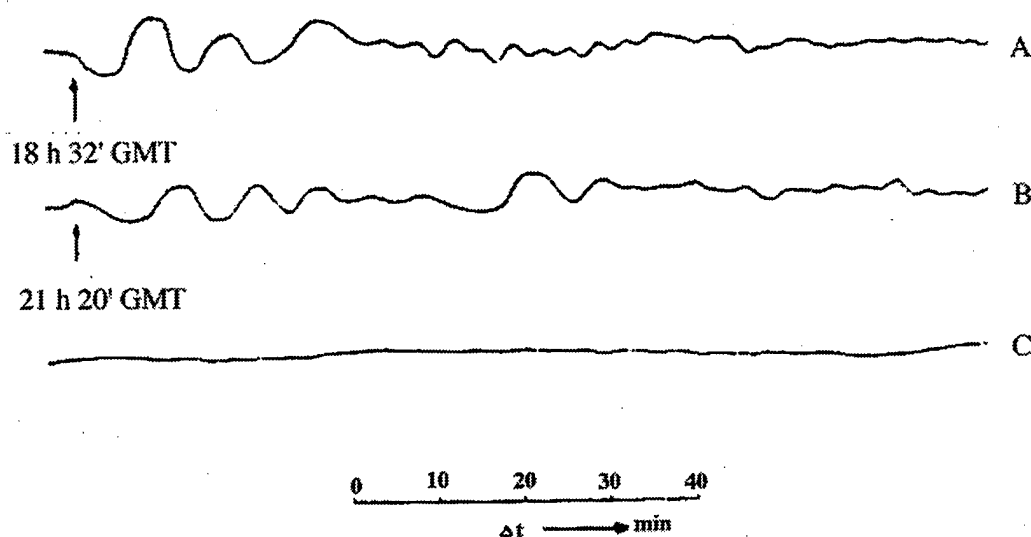


Figure 175. Recordings of the microbarograph at Sodankyla on October 31, 1961. A and B are the deflections of the backward and forward waves, respectively. C is a trace obtained under normal conditions. Pressure increases upwards. [Figure and caption adopted from *Rose, Oksman and Kataja (1961).*]

*Carpenter, Harwood and Whiteside (1961)* published waveform data from the 58 MT Soviet nuclear explosion detonated at Novaya Zemlya on October 30, 1961. The data were recorded in southern England and are clearly consistent with successive reflections from Novaya Zemlya and its antipode. Data were presented on the direct arrival, first antipodal reflection, first Novaya Zemlya reflection, second antipodal reflection and second Novaya Zemlya reflection. The waveform data recorded on microbarographs located at Foulness, England are shown in Figure 176.

*Jones (1962)* published waveform data recorded on two microbarographs at Aberdeen, England and from the Soviet 58 MT explosion of October 30, 1961. The microbarographs were described as differential sensors and "capable of a recording sensitivity of 0.1  $\mu$ bar per division." The direct wave which traveled a distance of 2,000 miles was reported to have had an amplitude of 1,000  $\mu$ bar as measured peak-to-trough. The first part of the pulse was reported to have a period of 4 min with the following higher frequency waves having a period of 2 min.



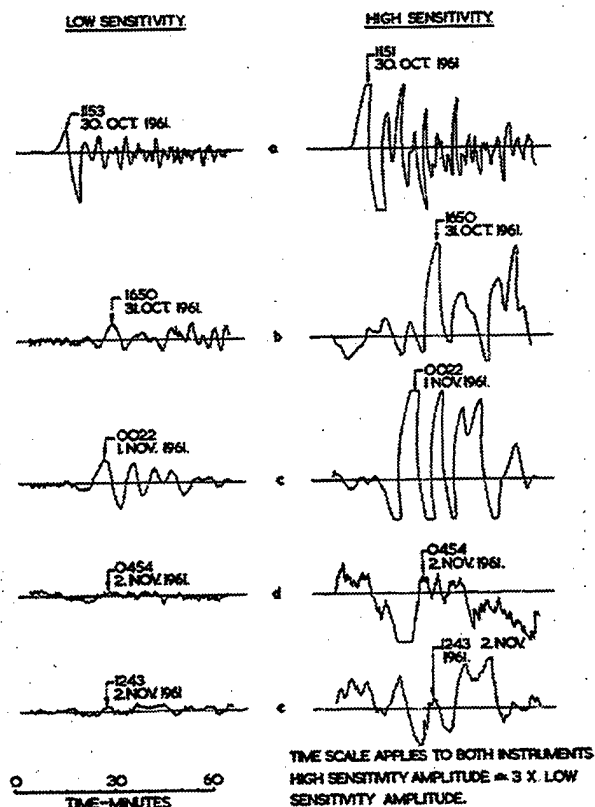


Figure 176. Waveform data from the 58 MT Soviet explosion of October 31, 1961 recorded in southern England. [Figure adopted from *Carpenter, Harwood and Whiteside (1961)*.]

The amplitude of the arrival from the antipode, which traveled some 23,000 miles, was reported to be 400  $\mu$ bar and to consist of 26 peaks. The earliest arrival in the pulse had a period of 9 min and the last arrival had a period of 2 min. The high amplitude of the arrival was attributed to focusing at the antipode.

Following the arrival of the antipodal pulse several additional arrivals were recorded: the wave rediverging from Novaya Zemlya was found to have an amplitude of 220  $\mu$ bar, the second passage of the direct wave was found to have an amplitude of 200  $\mu$ bar and the third direct wave arrival was reported to have an amplitude of 160  $\mu$ bar. Figure 177 shows the pressure waves recorded at Aberdeen with Panel A displaying the direct arrival, Panel B the antipodal arrival and Panel C the phase reflected from Novaya Zemlya.

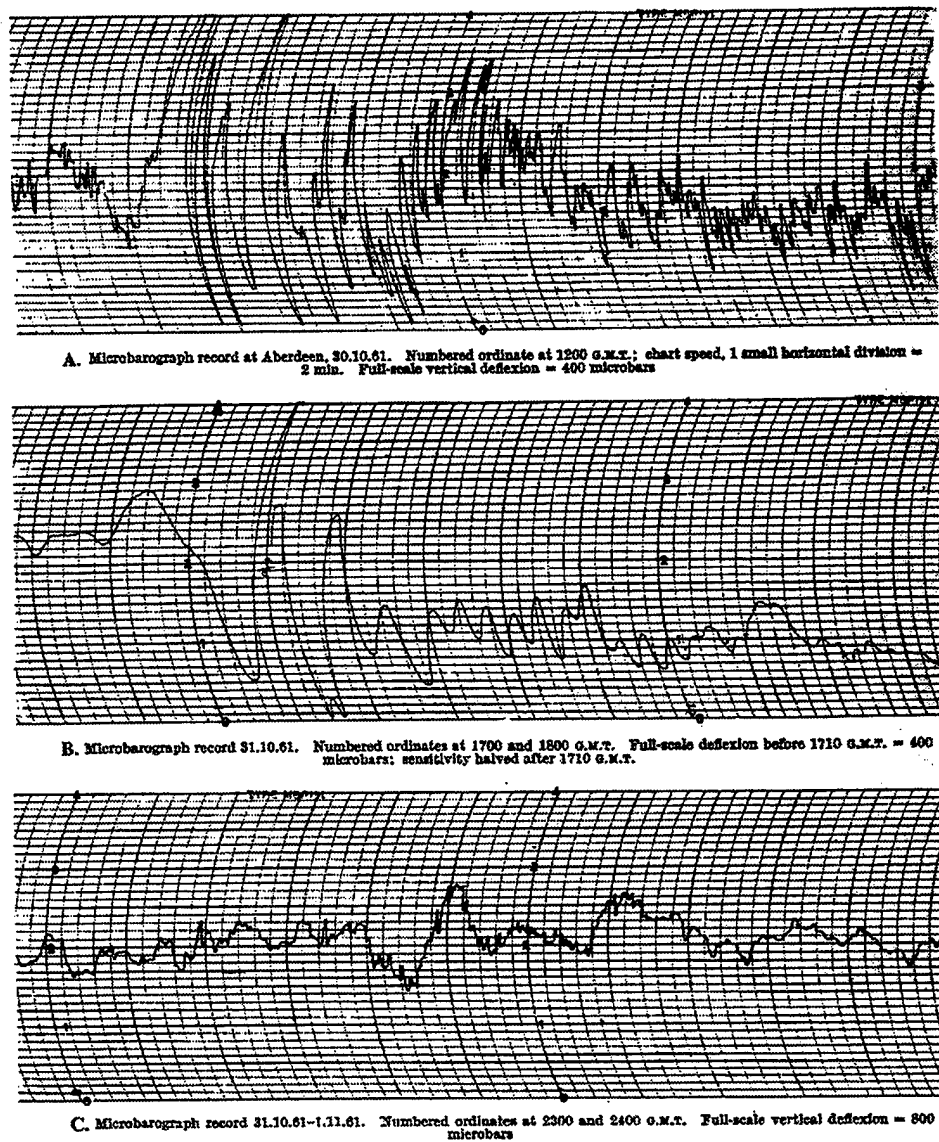


Figure 177. Waveforms recorded at Aberdeen, England from the Soviet 58 MT explosion on October 30, 1961. Panel A shows the direct arrival, Panel B the antipodal arrival and Panel C the reflected phase emerging from Novaya Zemlya. [Figure adopted from Jones (1962)].

Farkas (1962) discusses the detection of the 58 MT Soviet explosion of October 31, 1961 on seventeen widely distributed open-scale barographs of the New Zealand Meteorological Service. Waveform data were not presented. Only the times of arrival and amplitudes of the first, second and third waves were reported for the various stations making up the network. For the first, or direct wave, the reported amplitudes ranged from a

high of 700  $\mu$ bar to a low of 400  $\mu$ bar. The average speed of the pressure waves was calculated to be 306 m/s from the times of the first and second passages.

Araskog, Ericsson and H. Wagner (1962) published microbarograph recordings of Soviet atmospheric tests conducted on October 23, and October 30, 1961 at Novaya Zemlya. The recordings were made on a microbarograph located at Stockholm, Sweden which was described as the Shida type. The instrument was reported to have a "minimum discernible pressure variation of 0.5  $\mu$ bar, a sensitivity relative to middle frequencies of 3 db. at 0.01 and 0.5 c/sec, and stability of better than 5  $\mu$ bar/24 hr". Figure 178 shows the air pressure records recorded at Stockholm.

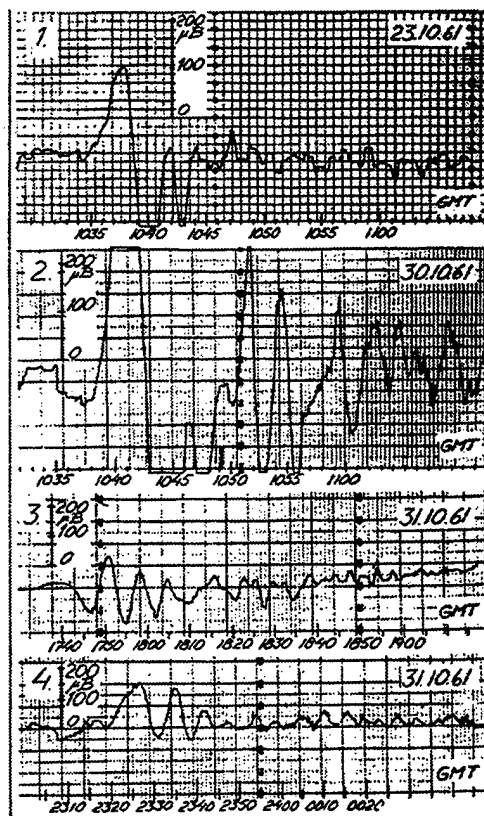


Figure 178. Air pressure records recorded at Stockholm, Sweden from Soviet explosions on October 23 and October 30, 1961. Panels 1 and 2 show the direct and antipodal arrivals from the October 23 test and Panels 3 and 4 show similar waveforms for the October 30 test. [Figure adopted from Araskog, Ericsson and Wagner (1962).]

The explosion which was detonated on October 23 had a direct wave amplitude of 500  $\mu$ bar peak-to-peak and the October 30 explosion had a direct wave amplitude of 1600

μbar peak-to-peak. On October 24, the antipodal arrival from Novaya Zemlya was recorded and on October 31, two antipodal arrivals from the October 30 explosion were also recorded.

*Donn and Ewing* (1962a) published records of acoustic-gravity wave records recorded at Lamont-Doherty and at stations in Japan and these records are provided in Figure 179. The left-hand panel (Panel A) displays the waveforms recorded at Lamont

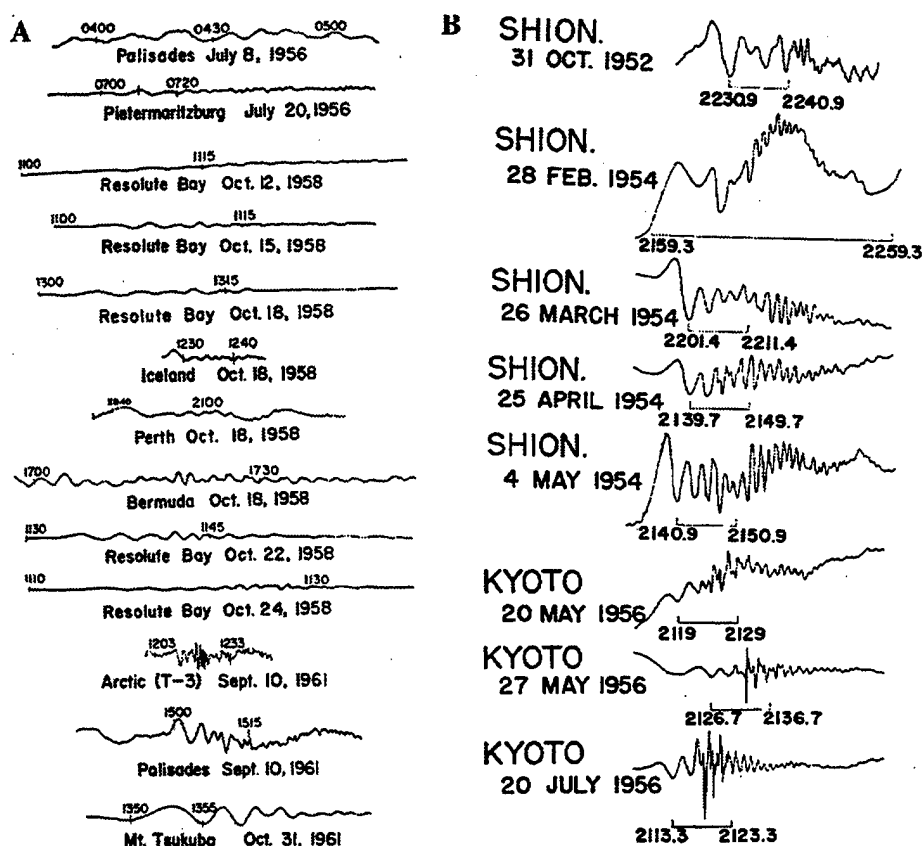


Figure 179. Acoustic-gravity wave records recorded utilizing Lamont-Doherty microbarographs from 1956 to 1961 (left-hand Panel A) and atmospheric waves recorded at stations in Japan (right-hand Panel B). On both panels, the indicated times are UT and SHION represents the city Shionomisaki. [Figure adopted from *Donn and Ewing* (1962a).]

and the right-hand panel displays the waveforms recorded at the indicated stations in Japan. The Lamont microbarographs are described by *Donn and McGuinness* (1958) and the Japanese instruments by *Namekawa* (1956).

In a sequel, *Donn and Ewing* (1962b) published additional data recorded at Lamont, from the Lamont global network stations at Terceira and Perth, from Foulness, England and from Japan. Figure 180 provides the recordings made a Lamont for the large

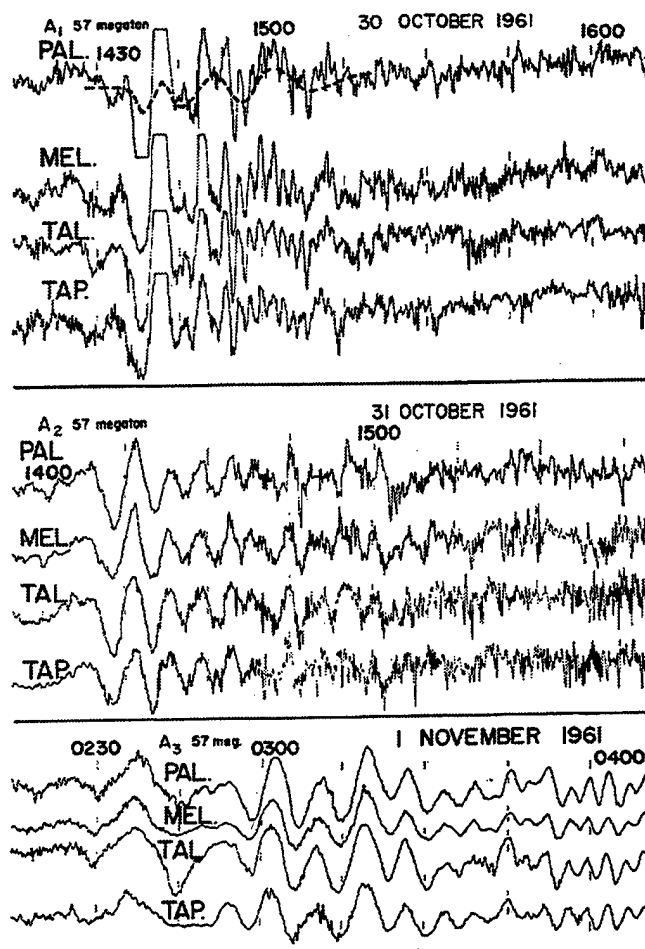


Figure 180. Pressure records from the Lamont multipartite microbarograph array due to the large Soviet nuclear explosion of October 30, 1961. The top panel is the A<sub>1</sub> group or direct arrival, the middle panel is the A<sub>2</sub> group or antipodal arrival and the lower panel is the A<sub>3</sub> group or the waves reflecting from Novaya Zemlya. [Figure adopted from *Donn and Ewing* (1962b).]

Soviet nuclear test of October 30, 1961 and Figure 181 provides records for the same event recorded at Perth, Australia, Terceira, Azores and Kyoto, Japan.

The Lamont records are for U.S. explosions detonated in Marshall Islands and for Soviet explosions detonated at Novaya Zemlya, and the Japanese records are for U.S. Explosions in the Marshall Islands during the period extending from 1952 to 1956.



observations were made on "customary 4-day meteorological barographs having a tape speed of 9 hours/inch."

Using the data set, *Wexler and Hass* (1962) developed isochrone plots of the A<sub>1</sub> arrival over the northern hemisphere, the arrival time of the A<sub>1</sub> primary wave over the southern hemisphere, the arrival time of the returning wave antipodal arrival (B<sub>1</sub>) in the southern hemisphere and the returning A<sub>1</sub> arrival in the northern hemisphere. In interpreting the results of the returning A<sub>1</sub> wave, there was noted a general and qualitative relationship between high amplitudes and propagation directions opposed to the direction of upper wind components and *vice versa*.

In addition, the measurements in signal amplitude from the source as measured by stations in the northern hemisphere were averaged over 10° latitude intervals with the results shown in Figure 182. As indicated, the amplitude function is of the general form,  $A = e^{-bx}$ , indicating a smaller rate of amplitude decay from the source than the geometrical  $1/r$ . This effect, as noted by *Wexler and Hass* (1962), "is most likely due in large part to augmentation of the selected primary wave forms of different modes."

*Wexler and Hass* (1962) also compared the composite waveform constructed by *Whipple* (1930) for the Siberian meteor of 1908 with waveforms recorded from the 25 MT Soviet explosion of October 23, 1961 (Figure 183). The conclusion is that the two man-made explosions were "comparable in their effects on the atmosphere" as was the Siberian meteorite event.

*Jones and Forbes* (1962) presented microbarograph recordings made at Aberdeen, England, which were attributed to the high altitude U.S. test referred to as the "rainbow bomb" of July 9, 1962 and to the 30 MT Soviet explosion of August 5, 1962. The maximum amplitude for the U.S. test was reported to be 25  $\mu$ bar whereas the direct wave arrival from the Soviet test was reported to be > 500  $\mu$ bar. In the case of the Soviet test, several other arrivals were also recorded with the following amplitudes: antipodal wave

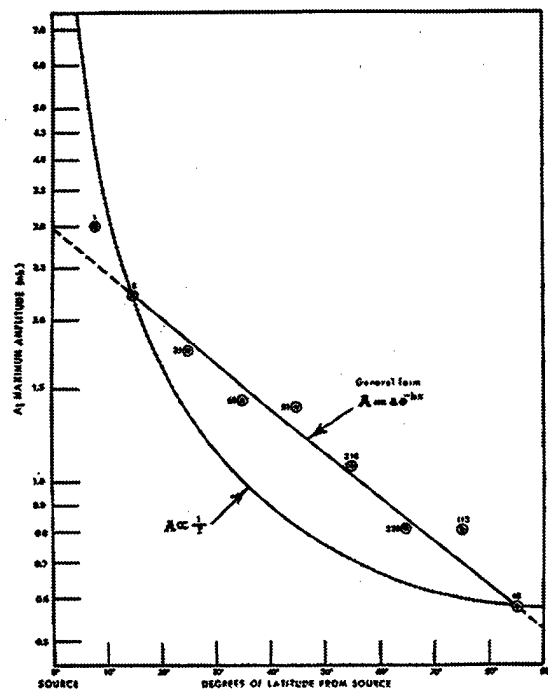


Figure 182. The variation of the direct wave amplitude ( $A_1$ ) with range (or latitude) from the source. The number of observations used per  $10^\circ$  of latitude interval are as indicated. [Figure adopted from *Wexler and Haas (1962)*.]

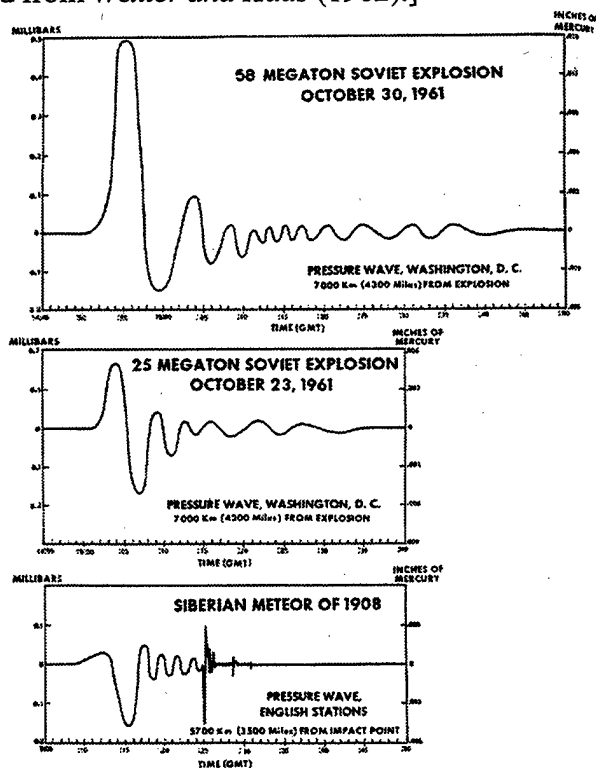


Figure 183. A comparison of recordings of the Soviet explosions of October 23 and 30, 1961 with the composite waveform constructed by *Whipple (1930)*. [Figure adopted from *Wexler and Haas (1962)*.]



(150  $\mu$ bar), direct wave-second transit (200  $\mu$ bar), antipodal wave-second transit (80  $\mu$ bar) and the direct wave-third arrival (80  $\mu$ bar). The relatively low amplitude of the U.S. test was attributed to its poor coupling to the atmosphere. *DOE* (1994) reports the altitude of the explosion as 400 km and the yield as 1.4 MT.

*Wagner and Ericsson* (1963) published an empirical fit of microbarograph peak-to-peak pressure,  $\Delta p$ , as a function of period,  $\tau$ , for Soviet explosions conducted at Novaya Zemlya during 1961 and 1962. The period is defined as the time difference between the first and second peaks in the record and the recordings were made on microbarographs located at Upsala Sweden at a propagation range extending from 1,900 km to 2,300 km. The empirical relation so derived is given by

$$\Delta p = 3.5 \times 10^{-3} \tau^2. \quad (7.1)$$

In what is basically an excellent review article on the propagation of air waves from nuclear explosions, *Donn, Pfeffer and Ewing* (1963) published waveform data recorded at several stations from Soviet tests conducted on October 23 and October 30, 1961, and on April 5, 1962. The stations recording the waves were located at Palisades, New York; Kyoto, Japan; Foulness, England; Terceira, Azores; Perth, Australia; Reno, Nevada; Troy, New York; Mt. Tsukuba, Japan; Suva, Fiji; Stockholm, Sweden; Whippany, New Jersey; and Honolulu, Hawaii. All stations reported receiving the A<sub>1</sub> arrival from each of the explosions in the test series, and the stations at Palisades, Foulness, Kyoto, and Stockholm reported receiving the A<sub>1</sub>, A<sub>2</sub> and A<sub>3</sub> arrivals from the 50 MT Soviet explosion of October 30, 1961.

*Donn, Shaw and Hubbard* (1963) published additional waveform data from Soviet tests which were recorded in Japan covering the period from October 31, 1952 through July 21, 1956. In addition, the Lamont microbarograph program and instrumentation are briefly described.

*Bhartendu and Currie* (1964) published A<sub>1</sub> waveforms recorded at Saskatoon, Canada (52.1° N, 106.6° W) from Soviet tests conducted at Novaya Zemlya on August 27, 1962, September 15, 19, and 25, 1962 and on October 22, 1962. In addition, group velocity dispersion curves were computed for each of the explosions and compared to those computed from model atmospheres considered by *Pfeffer and Zarichny* (1962). The computed dispersion curves were not found to be of the same shape as those measured and, for a fixed period, a maximum spread of about 40 m/s was observed in the experimental dispersion curves: a circumstance attributed to winds and differing atmospheric conditions along the propagation path.

*Bhartendu and McCrory* (1966) presented data from two chemical explosions having a yield of 10 T of TNT and detonated at the White Sands Missile Range on October 28, 1965 and on November 2, 1965. The pressure waves from the first explosion were detected at a site in Socorro 47.5 miles (12.03 km) distant and at a mountain site 50.5 miles (12.8 km) distant. The maximum reported overpressure at Socorro was 82  $\mu$ bar and at the mountain site a maximum value of 11  $\mu$ bar was recorded. Signal durations were reported as being 40 s. The amplitude differences were attributed to propagation inside and outside of a temperature inversion. No records were obtained from the second explosion presumably because of extant meteorological conditions. The sensors were hot-wire pressure transducers connected to a reference volume.

*Reed* (1966) reported microbarograph observations of waveforms recorded on a number of sensors deployed around the NTS from three HE explosive events intended to serve as calibration explosions for an underground nuclear test. Each of the charges were of size 1,090 kg but, because the charges were located on wooden towers 4.6 m above ground, the equivalent free-air blast size was 2,000 kg. Waveforms were reported for the St. George, Utah, station which was located at the longest range, 252 km, from the NTS. Shot times were such that waveform variability could be compared over periods of 3 min, 6 min and 9 min. Significant amplitude variation was observed at the individual stations

making up the network. By way of illustration, at St George the maximum peak-to-peak amplitudes of the first shot were 44.4  $\mu$ bar. For the second shot, which occurred 6 min later, the reported peak-to-peak amplitude was 28.8  $\mu$ bar and for the third shot, which occurred 9 min after the first and 3 min after the second, the reported amplitude was 16.1  $\mu$ bar. The observed variability was postulated to be due to atmospheric turbulence.

*Donn and Shaw* (1967) published the entire collection of nuclear explosion records recorded on the Lamont network of infrasound stations. Additionally, a discussion of the results of applying spectral analysis was reported which definitely confirmed the existence of inverse dispersion. The report also provides a listing of the station locations and a listing of atmospheric nuclear tests (and estimated yields) conducted by the United States in the Marshall Islands during the time period extending from February 28, 1954 to November 4, 1962 and by the Soviet Union for the period extending from October 12, 1958 to December 25, 1962. These records are reproduced in Appendix A of this report.

*Jones* (1967) published a microbarogram of the first Chinese nuclear explosion on June 17, 1967. The data was recorded on a microbarograph at the University of Aberdeen at an approximate range of 4,000 miles. The wavetrain from the explosion was superposed on one having an amplitude of 250  $\mu$ bar and a period of 12 minutes. The latter wavetrain was said to commonly occur during a temperature inversion. Full scale deflection of the largest portion of the explosion waveform was 270  $\mu$ bar and the reported period of this portion was 2 to 4 minutes. Reference is also made to the amplitudes of two Soviet explosions: 350  $\mu$ bar for the 25 MT test on October 23, 1961 and 1,000  $\mu$ bar for the 58 MT test on October 30, 1961. The explosive yield of the Chinese test was estimated to be between 20 MT and 30 MT. Figure 184 shows the received waveform

*Grover* (1968) presents data recorded from chemical explosions on a five element microbarograph array located at Blacknest, England. The dimension of the array was 25 km by 25 km and the basic sensor was a commercial bellows with the response controlled

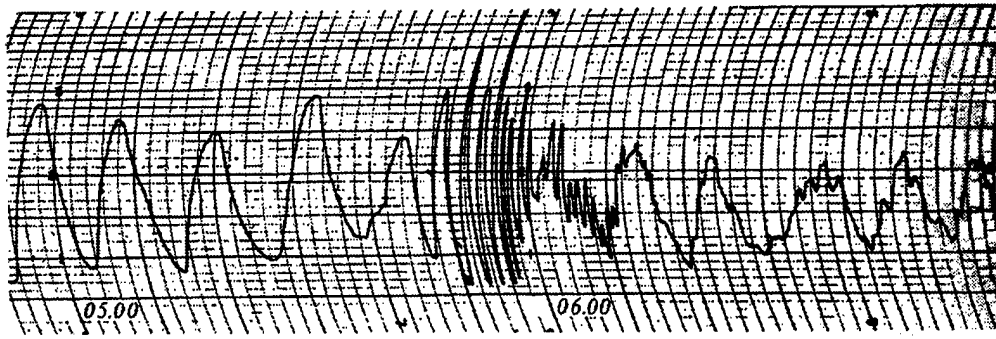


Figure 184. A microbarograph record of waves from the first Chinese nuclear explosion recorded at Aberdeen, England. Full scale deflection is approximately 270  $\mu$ bar for those waves having a period of 2 min-to-4 min. [Figure adopted from *Jones (1967)*.]

by an atmospheric leak to a backing volume. Changes in pressure, cause changes in the length of the bellows which is transferred to a d.c. displacement transducer.

The explosive sources were a "foundered ammunition ship three miles off Folkstone" and a fuel tank explosion "during a fire at an oil refinery near Rotterdam". The Rotterdam explosion produced a waveform of amplitude 5  $\mu$ bar and period of 8 s whereas the Folkstone explosion produced a waveform of widely varying amplitude. The maximum amplitude was reported to be 20  $\mu$ bar and to have a period of 4 s.

*MacKINNON (1968)* discusses microbarograph oscillations produced by nuclear explosions which were recorded in Great Britain and Eire with the goal of both presenting the data and of quantifying the influence of winds on the amplitudes of the recorded signals. Recordings were made using two types of barographs: the Shaw-Dines microbarograph [*Shaw and Dines (1905)*] and the Dines float microbarograph [*Dines (1929)*]. Tracings of recordings from the Dines-Shaw barograph were reported for the A1 arrival from the 25 MT Soviet test of October 23, 1961 and for the A1, A2 and A3 arrivals from the October 30, 1961 58 MT Soviet explosion. Figure 185 provides tracings of recordings of the ground level pressure fluctuations from explosions conducted at Novaya Zemlya.

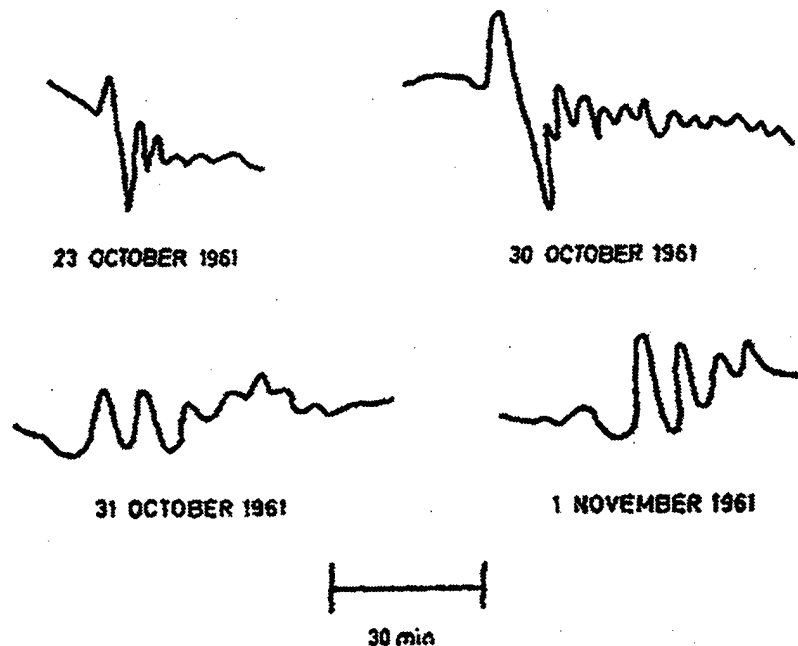


Figure 185. Waveform tracings of recordings from two explosions at Novaya Zemlya. The October 31, 1961 and November 1, 1961 records represent A2 and A3 arrivals. [Figure adopted from *MacKINNON* (1968).]

*MacKINNON* (1968) was able to demonstrate the effect of wind on the amplitude of the infrasonic arrivals by comparing the amplitudes of arrivals received in Great Britain and Eire with those from the same explosions recorded in Japan. In particular, it was shown that the maximum amplitudes of the wavetrains depend on wind conditions as does the speed of the waves. The practical implications are that the effect of winds on atmospheric propagation must be taken into account when estimating the yield of a nuclear explosion based on the pressure record from a microbarograph.

*Varghese and Kumar* (1970) report the observation of pressure waves from the Chinese atmospheric test of December 27, 1968. The waveforms were recorded on two tripartite microbarograph arrays separated by a distance of 1,670 km. One array was triangular (Array I) with sensors separated by 23 km, 29.6 km and 39.9 km. Sensors in the second array were separated by a distance of 22.5 km, 32.7 km and 23.25 km (Array II). However, signal levels and an estimate of the explosive yield were not reported. Noise levels at the array locations near Bombay, India were reported to be in the range from 5

$\mu\text{bar}$  to 80  $\mu\text{bar}$  and the sensors were described as being a sensitive bellows connected to a backing volume communicating to the atmosphere through a suitable leak. The pressure differential was measured by a displacement transducer. The microbarograph records for the event are provided in Figure 186.

*Tolstoy and Herron (1970)* report microbarographic observations of the Chinese explosion of June 17, 1967 and the "high energy" events which occurred on July 15 and August 24, 1967. The data were acquired on an array of 6 to 12 microbarographs dispersed around the Hudson Laboratories of Columbia University. Because of high noise levels, the signals were processed by first passing them through a 10-to-25 min filter and then beamforming them. The signals were found to have a predominant period of 15 min and to propagate with a group velocity of 600 m/s from the direction of the Lop Nor test site. The maximum peak-to-peak amplitude of the direct arrival was reported to be 115  $\mu\text{bar}$ . After storm related noise had subsided, the antipodal arrival was recorded and found to have a maximum peak-to-peak amplitude of 80  $\mu\text{bar}$ .

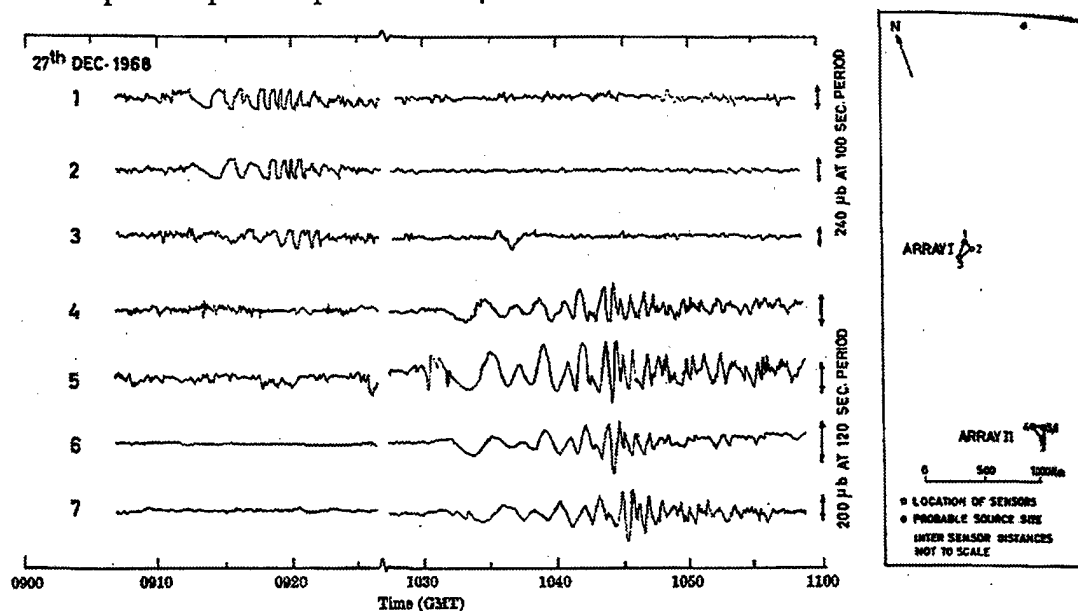


Figure 186. Microbarographic recordings from the Chinese atmospheric test of December 27, 1968. The indicated pressure records were recorded by the sensors making up the two arrays shown in the right-hand panel. [Figure adopted from *Varghese and Kumar (1970)*.]

Utilizing similar processing, the direct and antipodal arrivals were found, respectively, to be 50  $\mu\text{bar}$  and 30  $\mu\text{bar}$  for the high energy event of July 15 and 30  $\mu\text{bar}$  and 25  $\mu\text{bar}$  for the high energy event of August 24, 1967.

*Tolstoy and Herron (1970)* made the case that the observed arrivals were surface gravity waves traveling on what is effectively the top of the atmosphere and suggested the reason that other investigators had not reported the observation was because they had not beamformed their data.

In what is now a classic paper in the field, *Posey and Pierce (1971)* provided a very simple relationship for estimating the yield of a nuclear explosion given by

$$E = 13 p_{\text{FFT}} [r_e \sin(r / r_e)]^{1/2} H_s (c T_{1,2})^{3/2} \quad (7.2)$$

where in the above  $E$  is the energy release in ergs,  $p_{\text{FFT}}$  is the first peak to trough pressure amplitude,  $r_e$  is the radius of the earth,  $r$  is the great circle distance from the site of the explosion to the receiver location,  $H_s$  is the scale height of the lower atmosphere,  $c$  is the local sound speed at the receiver and  $T_{1,2}$  is the time interval between the first and second peaks of the earliest part of the wavetrain. Figure 187 defines  $p_{\text{FFT}}$  and  $T_{1,2}$  and

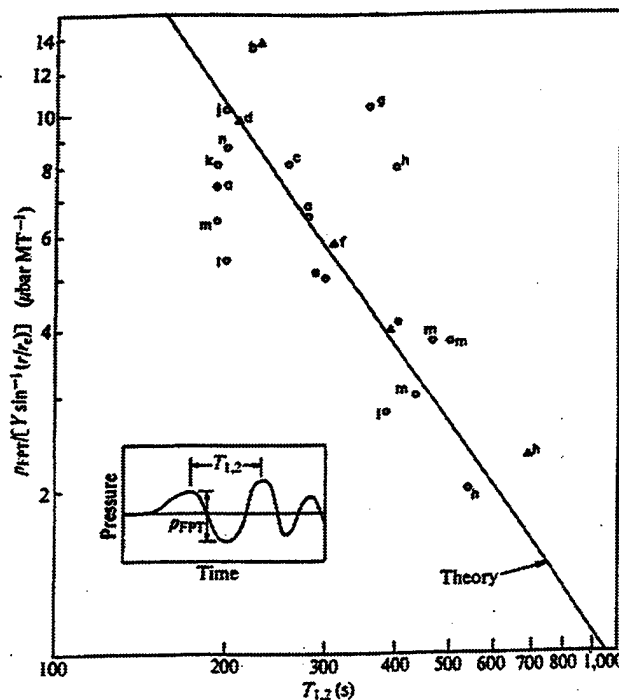


Figure 187. The *Posey and Pierce (1971)* edge wave model compared with experimental data. [Figure adopted from *Posey and Pierce (1971)*.]

provides a comparison of the theoretical predictions with data recorded at various stations from Soviet and U.S. Nuclear tests. The letters in the figure correspond to the listing provided in Table 9. The stations recording the events were reported to be located at Pasadena, CA; Berkeley, CA; Terceira, Azores; Fletcher's Ice Island; Whippany, NJ; Ewa Beach, HI; and Palisades, NY. In evaluating the theoretical expression,  $c$  was taken as 310 m/s and  $H_s$  as 8 km. The scatter in the data with respect to the theoretical curve was conjectured to be caused by "undulation in amplitude due to the horizontal refraction and subsequent focusing or defocusing caused by departures of the atmosphere from perfect stratification." It was also pointed out that most of the deviations from the theoretical curve were due to explosions above a yield of 11 MT.

Table 9. A listing of the nuclear explosions used to evaluate the *Posey and Pierce* (1971) relationship as provided in Figure 187.

---

Soviet Explosions

Event	Date	Yield (MT)
a	September 10, 1961	10
b	September 11, 1961	9
c	September 14, 1961	7
d	October 4, 1961	8
e	October 6, 1961	11
f	October 20, 1961	5
g	October 23, 1961	25
h	October 30, 1961	58
i	October 31, 1961	8

U.S. Explosions

j	May 4, 1962	3
k	June 10, 1962	9
l	June 12, 1962	6
m	June 27, 1962	24
n	July 11, 1962	12

---

*Cabre, de Celis and Flores*, (1971) very briefly report on infrasonic arrivals from French nuclear tests conducted on August 24, 1968, December 27, 1968, September 29, 1969 and October 14, 1970. The signals were recorded on sensors located at Pena, Bolivia



and waveform data from the explosion of September 29, 1969 was presented and is reproduced in Figure 188.

*Ben-Menachem* (1972), in a paper directed toward the announcement of a new mercury tiltmeter device for incorporation into seismometers, published data recorded on microbarographs which recorded the Chinese nuclear explosion which was detonated on October 14, 1970 with a reported yield of 5 MT. The particular waveforms from this explosion are displayed in Figure 189.

*Flores and Vega* (1975) report observations of infrasonic signals produced by French nuclear tests at French Polynesia as recorded on a seven element microbarograph array located at Penas, Bolivia at a range of 7,300 km from the test site. Each sensor in the

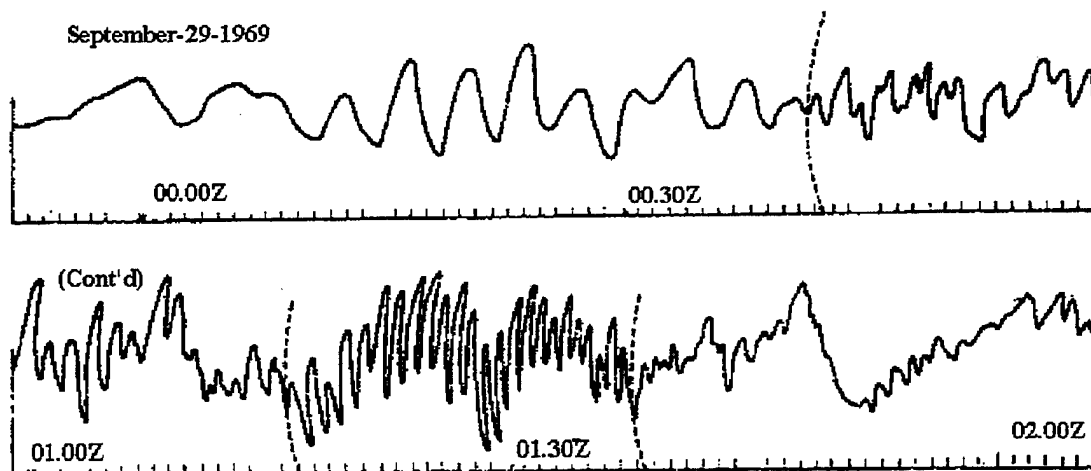


Figure 188. A sample record of infrasonic waves from French nuclear tests recorded at Penas, Bolivia. The various different trains of waves making up the entire record section have been indicated. [Figure adopted from *Cabre, Rubin de Celis and Flores* (1971).]

array was of the NBS type and equipped with a Daniels pipe front end noise filter. Table 10 provides a listing of the tests and an estimate of the explosive yield as computed from the *Posey and Pierce* (1971) equation. As indicated, the estimated explosive yields ranged from 0.14 MT to 3.9 MT. [The 8.4\* MT explosive yield in the table was revised downward to 3.9 MT due to the presence of long period noise at the time of the recording

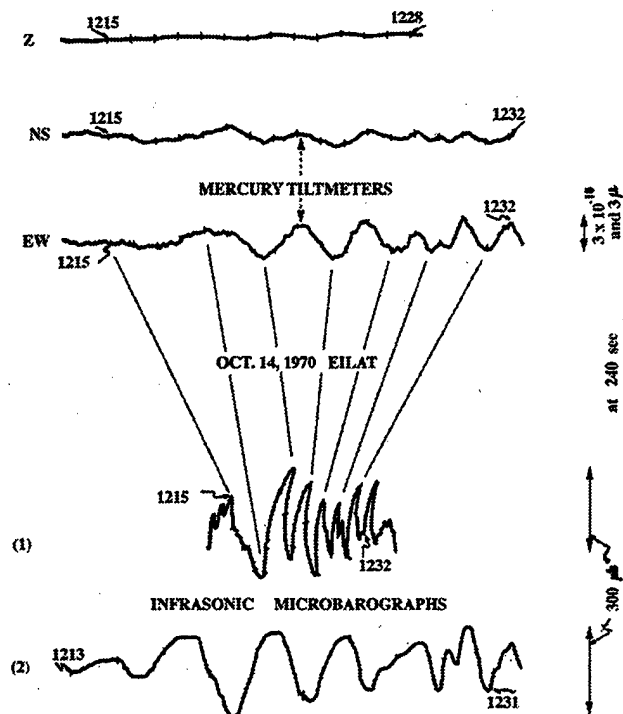


Figure 189. The waveforms recorded from a Chinese atmospheric nuclear explosion conducted on October 14, 1970. [Figure adopted from *Ben-Menachem* (1972).]

Table 10. A listing of French nuclear explosions recorded Penas, Bolivia during the time period extending from 1968 to 1971.  $T_{1,2}$  denotes the time between the first two peaks of the gravity wave portion of the received pulse,  $P_{fpt}$  denotes the first peak-to-trough amplitude, and the yield is that computed from the *Pierce and Posey* (1971) equation. [Figure adopted from *Flores and Vega* (1975)].

Event No.	Date	$T_{1,2}$ (s)	$P_{fpt}$ ( $\mu$ bar)	Yield (MT)
1	July 16, 1968	146	8.10	0.41
2	August 24, 1968	390	38.32	8.4*
3	September 9, 1968	231	9.00	0.89
4	May 30, 1970	172	12.10	0.77
5	July 3, 1970	128.5	11.11	0.46
6	August 7, 1970	180	9.48	0.65
7	June 12, 1971	110	4.56	0.14
8	August 15, 1971	315	11.11	1.7

Figure 190 provides the waveforms of the earliest arrivals of the eight nuclear explosions of this event listed in Table 10.

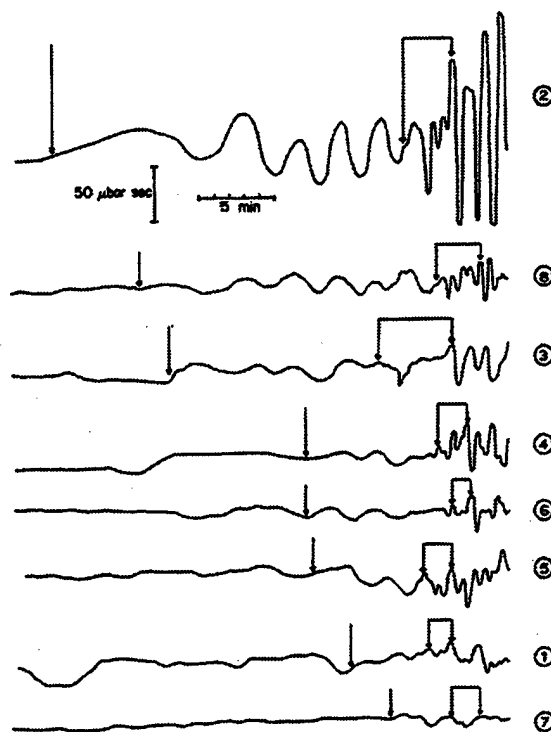


Figure 190. The earliest arrivals of the French Nuclear tests listed in Table 10. The waveforms are listed vertically in the order of decreasing apparent explosive yield. Increasing time runs from right-to-left. [Figure adopted from *Flores and Vega* (1975).]

In addition to presenting their data, *Flores and Vega* (1975) had the goal of developing a methodology or signal parametrization which would allow the estimation of explosive yields in a manner independent of the variation of local meteorological conditions. The approach was empirical rather than theoretical in nature, and involved dividing each record section into 5 partially overlapping segments of 34 min duration and computing the Fourier spectra for each window. The segments were chosen in such a way that the gravity wave portion of the wavetrain was centered in one segment and the acoustic portion of the wavetrain was centered in another. In following such a procedure, it was found that sections containing the acoustic wave portion always had a spectral peak in the period range extending from 45 s to 60 s, whereas sections containing the gravity wave portion exhibited spectral peaks near 100 s.

When the square-root of the spectral peaks of both the acoustic and gravity wave were plotted against yield very poor correlation was achieved. However, when longer

wave segments (90 min) were used the, spectral amplitude of the peaks occurring near 60 s were found to provide a good correlation with yield whereas the spectral amplitudes of the peaks near 100 s were found to provide a poor correlation. Accordingly, it was concluded that the acoustic peak "has a spectral amplitude which is proportional to yield. It is conjectured that this proportionality may hold for any given source-receiver geometry, but that the magnitude of the proportionality constant may vary but should be relatively insensitive to meteorological variations." For the waveforms recorded from the French tests, the proportionality was estimated to be  $300 \mu\text{bar sec}^{1/2}/\text{MT}$ .

The *Posey and Pierce* (1971) relation in Eq. (7.2) has been extensively used since its development to estimate the yields of atmospheric nuclear explosions in the megaton range. Its validity for very small yields in the one-to-four KT range is, at present, unclear. However, investigators at the Los Alamos National Laboratory have reported microbarograph observations of a number of ANFO (ammonium nitrate and fuel oil) explosions conducted at the White Sands Missile Range in New Mexico which indicate the existence of a linear relationship between peak-to-peak pressure amplitude and scaled range [Whitaker, *et al.*, (1990) and Davidson and Whitaker (1992)]. The data were acquired utilizing the "spider" microbarograph sensor shown in Figure 52, and Figure 191 shows the measured peak-to-peak pressure amplitude as a function of scaled range. The locations of the microbarograph sensors with respect to the White Sands test sight is shown in Figure 192 and Table 11 provides the data used in making the plot in Figure 191.

In related work, investigators at AFTAC (Air Force Tactical Applications Center) have derived a "pressure-range" curve developed by combining AFTAC data from infrasonic measurements of all country atmospheric tests during the 1950's and early 1960's which were in the yield range extending from 0.2 KT to 122 KT and more recent ANFO HE atmospheric chemical explosions. The resulting pressure-range curve is shown in Figure 193.

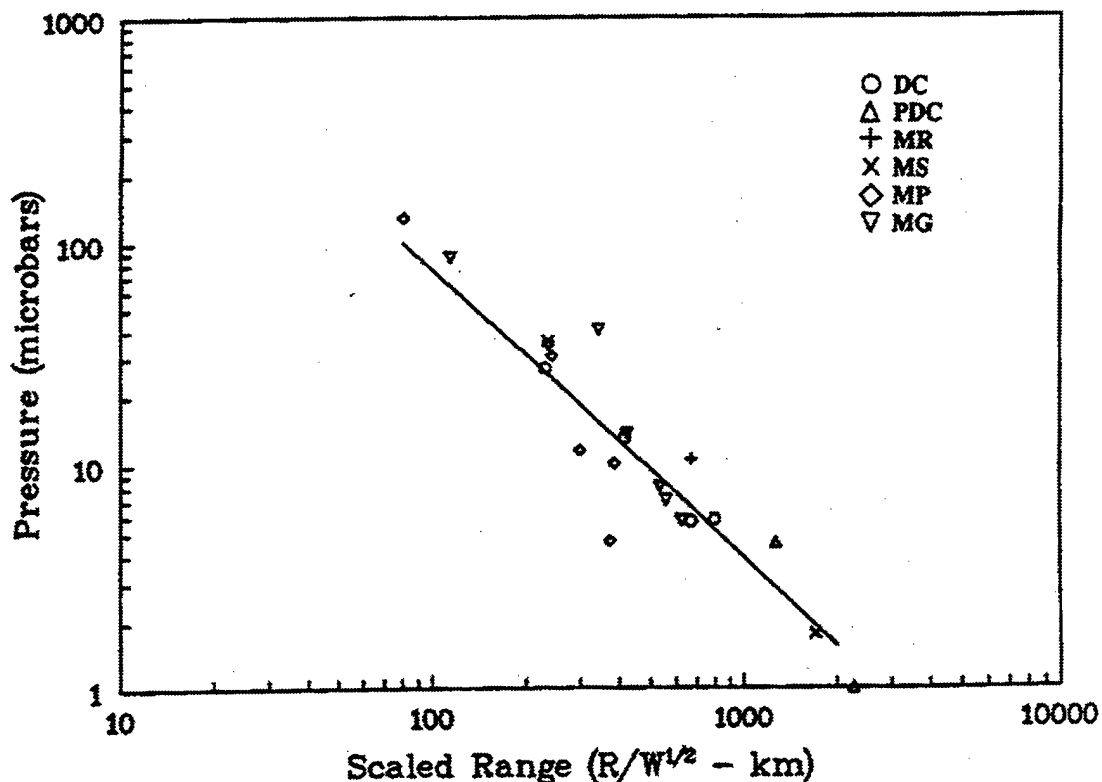


Figure 191. The peak-to-peak pressure amplitude resulting from the detonation of HE atmospheric chemical explosions as a function of the scaled range ( $R/W^{1/2}$ ), where  $R$  is the actual range in km and  $W$  is the charge weight in tons. [Figure adopted from Davidson and Whitaker (1992).]

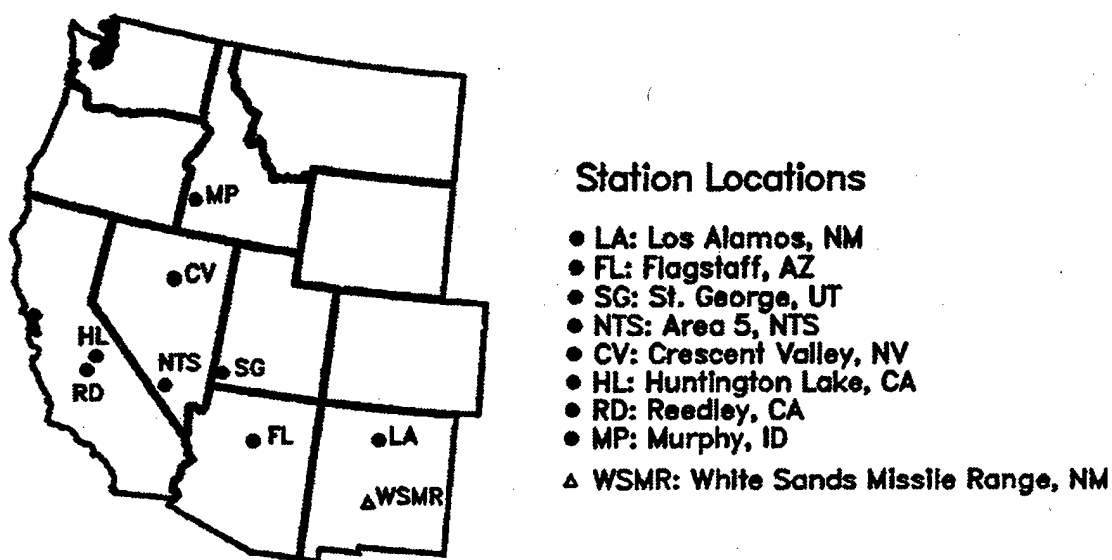


Figure 192. The locations of the Los Alamos National Laboratory's microbarograph stations used to monitor HE chemical explosions at the White Sands, NM test site. [Figure adopted from Davidson and Whitaker (1992).]

Table 11. A listing of ANFO explosions which were monitored utilizing an array of microbarographs deployed by the Los Alamos National Laboratory. [Data adopted from Whitaker, *et al.*, (1990).]

<u>Event</u>	<u>Date</u>	<u>Weight (Tons)</u>	<u>No. Sites</u>
Millrace	9/16/81	600	1
Pre-Direct Course	10/7/82	24	2
Direct Course	10/26/83	600	4
Minor Scale	6/27/85	4800	4
Misty Picture	5/14/87	4800	5
Misers Gold	6/1/89	2400	8

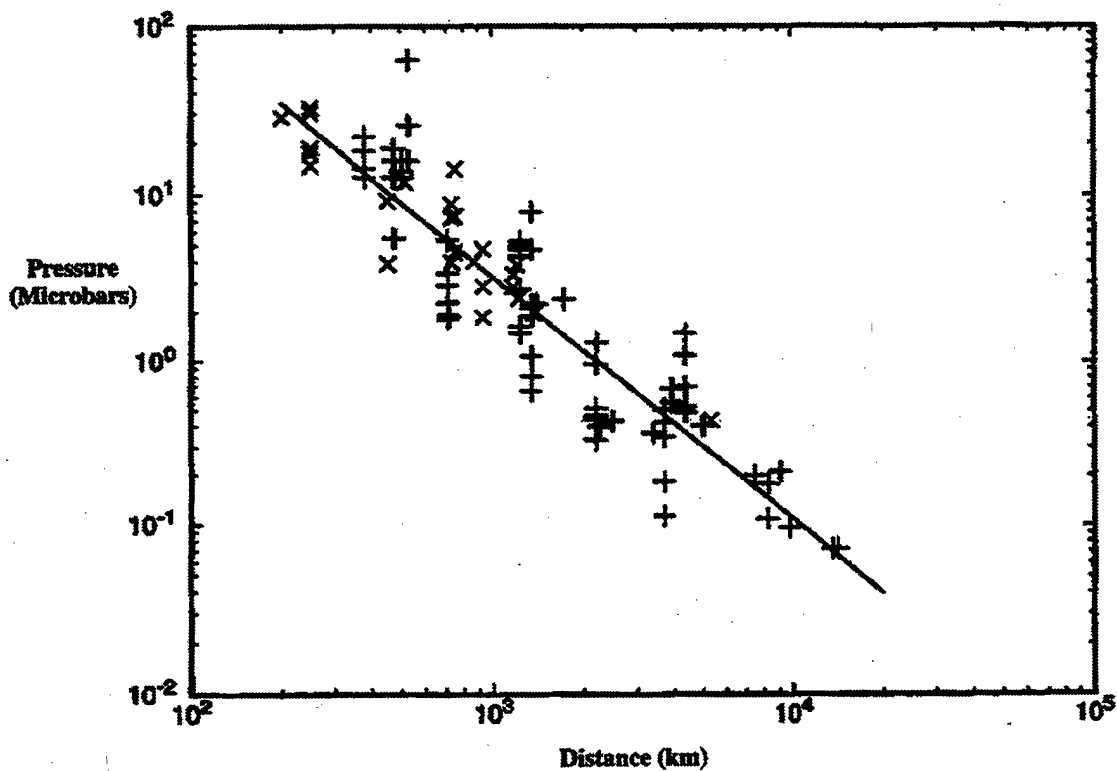


Figure 193. The pressure-range curve developed by AFTAC which was constructed from past infrasonic measurements of pressure waves from atmospheric nuclear explosions. The figure is based on a square-root scaling of yield to 1 KT and the +'s refer to nuclear explosions and the x's refer to ANFO data. [Figure provided by AFTAC {Clauter and Blandford (1996)}.]

## 8.0 REFERENCES

F.H. Abernathy and R.E. Kronrauer, "The formation of vortex streets," J. Fluid Mech. 13, 1 (1962).

**AFGL Handbook of Geophysics and the Space Environment**, U.S. Air Force Geophysics Laboratory, Hanscom AFB, MA (1985), AFGL-TR-85-0315, ADA167000.

ANS (American National Standard), "Estimating Airblast Characteristics for Single Point Explosions in Air, With a Guide to Evaluation of Atmospheric Propagation and Effects," ANSI S2.20, (ASA 20-1983), Published by the American Institute of Physics for the Acoustical Society of American (1983).

R. Araskog, Ericsson and Wagner, "Long-range Transmission of Atmospheric Disturbances," Nature 193, 970 (1962).

Air Force Geophysics Laboratory, **Handbook of Geophysics and the Space Environment**, (1985), AFGL-TR-85-0315, ADA167000.

E.M. Agee, J.T. Snow and P.R. Clarke, "Multiple vortex features in the tornado cyclone and the occurrence of tornado families," Mon. Weather Rev. 104, 552 (1976).

C.E. Anderson, "A study of the pulsating growth of cumulus clouds," Geophys. Res. Pap. 72, Air Force Cambridge Res. Lab., Bedford, Mass. (1960).

V.I. Arabadji, Doklady Akad. Nauk SSSR, 82, 377 (1952).

H.F. Baird and C.J. Banwell, "Recording of air-pressure oscillations associated with microseisms at Christchurch," New Zealand J. Sci. Technol, 21B, 314 (1940).

N.K. Balachandran, "Acoustic-Gravity Wave Propagation in a Temperature- and Wind-Stratified Atmosphere," J. Atmos. Sci. 25, 818 (1968).

N.K. Balachandran, "Effects of Winds on the Dispersion of Acoustic-Gravity Waves," J. Acoust. Soc. Am. 48, 211 (1969).

N.K. Balachandran and W.L. Donn, "On the Propagation of Infrasound from Rockets-Effects of Winds," J. Acoust. Soc. Am. 50, 397 (1971a).

N.K. Balachandran and W.L. Donn, "Characteristics of Infrasonic Signals from Rockets," Geophys. J.R. astr. Soc. 26, 135 (1971b).

N.K. Balachandran, W. Donn and D. Rind, "Concorde sonic booms as an atmospheric probe," Science 197, 47 (1977).

N.K. Balachandran, "Infrasonic Signals from Thunder," J. Geophys. Res. 84, 1735 (1979).

E.H. Barton, "On the Refraction of Sound by Wind," Quarterly Review 452, 159 (1901).

K.C. Bayer and J.N. Jordan, **"Seismic and acoustic waves from a meteor (abstract),"** J. Acoust. Soc. Am. 41, 1580 (1967).

C.S. Beals, **"Audibility of the aurora and its appearance at low atmospheric levels,"** Quart. J. Roy. Meteorol. Soc. London, 59, 71 (1933).

W.H. Beasley, T.M. Georges and M.W. Evans, **"Infrasound From Convective Storms: An Experimental Test of Electrical Source Mechanisms,"** J. Geophys. Res. 81, 3133 (1976).

A.J. Bedard, **"Some observations of travelling atmospheric pressure disturbances,"** NBS Report No. 9364 (1966).

A.J. Bedard and G.E. Greene, **"Using Arrays of Infrasonic Microphones to Detect and Locate Meteors and Meteorites: A Case Study,"** J. Acoust. Soc. Am. 65, 1277 (1981).

A.J. Bedard, **"Optimizing the Use of Surface Sensors for Wind Shear Detection,"** J. Aircraft 21, 971 (1984).

A.J. Bedard, J. Intrieri and G.E. Green, **"Infrasound Originating from Regions of Severe Weather,"** Proc. 12th Int. Congress on Acoustics, Toronto, Canada, July (1986).

A.J. Bedard, G.E. Greene, J. Intrieri and R. Rodriguez, **"On the Feasibility and Value of Detecting and Characterizing Avalanches Remotely by Monitoring Radiated Sub-Audible Atmospheric Sound at Long Distances,"** Engineering Foundation Conference, Santa Barbara, CA, 10-15-July, (1988).

A.J. Bedard, **"Infrasound from Natural Sources,"** Proc. Inter-Noise 88, Avignon, France, August (1988).

H. Benioff and B. Gutenberg, **"Waves and currents recorded by electromagnetic barographs,"** Bull. Am. Meteorol. Soc. 20, 421 (1939).

H.M. Benioff, M. Ewing and F. Press, **"Sound waves in the atmosphere generated by a small earth-quake,"** Proc. Natl. Acad. Sci. U.S., 37, 600 (1951).

T.B. Benjamin, **"Internal waves of permanent form in fluids of great depth,"** J. Fluid Mech. 29, 559 (1967).

A. Ben-Menachem, **"Mercury Tiltmeter as an Infrasonic Detector: Theory, Observations and Applications,"** J. Geophys. Res. 77, 818 (1972).

L.L. Beranek, **Noise Reduction**, McGraw-Hill Book Co., New York (1960).

Bhartendu, **"Acoustics of Thunder,"** Ph.D. Thesis, University of Saskatchewan, Canada (1964).

Bhartendu and B.W. Currie, **"Atmospheric Waves from U.S.S.R. Nuclear Test Explosions in 1962,"** Can J. Phys. 42, 632 (1964).

Bhartendu and R. McCrory, **"Atmospheric Pressure Wave from an Explosion,"** Nature 211, 396 (1966).



Bhartendu, "A study of atmospheric pressure variations from lightning discharges," Can. J. Phys. 46, 269 (1968).

D. Blokhintzev, "The Propagation of Sound in an Inhomogeneous and Moving Medium I," J. Acoust. Soc. Am. 18, 322 (1946).

D. Blokhintzev, "The Propagation of Sound in an Inhomogeneous and Moving Medium II," J. Acoust. Soc. Am. 18, 329 (1946).

J.L. Bohannon, A.A. Few and A.J. Dessler, "Detection of Infrasonic Pulses from Thunderclouds," Geophys. Res. Lett. 4, 49 (1977).

B.A. Bolt, "Seismic air waves from the great 1964 Alaskan earthquake," Nature 202, 1095 (1964).

H.S. Bowman, "Subsonic waves and severe weather phenomena," Proc. ESSA/ARPA Symposium on Acoustic-Gravity Waves in the Atmosphere, Boulder, CO, pp 215-222 (1968).

H.S. Bowman, "Hailstorm-related infrasound," oral presentation given at the American Geophysical Union, Washington Meeting, April (1970).

H.S. Bowman and A.J. Bedard, "Observations of Infrasound and Subsonic Disturbances Related to Severe Weather," Geophys. J.R. astr. Soc. 26, 215 (1971).

H.S. Bowman, "Frequency spectra information on storm-related infrasound," J. Acoust. Soc. Am. 55, 927 (1974).

F.P. Bretherton, "Lamb waves in a nearly isothermal atmosphere," Q. Jl R. met. Soc. 95, 754 (1969).

W.J. Breitling, R.A. Kupperman and G.J. Gassmann, J. Geophys. Res. 72, 307 (1967).

H.L. Brode, "The Blast Wave in Air Resulting from a High Temperature, High Pressure Sphere in Air," Rand Corporation Report, RM-1825-AEC (1956).

H.L. Brode, Rand Corporation Report, RM-1913-AEC (1957). A more recent reference is: H.L. Brode, "Review of nuclear effects," in Annual Review of Nuclear Science, Edited by E. Segre, Annual Reviews, Inc., Palo Alto, pp. 153-202 (1968).

J.P. Burg, "Three-dimensional filtering with an array of seismometers," Geophysics 29, 693 (1964).

R. Burridge, "The Acoustics of Pipe Arrays," Geophys. J. R. astr. Soc. 26, 53 (1971).

R. Cabre, J. Rubin de Celis and J. Flores, "Some Notes on Discrete Trains of Infrasonic Waves Produced by Point Sources," Geophys. J. R. astr. Soc. 26, 199 (1971).

W.H. Campbell and J.M. Young, "Auroral-Zone Observations of Infrasonic Pressure Waves Related to Ionospheric Disturbances and Geomagnetic Activity," J. Geophys. Res. 68, 5009 (1963).

J. Capon, R. Lacoss and R.J. Greenfield, "Long-period signal processing results for the Large Aperture Seismic Array," Geophysics 34, 305 (1969).

H.W. Carlson, "Correlation of Sonic-Boom Theory with Wind-Tunnel and Flight Measurements," NASA T-213 (1964).

E.W. Carpenter, G. Harwood and T. Whiteside, "Microbarograph Records from the Russian Large Nuclear Explosions," Nature 192, 857 (1961).

S. Chapman, Phil. Trans. A218, 1 (1919).

S. Chapman, "The semidiurnal oscillation of the atmosphere," Quart. J. Roy. Met. Soc. 50, 166 (1924).

G. Chimonas, "Internal gravity-wave motions induced in the earth's atmosphere by a solar eclipse," J. Geophys. Res. 75, 5545 (1970).

G. Chimonas and Hines, "Atmospheric gravity waves induced by a solar eclipse," J. Geophys. Res. 75, 875 (1970).

G. Chimonas and Hines, "Atmospheric gravity waves induced by a solar eclipse. 2," J. Geophys. Res. 76, 7003 (1971).

G. Chimonas, "Lamb waves generated by the 1970 solar eclipse," Planet. Space. Sci. 21, 1843 (1973).

D.R. Christie, K.J. Muirhead and A.L. Hales, "On solitary waves in the atmosphere," J. atmos. Sci. 35, 805 (1978).

D.R. Christie, K.J. Muirhead and A.L. Hales, "Intrusive-Density Flows in the Lower Troposphere: A Source of Atmospheric Solitons," J. Geophys. Res. 84, 4959 (1979).

D.R. Christie, K.J. Muirhead and R.H. Clark, "Solitary waves in the lower atmosphere", Science 293, 46 (1981).

P. Chrzanowski, G. Greene, K.T. Lemmon and J.M. Young, "Traveling Pressure Waves Associated with Geomagnetic Activity," J. Geophys. Res. 66, 3727 (1961).

P. Chrzanowski, J.M. Young and H.L. Marrett, "Infrasonic pressure waves from tornadic storms," National Bureau of Standards Report No. 7035 (1960).

CIRA (COSPAR [Committee on Space Research] International Reference Atmosphere)-86, NASA National Space Data Center.

J.F. Claerbout, "Electromagnetic effects of atmospheric gravity waves," Ph.D. Thesis, MIT (1967).

R.H. Clark, "The effect of wind on the propagation rate of acoustic-gravity waves," *Tellus* 5, 287 (1963).

D.A. Clauser and R.R. Blandford, "Capability Modeling of the Proposed International Monitoring System 60-Station Infrasonic Network," paper presented at the Fall Meeting of the American Geophysical Union, San Francisco, CA 12/15/96-12/19/96 (1996).

J.D. Cole and C. Greifinger, "Acoustic-gravity Waves Produced by Energy Release," Proc. of the ESSA/ARPA Symposium on Acoustic-Gravity Waves in the Atmosphere, Boulder, Colorado, July 15-17 (1968a).

J.D. Cole and C. Greifinger, "Acoustic-Gravity Waves from an Energy Source at the Ground in an Isothermal Atmosphere," Rand Corporation Technical Report RM-5828-ARPA/AFT (1968b).

J.L. Collins, W.C. Richie and G.E. English, "Solion Infrasonic Microphone," *J. Acoust. Soc. Am.* 36, 1283 (1964).

Conference on Disarmament, "International Monitoring System Infrasound Network Design (6 February-3 March 1995)," Working Paper CD/NTB/WP.184, February (1995a).

Conference on Disarmament, "Part I. Infrasound Monitoring," Working Paper CD/NTB/WP.xxx, February (1995b).

R.K. Cook and J.M. Young, "Strange sounds in the atmosphere, Part II," *Sound* 1, No. 3 (1962a).

R.K. Cook, "Radiation of Sound by Ocean Waves," in Fourth International Congress on Acoustics, Copenhagen, August (1962b).

R.K. Cook, "Atmospheric sound propagation," in Atmospheric Exploration by Remote Probes, Proceedings of the Scientific Meetings of the Panel on Remote Atmospheric Probing, Vol. 2, pp. 663-669 (published by the Committee on Atmospheric Sciences, NAS/NRC, Washington, D.C (1969).

R.K. Cook and A.J. Bedard, Jr., "On the Measurement of Infrasound," *Geophys. J. R. astr. Soc.* 26 5 (1971).

R.K. Cook, "Infrasound Radiated During the Montana Earthquake of 1959 August 18," *Geophys. J.R. astr. Soc.* 26, 191 (1971).

D. Cotten and W.L. Donn, "Sound from Apollo Rockets in Space," *Science* 171, (1971).

D.E. Cotten, W.L. Donn and A. Oppenheim, "On the Generation and Propagation of Shock Waves from Apollo Rockets at Orbital Altitudes," *Geophys. J.R. astr. Soc.* 26, 149 (1971).

D.H. Cowling, M.D. Webb and K.C. Yeh, Tech. Rep. 38, Ionosphere Radio Laboratory, University of Illinois, January (1970).

E.F. Cox, **"Microbarometric Pressures from Large High Explosive Blasts,"** J. Acoust. Soc. Am. 19, 832 (1947).

E.F. Cox, **"Abnormal Audibility Zones in Long Distance Propagation through the Atmosphere,"** J. Acoust. Soc. Am. 21, 6 (1949).

E.F. Cox, **"Sound Propagation in Air,"** in Handbuch der Physik, 48, Chapter 22, pp. 455-461, Springer-Verlag, Berlin, (1958).

F.B. Daniels, **"Acoustical energy radiated by the ocean waves,"** J. Acoust. Soc. Am. 24, 83 (1952).

F.B. Daniels, **"The mechanism of generation of infrasound by ocean waves,"** J. Acoust. Soc. Am. 25, 796 (1953).

F.B. Daniels, **"Noise-Reducing Line Microphone for Frequencies below 1 cps,"** J. Acoust. Soc. Am. 31, 529 (1959).

F.B. Daniels, **"Generation of Infrasound by Ocean Waves,"** 34, 352 (1962).

G.M. Daniels, **"Acoustic-Gravity Waves in Model Thermospheres,"** J. Geophys. Res. 72, 2419 (1967).

M. Davidson and R.W. Whitaker, **"Miser's Gold,"** Los Alamos National Laboratory Technical Report: LA-12074-MS, February (1992).

C. Delclos, E. Blanc, P. Broche, F. Glangeaud and J.L. Lacoume, **"Processing and Interpretation of Microbarograph Signals Generated by the Explosion of Mount St. Helens,"** J. Geophys. Res. 95, 5,485 (1990).

A.J. Dessler, **"Infrasound thunder,"** J. Geophys. Res. 78, 1889 (1973).

F. Dessauer, W. Graffender and J. Schaffhauser, **"Uberatmospharische pulsationen,"** Arch. Met. Geophys. Bioklim, A3, 453 (1951).

M. Dickenson, **"Three-dimensional atmospheric ray trace program using a hybrid computer,"** M.S. Thesis, Washington State University, (1971).

M.D. Dickenson, G.L. Hower, H.B. Rigas and J.W. Rockway, **"Ray tracing for atmospheric acoustic waves using a hybrid computer,"** IEEE Trans. Geoscience Elect.. GE-10, 166 (1972).

L.H. G. Dines, **"The Dines float barograph,"** Quart. J.R. Met. Soc. 55, 37 (1929).

DOE, **"United States Nuclear Tests: July 1945 through September 1992,"** Department of Energy Technical Report DOE/NV-209 (rev. 14), December (1984).

W.L. Donn and W. McGuinness, **"The microbarovariograph,"** Trans. Am. Geophys. Union 39, 366 (1958).

W.L. Donn and M. Ewing, **"Atmospheric Waves from Nuclear Explosions,"** J. Geophys. Res. 67, 1855 (1962a).

- W.L. Donn and M. Ewing, "Atmospheric Waves from Nuclear Explosions-Part II: The Soviet Test of 30 October 1961," J. atmos. Sci. 19, 264 (1962b).
- W.L. Donn, D.M. Shaw and A.C. Hubbard, "The Microbarograph Detection of Nuclear Explosions," Trans. Nucl. Sci. Instr. Elec. Engr. 10, 285 (1963).
- W.L. Donn, R.L. Pfeffer and M. Ewing, "Propagation of Air Waves from Nuclear Explosions," Science 139, 307 (1963).
- W.L. Donn and E.S. Posmentier, "Ground-Coupled Air Waves from the Great Alaskan Earthquake," J. Geophys. Res. 69, 5357 (1964).
- W.L. Donn and Posmentier, "Infrasound Waves for the Marine Storm of April 7, 1966," J. Geophys. Res. 72, 2053 (1967).
- W.L. Donn and Shaw, "Exploring the Atmosphere with Nuclear Explosions," Rev. Geophys. 5, 53 (1967).
- W.L. Donn and D. Rind, "Natural Infrasound as an Atmospheric Probe," Geophys. J.R. astr. Soc. 26, 111 (1971).
- W.L. Donn and D. Rind, "Microbaroms and the Temperature and Wind of the Upper Atmosphere," J. Atm. Sci. 29, 156 (1972).
- W.L. Donn and N.K. Balachandran, "Meteors and Meteorites Detected by Infrasound," Science 185, 707 (1974).
- W.L. Donn, N.K. Balachandran and G. Kaschak, "Atmospheric infrasound radiated by bridges," J. Acoust. Soc. Am. 56, 1367 (1974).
- W.L. Donn and N.K. Balachandran, "Meteor-Generated Infrasound," Science 189, 395 (1975).
- W.L. Donn, "Exploring the Atmosphere with Sonic Booms: Or How I Learned to Love the Concorde," American Scientist 66, 724 (1978).
- W.L. Donn and N.K. Balachandran, "Mount St. Helens eruption of 18 May 1980: Air waves and explosive yield," Science 213, 539 (1981).
- J. Ecollan and Y. Rocard, C.r. habd. Seanc. Acad. Sci., Paris 251, 523 (1960).
- F. Einaudi and C.O. Hines, "WKB approximation in application to acoustic-gravity waves," Can. J. Phys. 48, 1458 (1970).
- E. Farkas, "Transit of Pressure Waves through New Zealand from the Soviet 50 Megaton Bomb Explosion," Nature 193, 765 (1962).
- J.A. Feder and W.R. Banks, "Auroral Infrasound Wave Mechanism," Department of Applied Physics, UCSD, La Jolla, California (1970).
- U. Fehr, "Measurements of Infrasound from Artificial and Natural Sources," J. Geophys. Res. 72, 2403 (1967a).

U. Fehr, "Instrumentational Role in the Observation of Geoacoustical Phenomena from Artificial Sources," J. Acoust. Soc. Am. 42, 991 (1967b).

U. Fehr, B. Ben-Ary, and J.D. Ryan, "New Instrumentation Techniques for the Measurement of Infrasonic and Gravity Waves," Rev. Sci. Instr. 38, 778 (1967).

A.A. Few, A.J. Dessler, D.J. Latham and M. Brook, "A Dominant 200-Hertz Peak in the Acoustic Spectrum of Thunder," J. Geophys. Res. 74, 6926 (1967).

A.A. Few, "Thunder," Ph.D. Thesis, Rice University, Houston, Texas (1968).

A.A. Few, "Power Spectrum of Thunder," J. Geophys. Res. 74, 6926 (1969).

J.S. Flores and A.J. Vega, "Some relations between energy yield of atmospheric nuclear tests and generated infrasonic waves," J. Acoust. Soc. Am. 57, 1040 (1975).

S.H. Francis, "Acoustic-Gravity Modes and Large-Scale Travelling Ionospheric Disturbances of a Realistic, Dissipative Atmosphere," F. Geophys. Res. 78, 2278 (1973).

S.H. Francis, "Global propagation of atmospheric gravity waves," J. Atm. Terr. Phys. 37, 1011 (1975).

J.P. Friedman and B.W. Crawford, "Iterative series methods for finding exact solutions for a class of second order differential equations," in Acoustic Gravity Waves in the Atmosphere, Edited by T.M. Georges, U.S. Government Printing Office (1968).

C.J.R. Garrett, "The fundamental mode of acoustic gravity wave propagation in the atmosphere," Fluid Mech. Trans. Warsaw 4, 707 (1969a).

C.J.R. Garrett, "Atmospheric edge waves," Q. Jl R. met. Soc. 95, 731 (1969b).

Y.L. Gazaryan, "Infrasonic Normal Modes in the Atmosphere," Sov. Phys. Acoust. 7, 17 (1963).

T.M. Georges (Editor), Acoustic-Gravity Waves in the Atmosphere, Symposium Proceedings, U.S. Government Printing Office, 15-17 July (1968).

T.M. Georges and J.M. Young, "Passive Sensing of Natural Acoustic-Gravity Waves at the Earth's Surface," Chapter 21 in REMOTE SENSING OF THE TROPOSPHERE, Edited by V.E. Derr, U.S. Govt. Printing Office (1972).

T.M. Georges, "Infrasound from Convective Storms: Examining the Evidence," Rev. of Geophys. and Space Physics, 11, 571 (1973a)

T.M. Georges, "Infrasound from Severe Storms," Eighth Conference on Severe Local Storms, AMS, Boston, MA, October 15-17 (1973b).

T.M. Georges, "Infrasound from the 29-30 April Storms," NOAA Technical Memorandum ERL NSSL-69, pp. 185-193, May (1974).

T.M. Georges and G.E. Greene, "Infrasound from Convective Storms. Part IV. Is It Useful for Storm Warning?," J. Appl. Meteor. 14, 1303 (1975).

T.M. Georges, "Infrasound from Convective Storms, Part II: A Critique of Source Candidates," NOAA Technical Report ERL 380-WPL 49, October (1976).

T.M. Georges and W.H. Beasley, "Refraction of infrasound by upper-atmospheric winds," J. Acoust. Soc. Am. 61, 28 (1977).

T.M. Georges, "Infrasound from Thunderstorms," in Instruments and Techniques for Thunderstorm Observation and Analysis, Edited by E. Kessler, University of Oklahoma Press (1987).

G.S. Golitsyn, Grigor'yev and V.P. Dokuchayev, "Generation of Acoustic-Gravity Waves by Meteor Motion in the Atmosphere," 13, 633 (1977).

E.E. Gossard and W.H. Hooke, Waves in the Atmosphere: Atmospheric Infrasound and Gravity Waves - their Generation and Propagation, Elsevier Scientific Publishing Company, New York (1975).

A.E. Gill, Atmosphere-Ocean Dynamics, International Geophysics Series, Volume 30, Academic Press, New York (1982).

S. Glasstone (Editor), The Effects of Nuclear Weapons, Revised Edition, U.S. Atomic Energy Commission, Washington, D.C. (1962).

V.H. Goerke and M.V. Woodward, "Infrasonic observation of a severe weather system," Mon. Weath. Rev. 94, No. 6 (1966).

V.H. Goerke, "Infrasonic observations of a fireball," Sky Telesc. 32, 313 (1966).

V.H. Goerke and M.W. Woodward, Trans. Am. Geophys. Union 48, 81 (1967).

E.E. Gossard, "Spectra of atmospheric scalars," J. Geophys. Res. 65, 3339 (1960).

E.E. Gossard and W.H. Hooke, Waves in the Atmosphere, Elsevier Scientific Publishing Co., New York (1975).

G.E. Greene and J. Howard, "Natural Infrasound: A One Year Global Study," NOAA Technical Report ERL 317-WPL-37 (1975).

R.J. Greenfield and D.G. Harkrider, "Acoustic-Gravity Wave Calculations in a Layer with a Linear Temperature Variation," Geophys. J.R. astr. Soc. 26, 323 (1971).

F.H. Grover, "Research Notes: A Note on Infrasonics at U.K.A.E.A. Blacknest," Geophys. J.R. astr. Soc. 16, 311 (1968).

F.H. Grover, "Experimental Noise Reducers for an Active Microbarograph Array," Geophys. J.R. astr. Soc. 26, 41 (1971).

G.V. Groves, "Velocity of a body falling through the atmosphere and the propagation of its shock wave to earth," J. Atm. Terr. Phys. 10, 73 (1957).

B. Gutenberg, "The Velocity of Sound Waves and the Temperature in the Stratosphere in Southern California," Bull. Am. Meteorolog. Soc. 20, 192 (1939).

B. Gutenberg and H. Benioff, "Atmospheric pressure waves near Pasadena," Trans. Am. Geophys. Union, 22, 424 (1941).

B. Gutenberg, "Propagation of Sound Waves in the Atmosphere," J. Acoust. Soc. Am. 13, 151 (1942).

J.C. Hardin and D.S. Pope, "Prediction of the Spectrum of Atmospheric Microburst Noise in the Range 2-20 Hz," NASA Technical Report (1988).

D.G. Harkrider, "Theoretical and Observed Acoustic-Gravity Waves from Explosive Sources in the Atmosphere," J. Geophys. Res. 69, 5292 (1964).

N.A. Haskell, "The dispersion of surface waves on multi-layered media," Bull. Seis. Soc. Am. 43, 17 (1953).

R.A. Haubrich, "Array Design," Bull. Seism. Soc. Am. 58, 977 (1968).

B. Haurwitz, "The Propagation of Sound Through the Atmosphere," J. Aeron. Sci. 9, 35 (1941).

G.S. Hawkins, The Physics and Astronomy of Meteors, Comets, and Meteorites, McGraw-Hill, New York (1964).

S. Hearne, "Journey from Prince of Wales' Fort in Hudson Bay to the Northern Ocean in the Years 1769, 1770-1 and 1772," Champlain Society's edition, p 235, Toronto (1911).

E. Herrin and J.A. McDonald, "A Digital System for the Acquisition and Processing of Geoacoustic Data," Geophys. J.R. astr. Soc. 26, 13 (1971).

T.J. Herron, I. Tolstoy and D.W. Kraft, "Atmospheric Pressure Background Fluctuations in the Mesoscale Range," J. Geophys. Res. 74, 1321 (1969a).

T.J. Herron and I. Tolstoy, "Tracking Jet Stream Winds from Ground Level Pressure Signals," J. Atm. Sci. 26, 266 (1969b).

D.A. Hilton and H.R. Henderson, "Measurements of sonic-boom overpressures from Apollo space vehicles," J. Acoust. Soc. Am. 56, 323 (1974).

C.O. Hines, "Internal Atmospheric Gravity Waves at Ionospheric Heights," Can. J. Phys. 38, 1441 (1960).

C.O. Hines, "The upper atmosphere in motion," Quart. J. Roy. Meteor. Soc. 89, 1 (1963).

C.O. Hines, "Atmospheric gravity waves: a new toy for the wave theorist," Radio Sci. J. Res. NBS 69D, 375 (1965).

C.O. Hines and C.A. Reddy, "On the Propagation of Atmospheric Gravity Waves through Regions of Wind Shear," J. Geophys. Res. 72, 1015 (1967).



C.O. Hines, "On the Nature of Traveling Ionospheric Disturbances Launched by Low-Altitude Nuclear Explosions," J. Geophys. Res. 72, 1877 (1967).

E.J. Hopfinger, "Snow Avalanche Motion and Related Phenomena," Ann. Rev. Fluid Mech. 15, 47 (1983).

S.S. Hough, "On the application of harmonic analysis to the dynamical theory of the tides. Part I. On Laplace's 'oscillations of the first species', and on the dynamics of ocean currents," Phil. Trans. R. Soc. London A189, 201 (1897).

J.T. Houghton, The Physics of Atmospheres, Second Edition, Cambridge University Press, New York (1986).

J.N. Hunt, R. Palmer and W. Penney, "Atmospheric Waves Caused by Large Explosions," Phil. Trans. Roy. Soc. London A252, 275 (1960).

U. Ingard, "A Review of the Influence of Meteorological Conditions on Sound Propagation," J. Acoust. Soc. Am. 25, 405 (1953).

H.S. Jelstrup and C. Stormer, "The aurora of Oct 15, 1926, in Norway, and the sounds associated with it," Nature 119, 45 (1927).

C.T. Johnson and J.R. Chiles, "The NEL T21 microbarograph recording system," U.S. Navy Electronics Lab. Rept. 773 (1957).

R.E. Johnson, "An Infrasonic Pressure Disturbance Study of Two Polar Substorms," Planet. Space. Sci. 20, 313 (1972).

R.V. Jones, "Sub-Acoustic Waves from Large Explosions," Nature 193, 229 (1962).

R.V. Jones and S.T. Forbes, "Sub-Acoustic Waves from Recent Nuclear Explosions," Nature 196, 1170 (1962).

R.V. Jones, "Microbarograph record of waves from explosions in the atmosphere," Quart. J. Roy. Meteor. Soc. 93, 436 (1967).

A.R. Jordan, "Atmospheric Gravity Waves from Winds and Storms," J. Atm. Sci. 29, 445 (1972).

H. Kanamori and J. Mori, "Harmonic excitation of mantle Rayleigh waves by the 1991 eruption of Mount Pinatubo, Philippines," Geophys. Res. Lett. 19, 721 (1992).

H. Kanamori, J. Mori and D.G. Harkrider, "Excitation of atmospheric oscillations by volcanic eruptions," J. Geophys. Res. 99, 21,947 (1994).

S.K. Kao and H.D. Woods, "Energy spectra of mesoscale turbulence along and across the jet stream," J. atmos. Sci. 21, 513 (1964).

G. Kaschak, "Long-range Supersonic Propagation of Infrasonic Noise Generated by Missiles," J. Geophys. Res. (Space Physics), 74, 914 (1969).

G. Kaschak, W.L. Donn and U. Fehr, "Long-range Infrasound from Rockets," J. Acoust. Soc. Am. 48, 12 (1970).

S. Kato, Dynamics of the Upper Atmosphere, D. Reidel Publishing Company, Dordrecht, Boston (1981).

Lord Kelvin (W. Thomson), "On the thermodynamic acceleration of the earth's rotation," Proc. Roy. Soc. Edinburgh. 11, 396 (1882).

W.A. Kinney, "Mathematical Models of Acoustic and Acoustic-Gravity Wave Propagation in Fluids with Height-Dependent Sound Velocities," Ph.D. Dissertation, Georgia Institute of Technology, June (1976).

W. Kohl, "Acoustic gravity waves caused by the nuclear explosion on October 30th 1961," in Proc. NATO Advanced Study Inst. Skeikampen, Norway, April 17-26, 1963, 160, North Holland Publishing Company (1954).

V.P. Koroberikov, P.I. Chushkin and L.V. Shurshelov, "Gas dynamics of the flight and explosion of meteorites," Astronautica Acta 17, 339 (1972).

D.R. Kraemer and F.L. Bartman, "Infrasound from Accurately Measured Meteor Trails," Proc. Int. Symposium on Acoustic Remote sensing of the Atmosphere and Oceans, University of Calgary Press, Alberta, Canada, V-31 to V-49 (1981).

E.P. Krider, G.A. Dawson and M.A. Uman, "The peak power and energy dissipation in a single-stroke lightning flash," J. Geophys. Res. 73, 3335 (1968).

E.L. Krilov, in Principles of Meteorites (translated by I. Vidziunas), H. Brown, Ed., Pergamon Press, London (1960).

R.A. Kropfli and L.J. Miller, "Kinematic structure and flux quantities in a convective storm from dual-Doppler radar observations," J. Atmos. Sci. 33, 520 (1976).

S.N. Kulichkov, "Long-Range Propagation of Sound in the Atmosphere, A Review," Izv. Atm. and Ocean Phys. 28, 253 (1992).

H. Lamb, "On the Theory of Waves Propagated Vertically in the Atmosphere," London Math. Soc. 7, 122 (1909).

H. Lamb, "On the atmospheric oscillations," Proc. Roy. Soc. London 84A, 551 (1911).

H. Lamb, Hydrodynamics, Sixth Edition, Dover, New York (1932).

L.D. Landau and E.M. Lifshitz, Fluid Mechanics, Pergamon Press Ltd., Oxford (1959).

P.S. Laplace, "Recherches sur plusieurs points du systeme du monde," Mem. Acad. R. Sci. Paris (1778)

R.J. Larson, L.B. Craine, J.E. Thomas and C.R. Wilson, **"Correlation of winds and geographic features with production of certain infrasonic signals in the atmosphere,"** Geophys. J.R. astr. Soc. 26, 201 (1971).

M.J. Lighthill, **"On sound generated aerodynamically,"** Proc. Roy. Soc. London 222A, 1 (1954).

M.J. Lighthill, **"Viscosity effects in sound waves of finite amplitude,"** in Surveys of Mechanics, 250, Edited by G.K. Batchelor and H. Bondi, Jr., Cambridge University Press, Cambridge (1956).

F.A. Lindeman and G.M.B. Dobson, **"A Theory of Meteors, and the Density and Temperature of the Outer Atmosphere to which it Leads,"** Proc. Roy. Soc. 102, 411 (1923).

C.H. Liu and K.C. Yeh, **"Excitation of acoustic-gravity waves in an isothermal atmosphere,"** Tellus 23, 150 (1971).

L. Liszka and H. Westin, KGO Rept. No. 727, Kiruna Geophysical Observatory, Kiruna, Sweden (1972).

L. Liszka, **"Long-distance propagation of infrasound from artificial sources,"** J. Acoust. Soc. Am. 56, 1383 (1974).

L. Liszka and K. Waldemark, **"High Resolution Observations of Infrasound Generated by the Supersonic Flights of Concorde,"** IRF Scientific Report 224, May (1995).

M.S. Longuet-Higgins, **"A theory of the origin of microseisms,"** Phil. Trans. Roy. Soc. London 24, 1 (1950).

H. Mack and E. Smart, **"Automatic processing of multi-array long-period seismic data,"** Geophys. J.R. astr. Soc. 35, 215 (1973).

R.F. MacKINNON, **"The effects of winds on acoustic-gravity waves from explosions in the atmosphere,"** Quart. J. R. Met. Soc. 56, 436 (1968).

J.A. McDonald, E.J. Douze and E. Herrin, **"The Structure of Atmospheric Turbulence and its Application to the Design of Pipe Arrays,"** Geophys. J. R. astr. Soc. 26, 99 (1971).

J.A. McDonald, **"Naturally occurring atmospheric acoustical signals,"** J. Acoust. Soc. Am. 56, 338 (1974).

B.A. McIntosh, M.D. Watson and D.O. Revelle, **"Infrasound from a radar observed meteor,"** Can. J. Phys. 54, 655 (1976).

B.A. McIntosh, **"Natural and Unnatural Infrasound,"** Herzberg Institute of Astrophysics Report, Planetary Sciences SR-82-1, April (1982).

B.A. McIntosh and D.O. Revelle, **"Traveling Atmospheric Pressure Waves Measured During a Solar Eclipse,"** J. Geophys. Res. 89, 4953 (1984).

J.M. McKisic, **"Infrasound and the Infrasonic Monitoring of Atmospheric Explosions: An Annotated Bibliography,"** Phillips Laboratory Technical Report, PL-TR-96-2282, October 31, (1996a).

J.M. McKisic, **"Infrasound and the Infrasonic Monitoring of Atmospheric Explosions: Past Monitoring Efforts,"** Phillips Laboratory Technical Report, PL-TR-96-2190, October 31, (1996b).

J.M. McKisic, **"Infrasound and the Infrasonic Monitoring of Atmospheric Explosions: Supporting Environmental Data,"** Phillips Laboratory Technical Report, PL-TR-97-2124, December 5, (1996c).

K. Maeda and T. Wanatabe, **"Pulsating aurora and infrasonic waves in the polar atmosphere,"** J. Atmospheric Sci. (1963).

M. Margules, **"Über die Schwingungen periodisch erwärmter Luft,"** Sitzber. Akad. Wiss. Wien Abt. IIa 99, 204 (1890).

M. Margules, **"Luftbewegungen in einer rotierenden Spharoidschale,"** Sitzber. Akad. Wiss. Wien Abt. IIa 101, 597 (1892).

W.C. Meecham and G.W. Ford, **"Acoustic radiation from isotropic turbulence,"** J. Acoust. Soc. Am. 80, 318 (1958).

W.C. Meecham, **"Simplified Normal Mode Treatment of Long-Period Acoustic-Gravity Waves in the Atmosphere,"** Proc. IEEE 53, 2079 (1965).

W.C. Meecham, **"Short-Period Propagation of Infrasonic Waves from Nuclear Explosions,"** RAND Corporation Technical Report No: RM-5103-ARPA, October (1966).

W.C. Meecham, **"On aerodynamic infrasound,"** J. Atm. Terr. Phys. 33, 149 (1971).

J.E. Midgley and H.B. Liemohn, **"Gravity Waves in a Realistic Atmosphere,"** J. Geophys. Res. 71, 3729 (1966).

P.M. Millman, **"A tape recording of the Belfast meteorite,"** J. Roy. Astr. Soc. Canada 65, 57 (1970).

E.A. Milne, **"Sound Waves in the Atmosphere,"** Phil. Mag. 42, 96 (1921).

P.M. Morse and K.U. Ingard, **Theoretical Acoustics,** McGraw-Hill Book Co., New York (1968).

T. Namekawa, **"A study of the minor fluctuations of atmospheric pressure,"** Mem. Coll. Sci., Kyoto Imp. Univ., 19A, 237 (1936).

J.W. Nanda, J. Geophys. Res. 65, 1815 (1960).

National Aeronautics and Space Administration, **"Earth Photographs from Gemini III, IV and V,"** page 123 (1967).

S. Nichparenko, **"Aurorally Associated Infrasonic Waves,"** M.S. Thesis, University of Alaska (1967).

NOAA/NASA/USAF, "U.S. Standard Atmosphere 1976," Washington, D.C. (1976).

S.D. Noel and R.W. Whitaker, "Comparison of Noise Reduction Systems," Los Alamos National Laboratory Report LA-12008-MS, June (1991).

T. Obayashi, "Upper Atmospheric Disturbances Due to High Altitude Nuclear Explosions," *Planet. Space Sci.* 10, 47 (1963).

E. Opik, "The sonic boom of the Boveedy meteorite," *Irish. Astron. J.*, 9, 308 (1970).

I.P. Passechink, "Air waves occurring during the Gobi-Alti earthquake of December 4, 1957," *Bull. (Izv.) Acad. Sci. USSR, Geophys. ser.* 11, (1959).

C.L. Pekeris, "Atmospheric oscillations," *Proc. Roy. Soc. London* A158, 650 (1937).

C.L. Pekeris, "The propagation of a pulse in the atmosphere," *Proc. Roy. Soc. London* 171A, 434 (1939).

C.L. Pekeris, "The propagation of a pulse in the atmosphere, 2," *Phys. Rev.* 73, 145 (1948).

R.L. Pfeffer, "A Multi-layer Model for the Study of Acoustic-Gravity Wave Propagation in the Earth's Atmosphere," *J. atmos. Sci.* 19, 251 (1962).

R.L. Pfeffer and J. Zarichny, "Acoustic-Gravity Wave Propagation form Nuclear Explosions in the Earth's Atmosphere," *J. atmos. Sci.* 19, 256 (1962).

R.L. Pfeffer and J. Zarichny, "Acoustic-Gravity Wave Propagation in an Atmosphere with Two Sound Channels," *Geophys. Pura Appl.* 55, 175 (1963).

E.S. Posmentier, "A Theory of Microbaroms," *Geophys. J.R. astr. Soc.* 13, 487 (1967).

A.D. Pierce, "Transient Sound Propagation in a Simple Model of a Triple Layered Medium," RAND Corporation Technical Report RM-3478, April (1963a).

A.D. Pierce, "Propagation of Acoustic-Gravity Waves from a Small Source above the Ground in an Isothermal Atmosphere," *J. Acoust. Soc. Am.* 35, 1798 (1963b).

A.D. Pierce, "Propagation of Acoustic-Gravity Waves in a Temperature- and Wind-Stratified Atmosphere," *J. Acoust. Soc. Am.* 37, 218 (1965).

A.D. Pierce, "Justification of the Use of Multiple Isothermal Layers as an Approximation to the Real Atmosphere for Acoustic-Gravity Wave Propagation," *Radio Science* 1, 265 (1966a).

A.D. Pierce, "The Multilayer Approximation for Infrasonic Wave Propagation in a Temperature- and Wind Stratified Atmosphere," *J. Comp. Phys.* 1, 343 (1967). An earlier description of the theory was given by A.D. Pierce, "A Method for

**the Computation of Normal Mode Dispersion Curves of Atmospheric Gravity Waves in Windy Atmospheres,"** Avco Technical Report, RAD-TR-66-8, January (1966b).

A.D. Pierce and S.C. Coroniti, **"A Mechanism for the Generation of Acoustic-Gravity Waves During Thunderstorm Formation,"** Nature 210, 1209 (1966).

A.D. Pierce, **"The Multilayer Approximation for Infrasonic Wave Propagation in a Temperature and Wind-Stratified Atmosphere,"** J. Comp. Phys. 1, 343 (1967).

A.D. Pierce, J.W. Posey and E.F. Iliff, **"Variation of Nuclear Explosion Generated Acoustic-Gravity Wave Forms with Burst Height and with Energy Yield,"** J. Geophys. Res. 76, 5025 (1971).

A.D. Pierce and J.W. Posey, **"Theory of the Excitation and Propagation of Lamb's Atmospheric Edge Mode from Nuclear Explosions,"** Geophys. J.R. astr. Soc. 26, 341 (1971).

A.D. Pierce and W.A. Kinney, **"Geometric Acoustics Technique in Far Field Infrasonic Waveform Synthesis,"** Air Force Geophysics Laboratory Technical Report, AFGL-TR-76-0055, Hanscom AB (1976), ADA024721.

AD. Pierce and W.A. Kinky, **"Computational Techniques for the Study of Infrasonic Propagation in the Atmosphere,"** Air Force Geophysics Laboratory Technical Report ANGLE-TR.-76-0056, March 13 (1976), ADA024951.

AD. Pierce, **"Wave equation for sound in fluids with unsteady in homogenous flow,"** J. Accoust. Soc. Am. 87, 2292 (1990).

M.L.V. Pittway and C.O. Hinds, **"The Viscous Damping of Atmospheric Gravity Waves,"** Can. J. pH's. 41, 1935 (1963).

JAW. Poesy and AD. Pierce, **"Estimation of Nuclear Explosion Energies from Micro barograph Records,"** Nature 232 253 (1971).

E. Posmentier, **"Preliminary Observations of 1-16 Hz Natural Background Infrasonic and Signals from Apollo 14 and Aircraft,"** Geophys. J.R. astr. Soc. 26, 173 (1971).

A. Powell, **"Aerodynamic Noise and the Plane Boundary,"** J. Acoust. Soc. Am. 32, 982 (1960).

A. Powell, **"Theory of vortex sound,"** J. Acoust. Soc. Am. 36, 117 (1964).

E.S. Posmentier, **"A Theory of Microbaroms,"** Geophys. J. R. astr. Soc. 13, 487 (1967).

F. Press and D.G. Harkrider, **"Propagation of Acoustic-Gravity Waves in the Atmosphere,"** J. Geophys. Res. 67, 3889 (1962).

D.C. Pridmore-Brown and U. Ingard, **"Sound Propagation into the Shadow Zone in a Temperature-Stratified Atmosphere above a Plane Geometry,"** J. Acoust. Soc. Am. 27, 36 (1955).

D.C. Pridmore-Brown, **"Sound Propagation in a Temperature- and Wind-Stratified Medium,"** J. Acoust. Soc. Am. 34, 438 (1962).

J.T. Priestley, **"Correlation studies of pressure fluctuations on the ground beneath a turbulent boundary layer,"** NBS Report 8942, U.S. Department of Commerce, National Bureau of Standards (1966).

R.W. Procnier, **"Observations of Acoustic Aurora in the 1-16 Hz Range,"** Geophys. J. astr. Soc. 26, 183 (1971).

F.H. Proctor, **"The Terminal Area Simulation System, Volume 1: Theoretical Formulation,"** NASA CR 4046 (1987).

J.W.S. Rayleigh, **The Theory of Sound: Volume II**, The MacMillan Company, New York, (1896). Republished by Dover Publications, New York (1945).

J.W. Reed, **"Amplitude Variability of Explosion Waves at Long Ranges,"** J. Acoust. Soc. Am. 39, 980 (1966)

J.W. Reed, **"Air Pressure Waves from Mount St. Helens Eruptions,"** J. Geophys. Res. 92, 11979 (1987).

W.J. Remillard, **"The acoustics of thunder,"** Tech. Memo. 44, Acoustics Research Laboratory, Harvard University, Cambridge, MA (1960).

O. Reynolds, **"On the Refraction of Sound by the Atmosphere,"** Proc. Roy. Soc. 22, 531 (1874).

D.O. Revelle, **"Acoustics of meteors-Effects of the atmospheric temperature and wind structure on the sounds produced by meteors,"** Ph.D. Dissertation, University of Michigan, Ann Arbor Michigan, May (1974).

D.O. Revelle, **"Meteor generated infrasound,"** Science 189, 394 (1975).

D.O. Revelle, **"On Meteor-Generated Infrasound,"** J. Geophys. Res. 81, 1217 (1976).

D.O. Revelle and W.G. Delinger, **"Passive Acoustic Remote Sensing of Infrasound,"** in Proceedings of the International Symposium of Acoustic Remote Sensing of the Atmosphere and Oceans, Calgary University, Alberta, Canada V.6 to V.15 (1981).

O. Reynolds, **"On the Reflection of Sound by the Atmosphere,"** Proc. Roy. Soc. 22, 531 (1874).

D. Rind and W. Donn, **"Further use of infrasound as a continuous monitor of the upper atmosphere,"** J. Atmos. Sci. 32, 1694 (1975).

A.R. Ritsema, **"Observations of Mount St. Helens eruption,"** EOS Trans. AGU 61, 1201 (1980).

J.W. Rockway, G.L. Hower, L.B. Craine and J.E. Thomas, **"Applications of Ray-Tracing to Observations of Mountain-Associated Infrasonic Waves,"** Geophys. J.Q. astr. Soc. 36, 259 (1974).

G. Rose, J. Oksman and E. Kajita, **"Round the World Sound Waves produced by the Nuclear Explosion on October 30, 1961, and their Effect on the Ionosphere at Sodankyla,"** Nature 192, 1173 (1961).

R.V. Row, **"Acoustic-Gravity Waves in the Upper Atmosphere Due to a Nuclear Detonation and an Earthquake,"** J. Geophys. Res. 72, 1599 (1967).

J.S. Saby and W. L. Nyborg, **"Ray Computation for Non-Uniform Fields,"** J. Acoust. Soc. Am. 18, 316 (1946).

M.L. Salby, **Fundamentals of Atmospheric Physics**, Academic Press, New York (1996).

L. Saxer, **"Uber entstehung ausbreitung quasiperiodischer luftdruckschwanlungen,"** Arch. Met. geophys. Bioklim., A6, 451 (1954).

W. Schmidt, **"Uber den Donner,"** Z. Meteorol. 31, 487 (1914).

E. Schrodinger, **"On the acoustics of the Atmosphere,"** Physik. Zeits. 18, 445 (1917).

R.S. Scorer, **"The dispersion of a pressure pulse in the atmosphere,"** Proc. Roy. Soc. A201, 137 (1950).

R. Seebass, **"Sonic Boom Theory,"** J. Aircr. 6, 177 (1969).

W.N. Shaw and W.H. Dines, **"The study of fluctuations of atmospheric pressure,"** Quart. J.R. Met. Soc. 31, 39 (1905).

E.M. Shoemaker and C.J. Lowery, **"Airwaves associated with large fireballs and the frequency distribution of energy of large meteorites (abstract),"** Meteoritics 3, 123 (1967).

M. Siebert, **"Atmospheric Tides,"** Adv. Geophys. 7, 105 (1961).

S.M. Silverman and T.F. Tuan, **"Auroral audibility,"** Space Science Review (1971).

E. Smart, **"An examination of atmospheric pressure pulses recorded on microbarographs,"** MS Thesis, Colorado School of Mines, Colorado, (1966).

E. Smart and E.A. Flinn, **"Fast Frequency Wavenumber Analysis and Fisher Signal Detection in Real-Time Infrasonic Array Data Processing,"** Geophys. J.R. astr. Soc. 26, 279 (1971).

E. Smart, **"FKOMB, a fast general-purpose array processor,"** Teledyne Geotech, Seismic Array Analysis Center Report No. 9, Alexandria, Virginia (1972).

**"Special Issue on Infrasonics and Atmospheric Acoustics,"** Geophys. J.R. astr. Soc. 26, 1 (1971).



Stokes, British Association Report (1857).

C. Stormer, **"Photographic measurements of the great aurora of January 25-6,"** Nature 141, 955 (1938).

L.N. Stretenskii, **"Propagation of sound in an isothermal atmosphere,"** Izv. Akad. Nauk SSSR Ser. Geofiz. No. 2, 134 (1954).

D.W. Swift, **"The Generation of Auroral Infrasonic Waves by Electrojets,"** J. Geophys. Res. 78, 8205 (1973).

G.I. Taylor, **"Waves and tides in the atmosphere,"** Proc. Roy. Soc. London, 126A, 169 (1929).

G.I. Taylor, **"Oscillations of the atmosphere,"** Proc. Roy. Soc. London 156A, 318 (1936).

G.I. Taylor, **"The formation of a blast wave by a very intense explosion. I. Theoretical Discussion,"** Proc. Roy. Soc. A201, 159 (1959a).

G.I. Taylor, **"The formation of a blast wave by a very intense explosion. II. The atomic explosion of 1945,"** Proc. Roy. Soc. A201, 175 (1950b).

J.E. Thomas and L.B. Craine, **"Acoustic-Gravity Wave Propagation in a Measured Atmosphere,"** Geophys. J. R. astr. Soc. 26, 311 (1971).

J.E. Thomas, T.H. Kuckertz, J.D. Logan, T.K. Law and L.B. Craine, **"Possible source mechanisms for a frequently occurring infrasonic signal,"** J. Acoust. Soc. Am. 56, 1391 (1974).

W.T. Thomson, **"Transmission of elastic waves through a stratified solid medium,"** J. Appl. Phys. 21, 89 (1950).

I. Tolstoy, **"The Theory of Waves in Stratified Fluids Including the Effects of Gravity and Rotation,"** Rev. Mod. Phys. 35, 207 (1963).

I. Tolstoy, **"Long-Period Gravity Waves in the Atmosphere,"** J. Geophys. Res. 72, 4605 (1967).

I. Tolstoy and T.J. Herron, **"A Model for Atmospheric Pressure Fluctuations in the Mesoscale Range,"** J. Atm. Sci. 26, 270 (1969).

I. Tolstoy, **"Note on Long Gravity Waves in Layered Atmospheres,"** J. Geophys. Res. 74, 3436 (1969).

I. Tolstoy and T.J. Herron, **"Atmospheric Gravity Waves from Nuclear Explosions,"** J. atmos. Sci. 27, 55 (1970).

I. Tolstoy and P. Pan, **"Simplified Atmospheric Models and the Properties of Long-Period Internal and Surface Gravity Waves,"** J. atmos. Sci. 27, 31 (1970).

I. Tolstoy and J. Lau, **"Generation of Long Internal Gravity Waves in Waveguides by Rising Buoyant Air Masses and Other Sources,"** Geophys. J.R. astr. Soc. 26, 295 (1971).

I. Tolstoy, "Infrasonic Fluctuation Spectra in the Atmosphere, Geophys. J.R. astr. Soc. 34, 343 (1973).

W.W. Troutman, "Numerical Calculation of the Pressure Pulse from a Lightning Stroke," J. Geophys. Res. 74, 4595 (1969).

I. Van der Hoven, "Power spectrum of horizontal wind speed in the frequency range from 0.0007 to 900 cycles per hour," J. Meteorol. 14, 160 (1957).

D.B. van Hulsteyn, "The Atmospheric Pressure Wave Generated by a Nuclear Explosion," Air Force Cambridge Research Laboratories Technical Report, AFCRL-64-184, February (1964).

D.B. van Hulsteyn, "The Atmospheric Pressure Wave Generated by a Nuclear Explosion: Part 1," J. Geophys. Res. 70, 257 (1965a).

D.B. van Hulsteyn, "The Atmospheric Pressure Wave Generated by a Nuclear Explosion: Part 2," J. Geophys. Res. 70, 271 (1965b).

T.G. Varghese and V. Kumar, "Detection and Location of an Atmospheric Nuclear Explosion by Microbarograph Arrays," Nature 225, 259 (1970).

R.A. Vincent, "A criterion for the use of the multi-layer approximation in the study of acoustic-gravity wave propagation," J. Geophys. Res. 74, 2996 (1969).

G. von dem Borne, Physik. Zeits. 11, 483 (1910).

H. Wagner and U. Ericsson, "Period and Amplitude in Atmospheric Gravity Waves from Nuclear Explosions," Nature 197, 994 (1963).

J.W. Wallace and P.V. Hobbs, Atmospheric Science: An Introductory Survey, Academic Press, Inc., New York (1977).

K. Weeks and M.V. Wilkes, "Atmospheric oscillations and the resonance theory," Proc. Roy. Soc. London A192, 80 (1947).

V.H. Weston, "The Pressure Pulse Produced by a Large Explosion in the Atmosphere," Can. J. Phys. 39, 993 (1961).

V.H. Weston, "Gravity and Acoustical Waves," Can. J. Phys. 40, 446 (1962).

V.H. Weston, "The Pressure Pulse Produced by a Large Explosion in the Atmosphere. Part II," Can. J. Phys. 40, 471 (1962).

V.H. Weston and D.B. van Hulsteyn, "The Effect of Winds on the Gravity Wave," Can. J. Phys. 40, 797 (1962).

J. Wescott and S. Kushner, "Acoustic background at the earth's surface," Acoust. Seismic Lab., Inst. Sci. Tech., Univ. of Michigan, Rept. 3746-35-F, February (1963).

H. Wexler and W.A. Hass, "Global Atmospheric Pressure Effects of the October 30, 1961, Explosion," J. Geophys. Res. 67, 3875 (1962).

F.J.W. Whipple, "The High Temperature of the Upper Atmosphere as an Explanation of the Zones of Audibility," *Nature* 111, 187 (1923).

F.J.W. Whipple, "The great Siberian meteor and the waves, seismic and aerial, which it produced," *Quart. J. Roy. Meteorol. Soc.* 56, 287 (1930).

F.J.W. Whipple, *Quart. J. Roy. Met. Soc.* 60, 510 (1934).

R.W. Whitaker, J.P. Mutschlecner, M.B. Davidson and S.D. Noel, "Infrasonic Observations of Large-Scale HE Events," in Fourth International Symposium on Long-Range Sound Propagation, NASA Langley Research Center, Hampton, VA, May 16-17, 1990.

R.W. Whitaker, S.D. Noel, J.P. Mutschlecner and M. Davidson, "Infrasonic Monitoring of UGTs and Earthquakes for Discrimination," Los Alamos National Laboratory Technical Report-LA-UR-92-2473, December (1992).

A.F. Wickersham, Jr. "Identification of Acoustic-Gravity Wave Modes from Ionospheric Range-Time Observations," *J. Geophys. Res.* 71, 4551 (1966).

R. Widmer and W. Zurn, "Bichromatic excitation of long-period Rayleigh and air waves by the Mount Pinatubo and El Chicon volcanic eruptions," *Geophys. Res. Lett.* 19, 765 (1992).

E. Wiechert, *Nach. Wiss. Gottingen* 1, 49 (1925).

A. Wiin-Nielsen, "On the propagation of gravity waves in a hydrostatic, compressible fluid with vertical wind shear," *Tellus* 17, 306 (1965).

M.V. Wilkes, Oscillations of the Earth's Atmosphere, Cambridge University Press, Cambridge, England (1949).

C.T.R. Wilson, "Investigations on lightning discharges and on the electric field of thunderstorms," *Phil. Trans. Roy. Soc.* 221A, 73 (1920).

M.V. Wilkes, Oscillations of the Earth's Atmosphere, Cambridge University Press, (1949).

C.R. Wilson and S. Nichparenko, "Infrasonic waves and auroral activity," *Nature* 214, 1299 (1967).

C.R. Wilson, "Infrasonic waves from the aurora; a shock wave model," *Nature* 216, 131 (1967).

C.R. Wilson, "Auroral Infrasonic Waves," *J. Geophys. Res.* (1969a).

C.R. Wilson, "Two-Station Auroral Infrasonic Wave Observations," *Planet. Space Sci.* (1969b).

C.R. Wilson, "Auroral Infrasonic Waves and Poleward Expansions of Auroral Substorms at Inuvik, N.W.T. Canada," *Geophys. J.R. astr. Soc.* 26, 179 (1971).

C.R. Wilson, **"Auroral Infrasonic Wave Generation Mechanism,"** J. Geophys. Res. 77, 1820 (1972)]

C.R. Wilson, **"Infrasonic wave generation by aurora,"** J. Atm. Terr. Phys. 37, 973 (1975).

C.R. Wilson, J.V. Olson and B.D. Spell, **"Natural Infrasonic Waves in the Atmosphere: their characteristics, morphology and detection,"** University of Alaska Technical Report ARS-95-039, Prepared for ENSCO Corporation, October 16, (1995).

M.W. Woodward and V.H. Goerke, **"Infrasound from the September 18, 1966, meteorite (abstract),"** EOS Trans. AGU 48, 81 (1967).

C.C. Wylie, **"Sounds from meteors,"** Popular Astronomy 40, 289 (1932).

R. Yamamoto, **"The Microbarographic Oscillations Produced by the Explosions of Hydrogen Bombs in the Marshall Islands,"** Bull. Am. Met. Soc. 37, 406 (1956).

R. Yamamoto, **"A dynamical theory of microbarographs oscillations produced by the explosions of hydrogen bombs,"** Met. Soc. Japan ser 2, 35, 288 (1957).

K.C. Yeh and C.H. Liu, **"Acoustic-Gravity Waves in the Upper Atmosphere,"** Rev. Geophys. Space Res. 12, 193 (1974).

J.M. Young, G.E. Greene and H.S. Bowman, **"Infrasound from thunderstorm, frontal systems and squalls,"** oral presentation given at the Western American Geophysical Union Meeting, San Francisco (1968).

J.M. Young and G.E. Greene, **"Infrasound Radiation from Severe Storms,"** J. Acoust. Soc. Am. 51, 137(A) (1972).

A.J. Zuckerwar, **"Infrasonic Emissions from Local Meteorological Events: A Summary of Data Taken Throughout 1984,"** NASA Langley Technical Memorandum 87686, February (1986).

## APPENDIX A: THE LAMONT-DOHERTY WAVEFORM LIBRARY

For completeness purposes, this appendix is included to reproduce the waveforms recorded from atmospheric nuclear explosions conducted by the U.S. and former Soviet Union and which were recorded on microbarograph instrumentation operated and deployed by the Lamont-Doherty Geological Observatory of Columbia, University and published by *Donn and Shaw* (1967).

The stations which recorded the tests made up a world-wide array of infrasonic stations and are listed in Table A1.

Table A1. The recording stations which made up the Lamont-Doherty world-wide infrasonic network. [Table reproduced from *Donn and Shaw* (1967).]

Station	Latitude	Longitude	Instrument
AZO, Terceira, Azores	38.77°N	27.22°W	Lamont type A microbarograph
BDA, Fort George, Bermuda	32.38°N	64.68°W	Lamont type B microbarograph
BRK, Berkeley, California	37.87°N	122.27°W	Lamont type A microbarograph
HKC, Hong Kong	22.30°N	114.17°E	Long-period vertical seismograph
HON, Ewa Beach, Hawaii	21.18°N	158.09°W	Lamont type A microbarograph
ICE, Thorlakshöfn, Iceland	63.87°N	21.37°W	Lamont type A microbarograph
IT3, Fletcher's Ice Island (T-3)	71.90°N	160.33°W	Lamont type A microbarograph
MTJ, Mt. Tsukuba, Japan	36.21°N	140.11°E	Long-period vertical seismograph
PAL, Palisades, New York	41.00°N	73.91°W	Lamont type A microbarograph
PER, Perth, Australia	31.95°S	115.83°E	Lamont type B microbarograph
PIE, Pietermaritzburg, South Africa	29.62°S	30.40°E	Lamont type B microbarograph
POU, Poughkeepsie, New York	41.67°N	73.88°W	Lamont type A microbarograph
RES, Resolute Bay, Canada	74.68°N	94.90°W	Long-period vertical seismograph
SUV, Suva, Fiji	18.15°S	178.45°E	Long-period vertical seismograph
WHP, Whippany, New Jersey	40.82°N	74.41°W	Lamont type A microbarograph

As discussed by *Donn and Shaw* (1967) "most of the recordings were made by the Lamont microbarograph which includes the Wallace transducer [the complete unit having been described by *Donn, Shaw and Hubbard* (1963) and *Donn, Pfeffer and Ewing* (1963)] and is called the Lamont type A microbarograph. This instrument, which provided most of the records in the catalog, was initially adjusted to give a response that was essentially flat from near zero to 300 sec, with a long period time constant of about 400 sec. At three of the stations (Bermuda, Perth, and Pietermaritzburg) an older Lamont pressure recorder

[described by *Ewing and Press* (1953)] was used and referred to in this report as Lamont type B microbarograph".

Since the time the Lamont-Doherty waveform catalog was published, the U.S. has declassified the yields and parameters for both its atmospheric and underground tests from the detonation of TRINITY in 1945 through 1992 [DOE (1994)]. Accordingly, the table which was published by *Donn and Shaw* (1967) listing U.S. atmospheric nuclear tests has been modified to incorporate the newer information. Table A2 provides, the listing for the tests conducted by the former Soviet Union and Table A3. provides the listing of U.S. tests for which waveforms are provided in the catalog. Figure A1 provides a map of the hypocenter distributions for the Soviet tests conducted at Novaya Zemlya.

Table A2. A listing of dates, times, location, reliability estimates, elevations and yields for the atmospheric tests conducted by the former Soviet Union. [Table adopted from *Donn and Shaw* (1967).]

Date	Time,	Latitude	Longitude	Reliability Estimate	Elevation	Yield *
Oct. 12, 1958	0753:19	71.84°N	58.84°E	Fair		High MT range
Oct. 15, 1958	0751:14	74.00°N	51.80°E	Poor		High MT range
Oct. 18, 1958	0951:05	73.97°N	53.05°E	Fair		High MT range
Oct. 22, 1958	0821:06	73.77°N	53.28°E	Fair		High MT range
Sept. 10, 1961	0900:14	73.84°N	52.00°E	Poor		Several MT
Sept. 14, 1961	0956:16	74.58°N	51.63°E	Fair		Several MT
Oct. 6, 1961	0700:09	73.79°N	53.18°E	Fair		Several MT
Oct. 23, 1961	0831:21	73.84°N	53.52°E	Good	About 12,000 ft	About 25 MT
Oct. 30, 1961	0833:28	73.82°N	53.57°E	Good	About 12,000 ft	55-60 MT
Oct. 31, 1961	0838:00	75.10°N	56.70°E	Poor		Several MT
Aug. 5, 1962	0908:44	73.89°N	53.64°E	Good	Atmosphere	30 MT
Aug. 20, 1962	0902:17	74.29°N	51.28°E	Poor	Atmosphere	Order of several MT
Aug. 22, 1962	0900:14	73.12°N	51.99°E	Poor	Atmosphere	Low MT
Aug. 25, 1962	0900:20	73.90°N	57.32°E	Poor	Atmosphere	Order of several MT
Aug. 27, 1962	0900:20	74.08°N	52.64°E	Fair	Atmosphere	Several MT
Sept. 8, 1962	1017:59	73.81°N	53.29°E	Fair	Atmosphere	MT
Sept. 15, 1962	0802:11	74.05°N	52.98°E	Fair	Atmosphere	Several MT
Sept. 16, 1962	1059:04	73.48°N	54.15°E	Fair	Atmosphere	Several MT
Sept. 19, 1962	1100:58	73.56°N	53.34°E	Good	Atmosphere	Multi-MT
Sept. 21, 1962	0801:33	71.85°N	49.59°E	Poor	Atmosphere	Few MT
Sept. 25, 1962	1302:27	73.13°N	55.40°E	Poor	Atmosphere	Multi-MT
Sept. 27, 1962	0803:11	73.49°N	54.86°E	Fair	Atmosphere	Less than 30 MT
Oct. 22, 1962	0906:13	74.00°N	53.25°E	Fair	Atmosphere	Several MT
Dec. 24, 1962	1111:45	73.96°N	54.87°E	Poor	Atmosphere	About 20 MT
Dec. 25, 1962	1335:59	73.67°N	54.66°E	Poor	Atmosphere	Few MT

\* All the large Soviet tests were in the Novaya Zemlya test area.

Table A.3. Data on U.S. Atmospheric Nuclear Detonations. [Data adopted from Donn and Shaw (1967).]

Name	Date	Time, GMT	Location*	Hypocenter		Elevation	Yield
				Latitude	Longitude		
Bravo	Feb. 28, 1954	1845:00	B.I.	11.69°N	165.27°E	Surface	15 MT
Yankee	May 4, 1954	1810:00	B.I.	11.67°N	165.39°E	Barge	13.5 MT
Tewa	July 20, 1956	1746:00	B.I.	11.68°N	165.39°E	Barge	5 MT
Arkansas	May 2, 1962	1801:30	C.I.	1.57°N	157.26°W	Air drop	1.09 MT
Questa	May 4, 1962	1904:55	C.I.	1.57°N	157.26°W	Air drop	670 KT
Frigate Bird	May 6, 1962	2330:20	C.I.	4.83°N	149.82°W	Missile launched from Polaris submarine	
Yukon	May 8, 1962	1801:22	C.I.	1.65°N	157.30°W	Air drop	100 KT
Medilla	May 9, 1962	1701:00	C.I.	1.65°N	157.30°W	Air drop	100 KT
Truckee	June 9, 1962	1537:20	C.I.	1.65°N	157.30°W	Air drop	210 KT
Yesso	June 10, 1962	1601:32	C.I.	1.60°N	157.26°W	Air drop	3 MT
Harlem	June 12, 1962	1537:21	C.I.	1.55°N	157.23°W	Air drop	1.2 MT
Rinconada	June 15, 1962	1600:57	C.I.	1.55°N	157.23°W	Air drop	800 KT
Bighorn	June 27, 1962	1519:17	C.I.	1.36°N	157.26°W	Air drop	7.65 MT
Palmico	July 11, 1962	1537:11	C.I.	1.43°N	157.24°W	Air drop	3.88 MT
Chama	Oct. 18, 1962	1601:18	J.I.	14.63°N	168.70°W	Air drop	1.59 MT
Bluegill Triple Prime	Oct. 26, 1962	0930:48	J.I.	16.42°N	169.60°W	Tens of km	Sub-MT
Calamity	Oct. 27, 1962	1546:27	J.I.	14.52°N	168.26°W	Air drop	800 KT
Housatonic	Oct. 30, 1962	1601:56	J.I.	13.61°N	172.22°W	Air drop	8.3 MT
Kingfish	Nov. 1, 1962	1210:06	J.I.	16.11°N	169.68°W	Tens of km	Sub-MT
Tightrope	Nov. 4, 1962	0730:00	J.I.	16.71°N	169.54°W	Tens of km	Low

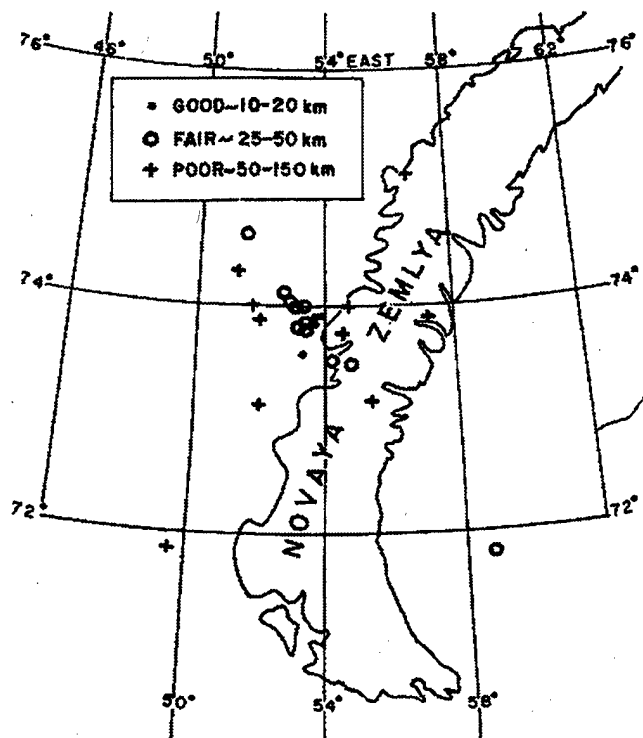


Figure A1. The hypocenter distribution for the tests conducted by the former Soviet Union at the Arctic island Novaya Zemlya. [Figure adopted from *Donn and Shaw (1967)*.]

*Donn and Shaw (1967)* provide the following comments regarding the catalog of records: "the pressure waves are arranged according to stations for each explosion. The test area is given first by a two-letter abbreviation, as in Tables A2 and A3. (All recorded United States tests were at Bikini Atoll, BI; Christmas Island, CI; and Johnson Island, JI. All Soviet tests were in the Novaya Zemlya region, NZ). The hypocenter coordinates and the date and time of the detonation (GMT) are on the line with the source identifier. Origin times to the nearest second for the United States tests were released by the AEC. Origin times computed for the Soviet tests are given the same precision".

"The stations for which we have records are arranged for each explosion according to the distance from the hypocenter, with the computed distance being given for each record. These values were determined with the use of standard Lamont seismological program for determining earthquake epicentral distances. If more than one set of waves were received at a given station from an explosion, they are labeled A1, A2, A3 and so



forth, with the A<sub>1</sub> set being the direct waves from the source, the A<sub>2</sub> being the wave train arriving after first traveling through the antipode, the A<sub>3</sub> being the second arrival of the direct (A<sub>1</sub>) waves, and so forth".

"Each trace is given with appropriate time marks and two or more labeled times. If the date of wave arrival is different from the explosion date, the date is also given with the recording. Most of the records are from the Lamont type A microbarograph and all such have the same scale. Some records, as indicated in Table A1, are from the type B microbarograph or from long-period seismographs. Although the time scales may differ, all records from the same station have the same scale and all the printed records have had the same reduction from the original. In order to clearly separate the groups of records from each other, a heavy line has been drawn below the last trace from each shot".

"The pressure records have all been arranged so that an increase of pressure is upward. No exact amplitude scale can be given because of the variety of types of instruments and of field maintenance conditions" [*Donn and Shaw (1967)*]"

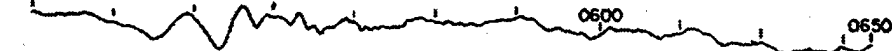
# The Lamont Catalog of Pressure Waves from Atmospheric Tests

## Catalog of Records of Pressure Waves from United States and Soviet Thermonuclear Explosions as Recorded by the Lamont Global Network of Sensitive Microbarograph

BI (11.69°N, 165.27°E) 28 FEB '54-18:45:00

PAL (11,611 km)

0415-1 March



BDA (12,801 km)

0545-1 March



BI (11.67°N, 165.39°E) 4 MAY '54-18:10:00

PAL (11,590 km)

0450-5 May

0515 0540



BDA (12,793 km)

0508-5 May

0600 0606



PIE (14,952 km)

0720-5 May

0800 0921



Az (25,088 km)

1545-5 May

1800 1827

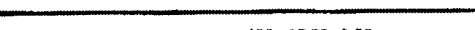


BI (11.66°N, 165.39°E) 20 JUL '56-17:46:00

PIE (11,532 km)

0700

0800



NZ (71.84°N, 58.84°E) 12 OCT '58-07:53:19.66

RES (3643 km)

1100

1115 1130

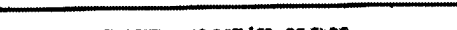


NZ (74.00°N, 51.80°E) 15 OCT '58-07:58:14

RES (3355 km)

1100

1115



NZ (73.97°N, 53.05°E) 18 OCT '58-09:51:05

ICE (2954 km)

1230

1240



RES (3367 km)

1300

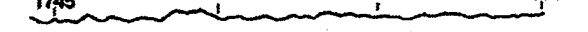
1315



BDA (7362 km)

1650

1700 1730



PIE (11,602 km)

2035

2100 2200 2245



PER (12,604 km)

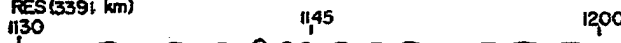
2030

2200



NZ(73.77°N, 53.28°E) 22 OCT '58 - 08:21:06

RES (3391 km)  
1130 1145 1200



PIE (11584 km)  
1845 2000 2045



PER (12585 km)  
1900 2030



NZ(73.84°N, 52.00°E) 10 SEP '61 - 09:00:14

IT3 (3676 km)  
1145 1245



MTJ (6122 km)  
1445 1445

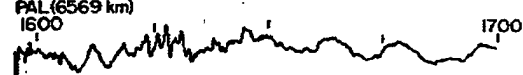


PAL (6644 km)  
1445 1630



NZ(74.58°N, 51.63°E) 14 SEP '61 - 09:56:16

PAL (6569 km)  
1600 1700




NZ(73.79°N, 53.18°E) 6 OCT '61 - 07:00:09

PAL (6674 km)  
1300 1400



NZ(73.84°N, 53.52°E) 23 OCT '61 - 08:31:21

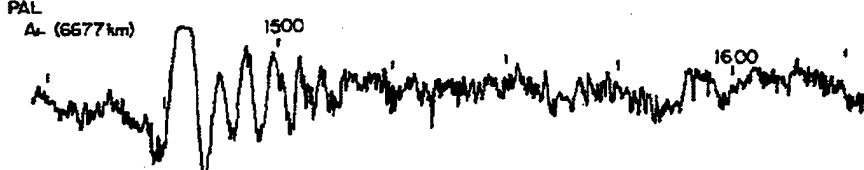
AZ0  
Az- (5628 km)  
1323 1408



Az- (34.412 km)  
1438 - 24 Oct. 1538



PAL  
Az- (6677 km)  
1500 1600

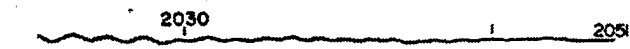


Az- (33363 km)  
1330 1430

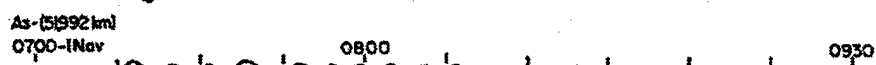
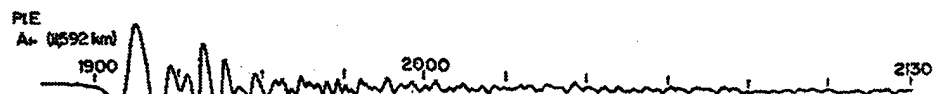
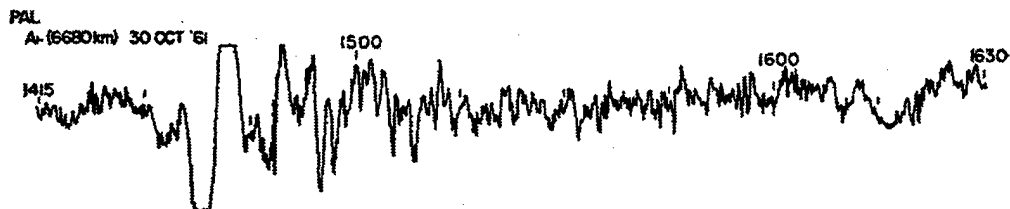
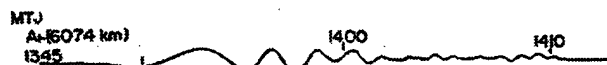
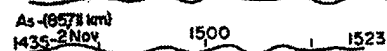
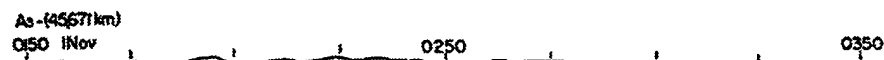
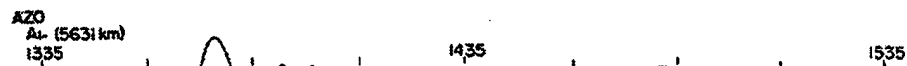


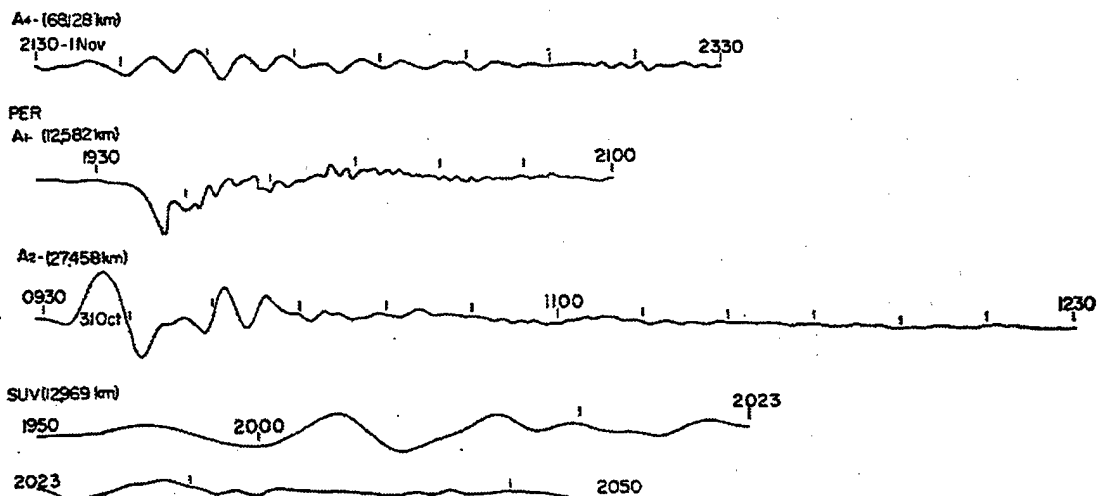
SUV (12909 km)  
1952 2015



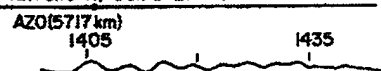


NZ (73.82°N, 53.57°E) 30 OCT '61 - 093328

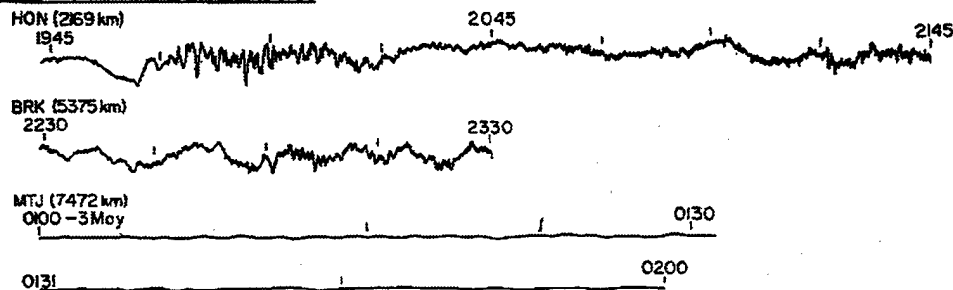




NZ (75.10°N, 56.70°E) 31 OCT '61 08:38:00



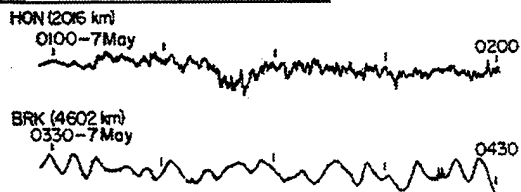
CI (157°N, 157.26°W) 2 MAY '62-18:01:30



CI (157°N, 157.26°W) 4 MAY '62-19:04:55



CI (483°N, 149.82°W) 6 MAY '62-23:30:20



CI(165°N, 15730°W) 8 MAY '62-180122



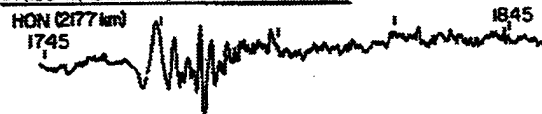
CI(165°N, 15730°W) 9 MAY '62-170100



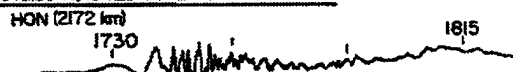
CI(165°N, 15730°W) 9 JUN '62-153720



CI(150°N, 15726°W) 10 JUN '62-160102



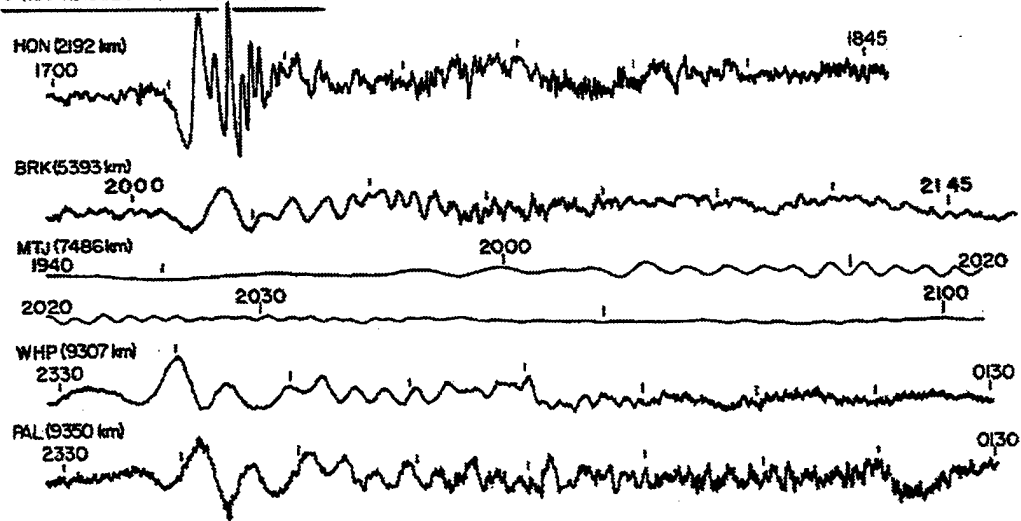
CI(155°N, 15723°W) 12 JUN '62-153721



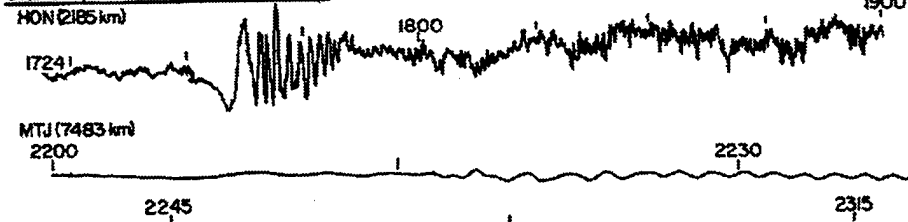
CI(155°N, 15723°W) 15 JUN '62-160057



CI(136°N, 15726°W) 27 JUN '62-151917



CI(143°N, 15724°W) 11 JUL '62-153711



NZ (73.89°N, 53.64°E) 5 AUG '62-090844

AZ0

A1- (5632 km)

1420 1517

A2- (34408 km)

1420-6 Aug 1618

MTJ (6071 km)

1420 1500

1515 1530

1545 1620

PAL

A1- (6675 km)

1445 1645

A2- (33365 km)

1445-6 Aug 1545

WHP

A1- (6705 km)

1445 1645

A2- (33335 km)

1500-6 Aug 1545

BRK

A1- (7610 km)

1545 1745

A2- (32430 km)

1400-6 Aug 1600

A3- (47650 km)

0330-7 Aug 0500

HON

A1- (9213 km)

1700 1830

A2- (30827 km)

1300-6 Aug 1430

PIE

A1- (11601 km)

1915 2115

Az- (28439 km)  
1445 - 6 Aug 1445

PER  
Az- (12584 km)  
2000 2200

Az- (27456 km)  
1100 - 6 Aug 1200

NZ(7429°N 5128°E) 20 AUG '62-0902:17

PAL(6593 km)  
1445 1545

WHP(6623 km)  
1445 1545

BRK(7560 km)  
1545 1645

HON(9208 km)  
1700 1800

PIE(11619 km)  
1915 2015

PER(12570 km)  
2000 2200

NZ(7312°N 5199°E) 22 AUG '62-0900:14

PAL(6701 km)  
1445 1545

WHP(6731 km)  
1445 1545

BRK(7693 km)  
1600 1730

HON(9314 km)  
1700 1800

NZ(7390°N 5732°E) 25 AUG '62-0900:20

PAL(6752 km)  
1500 1600

WHP(6781 km)  
1500 1600

BRK(7613 km)  
1545 1730

HON(9153 km)  
1700 1800



NZ(74.08°N, 52.64°E) 27 AUG '62-09:00:20

AZO(5605 km)

1400 1415

PAL(6639 km)

1500 1600

BRK(7588 km)

1530 1730

HON(9210 km)

1700 1900

PER(12622 km)

2000 2130

NZ(73.8°N, 53.29°E) 8 SEP '62-10:17:59

MTJ(6083 km)

1520 1600

1615

1630

1645

1715

POU(6602 km)

1615 1715

PAL(6674 km)

1615 1715

WHP(6704 km)

1615 1715

BRK(7619 km)

1645 1745

HON(9227 km)

1800 1930

PIE(11589 km)

2039 2239

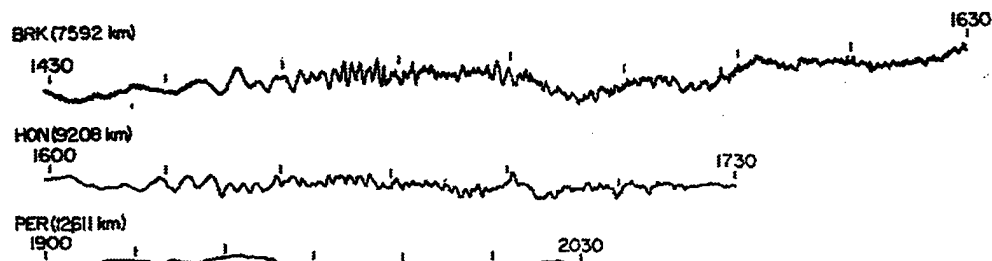
PER(12589 km)

2100 2200

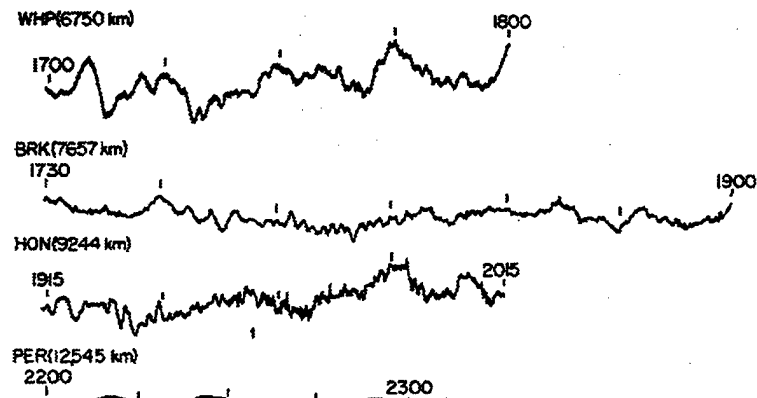
NZ(74.05°N, 52.98°E) 15 SEP '62-08:02:11

WHP(6679 km)

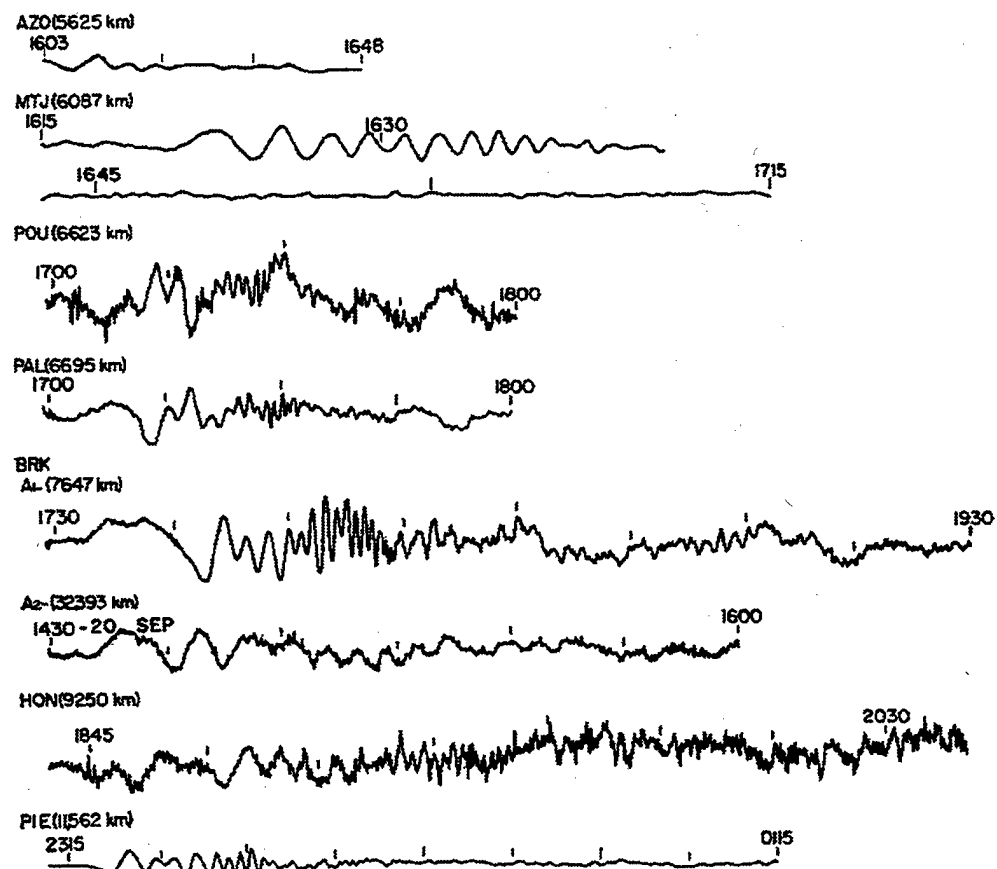
1400 1500



NZ (73.48°N, 54.15°E) 16 SEP '62-10:59:04



NZ (73.56°N, 53.34°E) 19 SEP '62-11:00:58



PER  
A<sub>1</sub> (12571 km)  
2200 0000

A<sub>2</sub> (22469 km)  
1200 -20 SEP 1400

NZ (71.85°N, 49.59°E) 21 SEP '62-08:01:33

POU (6670 km)  
1400 1500

PAL (6742 km)  
1400 1500

WHP (6773 km)  
1400 1500

BRK (7825 km)  
1500 1600

HON  
A<sub>1</sub> (9477 km)  
1600 1700

PIE (11342 km)  
1800 2000

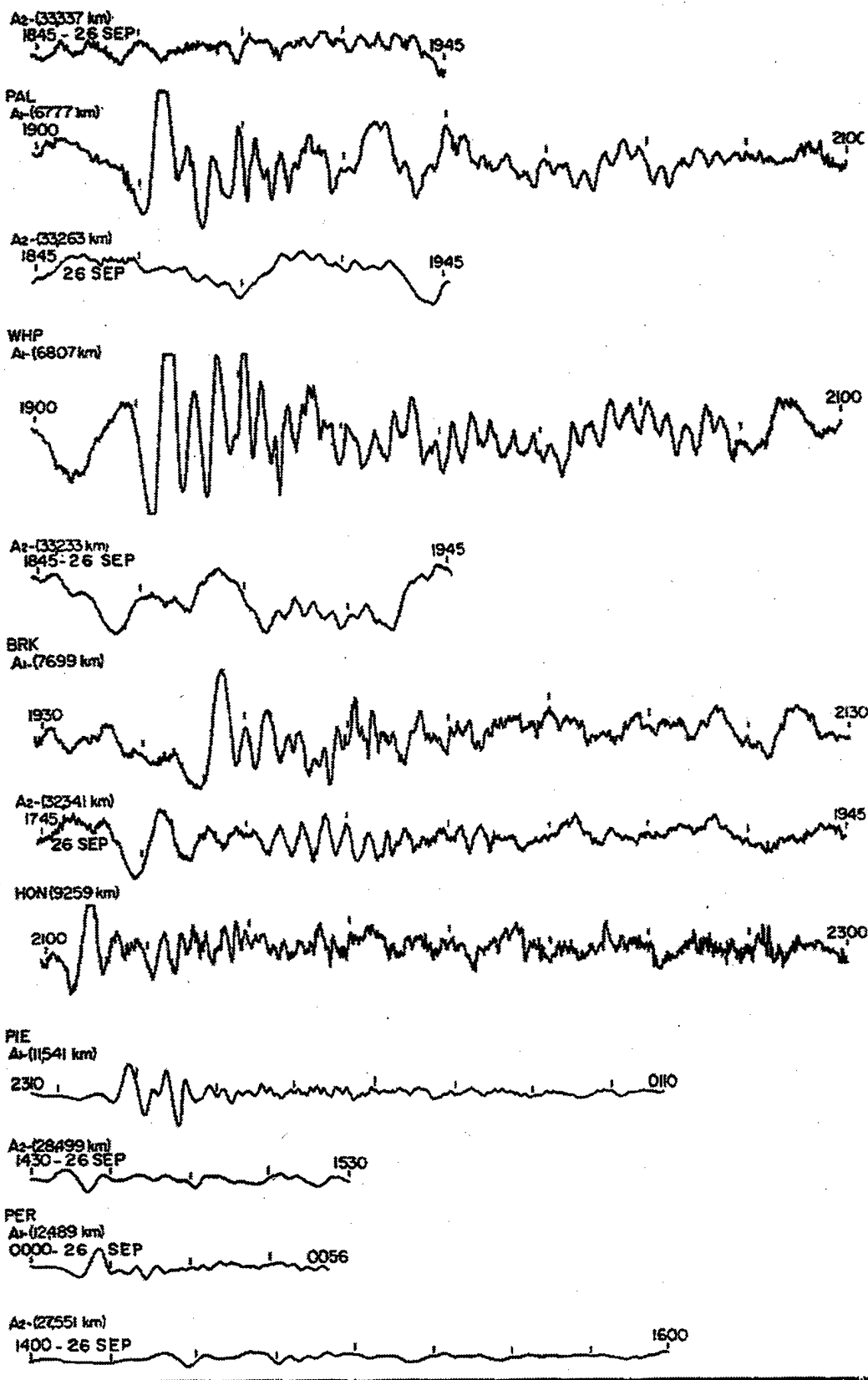
PER (12570 km)  
1900 2000

NZ (73.13°N, 55.40°E) 25 SEP '62-13:02:27

AZO (5695 km)  
1803 1903

MTJ (6028 km)  
1810 1900 1945 1930 2010

POU  
A<sub>1</sub> (6703 km)  
1900 2000



NZ(73.49°N 54.86°E) 27SEP '62-08:03:11

AZO(5680 km)

1306 1351

MTI(6040 km)

1310 1345 1330 1410

POU(6662 km)

1400 1600

PAL

Az-(6734 km)

1400 1600

Az-(33306 km)

28 SEP

1400 1500

WHP(6764 km)

1400 1600

BRK

Az-(7657 km)

1445 1645

Az-(32383 km)

1715-28 SEP 1800

HON

Az-(9232 km)

1545 1730

Az-(30908 km)

1145-28 SEP 1300

PIE(11573 km)

1820 2030

PER

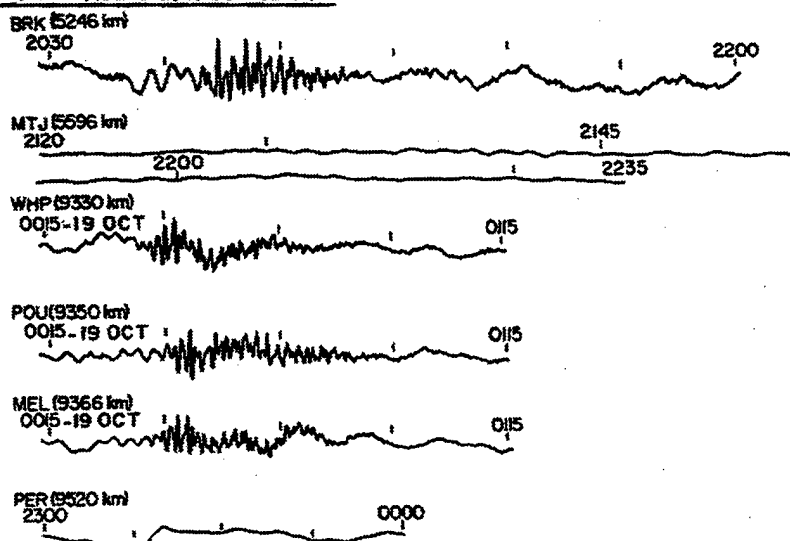
Az-(12528 km)

1900 2100

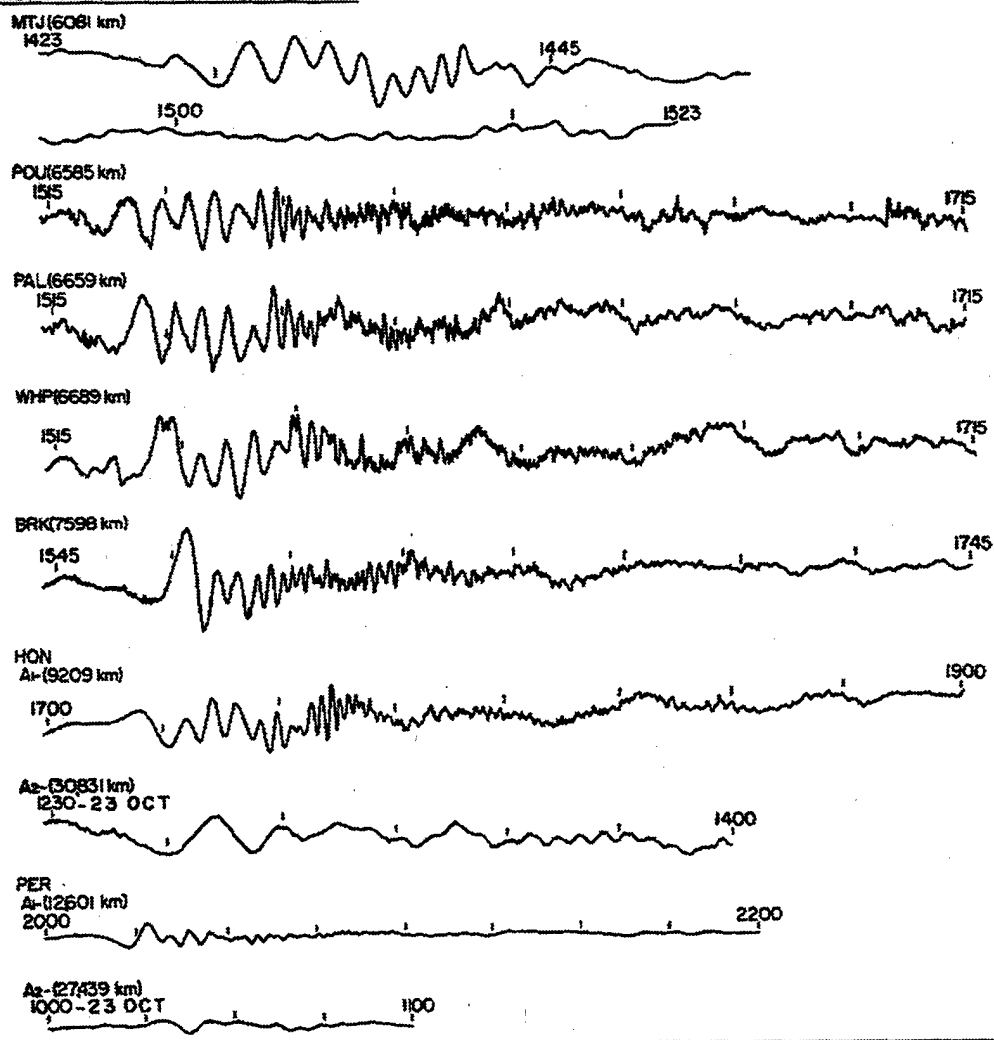
Az-(27512 km)

0900-28SEP 1100

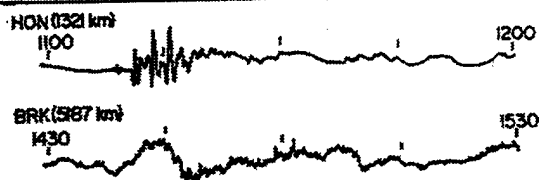
J1 (14.53°N, 168.79°W) 18 OCT '62-16:018



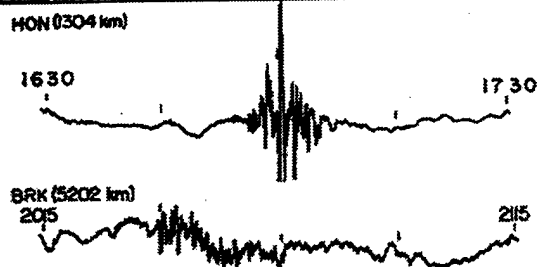
NZ (74.00°N, 53.25°E) 22 OCT '62-09:0613



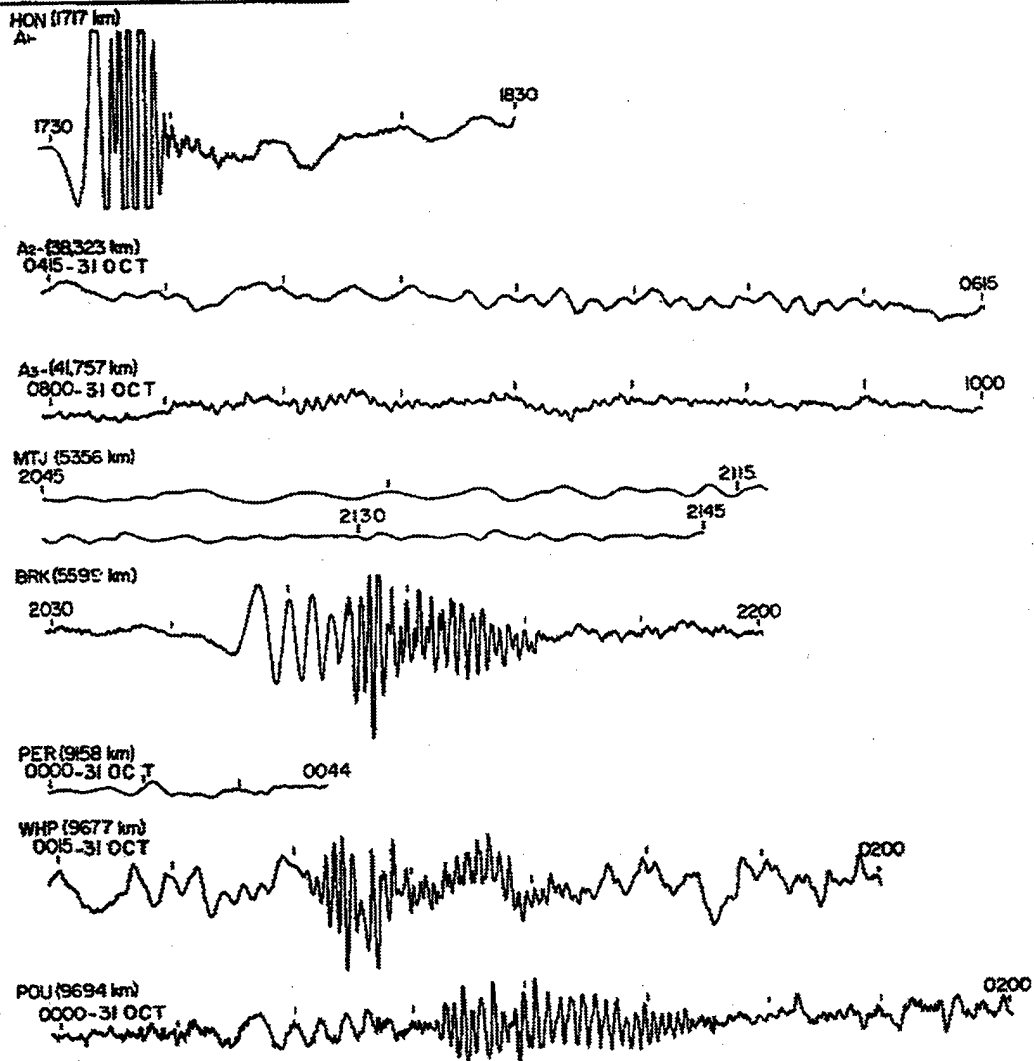
J1(16.42°N, 159.60°W) 26 OCT '62-09:59:48

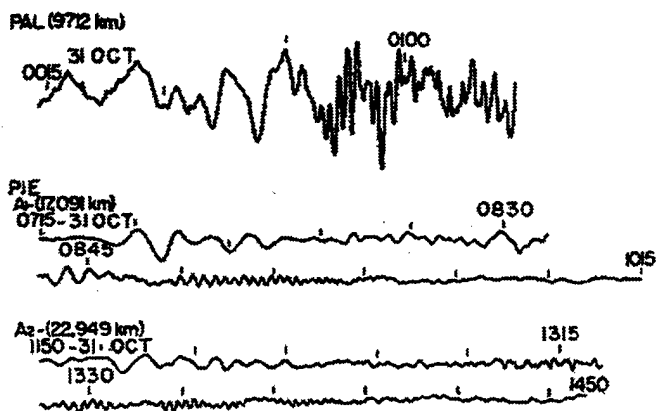


J1(14.52°N, 168.26°W) 27 OCT '62-15:46:27



J1(13.6°N, 172.22°W) 30 OCT '62-16:01:56





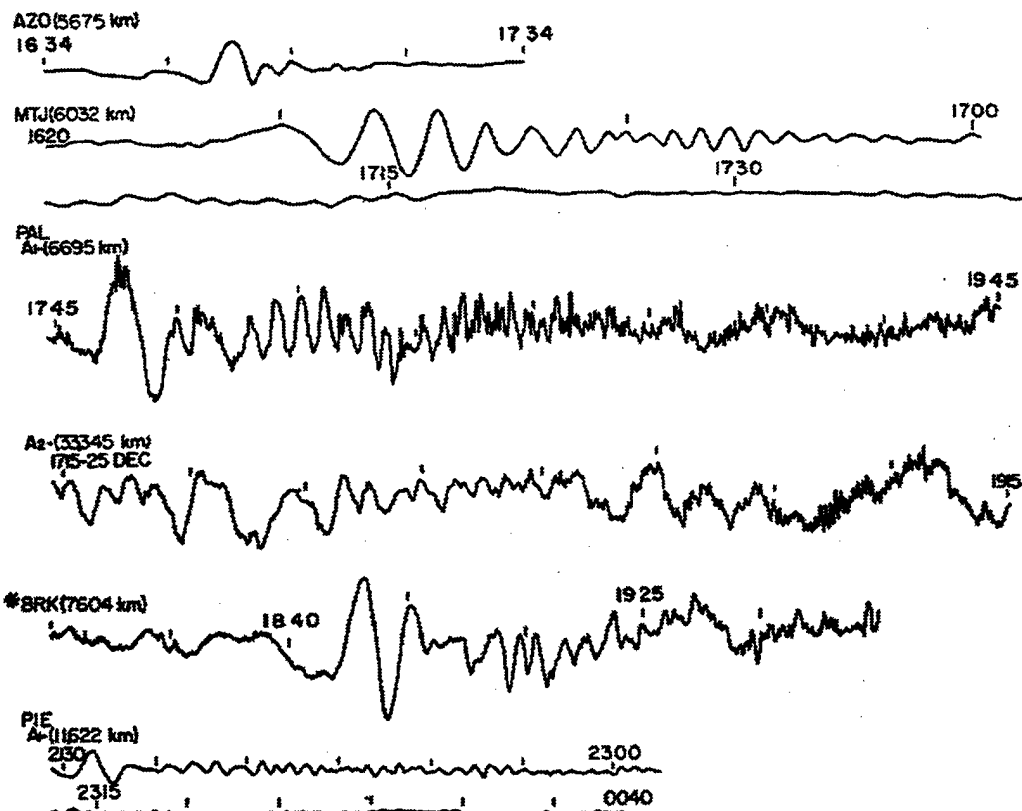
J1 (16.11°N, 169.68°W) 1 NOV '62-21:00



J1 (16.71°N, 169.54°W) 4 NOV '62-07:30:00



NZ (73.96°N, 54.87°E) 24 DEC '62-11:11:45





Az-(28418 km)  
1321 25 DEC 1345 1411

PER  
A-(12559 km)  
2200 2330

Az-(27481 km)  
1300-25 DEC 1500

---

NZ(73.67°N, 54.66°E) 25 DEC '62-13:35:59

PAL(6715 km)  
2030 2200

WHP(6745 km)  
2030 2200

BRK(7637 km)  
2000 2100

PIE(11589 km)  
0000 0200

---

Gerald Afflerback  
ASC  
Detachment 3, 1031 S. Hwy. A1A  
Patrick AFB, FL 32925  
USA

Don Albert  
U.S. Army, CRREL  
72 Lyme Road  
Hanover, NH 03755-1290USA

Terrance Barker  
Maxwell Technologies  
8888 Balboa Ave.  
San Diego, CA 92123  
USA

Jonathan Berger  
IGPP/SIO  
9500 Gilman Dr.  
La Jolla, CA 92093-0225  
USA

Robert Blandford  
AFTAC  
Suite 1450, 1300 N17th St.  
Arlington, VA 22209  
USA

David Brown  
Australian National University  
Research School of Earth Sciences  
Canberra, ACT 0200  
Australia

Edwin Bullard  
Chaparral Physics Consultants  
7405 Capulin Road NE  
Albuquerque, NM 87109  
USA

Leslie Casey  
U.S. Department of Energy  
NN-20, 1000 Independence Av., SW  
Washington, DC 20585-0420  
USA

Douglas Christie  
Provisional Technical Secretariat, CTBTO  
Vienna Int'l. Center, P.O. Box 1200  
Vienna, A-1400  
Austria

Pierce Corden  
Arms Control and Disarmament Agency  
3020 21st St. NW, Rm. 5499, MA/NTP  
Washington, DC 20451  
USA

Haydar Al-Shukri  
ENSCO Inc.  
445 Pineda Court  
Melborne, FL 32940  
USA

William Armstrong  
Los Alamos National Laboratory  
EES-8, MS F659  
Los Alamos, NM 87545  
USA

Al Bedard  
NOAA, Environmental Tech. Laboratory  
Mail Code R/E/ET4 325 Broadway  
Boulder, CO 80303-3328  
USA

Elisabeth Blanc  
Commissariat A L'Energie Atomique  
Laboratoire de Detection et de Geophysique BP 12,  
Bruyeres le Chatel, 91680  
France

Dale Breeding  
Sandia National Laboratories  
MS 0979, Org. 5704  
Albuquerque, NM 87185  
USA

Wendee Brunish  
Los Alamos National Laboratory  
EES-DO, MS F659  
Los Alamos, NM 87545  
USA

Peter Cable  
BBN Systems and Technologies  
Union Station  
New London, CT 06320  
USA

Luis Cella  
Autoridad Regulatoria Nuclear (ARN)  
Av.del Libertador 8250  
Buenos Aires 1429,  
Argentina

Dean Clauter  
HQ AFTAC/TTR  
1030 South Highway A1A  
Patrick AFB, FL 32925-3002  
USA

Ola Dahlman  
Vienna International Center  
P.O Box 1200  
Vienna A-1400,  
Austria

Kalpak Dighe  
Los Alamos National Laboratory  
PO Box 1663, MS C300  
Los Alamos, NM 87545  
USA

Milton Garcés  
University of Alaska  
903 Koyukuk Dr., P.O Box 757320  
Fairbanks, AK 99775-7320USA

Georgui Golitsyn  
Institute of Physics of the Atmosphere RAS  
3 Pyshevsky  
Moscow, 109017  
Russia

K. Guthrie  
Defense Scientific Establishment  
Private Bag 3290  
Auckland,  
New Zealand

Vincent Harman  
ASC/RAKBS  
Building 557 2640 Loop Road West  
Wright Patterson AFB, OH 45433-7607

David Havelock  
National Research Council Canada  
M-36 Montreal Road  
Ottawa, ONT K1A OR6  
Canada

Eugene Herrin  
Southern Methodist University  
P.O Box 395, SMU Dept of Geology  
Dallas, TX 75275  
USA

Mark Hodgson  
Los Alamos National Laboratory  
MS D460  
Los Alamos, NM 87545  
USA

James Hunter, Jr.  
University of Florida  
414 NE 6th St.  
Gainesville, FL 32601  
USA

Rong-Song Jih  
Defense Special Weapons Agency  
HQ DSWA/PMP, 6801 Telegraph Road  
Alexandria, VA 22310  
USA

Pierre-Andre Duperrex  
Defense Procurement Agency  
FS 161 Stauffacherstrasse 65  
3000 Bern 22,  
Switzerland

Robert Gibson  
BBN Corporation  
1300 N. 17th St., Suite 1200  
Arlington, VA 22209  
USA

Gerhard Graham  
Council for Geoscience  
Private Bag X112  
Pretoria, 0001  
South Africa

Heinrich Haak  
Royal Netherlands Meteorological Institute  
Seismology Division, P.O. Box 201  
DeBilt, 3730 AE  
Netherlands

Gernot Hartmann  
BGR Hannover  
Postfach 510153  
30631 Hannover,  
Germany

Michael Hedlin  
University of California San Diego  
9500 Gilman Drive  
La Jolla, CA 92093-0225  
USA

Preston Herrington  
Sandia National Laboratories  
P.O Box 5800, MS 0655  
Albuquerque, NM 87185-0655  
USA

Wolfgang Hoffmann  
Vienna International Centre  
P.O Box 1200, Room E0754  
Vienna A-1400,  
Austria

Kevin Hutchenson  
ENSCO Inc.  
445 Pineda Court  
Melbourne, FL 32940  
USA

Charles Katz  
Science Applications International Corporation  
10260 Campus Point Drive  
San Diego, CA 92121  
USA

Robert Kemerait  
HQ/AFTAC  
AFTAC/TT, 1930 Highway A1A  
Patrick AFB, FL 32925  
USA

Sergey Kulichkov  
Institute of Atmospheric Physics  
3 Pyzevsky  
Moscow, 109017 Russia

Peter Marshall  
Ministry of Defense  
Blacknest/Brimpton  
Reading F67-4RS,  
UK

David McCormack  
Geological Survey of Canada  
1 Observatory Crescent  
Ottawa, ONT KIA 0Y3  
Canada

Richard Morrow  
U.S. Arms Control and Disarmament Agency  
320 21st.  
Washington, DC 20451  
USA

Timothy Murphy  
ACIS  
7105 Norwalk St.  
Falls Church, VA 22043  
USA

Vladimir Ostashev  
New Mexico State University  
Department of Physics, Box 30001 / Dept. 3D  
Las Cruces, NM 88003-8001  
USA

Oleg Raspopov  
Russian Academy of Sciences  
Terrestrial Magnetism, Ionosphere and Radio Waves Prop., Box 188  
St. Petersburg, 191023 Russia  
Russia

Douglas Revelle  
Los Alamos National Laboratory  
P.O. Box 1663, MS F659  
Los Alamos, NM 87545  
USA

David Russell  
HQ/AFTAC/TTR  
Air Force Tech. Applications Center 1030 S. Highway A-1A  
Patrick AFB, FL 32925-3002  
USA

Richard Kromer  
Sandia National Laboratories  
MS 0655  
Albuquerque, NM 87185  
USA

Ludwik Liszka  
Swedish Institute of Space Physics  
Sorfors 634  
UMEA, S-90588  
Sweden

Bernard Massinon  
Laboratoire de Detection et de Geophysique  
Centre de Bruyeres-le-Chatel BP 12  
Bruyeres le Chatel, 91680  
France

J. Michael McKisic  
TRACOR Applied Sciences  
1601 Research Boulevard  
Rockville, MD 20850-3191  
USA

Philip Munro  
Geological Survey of Canada  
1 Observatory Crescent  
Ottawa, ONT KIA 0Y3  
Canada

Joseph Mutschlecner  
Los Alamos National Laboratory  
121 Sierra Vista  
Los Alamos, NM 87544  
USA

Frank Pilotte  
AFTAC/TT  
1030 South Highway A1A  
Patrick AFB, FL 32925-3002  
USA

Terrill Ray  
U.S Arms Control and Disarmament Agency  
320 21st. Street NW  
Washington, DC 20451  
USA

Jose Roca  
Autoridad Regulatoria Nuclear (ARN)  
Av. del Libertador 8250  
Buenos Aires 1429,  
Argentina

Tom Sandoval  
Bechtel/Nevada  
P.O Box 809  
Los Alamos, NM 87544  
USA

David Simons  
Los Alamos National Laboratory  
PO Box 1663, MS D460  
Los Alamos, NM 87545  
USA

Warwick Smith  
Institute of Geological and Nuclear Science  
P.O. Box 30-368  
Lower Hutt, New Zealand

Bruno Stork  
Fed. Inst. for Geosciences and Natural Res.  
Stilleweg 2  
Hannover, 30655  
Germany

Vladimir Timofeev  
Cabinet of Ministers of Ukraine  
Deputy Chief, Dept. on Issues of Technology, Ecology, Safety and  
Civil Protection M. Hrushevsky St., 12/2  
Kyjiv-002,  
Ukraine  
Alberto Veloso  
Preparatory Commission for CTBTO  
P.O Box 1250  
Vienna A-1400,  
Austria

Joseph Wheeler  
Boeing Company  
PO Box 21233  
Kennedy Space Center, FL 32813  
USA

Raymond Willemann  
Center for Monitoring Research  
1300 North 17th Street, Suite 1450  
Arlington, VA 22209  
USA

Jin Lai Xie  
Chinese Academy of Sciences  
Institute of Acoustics, P.O Box 2712  
Beijing 100080,  
China

Eugene Smart  
HQ/AFTAC/TTR  
Air Force Tech. Applications Center 1030 S. Highway A-1A  
Patrick AFB, FL 32925-3002  
USA

David Spell  
609 Chena Ridge Road  
Fairbanks, AK 99709  
USA

Alexander Sytolenko  
Cabinet of Ministers of Ukraine  
Chief, National Space Agency of Ukraine, M. Hrushevsky St., 12/2  
Kyjiv-002,  
Ukraine

Lawrence Trost  
Sandia National Laboratories  
Org. 5415, MS-0425, Sandia National Laboratories  
Albuquerque, NM 87185  
USA

Robert Waldron  
Department of Energy  
NN-20 1000 Independence Ave. SW  
Washington, DC 20585-0420  
USA

Rodney Whitaker  
Los Alamos National Laboratory  
EES-8 MS F659  
Los Alamos, NM 87545  
USA

Charles Wilson  
University of Alaska  
Geophysical Institute, 1812 Musk Ox Trail  
Fairbanks, AK 99709  
USA

Zhao Hua Xie  
Chinese Academy of Sciences  
Computer Network Info. Ctr, P.O Box 2719  
Beijing 100080,  
China